Institut für Physik und Astronomie
Astrophysik I

Comprehensive analyses of massive binaries and implications on stellar evolution

Kumulative Dissertation
zur Erlangung des akademischen Grades
“doctor rerum naturalium”
(Dr. rer. nat.)
in der Wissenschaftsdisziplin Astrophysik

eingereicht an der
Mathematisch-Naturwissenschaftlichen Fakultät
der Universität Potsdam

von
Tomer Shenar

Potsdam, den 02. September 2016

Published online at the
Institutional Repository of the University of Potsdam:
URN urn:nbn:de:kobv:517-opus4-104857
http://nbn-resolving.de/urn:nbn:de:kobv:517-opus4-104857

Abstract (English / Deutsch)

Via their powerful radiation, stellar winds, and supernova explosions, massive stars ($M_{\rm ini} \gtrsim 8\,M_{\odot}$) bear a tremendous impact on galactic evolution. It became clear in recent decades that the majority of massive stars reside in binary systems. This thesis sets as a goal to quantify the impact of binarity (i.e., the presence of a companion star) on massive stars. For this purpose, massive binary systems in the Local Group, including OB-type binaries, high mass X-ray binaries (HMXBs), and Wolf-Rayet (WR) binaries, were investigated by means of spectral, orbital, and evolutionary analyses.

The spectral analyses were performed with the non-local thermodynamic equillibrium (non-LTE) Potsdam Wolf-Rayet (PoWR) model atmosphere code. Thanks to critical updates in the calculation of the hydrostatic layers, the code became a state-of-the-art tool applicable for all types of hot massive stars (Chapter 2). The eclipsing OB-type triple system δ Ori served as an intriguing test-case for the new version of the PoWR code, and provided key insights regarding the formation of X-rays in massive stars (Chapter 3). We further analyzed two prototypical HMXBs, Vela X-1 and IGR J17544-2619, and obtained fundamental conclusions regarding the dichotomy of two basic classes of HMXBs (Chapter 4). We performed an exhaustive analysis of the binary R 145 in the Large Magellanic Cloud (LMC), which was claimed to host the most massive stars known. We were able to disentangle the spectrum of the system, and performed an orbital, polarimetric, and spectral analysis, as well as an analysis of the wind-wind collision region. The true masses of the binary components turned out to be significantly lower than suggested, impacting our understanding of the initial mass function and stellar evolution at low metallicity (Chapter 5). Finally, all known WR binaries in the Small Magellanic Cloud (SMC) were analyzed. Although it was theoretical predicted that virtually *all* WR stars in the SMC should be formed via mass-transfer in binaries, we find that binarity was not important for the formation of the known WR stars in the SMC, implying a strong discrepancy between theory and observations (Chapter 6).

Durch ihre intensive Strahlung, Sternwinde und Supernovaexplosionen tragen massereiche Sterne ($M_{\rm initial} \gtrsim 8\,M_{\odot}$) erheblich zur Entwicklung von Galaxien bei. In den letzten Jahren wurde es immer klarer, dass sich die Mehrheit der massereichen Sterne in Doppelsternsystemen befindet. Die vorliegende Doktorarbeit hat das Ziel, den Einfluss dieser Tatsache auf die Entwicklung massereicher Sterne quantitativ zu untersuchen. Um dies zu erreichen, haben wir eine Analyse der Umläufe, Spektren und Entwicklung verschiedener Doppelsternsysteme in der lokalen Gruppe durchgeführt, die OB-Sterne, massereicher Röntgendoppelsterne (HMXBs) und Wolf-Rayet-(WR)-Doppelsterne einschließt.

Die Spektralanalyse wurde mithilfe des Potsdam-Wolf-Rayet-(PoWR)-Modellatmosphären-Programms für Strahlungstransport in Abwesenheit von lokalem thermodynamischen Gleichgewicht (non-LTE) durchgeführt. Das PoWR-Programm wurde im Laufe der Arbeit aktualisiert, sodass die Berechnung der hydrostatischen Schichten des Sternes nun wesentlich genauer erfolgt, was die Verwendung dieses Programms für alle Typen heißer massereicher Sterne erlaubte (Kapitel 2). Das bedeckungsveränderliche Dreifachsternsystem δ Ori diente als Test für diese neue Version von PoWR, und lieferte wesentliche Informationen bezüglich der Entstehung von Röntgenstrahlung in massereichen Sternen (Kapitel 3). Die Analyse zweier prototypischer massereicher Röntgendoppelsterne, Vela X-1 und IGR J17544-2619, machte den Ursprung der Dichotomie der zwei Hauptklassen der Röntgendoppelsterne deutlich (Kapitel 4). Eine umfassende Analyse des Doppelsterns R 145 in der Großen Magellanschen Wolke (LMC), der angeblich aus den massereichsten uns bekannten Sternen besteht, wurde durchgeführt. Mithilfe einer Dekomposition des Spektrums, einer Orbital- und Spektralanalyse, sowie einer Analyse der Kollision von Sternwinden in diesem System konnten wir zeigen, dass die Massen der Komponenten wesentlich kleiner sind als bisher angenommen. Dies ist ein wichtiger Beitrag zu unserem Verständnis der Anfangsmassenfunktion und der Entwicklung massereicher Sterne in Umgebungen geringer Metalizität (Kapitel 5). Schließlich wurde die Gesamtpopulation der WR-Doppelsterne in der Kleinen Magellanschen Wolke (SMC) analysiert. Im Widerspruch zur theoretischen Vorhersage, alle WR-Doppelsterne in der SMC seien dank Massentransfer in Doppelsternsystemen entstanden, finden wir, dass Massentransfer unerheblich für die Entstehung der uns bekannten WR-Sterne in der SMC war (Kapitel 6).

CONTENTS

Chapter 1.

Introduction

Few objects can be said to relate to as many astrophysical phenomena as massive stars ($M_\mathrm{i} \gtrsim 8\,M_\odot$). Be it chemical enrichment, supernovae and Gamma-ray bursts (GRBs), star formation, galactic evolution, relativistic physics of compact objects such as neutron stars (NS) or black holes (BHs), or gravitational waves (GWs): it the physics of massive stars that underlies the properties of these phenomena. Thus, albeit rare, massive stars bear an enormous impact on stellar and galactic evolution. Nonetheless, our understanding of the evolution and life cycle of massive stars remains largely hampered with unresolved issues. A central question in modern research of massive stars concerns the impact of binarity (i.e. the presence of a companion star) on the evolution of massive stars. This thesis aims to provide new insights regarding this question, focusing primarily on massive Wolf-Rayet (WR) stars.

All massive stars exhibit stellar winds - a continuous flow of matter emanating from the stellar surface and ejected into the star's environment - though their strengths can vary over several orders of magnitude. These winds are generally understood to be radiatively driven (Beals 1929; Lucy & Solomon 1970; Castor et al. 1975). The most direct consequence of stellar winds is that stars lose mass, adjusting their internal structure and properties accordingly. Besides the continuous mass-loss, massive stars may also shed a significant amount of their mass in eruptive processes (Smith 2014). Stars may lose more mass due to stellar winds during their lifetime than they consume during nuclear burning, making mass-loss a key driver for the evolution of massive stars.

OB-type stars typically have mass-loss rates in the range $-8 \lesssim \log \dot{M} \lesssim -6\,[M_\odot/\mathrm{yr}]$, their winds reaching terminal velocities of the order of $1000 - 2000\ \mathrm{km\,s^{-1}}$. Massive WR stars, which are commonly understood to be the descendents of O stars (Sect. 1.2), have some of the strongest stellar winds known, with mass-loss rates in the range $-5 \lesssim \log \dot{M} \lesssim -4\,[M_\odot/\mathrm{yr}]$ and expansion velocities of $1000 - 5000\,\mathrm{km\,s^{-1}}$. As most WR stars are evolved stars which have suffered extreme mass-loss, their spectra typically show evidence for nuclear burning products and strong hydrogen-depletion. Hydrogen-free WR stars are suggested to be the progenitors of type Ib/c supernovae (Woosley et al. 1993; Langer 2012; Groh et al. 2013), although no direct link has been established yet. With the help of modern model atmospheres such as those generated by the Potsdam Wolf-Rayet (PoWR) code (Gräfener et al. 2002; Hamann & Gräfener 2004), used extensively in my thesis, physical parameters of massive stars and their winds can be derived (e.g., Hillier & Miller 1998; Kubát et al. 1999).

The evolutionary course of a massive star in isolation is determined primarily by its initial mass M_i, along with the initial metallicity content Z_i and rotation $v_{\mathrm{rot,\,i}}$. Despite tremendous advances in recent decades, many questions persist regarding the detailed influence of the metallicity content, rotation, convection, and magnetic fields on the structure and evolution of massive single stars and their winds (Maeder et al. 2008; Muijres et al. 2012; Gräfener & Vink 2013; Hainich et al. 2014). The situation worsens significantly, however, if one considers the fact that the majority of massive stars do not reside in isolation, but rather in binary or multiple systems (Maíz Apellániz 2010; Sana et al. 2012; Sota et al. 2014; de Mink et al. 2014; Aldoretta et al. 2015). As far as the incidence of binarity goes, massive WR stars are no exception: At least 40 % of the known WR stars are binaries (van der Hucht 2001; Foellmi et al. 2003a,b). The real binary fraction is likely larger due to observational bias (de Mink et al. 2014). The companions to WR stars in confirmed binaries are almost always OB-type stars.

By far the most important form of binary interaction is mass-transfer during Roche lobe overflow (RLOF). In a binary, each star is surrounded by an imaginary critical surface called a "Roche lobe", its apex coinciding with the inner Langrangian point. Once a star becomes larger than its Roche lobe, RLOF occurs, and matter starts flowing from it onto its companion. During several thousand years (a fraction of

the stellar lifetime), a significant fraction of the donor's mass may be transferred to the secondary or lost from the system. This can completely alter the evolutionary path of both companions. According to Sana et al. (2012), at least 70% of the massive stars would interact with a companion via mass-transfer during their lifetime. Hence, a true understanding of the evolution of massive stars is incomplete without a proper understanding of binary interaction.

Binaries make the analysis as well as interpretation of observations significantly more difficult. However, they also offer a unique laboratory for measuring orbital stellar masses. A construction of radial velocity (RV) curves for both binary components in a spectroscopic binary enables the measurement of stellar masses using simple Newtonian dynamics. This is the only reliable way to derive stellar masses of massive stars, and so it serves as a critical calibration for existing models.

Binary evolution offers an alternative formation channel for WR stars (see Sect. 1.2 and 1.3). Instead of getting rid of its hydrogen-rich envelope via stellar wind ("The Conti scenario", Conti 1976), a star can remove its outer layers during RLOF in a binary system. The resulting "stripped" star should be hydrogen depleted and be overluminous for its mass, i.e., it should have the characteristics of a WR star (Paczynski 1973). One of the research questions of my thesis is: How important is this formation channel? This would depend on both the frequency with which RLOF occurs, as well as on the efficiency of stellar winds and/or eruptions to remove the outer layers of a massive star. Hence, studying the structure and properties of stellar winds is intimately related to the impact of binarity on massive stars.

The series of papers presented in this thesis involves different aspects concerning WR binaries, their progenitors and their descendents. The papers "On the consistent treatment of the quasi-hydrostatic layers in hot star atmospheres" (Chapter 2) and "A coordinated X-ray and Optical Campaign of the Nearest Massive Eclipsing Binary, δ Orionis Aa: A Multiwavelength, Non-LTE spectroscopic analysis" (Chapter 3) focus on the progenitors of WR stars, namely, OB-type stars, while the paper "Measuring the stellar wind parameters in IGR J17544-2619 and Vela X-1 constrains the accretion physics in Supergiant Fast X-ray Transient and classical Supergiant X-ray Binaries" (Chapter 4) involves their progenitors: high mass X-ray binaries (HMXB). We conclude the study with two extensive analyses of WR binaries in the Magellanic Clouds. In the paper "The Tarantula Massive Binary Monitoring project: II. A first SB2 orbital and spectroscopic analysis for the Wolf-Rayet binary R 145", we analyze a WR binary which was claimed to host the most massive star known, while in the paper "Wolf-Rayet stars in the Small Magellanic Cloud: Analysis of the binaries", we present an analysis of all known WR binaries in the Small Magellanic Cloud, drawing important conclusions on the impact of mass-transfer on WR stars.

1.1. Stellar winds

The high effective temperatures ($10\,\mathrm{kK} \lesssim T_* \lesssim 200\,\mathrm{kK}$) and luminosities ($4 \lesssim \log L/L_\odot \lesssim 7$) of massive stars imply an immense outflow of energetic photons. A large fraction of these photons get absorbed and scattered in the stellar atmosphere, leading to the formation of a radiatively driven stellar wind. Especially the iron elements group (e.g., Fe, Ni) contribute significantly to the opacity, although CNO ions, along with all other metal ions (i.e. ions belonging to elements heavier than helium) may contribute significantly to the line driving as well (Lucy & Solomon 1970; Castor et al. 1975). We know today that radiatively driven winds are ubiquitous among massive stars (see e.g., review by Kudritzki & Puls 2000). Integrated over their lifetime, massive stars can lose more than half their original mass via stellar winds or eruptions, implying that mass-loss is an important - if not a dominant - driver of the evolution of a massive star (Hamann et al. 1995; Smith 2014). Hence, a complete understanding of the evolution of massive binaries is impossible without a proper consideration of the impact of stellar winds on massive stars.

Spectroscopically, stellar winds manifest in mainly in two forms: P-Cygni profiles and emission lines stemming from recombination. P-Cygni profiles are most evident in UV spectra and are associated primarily with resonance lines, i.e. lines whose low transitional state is the ground state of the corresponding ion. Recombination lines are more common in optical spectra, typically seen in the hydrogen Balmer series and He lines.

Because mass-loss increases with increased surface opacity, changes in the chemical composition of the stellar atmosphere can change the properties of the stellar wind. The mass-loss of stars depends on their

initial metallicity content (e.g., Vink et al. 2000), a fact which was empirically confirmed (e.g., Crowther & Hadfield 2006; Mokiem et al. 2007; Hainich et al. 2014). Thus, in galaxies such as the Large and Small Magellanic Clouds (LMC and SMC), characterized by metallicity content which is roughly a factor 1/2 and 1/10 solar, respectively (Hunter et al. 2007; Trundle et al. 2007), we expect stars of a given mass and luminosity to exhibit significantly lower mass-loss rates compared to their Galactic counterparts.

The most fundamental property characterizing stellar winds is the mass-loss rate $\dot{M}$. Unfortunately, empirically derived mass-loss rates suffer the largest uncertainty, which can reach up to two orders of magnitude (e.g., Fullerton et al. 2006). The primary reason for this uncertainty is the unknown structure of the stellar wind. Initially, winds were considered as homogeneous flows (e.g., de Jager et al. 1988), but much evidence accumulated since which implies that stellar winds are in fact ridden with clumpy structures and turbulence (Moffat et al. 1988; Lépine & Moffat 1999; Markova et al. 2005; Oskinova et al. 2007; Prinja & Massa 2010; Šurlan et al. 2013). Not only the amount, but also the stratification of clumping is highly uncertain. This is mostly because it is still not known whether clumps originate in the stellar wind due to instabilities in the line-driving mechanism (Owocki et al. 1988; Feldmeier et al. 1997) or in sub-photospheric convective layers (Cantiello et al. 2009). Accounting for clumping leads to a systematic reduction of the mass-loss rates, which, in turn, has a strong impact on evolutionary models of massive stars.

1.2. Wolf-Rayet stars

Massive Wolf-Rayet (WR) stars are a class of objects whose spectra are dominated by wind features, most prominently He II 4686 and Hα, Hβ (e.g., van der Hucht 2001). The winds of WR stars are often so dense that their surfaces (i.e. hydrostatic layers) cannot be observed directly. This makes the determination of stellar parameters such as the effective temperature, gravity, and rotational velocity very hard to derive. Indeed, sophisticated model atmospheres are necessary to obtain reliable constrains on these parameters for WR stars (Hamann et al. 2006; Sander et al. 2012; Shenar et al. 2014).

Classical WR stars are commonly believed to be descendents of O-stars ("the Conti scenario", Conti 1976) that have shed much, or all, of their hydrogen envelope to reveal their helium cores. The initial mass necessary for a star to reach the WR phase is $\approx 20\,M_\odot$ in the Galaxy, increasing to $\approx 45\,M_\odot$ in a low metallicity galaxy such as the SMC (Meynet & Maeder 2005). The hydrogen deficiency of WR stars makes them promising progenitor candidates for the hydrogen-free type Ib/c core collapse supernovae (Woosley et al. 1993), although it is still unclear whether very massive stars really do generate supernovae explosions (Heger et al. 2003; Gerke et al. 2015). The spectra of WR stars imply strong enrichment of nuclear burning products such as nitrogen (WN stars), carbon (WC stars), and oxygen (WO stars). These stars are therefore associated with an advanced evolutionary stage of massive stars (e.g., Lamers et al. 1991). However, their spectral definition also encompasses very massive, young objects which exhibit the appearance of WR stars by merit of their strong winds at birth (Crowther & Hadfield 2006). WR stars are subdivided into the subclasses "early" (e.g., WNE) and "late" (e.g., WNL) according to the ionization balance in their spectra (Smith 1968). Early WR stars are typically understood to have He-burning cores, while most late WR stars, which tend to exhibit hydrogen in their spectra, are believed to still be core H-burning (Smith et al. 1996; Hamann et al. 2006).

Before it became clear that stellar winds can account for the hydrogen depletion observed in WR stars, it was originally believed that the majority (or all) of WR stars form in binary systems via RLOF mass transfer (Paczyński 1967). This is the so-called "binary formation channel" for WR stars (see Sect. 1.3). Since then, analytical models (Castor et al. 1975) and numerical simulations (Hillier 1987; Gräfener & Hamann 2005) made clear that the radiation fields of single stars with large enough initial masses can drive the stellar winds necessary for them to reach the WR phase. This caused the binary formation channel to be pushed aside for quite a few decades. Yet the fact that single stars can become WR stars does not deem the binary formation channel irrelevant (e.g., Vanbeveren et al. 1998). The recent revelation that binarity is extremely common among massive stars, together with the downwards revision of mass-loss rates due to clumping, raises a need for a detailed investigation of the impact of binarity on WR stars.

1.3. Binary interaction and evolution

Two stars which are gravitationally bound form a binary system. The components of a binary are typically assumed to have formed simultaneously. Although some confusion exists in the literature, it is common to define the binary component which was more massive at birth as the primary and its companion the secondary. In principle, the evolution of a binary system is a function of the initial properties of the stellar components (e.g., initial mass $M_{\rm i}$, initial rotation velocity $v_{\rm rot,\,i}$, and metallicity content $Z_{\rm i}$), as well as the initial orbital parameters: the initial period $P_{\rm i}$ and the initial eccentricity $e_{\rm i}$. Instead of specifying both stellar masses, it is convenient to parametrize the system using the primary's mass M_1 and the mass ratio $q = M_2/M_1$. All these quantities are, in principle, time-dependent, i.e. they change along the system's evolution. To which extent binary interaction is important in the system depends on this set of initial parameters.

Table 1.1.: Orbital mass determinations for some of the most massive stars

Object	spectral type	$M_1[M_\odot]$	$M_2[M_\odot]$	P [d]	reference
NGC 3603-A1	WN6h + WN6h	116	89	3.77	Schnurr et al. (2008a)
WR 21a	O3/WN5ha + O	104	58	31.7	Tramper et al. (2016)
WR 20a	WN6ha + WN6ha	83	82	3.69	Bonanos et al. (2004) ; Rauw et al. (2004)
R 139	O6.5 Iafc + O6 Iaf	$> 78\,M_\odot$	$> 66\,M_\odot$	153.9	Taylor et al. (2011)
HD 5980	WN6h + WNh6-7	61	66	19.3	Koenigsberger et al. (2014)

Orbital periods P of known massive binaries can range from mere hours (e.g., Belczynski et al. 2013) to tens and hundreds of years (e.g., Lefèvre et al. 2005; Mason et al. 2009a). The initial period distribution is essentially flat on a logarithmic scale, as is the distribution of the initial mass-ratio (Sana et al. 2012). The distribution of the initial eccentricity is often assumed to be $f(e) = 2\,e$, following Heggie (1975).

The most important observational advantage of binary stars is the fact that they allow the derivation of the stellar masses using simple Newtonian dynamics. This is extremely crucial for massive stars, and especially for WR stars, whose masses can otherwise only be constrained by means of indirect methods. To derive the masses of the components of a spectroscopic binary, RV curves for both components need to be constructed. To obtain the true masses, the inclination angle i has to be measured. Unfortunately, measuring i in non-eclipsing binaries is very tricky, although polarimetry and wind-wind collisions (see below) can yield helpful constraints on the inclination angle. A few examples for the most massive stars which have been "weighed" reliably in binaries are given in Table 1.1.

A multitude of evolutionary scenarios exist for binary systems, depending on the properties of the binary components and on the orbital parameters. For example, a common scenario for close massive binaries ($P \lesssim 10\,$d) is the following (van den Heuvel & Heise 1972)

$$\text{OB+OB} \xrightarrow{\text{1. RLOF}} \text{WR + OB} \xrightarrow{\text{SN Ib/c}} \text{BH + OB} \xrightarrow{\text{2. RLOF}} \text{HMXB} \xrightarrow{\text{SN Ib/c}} \text{BH binary} \xrightarrow{\text{merging}} \text{GW} \qquad (1.1)$$

Hence, binary evolution may trigger and/or influence many phenomena which are of great scientific interest. For example, the study of SNe and their progenitors is critical for testing current SNe models and for the calibration of distances on a cosmic scale. HMXBs, which are binary systems consisting of a non-degenerate mass donor and a compact object (NS or BH), emit copious amounts of X-rays, and belong to some of the most energetic stellar objects known. Close massive binaries are also one of the primary candidates for the creation of GW signals originating in the merger event of two massive black holes (Marchant et al. 2016), the first of which detected very recently by the LIGO collaboration (Abbott et al. 2016). During such an evolutionary sequence, the binary components may interact in several ways,

the most dramatic of which is mass-transfer during RLOF. Below, the main forms of interaction in a binary are shortly described.

Tidal interaction: As the binary components are gravitationally bound, there always exists some tidal interaction between the binary components. Tidal interaction tends to circularize the system and to synchronize the rotational periods of the stars with the orbital period (Zahn 1975; Hurley et al. 2002), and it can induce shear chemical mixing in the stars (e.g., Maeder & Meynet 1996; Song et al. 2013). The time scale over which these processes happen depends heavily on the separation of the stars, their masses, and on whether they have radiative or convective envelopes. The circularization, synchronization, and mixing of the stars can heavily influence their observed properties and their evolution (e.g., de Mink et al. 2009).

Mutual irradiation: Since the radiation of stars determines the conditions in their own atmospheres, one may expect that stars in a binary also interact via their radiation fields (Drechsel et al. 1995). Via radiation pressure, irradiation counteracts gravity and causes a reduction of the "effective mass" of both stars, thus changing the dynamics and potential surfaces of the system (Palate et al. 2013). Moreover, just as the intrinsic radiation of a star exerts pressure on its atmosphere to induce a wind, it can also decelerate the wind of its companion (Radiative Breaking, Stevens & Pollock 1994; Gayley et al. 1997).

Wind-wind collisions (WWC): When both components of a binary system exhibit significant stellar winds, these winds are expected to form a cone-shaped wind-wind collision (WWC) surface. The cone engulfs the weaker-wind component. The high kinetic energy of the colliding plasmas of the stars suggest that the collision of the two winds produces X-ray emission (Cherepashchuk 1976; Corcoran et al. 1996). As the plasma streams along the cone arms, it cools down via radiation, which can be seen in the infrared and optical both spectroscopically (e.g., Rauw et al. 1999; Hill et al. 2000) as well as photometrically (Williams et al. 1997). WWC is not expected to have a very significant impact on the evolution of a binary, although the collision of the winds can partially inhibit wind accretion. However, their analysis can yield helpful constraints on the orbit, specifically on the inclination i (Luehrs 1997).

Wind-fed accretion: Companions in a binary can transfer mass without overfilling their Roche lobes via wind-fed accretion, often described using the Bondi-Hoyle formalism (Bondi & Hoyle 1944). This interaction form is usually not important for binaries where both companions are non-degenerate, because radiation pressure and the collision of winds efficiently inhibit the accretion of matter. However, wind-fed accretion can lead to extreme X-ray emission if the accreting companion is a degenerate object such as a neutron star or a black hole. This is the standard model for explaining the strong X-ray emission of HMXBs.

By far the most dramatic form of interaction in a binary is, however, mass-transfer during RLOF.

1.4. Roche Lobe overflow

The Roche lobe of a star in a binary is an imaginary surface at which a test particle co-rotating with the binary system would feel no force acting on it. The implication is that particles outside the Roche lobe of a star are no longer gravitationally bound to it, and will either be transferred to the other star, or would be lost from the binary system. Thus, once a star becomes larger than its Roche lobe, Roche lobe overflow (RLOF) is said to occur, typically leading to immense mass-transfer onto the companion and mass-loss from the system (Lubow & Shu 1975; Vanbeveren et al. 1998). A very common approximation for the critical Roche radius is (Eggleton 1983):

$$R_{\mathrm{RLOF},\,1} = \frac{0.49q^{-2/3}}{0.6q^{-2/3} + \ln\left(1 + q^{-1/3}\right)}\, a, \tag{1.2}$$

where a is the semi major axis of the orbit. $R_{\mathrm{RLOF},\,2}$ is obtained by replacing $q \rightarrow 1/q$. When both stars are safely within their Roche lobes, the system is termed *detached binary*. When one star overfills its Roche lobe, one speaks of a *semi-detached binary*. When both stars overfill their Roche lobes, the stars are per definition in contact (recall that both Roche lobes pass through the inner Lagrangian point), and the system becomes a *contact binary*.

One generally distinguishes between three cases of RLOF mass-transfer (Kippenhahn & Weigert 1967; Paczyński 1967): *Case A* occurs when a star overfills its Roche lobe while being on the main sequence (hydrogen burning core). *Case B* occurs when a star undergoes RLOF after exhausting all hydrogen in the

core, but prior to He-core burning. Lastly, *Case C* is defined when RLOF occurs after He-core burning initiated. The amount of mass lost and the impact the mass-loss will have on the star undergoing RLOF heavily depends on when mass-transfer occurred. Since a star only grows mildly in size during its life on the main sequence, case A mass-transfer will only occur in very close binaries. The amount and rate of mass-loss, as well as whether or not this mass is accreted by mass-gainer or simply lost from the system, generally depend on the rate of change of the gainer's radius and mass (cf. Tout et al. 1997). In most cases, mass-transfer via RLOF occurs over the primary's thermal timescale $\tau_{\rm th}$.

How does a post-RLOF mass donor look like? While the answer generally depends on the detailed form of mass-transfer, we expect to see a star which has lost much of its H-rich envelope. It will therefore likely be H-depleted, may show nuclear burning produces in its atmosphere, and it will be overluminous for its mass (compared with a main-sequence star) due to the higher mean molecular weight in its core. Paczyński (1967) performed a detailed evolutionary calculation and showed that the product of such a process will likely have the characteristics of a WR star. Indeed, RLOF has since been commonly claimed to lead to the formation of WR stars, including known WR binaries (e.g., V444 Cyg, Vanbeveren et al. 1998).

There is an increasing amount of evidence that RLOF tremendously affects the evolution of massive stars. However, while population synthesis and binary evolution models suggest that binarity heavily influences, and even dominates, the WR population (Vanbeveren et al. 1998; Bartzakos et al. 2001a; Foellmi et al. 2003a), this was not yet demonstrated to be in line with observed WR stars. This thesis attempts to provide a quantitative answer to this question. As we embark upon this journey, questions related to mass-loss in stars and the structure of their winds, which are inseparable from a true understanding of the impact of binarity on massive stars, will be addressed.

1.5. Overview of the manuscripts

This thesis encompass five scientific papers already published or submitted for publication in a refereed journal. The manuscripts of these studies are reprinted in the following five chapters of this thesis, preceded by a brief overview.

1.5.1. Manuscript I.

Status: published in *Astronomy & Astrophysics*, Volume 577, 13 pp. (2015), DOI: 10.1051/0004-6361/201425356

Title: On the consistent treatment of the quasi-hydrostatic layers in hot star atmospheres

Authors: A. Sander, T. Shenar, R. Hainich, A. Gímenez-García, H. Todt, W.-R. Hamann

Objective: The objective of this work was the introduction of critical updates in the PoWR code which enable the analysis of OB-type stars.

My contribution: During this work, I tested the updated calculation of the radiative pressure in the code, and introduced depth-dependent microturbulence in the code. I performed extensive comparisons between the PoWR code and the established non-LTE, plane-parallel model atmosphere code TLUSTY. I contributed to much of the text.

1.5.2. Manuscript II.

Status: published in 2015 in *The Astrophysical Journal*, Volume 809, 20 pp. (2015), DOI: 10.1088/0004-637X/809/2/135

Title: A coordinated X-ray and Optical Campaign of the Nearest Massive Eclipsing Binary, δ Orionis Aa: A Multiwavelength, Non-LTE spectroscopic analysis

Authors: T. Shenar, L. Oskinova, W.-R. Hamann, M. F. Corcoran, A. F. J. Pablo, N. D. Richardson, W. L. Waldron, D. P. Huenemoerder, J. Maíz Apellániz, J. S. Nichols, H. Todt, Y. Nazé, J. L. Hoffman, A. M. T. Pollock, I. Negueruela

Objective: The main objective of this study is a multiwavelength spectroscopic analysis of the nearby multiple eclipsing system δ Ori A. This study, together with three additional published studies which resulted from this project, set as an objective to take advantage of the binarity and eclipses in the system to understand the formation of X-rays O stars.

My contribution: As the first author, almost all results put forth in this study were obtained by myself, including the spectral analysis, treatment of clumping and turbulence, and f/i analysis to constrain the formation region of X-rays in the system. The paper was fully written by myself.

1.5.3. Manuscript III.

Status: published in *Astronomy & Astrophysics*, Volume 591, 25 pp (2016), DOI: 10.1051/0004-6361/201527551

Title: Measuring the stellar wind parameters in IGR J17544-2619 and Vela X-1 constrains the accretion physics in Supergiant Fast X-ray Transient and classical Supergiant X-ray Binaries

Authors: A. Giménez-García, T. Shenar, J. M. Torrejón, L. Oskinova, S. Martínez-Núñez, W.-R. Hamann, J. J. Rodes-Roca, A. González-Galán, J. Alonso-Santiago, C. González-Fernández, G. Bernabeu, A. Sander

Objective: The objective of this study is to examine whether differences in the properties of donor stars in high mass X-ray binaries can explain the dichotomy between the two distinct subclasses "supergiant fast X-ray transient binaries" and "classical supergiant X-ray binaries".

My contribution: During this project, I mentored and instructed the first author, A. Giménez-García, who was interested in learning how to perform spectroscopic analyses of massive stars. I contributed much of the text, especially the discussion, to the published manuscript.

1.5.4. Manuscript IV.

Status: published in *Astronomy & Astrophysics*, Volume 598, 16 pp (2017), DOI: 10.1051/0004-6361/201629621

Title: The Tarantula Massive Binary Monitoring: II. First SB2 orbital and spectroscopic analysis for the Wolf-Rayet binary R 145

Authors: T. Shenar, R. N. D. Richardson, D. Sablowski,R. Hainich, A. F. J. Moffat, H. Todt, H. Sana, W.-R. Hamann, L. M. Oskinova, A. Sander, F. Tramper, N. Langer, A. Z. Bonanos, S. E. de Mink, G. Gräfener, P. A. Crowther, J. S. Vink, L. A. Almeida, A. de Koter, R. Barbá, A. Herrero, C. J. Evans, K. Ulaczyk

Objective: The objective of this study is an exhaustive analysis of the LMC WR binary R 145, supposedly composing two of the most massive stars known. This was achieved via a spectral disentanglement, spectroscopic analysis, polarimetric analysis, and wind-wind collision analysis.

My contribution: As the first author, almost all results portrayed in this study were obtained by myself, including the derivation of the orbital solution, spectroscopic analysis, polarimetric analysis, and wind-wind collision analysis. The comparison with evolutionary tracks and their interpretation was done by myself. The paper was fully written by myself.

1.5.5. Manuscript V.

Status: published in *Astronomy & Astrophysics*, Volume 591, 25 pp (2016), DOI: 10.1051/0004-6361/201527916

Title: Wolf-Rayet stars in the Small Magellanic Cloud: Analysis of the binaries

Authors: T. Shenar, R. Hainich, H. Todt, A. Sander, W.-R. Hamann, A. F. J. Moffat, J. J. Eldridge, H. Pablo, L. M. Oskinova, N. D. Richardson

Objective: This study aims to quantify the impact of binarity on WR stars. It includes the spectroscopic analysis of the known WR binaries in the SMC and a detailed evolutionary analysis, resulting in important constraints on the impact of binarity.

My contribution: All the results given in this work were obtained by myself. The manuscript was fully written by myself.

Chapter 2.

On the consistent treatment of the quasi-hydrostatic layers in hot star atmospheres (Manuscript I)

A. Sander, T. Shenar, R. Hainich, A. Gímenez-García, H. Todt, W.-R. Hamann

Astronomy & Astrophysics, 2015, Volume 577, 13 pp.

Abstract

Spectroscopic analysis remains the most common method to derive masses of massive stars, the most fundamental stellar parameter. While binary orbits and stellar pulsations can provide much sharper constraints on the stellar mass, these methods are only rarely applicable to massive stars. Unfortunately, spectroscopic masses of massive stars heavily depend on the detailed physics of model atmospheres. We demonstrate the impact of a consistent treatment of the radiative pressure on inferred gravities and spectroscopic masses of massive stars. Specifically, we investigate the contribution of line and continuum transitions to the photospheric radiative pressure. We further explore the effect of model parameters, e.g., abundances, on the deduced spectroscopic mass. Lastly, we compare our results with the plane-parallel TLUSTY code, commonly used for the analysis of massive stars with photospheric spectra. We calculate a small set of O-star models with the Potsdam Wolf-Rayet (PoWR) code using different approaches for the quasi-hydrostatic part. These models allow us to quantify the effect of accounting for the radiative pressure consistently. We further use PoWR models to show how the Doppler widths of line profiles and abundances of elements such as iron affect the radiative pressure, and, as a consequence, the derived spectroscopic masses. Our study implies that errors on the order of a factor of two in the inferred spectroscopic mass are to be expected when neglecting the contribution of line and continuum transitions to the radiative acceleration in the photosphere. Usage of implausible microturbulent velocities, or the neglect of important opacity sources such as Fe, may result in errors of approximately 50% in the spectroscopic mass. A comparison with TLUSTY model atmospheres reveals a very good agreement with PoWR at the limit of low mass-loss rates.

2.1. Introduction

The initial mass of a star determines its evolutionary path, and is thus considered one of the most fundamental stellar parameters. Yet stellar masses derived for massive stars via spectral analyses are generally prone to large uncertainties, greatly hampering an accurate calibration of stellar masses with their spectral types and evolutionary status. The so-called "mass discrepancy" problem, which arises when comparing stellar masses obtained from spectroscopy, to orbital, wind, and evolutionary models, has been of concern to stellar physicists for a few decades (Herrero et al. 1992; Repolust et al. 2004; Massey et al. 2012). While recent

studies suggest a solution of this problem over the years (Weidner & Vink 2010; Markova & Puls 2014), discrepancies still exist, especially in the range of giants to supergiants.

In principle, orbital masses are independent of stellar atmosphere models and are therefore considered to be more robust (e.g., Torres et al. 2011). However, orbital masses are only attainable in the rare case of binary systems with well-constrained inclination, usually owing to eclipses. Immense progress has also been made in the field of asteroseismology, which allows the measurement of stellar masses with very high accuracies from observed stellar pulsations. Unfortunately, the high variability in the outer layers of massive stars make the study of their pulsational behavior very difficult, often hindering an effective implementation of asteroseismological methods to massive stars (see recent review by Aerts 2014, and references therein). Indeed, spectroscopy remains the primary method to infer stellar masses for the majority of the massive stars.

The spectroscopic mass of a star is derived from its radius R_* and surface gravity g_* via $M_* = G^{-1}\, g_*\, R_*^2$, and therefore any uncertainties in R_* and g_* propagate into uncertainties in M_*. Except for the rare case where the angular diameter of a star can be directly measured, R_* is derived from the luminosity L and effective temperature $T_{\rm eff}$ of the star via the Stefan-Boltzmann relation $R_* = (4\pi\sigma_{\rm SB})^{-1/2}\ L^{1/2}\, T_{\rm eff}^{-2}$. Since the effective temperature can in principle be constrained with decent accuracy, the main cause for uncertainty in the stellar radius is the error in the distance d, which propagates in the error in L, according to $R_* \propto \sqrt{L} \propto d$. If the distance is well constrained and thus the spectroscopic radius is known, the stellar mass M_* is directly proportional to g_* and thus all uncertainties in the gravity determination propagate directly into mass uncertainties.

The gravity g_* is by no means a directly measurable quantity. It is derived by comparing synthetic spectra from model atmospheres with observations. The surface gravity of a star determines the stratification of its atmospheric pressure, and most prominently affects the pressure-broadened wings of hydrogen and helium lines. The determination of g_* thus relies on both the pressure broadening theory adopted, as well as the model atmosphere.

Different broadening theories can lead to systematic differences of ~ 0.15 dex in inferred $\log g_*$ values, which alone corresponds to $\sim 40\%$ error in the inferred spectroscopic mass. It is an even harder task, however, to constrain the systematic errors that arise because of different assumptions and techniques in stellar atmosphere codes. The radiative pressure in massive stars depends on the stellar parameters as well as the opacity, which in turn depends on the elements, abundances, atomic data, and line Doppler widths. As we illustrate in this study, g_* is highly model-dependent, and systematic errors can easily occur if the radiative pressure is not fully and consistently accounted for.

Two domains can be distinguished in the atmosphere of a massive star: a hydrostatic domain, where gravity is balanced by pressure (e.g., gas pressure, radiation pressure), and a wind domain, where the outward pressure exceeds gravity and the matter is accelerated.

The spectra of O- and B-type stars are mostly formed in the outer layers of their quasi-hydrostatic domains. For the modeling of such stars, a detailed treatment of the hydrostatic regime is imperative. Specifically, the contribution of line and continuum transitions to the total radiative pressure in the quasi-hydrostatic domain is far from negligible. Proper knowledge of the velocity field in the layers close to the stellar surface is a key ingredient for a better understanding of a variety of theoretical and observational phenomena (see, e.g., Hamann 1981; Cidale & Ringuelet 1993; Owocki & Puls 1999; Cantiello et al. 2009; Shenar et al. 2014).

In this paper, we thoroughly document the current calculation of the radiative pressure in the Potsdam Wolf-Rayet (PoWR) code (see, e.g. Gräfener et al. 2002; Hamann & Gräfener 2003a) and illustrate the importance of accounting for it consistently. While we focus on the PoWR code, the major concepts and equations are representative of the majority of current state-of-the-art stellar atmosphere codes, as we illustrate in a brief comparison. We further discuss and quantify the large impact of a proper hydrostatic treatment on inferred stellar parameters, and particularly on the stellar mass M_*. We demonstrate the sensitivity of the radiative pressure to the Doppler width of spectral lines and to the iron abundance. Lastly, we compare our results with the plane-parallel TLUSTY O-grid models from Lanz & Hubeny (2003), which are widely used for the analysis of hot stars with negligible winds.

The structure of this paper is as follows: In Sect. 2.2, we briefly summarize the main assumptions of the PoWR code and thoroughly discuss the treatment of the quasi-hydrostatic domain. The outcome of our test

calculations are shown and discussed in Sect. 2.3. In Sect. 2.4, we compare our spectra with corresponding TLUSTY models, before drawing the general conclusions in Sect. 2.5.

2.2. The PoWR code

2.2.1. The Basics

The Potsdam Wolf-Rayet models describe atmospheres of spherically symmetric stars with a stationary outflow[1]. To achieve a consistent solution, the equations of statistical equilibrium and radiative transfer are iteratively solved to yield the population numbers without the approximation of a local thermodynamic equilibrium (non-LTE). The radiative transfer is solved in the comoving frame, which avoids simplifications such as the Sobolev approximation. After an atmosphere model is converged, the synthetic spectrum is calculated via a formal integration along emerging rays. Some description of the PoWR code can be found in Gräfener et al. (2002) and Hamann & Gräfener (2004). The temperature stratification is updated iteratively to ensure energy conservation in the expanding atmosphere, as described in Hamann & Gräfener (2003a). Recently, the PoWR code has been extended by the so-called thermal balance-method, which goes back to ideas of Hummer & Seaton (1963) and Hummer (1963) and is described in detail for stellar atmospheres by Kubát et al. (1999) and Kubát (2001). This method provides better numerical stability in optically thin domains.

In the comoving frame calculations during the non-LTE iteration, we assume that the line profiles are Gaussians with a constant Doppler broadening velocity $v_{\rm dop}$, which approximately accounts for the thermal and turbulent velocity. A constant broadening velocity is a well-established simplification in comoving frame methods. While PoWR uses directly a velocity $v_{\rm dop}$ as input, the "Comoving Frame General" (CMFGEN) code requires three input parameters $T_{\rm dop}$, $A_{\rm dop}$, and $v_{\rm T}$, which are then combined to a constant velocity $v_{\rm dop} = \sqrt{2\frac{k_{\rm B}T_{\rm dop}}{m_{\rm H}A_{\rm dop}} + v_{\rm T}^2}$ (see, e.g., Martins et al. 2002, CMFGEN description). In the FASTWIND[2] code a velocity similar to PoWR has to be given and is referred to just as mircroturbulence $v_{\rm turb}$ (Puls et al. 2005).

The value of $v_{\rm dop}$ is chosen such that it approximately reflects the order of the averaged thermal speed combined with the microturbulence, i.e.,

$$v_{\rm dop} \approx \sqrt{\bar{v}_{\rm th}^2 + v_{\rm turb}^2}. \tag{2.1}$$

For O and B stars typical values for $v_{\rm dop}$ range between 10 and 30 km/s. Only for stars without photospheric lines, such as classical Wolf-Rayet stars, higher values can be chosen to speed up the calculations without changing the emergent spectrum. The influence of $v_{\rm dop}$ on an O-star model spectrum is discussed and illustrated in Sect. 2.3.4.

Pressure broadening is neglected during the comoving frame calculations, which is sufficient for the current applications of the PoWR models. For stars with considerably higher values of $\log g_*$, e.g. , subdwarfs, specific codes, such as the Tübingen Model-Atmosphere Package (TMAP) (e.g., Werner et al. 2003) exist which include this effect. Some codes, such as the TLUSTY code, have the option to switch on pressure broadening in the iteration if needed. In the formal integration in PoWR, detailed thermal, microturbulent and pressure broadening are accounted for in a depth-dependent manner.

The basic parameters of a PoWR model are the stellar temperature T_*, luminosity L, mass-loss rate $\dot{M}$, surface gravity g_* and the chemical abundances. The stellar temperature T_* is defined as the effective temperature of a star with the luminosity L and radius R_* (referred to as the "stellar radius"), defined at the Rosseland continuum optical depth $\tau_{\rm max} = 20$. The total Rosseland optical depth $\tau_{\rm Ross}(R_*)$ including lines is larger. To ensure $\tau_{\rm max} = 20$ at the inner boundary, the velocity $v_{\rm min} = v(R_*)$ is iteratively adjusted. The surface gravity g_* is defined at the stellar radius R_* via $g_* = G\,M_*\,R_*^{-2}$. For OB stars, the difference between the radius where $\tau_{\rm max} = 20$ and the "photospheric radius" at $\tau_{\rm Ross} = 2/3$ is usually very small. However, in

[1] For Wolf-Rayet stars, model grids are available online at `http://www.astro.physik.uni-potsdam.de/PoWR/`

[2] acronym for "fast analysis of stellar atmospheres with winds"

supergiants the effective temperature can differ up to ~ 1 kK between these two points, and this difference in definition is apparent when compared with other studies.

The density stratification in the quasi-hydrostatic domain follows from an integration of the hydrostatic equation, thoroughly discussed in Sect. 2.2.2. In the wind domain, the radial wind velocity $v(r)$ is usually prescribed in the model by a so-called β-law

$$v(r) = v_\infty \left(1 - \frac{R_*}{r}\right)^\beta , \tag{2.2}$$

where v_∞ is the terminal velocity of the wind, and β is a free input parameter whose value typically ranges between $\beta = 0.6$ and $\beta = 2.0$,(e.g., Puls et al. 2008). With the mass-loss rate $\dot{M}$ specified, the density stratification $\rho(r)$ in the wind follows from the continuity equation

$$\dot{M} = 4\pi r^2 v(r)\, \rho(r). \tag{2.3}$$

In the calculation, we use complex model atoms, with a superlevel approach for iron group elements (see Gräfener et al. 2002, for details), and an explicit set of quantum levels for all other elements. The detailed chemical composition for our calculations is given in Sect. 2.3, together with the rest of the model parameters.

We do not use any clumping in the models and instead assume a smooth wind. The potential existence of clumping in the subsonic photosphere is a constant debate in the massive star community (see, e.g., Runacres & Owocki 2002; Oskinova et al. 2007; Cantiello et al. 2009; Sundqvist & Owocki 2013). While clumping would significantly affect the derived absolute stellar parameters in any case, the goal of this work is to demonstrate effects that are independent of any clumping formalism. Therefore, we refrain from assuming a particular clumping approximation and calculate our test models (see Sect. 2.3) with a smooth wind.

2.2.2. The quasi-hydrostatic domain

The Potsdam Wolf-Rayet (PoWR) model atmosphere code was originally developed for WR stars where the emergent spectrum is formed almost exclusively in the stellar wind. For these objects, it is sufficient to treat the quasi-hydrostatic domain of WR stars with a simple barometric formula using a constant scale height

$$H_\mathrm{c} := \frac{\frac{\mathcal{R}T_*}{\mu} + v_\mathrm{turb}^2}{g_\mathrm{eff}\, R_*}, \tag{2.4}$$

in units of R_* while ensuring a smooth transition of the velocity field and its gradient between the two quasi-hydrostatic domain and the wind. Here, g_eff is the gravity corrected for radiative pressure in the hydrostatic domain (see details below), μ the mean particle mass (including electrons) in units of the hydrogen atom mass m_H, and v_turb the turbulent velocity, which is a free input parameter. The parameter $\mathcal{R}$ denotes the specific gas constant for hydrogen, i.e., $\mathcal{R} = k_\mathrm{B}/m_\mathrm{H}$.

For a proper treatment of O- and B-star atmospheres, the barometric formula with a constant scale height is not an appropriate solution of the hydrostatic equation. The hydrostatic equation is one of the fundamental equations of stellar structure. For massive stars, one has to account for the outward radiative force acting against gravitation, yielding the radial stratification of pressure $P(r)$ in the hydrostatic domain,

$$\frac{\mathrm{d}P}{\mathrm{d}r} = -\rho(r) g(r) \left[1 - \Gamma(r)\right]. \tag{2.5}$$

Here, $\rho(r)$ is the mass density, $g(r) = G\, M_*/r^2$ the gravity, and $\Gamma(r)$ the ratio between the outward radiative acceleration and gravitational acceleration. The term $[1 - \Gamma(r)]$ describes the effective reduction of the gravity due radiative pressure, as discussed below.

With the assumption of an ideal gas, the pressure P can be expressed by

$$P(r) = \rho(r) \left[\frac{\mathcal{R}T(r)}{\mu(r)} + v_\mathrm{turb}^2\right] \tag{2.6}$$

$$= \rho(r) \left[a^2(r) + v_\mathrm{turb}^2\right], \tag{2.7}$$

where T is the electron temperature. In the second line we further introduce the sound speed

$$a(r) := \sqrt{\frac{\mathcal{R}T(r)}{\mu(r)}} \tag{2.8}$$

in order to simplify the expression. The turbulent velocity v_{turb} is a free depth-independent input parameter reflecting a possible microturbulence. While in the formal integral the microturbulence is combined with the actual thermal velocity of each element to obtain the precise depth-dependent Doppler broadening velocity, it is not directly connected to the value of v_{dop} used in the comoving-frame calculation. To avoid physically inconsistent situations, the value of v_{dop} should be higher than for v_{turb}. So far this has been ensured by the user, but we are planning to implement a more detailed treatment of microtubulence in the comoving-frame calculations, also allowing for depth-dependent changes.

The current implementation allows us to compare our OB-type models with those of other stellar atmosphere codes, as they adopt similar approaches (cf. Table 2.1). Stellar atmosphere analyses with several codes (see, e.g., Massey et al. 2013) have demonstrated that microturbulent velocities of the order of 10 to 20 km/s help to reproduce the observed spectral lines in certain parameter regimes. It is an ongoing debate whether such velocities represent a real turbulent motion in the photosphere, as originally suggested for hot stars by Struve & Elvey (1934) and prominently reintroduced by Hubeny et al. (1991), or if they are rather a "fudge factor". Related to this open question is the discussion whether such a turbulent term should be included in the hydrostatic equation or not. In the PoWR code the term is included, but because of its currently depth-independent implementation there are no additional derivatives occuring and it merely leads to an offset of the sound speed.

For simplicity, we will set $v_{\mathrm{turb}} = 0$ km/s in the following calculations, but the full result can always be recovered by replacing a^2 with $a^2 + v_{\mathrm{turb}}^2$. Upon dividing Eq. (2.5) by $-\rho$, the term on the left side, which we will refer to as

$$a_{\mathrm{press}}(r) := -\frac{1}{\rho}\frac{\mathrm{d}P}{\mathrm{d}r} \tag{2.9}$$

describes the outward acceleration due to gas pressure and turbulent motion. Thus the hydrostatic equation can be written as

$$a_{\mathrm{press}}(r) = g(r)\,[1 - \Gamma(r)]\,, \tag{2.10}$$

illustrating that in the hydrostatic domain the outward acceleration due to gas pressure has to balance gravity reduced by the radiative acceleration. In a strictly hydrostatic domain, we have therefore no net velocity, i.e., no stellar wind.

For an accurate description of an expanding stellar atmosphere, i.e., with $v \neq 0$, one would have to use the hydrodynamic equation, which can be written for a stationary, symmetric outflow in the following form:

$$\frac{1}{\rho}\frac{\mathrm{d}P}{\mathrm{d}r} + v\frac{\mathrm{d}v}{\mathrm{d}r} = -g(r)\,[1 - \Gamma(r)\,]. \tag{2.11}$$

This means there is only one additional term in Eq. (2.11) compared to the hydrostatic Eq. (2.5). This inertia term $a_{\mathrm{mech}}(r) := v\frac{\mathrm{d}v}{\mathrm{d}r}$ is of fundamental importance in the outer wind, but becomes negligible quickly below the sonic point. This also holds for a β-type velocity law with $\beta > 0.5$ where a_{mech} approaches zero for $r \to R_*$. Thus in the subsonic domain the hydrodynamic equation (2.11) transitions into the hydrostatic form (2.5) and we obtain a quasi-hydrostatic stratification.

In such a quasi-hydrostatic situation, we can still have a nonvanishing velocity, even though its value is subsonic and, as we will see in the comparison with purely hydrostatic models in Sect. 2.4, negligible for the observed spectrum. Furthermore this small velocity still fulfills the equation of continuity (2.3). This can be used to obtain the consistent solution for the velocity field in the quasi-hydrostatic domain. First, we replace the pressure gradient in a_{press} with the help of Eq. (2.7),

$$a_{\mathrm{press}} = -\frac{1}{\rho}\frac{\mathrm{d}P}{\mathrm{d}r} \tag{2.12}$$

$$= -\frac{\mathrm{d}a^2}{\mathrm{d}r} - \frac{a^2}{\rho}\frac{\mathrm{d}\rho}{\mathrm{d}r}. \tag{2.13}$$

We then eliminate the density in the second term by using the equation of continuity (2.3) and thus write

$$a_{\rm press} = -\frac{{\rm d}a^2}{{\rm d}r} - a^2 r^2 v \frac{\rm d}{{\rm d}r}\left(\frac{1}{r^2 v}\right) \tag{2.14}$$

$$= -\frac{{\rm d}a^2}{{\rm d}r} + \frac{2a^2}{r} + \frac{a^2}{v}\frac{{\rm d}v}{{\rm d}r}. \tag{2.15}$$

Finally, by combining Eqs. (2.10) and (2.15), we obtain an equation for the velocity gradient in the quasi-hydrostatic regime,

$$\frac{{\rm d}v}{{\rm d}r} = \frac{v}{a^2}\left[\frac{GM_*}{r^2}\left(1-\Gamma(r)\right) - \frac{2a^2}{r} + \frac{{\rm d}a^2}{{\rm d}r}\right]. \tag{2.16}$$

In principle, given a value $v(R_*) = v_{\rm min}$ at the inner boundary, one can obtain the velocity field in the quasi-hydrostatic part via direct integration of this equation. In practice, we transform this equation and split off the main exponential trend as this turned out to work better in terms of numerical stability. Thus our solution for the quasi-hydrostatic velocity field is

$$v(r) = v_{\rm min}\frac{a^2(r)}{a^2(R_*)}\frac{R_*^2}{r^2}\exp\left(\frac{r-R_*}{H_{\rm c}} - b(r)\right), \tag{2.17}$$

with a yet to be determined function $b(r)$. We now calculate the derivative of Eq. (2.17) with respect to r,

$$\frac{{\rm d}v}{{\rm d}r} = -\frac{2v}{r} + 2\frac{v}{a^2}\frac{{\rm d}a^2}{{\rm d}r} + v\left[\frac{1}{H_{\rm c}} - \frac{{\rm d}b}{{\rm d}r}\right], \tag{2.18}$$

combine this with Eq. (2.16), and obtain

$$-\frac{2}{r} + \frac{1}{a^2}\frac{{\rm d}a^2}{{\rm d}r} + \frac{1}{H_{\rm c}} - \frac{{\rm d}b}{{\rm d}r} = \frac{GM_*}{a^2 r^2}\left(1-\Gamma(r)\right) - \frac{2}{r} + \frac{1}{a^2}\frac{{\rm d}a^2}{{\rm d}r}. \tag{2.19}$$

$$\frac{1}{H_{\rm c}} - \frac{{\rm d}b}{{\rm d}r} = \frac{GM_*}{a^2 r^2}\left(1-\Gamma(r)\right) \tag{2.20}$$

The righthand side of Eq. (2.20) is now defined as $H(r)^{-1}$, as it is analogous to the definition of $H_{\rm c}$ (Eq. 2.4). Thus the numerical integration of the velocity gradient is replaced by the integration of

$$\frac{{\rm d}b}{{\rm d}r} = \frac{1}{H_{\rm c}} - \frac{1}{H(r)}. \tag{2.21}$$

The required boundary value $b(R_*) = 0$ follows from the inner boundary, where it is required in Eq. (2.17) that $v(R_*) = v_{\rm min}$.

So far, we did not discuss what enters $\Gamma(r)$ and thus $H(r)$. In general, the letter Γ is used to describe a ratio between a radiative acceleration and gravity. The most common use is the so-called "electron gamma",

$$\Gamma_{\rm e} = \frac{a_{\rm thom}(r)}{g(r)} = \frac{\sigma_{\rm e}}{4\pi c m_{\rm H} G} q_{\rm ion}(r)\frac{L}{M_*}, \tag{2.22}$$

which accounts only for the radiative pressure because of scattering of free electrons. Note that r^2 cancels out in the last expression, since the acceleration because of Thomson scattering is defined as

$$a_{\rm thom}(r) := \frac{\sigma_{\rm e} L}{4\pi c m_{\rm H} r^2} q_{\rm ion}(r), \tag{2.23}$$

with the ionization parameter,

$$q_{\rm ion}(r) = m_{\rm H}\frac{n_{\rm e}(r)}{\rho(r)} = \frac{n_{\rm e}(r)}{n_{\rm tot}(r)\mathcal{A}}. \tag{2.24}$$

The mean atomic mass $\mathcal{A}$ is constant in an atmosphere model. The two density factors can be replaced by the slowly varying mean particle mass $\mu(r) = \mathcal{A}\left(1 + \frac{n_e(r)}{n_{tot}(r)}\right)^{-1}$ such that

$$q_{ion}(r) = \frac{1}{\mu(r)} - \frac{1}{\mathcal{A}}, \tag{2.25}$$

illustrating that q_{ion} is nearly constant throughout the atmosphere. As a consequence, Γ_e has only a very weak radial dependence.[3]

While Eq. (2.22) is the common definition for Γ in the context of the Eddington limit, it is only a fraction of the total outward radiative acceleration a_{rad}. Apart from the Thomson opacity corresponding to scattering of free electrons, additional opacities originate in line (bound-bound) and continua (bound-free, free-free) transitions, contributing to the total radiative acceleration. a_{rad} is thus separated into three parts:

$$a_{rad} = a_{thom} + a_{lines} + a_{true\ cont}. \tag{2.26}$$

The last term $a_{true\ cont}$ refers to the acceleration originating from bound-free and free-free continuum transitions. As the electron opacity also forms a continuum, these two terms are combined and referred to as the "continuum". In contrast, the term without electron scattering is sometimes called the "true continuum". To avoid any confusion, we will adopt this notation in the following.

Similar to Eq. (2.22), we can thus define a Γ, which corresponds to the total acceleration,

$$\Gamma_{rad}(r) := \frac{a_{rad}(r)}{g(r)} = \frac{1}{g(r)} \frac{4\pi}{c} \frac{1}{\rho(r)} \int_0^\infty \kappa_\nu(r)\, H_\nu(r)\, \mathrm{d}\nu, \tag{2.27}$$

where κ_ν and H_ν are the opacity and Eddington flux at the frequency ν, respectively, and c is the speed of light. This "full" Γ_{rad} is then used in the quasi-hydrostatic domain. A similar approach was also adopted by Lanz & Hubeny (2003) in their plane-parallel TLUSTY code, which is widely used for calculating photospheric spectra of static atmospheres.

In contrast to Γ_e, which is already known at the start of a non-LTE model atmosphere calculation, with the exception of the exact value of $q_{ion}(r)$, the full Γ_{rad} has to be calculated iteratively. The radiative acceleration is calculated from the population numbers, which in turn depend on the radiation field and also on the density which itself is connected to Γ_{rad} via the hydrostatic equation. To ensure a consistent solution, the velocity field in the quasi-hydrostatic domain is constantly updated as soon as the hydrostatic equation is violated by more than 5%. This turned out to be sufficient in all test cases, as long as $\Gamma_{rad}(r) < 1$ in the quasi-hydrostatic part. In reality, values larger than unity in the (quasi-)hydrostatic domain would reflect additional physical phenomena occurring in the photosphere (e.g., subphotospheric convection, Cantiello et al. 2009), which are not handled by our model atmospheres. The plane-parallel TLUSTY code treats only values of $\Gamma_{rad} \leq 0.9$ in the hydrostatic equation (Lanz & Hubeny 2003) as the hydrostatic equation fails for values larger than unity and numerical instabilities already occur when Γ_{rad} gets close to this limit. We use a similar approach in PoWR for the quasi-hydrostatic equation, i.e., the value of Γ_{rad} is limited to 0.9 for our velocity calculations.

2.2.3. The quasi-hydrostatic treatment in different stellar atmosphere codes

A couple of non-LTE stellar atmopshere codes are used in the field of hot and massive stars. Widely used are CMFGEN (Hillier & Miller 1998), FASTWIND (Santolaya-Rey et al. 1997), and, in case of negligible stellar winds, TLUSTY (Hubeny & Lanz 1995). While these codes have a lot of similarities in their concepts, they also differ in certain approaches, such as their treatment of the radiative transfer or their superlevel approach. Recent comparisons between CMFGEN and FASTWIND (Massey et al. 2013) for particular objects have shown a good agreement in the derived temperatures, but also revealed that the surface gravities derived with FASTWIND are abound 0.12 dex lower than with CMFGEN. As the derived

[3] Instead of using q_{ion}, one also finds the specific electron-scattering coefficient $s_e = n_e\sigma_e/\rho$ in the literature (e.g., Mihalas 1978).

Table 2.1.: Characteristics of different stellar atmosphere codes concerning their treatment of the (quasi-)hydrostatic regime

	PoWR	CMFGEN	FASTWIND	TLUSTY
radiative transfer	comoving frame	comoving frame	CMF/Sobolev[a]	static (obs. frame)
blanketing	full	full	approximative	full
temperature strat.	radiative equilibrium[b] or thermal balance	radiative equilibrium[b,c]	thermal balance	radiative equilibrium[b]
photosphere	quasi-hydrostatic	quasi-hydrostatic	quasi-hydrostatic	hydrostatic
(ρ,v)-update	consistent	injections[d]	start iterations[e]	$v \equiv 0$, ρ consistent[f]
radiative acc.	full $a_{\rm rad}$	full $a_{\rm rad}$	$a_{\rm cont}$ approximation[g]	full $a_{\rm rad}$
$v_{\rm turb}$?	yes	yes	no	yes
domain connection	continuous $\mathrm{d}v/\mathrm{d}r^h$	$0.75\,v_{\rm sonic}$[i]	$0.1\,v_{\rm sonic}$ (adjustable)	no wind domain

Notes. [(a)] Comoving frame (CMF) method for main elements, Sobolev approximation for trace elements. Details are given in Puls et al. (2005). [(b)] In PoWR and TLUSTY, the radiative equilibrium is considered in two different flavors, the so-called integral form, $4\pi \int \kappa_\nu (S_\nu - J_\nu)\,\mathrm{d}\nu = 0$, and the flux consistency $4\pi \int H_\nu \mathrm{d}\nu = \sigma_{\rm SB} T_{\rm eff}^4$ (Hubeny & Lanz 1995; Hamann & Gräfener 2003a). CMFGEN instead only uses the integral form (Hillier 2003). [(c)] In CMFGEN, the thermal balance is called "electron energy balance" (EEB) and used to check convergence and superlevel assignments, but not explicitly for temperature corrections (Hillier & Miller 1998; Hillier 2003). [(d)] After convergence of the statistical equations, the stratification in the quasi-hydrostatic part is adjusted and the model calculation is "restarted" from a gray temperature distribution. The total number of these "restarts", which are also referred to as "injections", must be specified beforehand. [(e)] At the start of a model an iteration is done for the quasi-hydrostatic domain, where a Rosseland optical depth based on LTE opacities is calculated along with the calculation of the temperature and density stratification. The details are explained in Santolaya-Rey et al. (1997). [(f)] The hydrostatic equation is part of the set of linearized equations, which are solved consistently in every iteration (Hubeny & Lanz 1995). [(g)] The continuum acceleration is approximated by a nonintegral term with a parameterized Rosseland opacity (Santolaya-Rey et al. 1997). [(h)] The continuous velocity gradient is the standard option in PoWR to find a connection point. Alternatively, the user can specify that the connection point is forced at $v = f \cdot v_{\rm sonic}$. [(i)] Models before ~2013 used $v = 0.5\,v_{\rm sonic}$ for the connection point (Massey et al. 2013).

surface gravities are directly connected to the treatment of the quasi-hydrostatic layers, it is of major interest to understand the difference between the codes in this regime.

Table 2.1 provides an overview of the features affecting the quasi-hydrostatic treatment of PoWR, CMFGEN, and FASTWIND together with the completely hydrostatic treatment in TLUSTY. The latter provides an interesting test case in the limit of negligible mass-loss rates, which will be further discussed in Sect. 2.4, where we compare spectra from TLUSTY models with those from PoWR. In CMFGEN, TLUSTY model atmospheres can also be used as a start approach.

The most striking difference in the quasi-hydrostatic treatment between the different wind codes (PoWR, CMFGEN, FASTWIND) is the update mechanism of the density and velocity stratification:

- In PoWR, we update the velocity field as described in Sect. 2.2.2 as part of the main iteration as soon as the hydrostatic equation is violated by more than 5% or the specified value of $\tau_{\rm max}$ is missed by

more than a specified ϵ_τ. For each update, $\Gamma_{\rm rad}(r)$ is applied in the hydrostatic equation, using $a_{\rm rad}(r)$ from the comoving frame (CMF) calculations. With the new velocity field given, the stratification is updated according to the equation of continuity (2.3).

- In CMFGEN (Hillier & Miller 1998), the hydrostatic domain is first taken from a TLUSTY model or an old CMFGEN model, but can be updated with regards to the hydrostatic equation after a first convergence of the population numbers and the radiation field. After each such stratification update, sometimes referred to as "injection", the model iteration has to be continued to reachieve convergence (see, e.g., Martins et al. 2012, for a brief description). Similar to PoWR, the radiative acceleration used in the hydrostatic equation is taken from the CMF radiative transfer calculations.
- In FASTWIND (Santolaya-Rey et al. 1997), the line contributions are instead neglected in the quasi-hydrostatic domain and uses an approximate handling for the continuum acceleration, including both Thomson and true continuum term. This simplification allows FASTWIND to set up the quasi-hydrostatic domain in an iteration right at the start of a model, in line with the goal of the code of being significantly faster than PoWR and CMFGEN.

Furthermore, all three wind codes use a different criterion for the connection point between the quasi-hydrostatic and the wind domain. While FASTWIND and CMFGEN use a fixed fraction of the sound speed to define this connection point, PoWR puts the condition of a smooth velocity gradient between the two regimes.

Instead of treating only the quasi-hydrostatic part consistenly, one could also aim at a hydrodynamically consistent treatment throughout the whole model atmosphere, i.e., including the wind domain. These calculations are typically not included in state-of-the-art stellar atmosphere codes, especially as a prescribed β-law provides a good approximation for the outer wind regime of OB stars. A self-consistent calculation of the velocity field in the whole stellar atmosphere has been implemented as a nonstandard option in PoWR in order to discuss WR winds (Gräfener & Hamann 2005, 2008). However, such models require much longer computation times and this option is not required for the purpose, in which we focus on the quasi-hydrostatic regime. The implementation presented here is completely sufficient in achieving a self-consistent stratification of the quasi-hydrostatic layers. Nevertheless, a revised implementation of completely hydrodynamically consistent model atmospheres in the PoWR code will be addressed in detail in a future work.

2.2.4. The effective gravity

The hydrostatic Eq. (2.5) can be written in an even shorter form with the definition of the *effective gravity,*

$$g_{\rm eff}(r) := \frac{GM_*}{r^2}\,[1-\Gamma(r)]\,. \tag{2.28}$$

To avoid any confusion, we will use $g_{\rm grav}(r)$ instead of $g(r)$ with $g_* = g_{\rm grav}(R_*)$ to denote the full gravity from here on. The effective gravity $g_{\rm eff}$ is a fundamental fitting parameter for O- and B-stars when comparing models with observations. The pure gravitational acceleration $g_{\rm grav}(r) = GM_* r^{-2}$, from which the stellar mass is derived, can only be calculated if $\Gamma_{\rm rad}$ is known. Therefore, $g_{\rm grav}$ is model dependent. In these models an accurate treatment of the complete radiative pressure is required. Correcting the observed $g_{\rm eff}$ for Thomson pressure $\Gamma_{\rm e}$ only neglects a large part of the radiative pressure, and leads to an underestimated stellar mass, as we will demonstrate in Sect. 2.3. In the cases of negligible radiative pressures only do $\log g_{\rm grav}$ and $\log g_{\rm eff}$ become indistinguishable. Otherwise, spectroscopic masses are underestimated if calculated directly via $R_*^2\, g_{\rm eff}/G$.

As the shape of a spectral line like Hδ depends on $g_{\rm eff}$ and not $g_{\rm grav}$, there is a parameter degeneracy. A star with a weaker radiative pressure will produce the same line profiles as a star with a higher radiative pressure and a higher gravity.

One of the major reasons for a strong model dependency of the stellar mass is the large impact of the opacity on the radiative pressure. It is significant which opacities are taken into account in the model. Neglecting elements such as Fe or Ne will result in a lower $\Gamma_{\rm rad}$ and is not legitimate, even if

the corresponding element is not under consideration in the intended analyses. The inferred stellar mass therefore depends not only on the adopted stellar parameters, but also on the details of the model atoms.

The adopted Doppler broadening velocity $v_{\rm dop}$ used in the comoving-frame calculations also has a significant impact: larger velocities allow atoms to absorb photons in a wider frequency range, and thus generally increase the radiative pressure in the atmosphere.

Even though $g_{\rm eff}(r)$ and $\Gamma_{\rm rad}(r)$ are calculated for each depth point in the PoWR code to fulfill the hydrostatic equation, there is a need for a certain "reference value" , which can be used for comparisons. As the emergent spectrum is mainly formed at $\tau_{\rm Ross} \approx 2/3$ in the photosphere, the first idea would be to use $g_{\rm eff}$ at this value. However, such a fixed point might already be located in the wind. Therefore we define a weighted mean of $\Gamma_{\rm rad}$ as

$$\overline{\Gamma}_{\rm rad} := \int_{\tau_{\rm max}}^{\tau_{\rm sonic}} \Gamma_{\rm rad}(\tau_{\rm Ross})\, e^{-\tau_{\rm Ross}}\, {\rm d}\tau_{\rm Ross}. \tag{2.29}$$

The upper limit of the integral $\tau_{\rm sonic}$ usually denotes the optical depth of the sonic point. However, we do not allow that this value drops below 0.1, even in the rare cases where the actual sonic point would be in such a regime. The calculated value of $\overline{\Gamma}_{\rm rad}$ is used to relate $\log g_{\rm eff}$ and $\log g_* = \log g_{\rm grav}(R_*)$ via

$$\log g_{\rm eff} = \log g_* + \log\left(1 - \overline{\Gamma}_{\rm rad}\right). \tag{2.30}$$

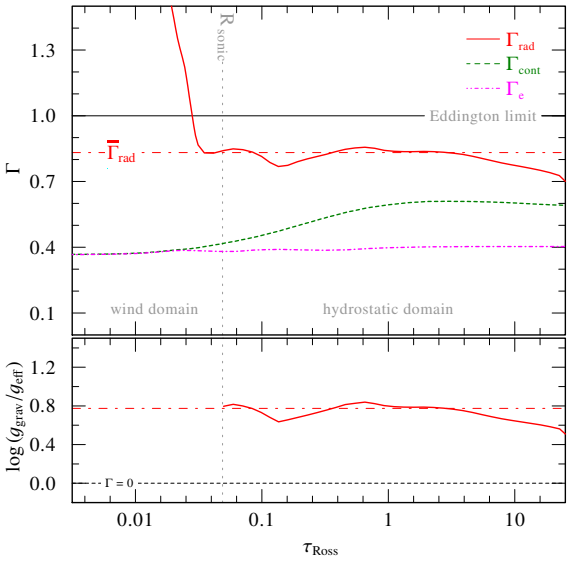

Figure 2.1.: Radial dependence of $\Gamma_{\rm rad}$ (red, solid line, upper panel) for our supergiant test model, plotted over the Rosseland optical depth $\tau_{\rm Ross}$. The mean value obtained with Eq. (2.29) is indicated as a dashed-dotted line. For comparison, $\Gamma_{\rm e}$ and the total continuum contribution $\Gamma_{\rm cont}$ are also shown. In the lower panel, the difference between $g_{\rm grav}$ and $g_{\rm eff}$ is illustrated: the red solid curve marks the actual difference at each optical depth, while the dashed-dotted line denotes the difference using $\overline{\Gamma}_{\rm rad}$. The gray dashed vertical line denotes the location of the sonic point.

The radial dependence of $\Gamma_{\rm rad}$ for a supergiant test model is illustrated in Fig. 2.1, where it is plotted against the total Rosseland opacity. It is evident that in the quasi-hydrostatic regime not only the line transitions, but also the atomic continuum transitions cannot be neglected, while this quickly changes as soon as we enter the supersonic domain, where $\Gamma_{\rm cont}$ consists only of $\Gamma_{\rm e}$. One can see that the calculated value of $\overline{\Gamma}_{\rm rad}$ is indeed representative for the difference between $g_{\rm grav}$ and $g_{\rm eff}$ in the photosphere. Values of $\overline{\Gamma}_{\rm rad}$ for a series of test models are shown and discussed in Sect. 2.3.

The reference radius for all values of $g_{\rm eff}$ given in this work is R_*. However, other radii are also used in the literature, typically $R_{\frac{2}{3}} = R\left(\tau_{\rm Ross} = \frac{2}{3}\right)$ or the radius of the sonic point $R_{\rm s}$. The latter roughly indicates the outer end of the quasi-hydrostatic domain. It is therefore interesting to check how much the values of $g_{\rm eff}$ and $g_{\rm grav}$ are affected when referring to different radii. As this effect is largest for supergiants, we examine an O-star model with $T_* = 32.5\,$kK, $\log L/L_\odot = 5.6$, $\log g_{\rm grav}(R_*) = 3.25$ and $\log \dot{M} = -5.75\,[{\rm M}_\odot/{\rm yr}]$. For this model, we have $R_{\frac{2}{3}} = 1.06\,R_*$ and the sonic point is located at $R_{\rm s} = 1.11\,R_*$, leading to differences of 0.05 dex and 0.09 dex in $\log g$. Especially the latter value is approximately what can be achieved by accurate fitting of high quality spectra and, therefore, we have to take the reference radius into account when analyzing these objects. This effect is lower for giants and dwarfs, namely on the order of 0.03 dex and 0.01 dex for the sonic point, respectively.

In the literature, the term $g_{\rm eff}$ may not always have the same meaning. Especially when dealing with observations, it is often not clearly stated whether values termed as $\log g$ have been corrected for radiative acceleration. Values that have been corrected for centrifugal acceleration in a statistical sense are sometimes labeled as "true" gravities $g_{\rm true}$ or $g_{\rm c}$ with the relation

$$g_{\rm c} = g + \frac{(v \sin i)^2}{R_*} \tag{2.31}$$

(Repolust et al. 2004). The term labeled as g in this equation is sometimes called $g_{\rm eff}$ (e.g., Massey et al. 2013). We would like to stress that this is not identical to our definition of the effective gravity in this work. The variable g in (2.31) refers to the gravitational acceleration specified in a non-rotating stellar atmosphere model, which has not been reduced by radiative acceleration. As such, g would be referred to as $g_{\rm grav}$, following the notation of this work. Caution is therefore adviced when dealing with the term "effective gravity", as its definition might differ significantly between different authors.

2.3. Results and discussion

2.3.1. Test model details

To illustrate the impact of accounting for the full radiative pressure consistently, we calculate a set of PoWR models for a fixed temperature of $T_* = 32.5\,$kK , which corresponds to a late O-star. For this temperature, we calculate three types of models with different surface gravities, corresponding to the luminosity classes I (supergiant), III (giant), and V (dwarf). As we focus on the quasi-hydrostatic part, we adopt only schematic parameters for the wind, i.e., all models have the same terminal wind velocity of $v_\infty = 2000\,$km/s. The outer model boundary is set to $100\,R_*$. The velocity field in the wind domain can be prescribed by a $\beta-$law with $\beta = 0.8$ (see Eq. 2.2), which is accurate enough for our purposes as we do not want to analyze the outer wind. The luminosities are "typical" representatives of their class according to Martins et al. (2005). We chose the surface gravities similarly, but with slight adjustments of up to 0.1 dex, corresponding to the closest grid point in the TLUSTY O-star model grid (Lanz & Hubeny 2003) for a later comparison (see Sect. 2.4). We adopted mass-loss rates from Vink et al. (2000), and the wind is assumed to be smooth (no density contrast, i.e., $D = 1$ in the notation of Hamann & Koesterke 1998). The chemical compositions are taken to be solar. Here, we use the abundances inferred by Grevesse & Sauval (1998) instead of the newer ones obtained by Asplund et al. (2009) to have identical values to those used in the TLUSTY O-grid. All parameters of the models are compiled in Table 2.2.

For each of the three luminosity classes, we calculate three models, which we refer to as (a), (b), and (c) in the following, making nine models in total period. Models (a) and (b) have a fixed $g_{\rm grav}$, which corresponds to the respective luminosity class and differ only in the treatment of the radiative acceleration in the quasi-hydrostatic part: models (a) are only calculated with $\Gamma_{\rm e}$, while models (b) include the full $\Gamma_{\rm rad}$, i.e., they account for the complete radiative pressure. Typical examples are shown in Fig. 2.2 and Fig. 2.3, where we plot the acceleration stratifications for a dwarf (class V) model. One can see that Fig. 2.2 shows the consistent (b)-model, where the sum of the total radiative acceleration and gas pressure equals gravitation in the quasi-hydrostatic domain. The result of the (a)-model is shown in Fig. 2.3. Now only $\Gamma_{\rm e}$ and gas pressure are taken into account for the hydrostatic equation and thus the sum of the total radiative

Table 2.2.: O-star test model parameters

Luminosity class	I	III	V
T_* [kK]		32.5	
$\log g_{\rm eff}$ [cm s^{-2}]^a	2.47	3.02	3.79
$\log g_{\rm grav}$ [cm s^{-2}]^a	3.25	3.50	4.00
$\overline{\Gamma}_{\rm rad}$	0.83	0.67	0.39
$\Gamma_{\rm e}$	0.40	0.22	0.07
R_* [$R_\odot$]	20.0	14.1	8.1
$\log \dot{M}$ [$M_\odot$ yr^{-1}]	−5.75	−6.25	−7.1
$\log L$ [$L_\odot$]	5.60	5.30	4.82
M_* [$M_\odot$]	25.9	23.0	24.1
β		0.8	
v_∞ [km/s]		2000	
$v_{\rm turb}$ [km/s]		10	
$v_{\rm dop}$ [km/s]		20	
$X_{\rm H}{}^b$		0.704	
$X_{\rm He}{}^b$		0.282	
$X_{\rm C}{}^b$		2.78×10^{-3}	
$X_{\rm N}{}^b$		8.14×10^{-4}	
$X_{\rm O}{}^b$		7.56×10^{-3}	
$X_{\rm Mg}{}^b$		6.45×10^{-4}	
$X_{\rm Al}{}^b$		5.56×10^{-5}	
$X_{\rm Si}{}^b$		6.96×10^{-4}	
$X_{\rm P}{}^b$		6.10×10^{-6}	
$X_{\rm S}{}^b$		4.79×10^{-4}	
$X_{\rm Fe}{}^{b,c}$		1.34×10^{-3}	

Notes. $^{(a)}$ Values refer to the consistent models. Comparison model results are given in Table 2.4. $^{(b)}$ Solar abundances, as obtained by Grevesse & Sauval (1998), specified here as mass fractions. $^{(c)}$ Fe includes also the further iron group elements Sc, Ti, V, Cr, Mn, Co, and Ni. See Gräfener et al. (2002) for relative abundances.

Table 2.3.: O-star test model type overview

Model type	(a)	(b)	(c)
$g_{\rm grav}$	fixed^2	fixed^2	calculated
Γ^1	$\Gamma_{\rm e}$	$\overline{\Gamma}_{\rm rad}$	$\Gamma_{\rm e}$
$g_{\rm eff}$	calculated	calculated^3	fixed^3

Notes. $^{(1)}$ Γ value used to relate $g_{\rm geff}$ and $g_{\rm grav}$ $^{(2)}$ Type (a) and (b) models within the same luminosity class have the same $g_{\rm grav}$ $^{(3)}$ A type (c) model has the same $g_{\rm geff}$ as the type (b) model of the same luminosity class

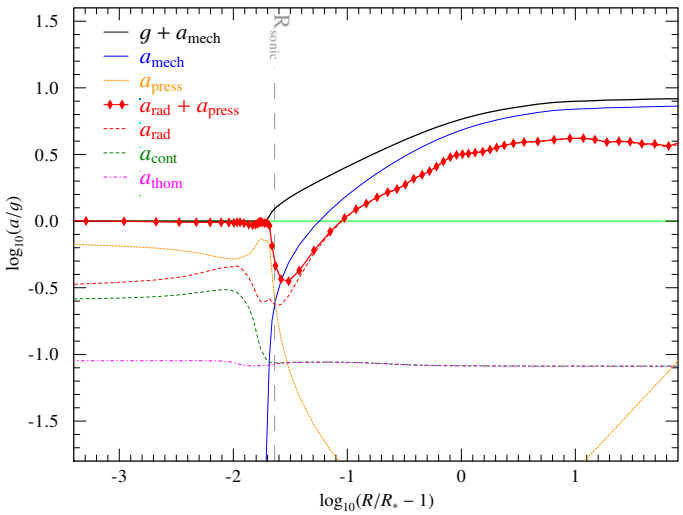

Figure 2.2.: Acceleration stratification for a model with a consistent quasi-hydrostatic domain (Type (b) models). The wind acceleration (thick red diamond line) is compared to the repulsive sum of inertia and gravitational acceleration $g(r)$ (black line). All terms have been normalized to $g(r)$.

acceleration and gas pressure is larger than the local gravity in the subsonic part. The outer parts of both models are very similar as both use the same prescribed β-velocity law.

In models (c), like in models (a), we account only for the Thomson term $\Gamma_{\rm e}$ in the quasi-hydrostatic domain, but instead of specifying $\log g_{\rm grav}$, we specify the effective gravity $\log g_{\rm eff}$ and adopt its value from the corresponding model (b), calculated from Eq. (2.30). An overview of the basic similarities and differences between all three model types is given in Table 2.3. Since models (b) and (c) of a given luminosity class have the same effective gravity, the wings of pressure-broadened lines are expected to be identical in both models. However, because of different treatment of the quasi-hydrostatic domain, the actual surface gravities $g_{\rm grav}$ and spectroscopic masses M_* implied from both models will differ.

2.3.2. Comparison with fixed $g_{\rm grav}$

Figure 2.4 illustrates the impact of accounting for the full radiative pressure on prominent Balmer lines (left to right: Hδ, Hγ, Hβ, Hα) for dwarfs (upper panels), giants (middle panels), and supergiants (lower panels). The impact of either including only the Thomson term $\Gamma_{\rm e}$ (model a, blue dashed lines) or including the full radiative term $\Gamma_{\rm rad}$ (model b, red solid lines) can be seen in the line wings. Because of their larger outward pressures, the quasi-hydrostatic domains of models (b) are less dense than those of models (a), and, as a consequence, the line wings obtained by models (b) are narrower. For the same reason, the value of $g_{\rm eff}$ is always smaller in models (b) compared to models (a) (see below).

A further inspection of Fig. 2.4 reveals that the difference between models (a) and (b) increases with luminosity class. A look at Eq. (2.27) reveals that lower values of $\log g_{\rm grav}$ will increase $\Gamma_{\rm rad}$, which is indeed much larger for the supergiant than for the dwarf. Even though the difference between $\Gamma_{\rm rad}$ and $\Gamma_{\rm e}$ is not getting much stronger with lower $\log g_{\rm grav}$, as $\Gamma_{\rm e}$ also changes proportional to R_*^2, both values are significantly larger for the supergiant and thus the difference in the derived $g_{\rm eff}$ value increases, which is reflected in the increasing line wing difference in Fig. 2.4.

Even for our dwarf models ($\log g_{\rm grav} = 4.0$, upper panels), where the dashed and solid lines can only barely be distinguished, we obtain a difference of $\Delta \log g_{\rm eff} = 0.21$ dex when accounting for the full radiative pressure via $\Gamma_{\rm rad}$ ($\log g_{\rm eff} = 3.97$ for model (a) vs. $\log g_{\rm eff} = 3.78$ for model (b)). For our giant models ($\log g_{\rm grav} = 3.5$, middle panels) the difference increases to 0.37 dex (3.39 vs. 3.02). Finally, for the supergiant models ($\log g_{\rm grav} = 3.25$, lower panels), a formidable difference of 0.56 dex (3.03 vs. 2.47) is

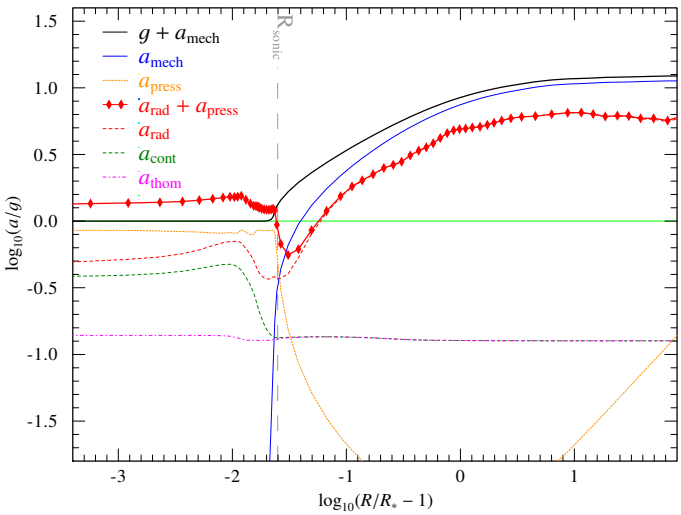

Figure 2.3.: Same as Fig. 2.2, except with a velocity law in the quasi-hydrostatic domain accounting only for $\Gamma_{\rm e}$ (Type (a) models). While the wind domain is not affected, the acceleration balance in the quasi-hydrostatic part is significantly different.

obtained. Even though the impact on the spectral appearance of the hydrogen lines might not be particularly striking in Fig. 2.4, the differences in the corresponding values of $\log g_{\rm eff}$ are quite remarkable.

2.3.3. Comparison with fixed $g_{\rm eff}$

In the models (a) and (b) discussed above, we specify $g_{\rm grav}$, T_*, and L, and therefore the radii, the spectroscopic masses are known a priori. When dealing with observations, however, it is $g_{\rm eff}$, and not $g_{\rm grav}$, which is empirically measurable. Thus, one would fix the effective gravity that best reproduces the observation, and let the actual gravity $g_{\rm grav}$ be a model output. Based on the detailed physics implemented in the model atmosphere, the gravity $g_{\rm grav}$ and the spectroscopic mass M_* follow from $\log g_{\rm eff}$. This scenario is reflected in models (b) and (c), which are calculated with identical effective gravities, but with a different treatment of the radiation pressure in the quasi-hydrostatic domain. Fig. 2.5 shows the Balmer lines Hγ (left panel) and Hβ (right panel) as obtained from the supergiant models (b),, which account for $\Gamma_{\rm rad}$ (red solid line), and (c), which only include $\Gamma_{\rm e}$ (green dotted line). As both models have the same $g_{\rm eff}$, the line wings obtained from both models can hardly be distinguished. However, some differences are seen in the line cores and in the helium and metal lines.

To illustrate the effect of this different treatment, we show the velocity stratification for all three supergiant models in Fig. 2.6. All models agree in the outer part where we have prescribed the β-law. However, in the inner part it becomes evident that fixing $g_{\rm eff}$ indeed leads to relatively similar velocity stratifications with both the consistent $\overline{\Gamma}_{\rm rad}$-approach and the $\Gamma_{\rm e}$-approach, which is reflected in the agreement of line profiles between the models (b) and (c). If one fixes instead the more fundamental parameter $g_{\rm grav}$, the resulting velocity stratification is significantly different in the inner part, if accounting only for $\Gamma_{\rm e}$, including a huge difference in the radial location of the sonic point. These discrepancies explain the spectral differences between models (a) and (b) shown in Fig. 2.4.

Despite the similarities between the models (b) and (c) seen in the line wings and in the velocity law, their values of $\log g_{\rm grav}$ and M_* differ significantly. Table 2.4 shows the values of $\log g_{\rm grav}$ and M_* for the dwarf, giant, and supergiant models. As could be anticipated from Eq. (2.30), the models that account for the full radiative pressure (models b) have larger values for $\log g_{\rm grav}$ and M_* because their Γ, which is used to relate $g_{\rm eff}$ and $g_{\rm grav}$, is larger in these models. The spectroscopic masses deviate by roughly a factor of two. Interestingly, there is no clear trend for increasing deviation with increasing luminosity class. Intuitively, one might expect that the deviation would have to be larger for the supergiant model, compared

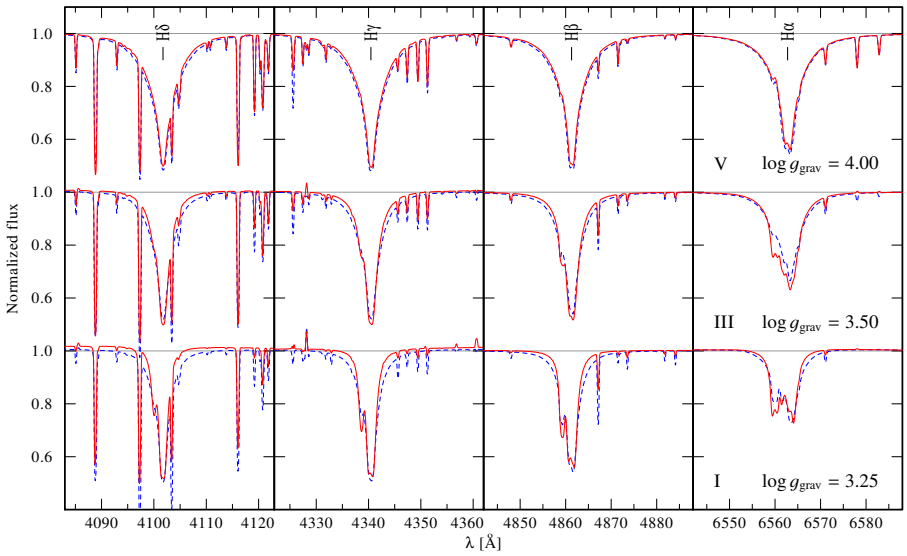

Figure 2.4.: Balmer line profiles of Hδ (left) to Hα (right) for test models with fixed $g_{\rm grav}$. The spectra from the (a)-type models with a quasi-hydrostatic stratification calculated using only the Thomson term $\Gamma_{\rm e}$ are shown as blue dashed line. The red solid lines display the profiles from the (b)-type models accounting for the full radiative term $\Gamma_{\rm rad}$.

to the dwarf model, as we obtained it in spectral comparison of the models (a) and (b) which were shown in Fig. 2.4. However, the calculation of the (c) models is quantitatively different from the (a) models. Even though both consider only $\Gamma_{\rm e}$ for obtaining the velocity field in the quasi-hydrostatic part, the (c) models are specifically designed to reproduce the $g_{\rm eff}$-value obtained with the full $\Gamma_{\rm rad}$, while the (a) models have a completely different approach, with the $g_{\rm grav}$-value being identical to the (b) models. In fact, we can estimate the masses of the (c) models with an easy calculation. Starting from the requirement that both, (b) and (c) models should have the same $g_{\rm eff}$, it immediately follows via Eq. (2.28) that

$$M_*^{(c)}\left(1-\Gamma_{\rm e}^{(c)}\right) = M_*^{(b)}\left(1-\overline{\Gamma}_{\rm rad}^{(b)}\right). \tag{2.32}$$

The small superscripts indicate the value from the corresponding model family, i.e., $M_*^{(c)}$ is short for $M_*(\Gamma_{\rm e})$ in the (c) models. As we do not know $\Gamma_{\rm e}^{(c)}$ in advance, since it contains $M_*(\Gamma_{\rm e})$ itself by definition (2.22),

Table 2.4.: Deduced stellar masses with different quasi-hydrostatic approaches

Luminosity class	I	III	V
$\log g_{\rm eff}$ [cm s^{-2}]^a	2.47	3.02	3.79
$\log g_{\rm grav}(\Gamma_{\rm e})$ [cm s^{-2}]^b	3.00	3.25	3.82
$\log g_{\rm grav}(\Gamma_{\rm rad})$ [cm s^{-2}]	3.25	3.50	4.00
$M_*(\Gamma_{\rm e})$ [M$_\odot$]^b	14.5	12.9	16.2
$M_*(\Gamma_{\rm rad})$ [M$_\odot$]	25.9	23.0	24.1

Notes. $^{(a)}$ The effective gravity (cf. Sect. 2.2.4) is fixed for all models here $^{(b)}$ These values are derived from models that were calculated as if only the Thomson radiative pressure would enter the hydrostatic equation.

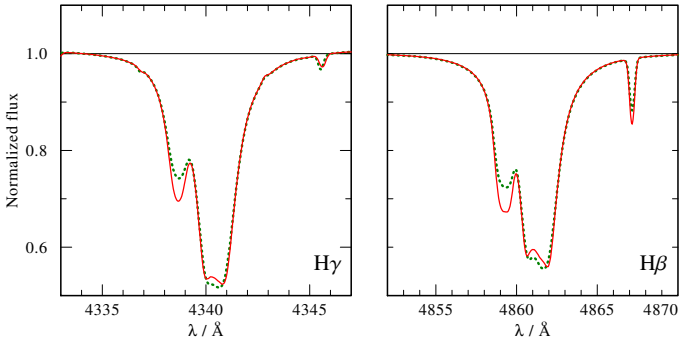

Figure 2.5.: The Hγ and Hβ lines (left and right panels, respectively), as obtained from models (b) and (c) (red solid and green dotted lines, respectively), both with an effective gravity of $\log g_{\rm eff} = 2.47$. Although the strengh of the line wings is the same, the two models imply masses and gravities, which strongly differ because of the different treatment of the radiative pressure (cf. Table 2.4)

we need to replace it with a value from the (b) model. Because the luminosity L is the same in the (b) and the (c) models and the ionization parameter $q_{\rm ion}$ only changes marginally, we can deduce from Eq. (2.22) that the product of $\Gamma_{\rm e}$ and M_* will be approximately the same for both models. Hence we get an expression that allows us to replace $\Gamma_{\rm e}^{(c)}$ with the known $\Gamma_{\rm e}^{(b)}$, i.e.,

$$\Gamma_{\rm e}^{(c)} \approx \frac{M_*^{(b)}}{M_*^{(c)}} \Gamma_{\rm e}^{(b)}. \tag{2.33}$$

Using that in (2.32) yields

$$M_*^{(c)} - M_*^{(b)} \Gamma_{\rm e}^{(b)} \approx M_*^{(b)} \left(1 - \overline{\Gamma}_{\rm rad}^{(b)}\right) \tag{2.34}$$

$$M_*^{(c)} \approx M_*^{(b)} \left[1 - \left(\overline{\Gamma}_{\rm rad}^{(b)} - \Gamma_{\rm e}^{(b)}\right)\right]. \tag{2.35}$$

This means that masses of the (c) models only depend on the difference between $\overline{\Gamma}_{\rm rad}$ and $\Gamma_{\rm e}$ in the consistent (b) models, not on the absolute values. The difference is comparable for all three luminosity classes, and so is the mass deviation in Table 2.4.

2.3.4. Blanketing and Doppler velocity influence

It is unfortunate that the spectroscopic mass greatly depends on various parameters adopted in the calculation. Two important examples will be discussed here. The first is the importance of the iron group elements. Since they are a dominant source for opacity in the atmosphere of a massive star, their abundances significantly affect the radiative pressure, and thus the inferred spectroscopic mass. Therefore iron group elements have to be included in model atmosphere calculations, even if these models are only used to analyse spectral regimes without visible iron lines. The effect, which is called "line blanketing", does not only affect the temperature stratification, but also the density structure of a stellar atmosphere. This is illustrated in left panel of Fig. 2.7, where we compare the Hγ line from our supergiant model (see Table 2.2 for parameters) to that of an identical model without iron. It impressively demonstrates that neglecting elements, which greatly contribute to the total opacity, is not legitimate. When the iron elements are not included, the radiative pressure is smaller, and the line wings appear broader in the synthetic spectrum, leading to an underestimation of the gravity by ≈ 0.3 dex. These elements should thus be included in any consistent calculation, even if there is no observational abundance indicator. Using "typical" abundances from the local region or similar objects will usually cause a smaller error than neglecting such elements completely.

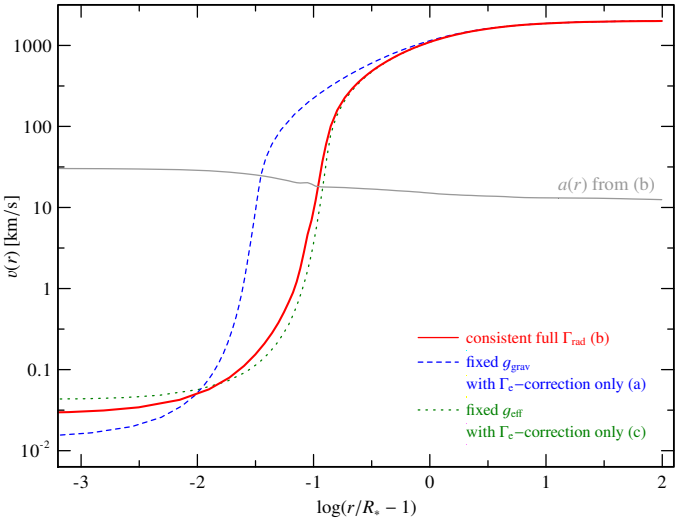

Figure 2.6.: Velocity stratification for three supergiant test models: the consistent quasi-hydrostatic model (b) (red solid) is compared to a model (a) (blue dashed) with the same $g_{\rm grav}$, but where only $\Gamma_{\rm e}$ is taken into account in the quasi-hydrostatic part (blue). The third model (c) (green dotted) shares $g_{\rm eff}$ with model (b), except it accounts only for $\Gamma_{\rm e}$ and thus has a different $g_{\rm grav}$.

Another quantity that is of major influence on the spectral appearance of OB star atmosphere models is the adopted Doppler broadening velocity $v_{\rm dop}$. This velocity is used in the comoving frame calculations and reflects the combined influence of the thermal and microturbulent velocities. While the thermal velocity is calculated for each element as a depth-dependent manner in the formal integral, the comoving frame calculations are currently using a constant $v_{\rm dop}$ for all elements. For the spectral appearance of Wolf-Rayet atmospheres the value of $v_{\rm dop}$ is of minor importance, but it has a notable impact on the spectra of our OB models, as it affects the total radiative pressure in the atmosphere. This is illustrated in the right panel of Fig. 2.7, where we again compare the region around Hγ for our supergiant test model, but now compare with a model that has been calculated with a larger Doppler velocity. In the O-star regime, the value of $v_{\rm dop} = 20$ km/s has proved to be sufficient. This demonstrates that it is imperative to choose a $v_{\rm dop}$ reflecting the true thermal and turbulent velocity in the stellar atmosphere, despite the significantly longer computing times in the comoving frame calculations that come along with smaller values of $v_{\rm dop}$.

2.4. Comparison with TLUSTY

The TLUSTY code (Hubeny & Lanz 1995) provides plane-parallel model atmospheres. The synthetic spectra that can be calculated from these models, e.g., with the SYNSPEC program from the same authors, are widely used for the analysis of photospheric spectra of OB-type stars. In the following section, we compare PoWR and TLUSTY model results. In all cases where spectra based on TLUSTY models are shown, they were obtained with the SYNSPEC code and are labeled as TLUSTY. [4]

While both PoWR and TLUSTY are non-LTE codes, a major difference is that the PoWR models include the stellar wind. PoWR therefore adopts a spherical geometry, while TLUSTY assumes a plane-parallel geometry. As thoroughly discussed by Lanz & Hubeny (2003), the assumption of static, plane-parallel atmospheres is a fairly solid approximation for the photospheres of OB stars, which show negligible signs of stellar winds and curvature effects. One can therefore expect that in the limit of negligible mass-loss rates

[4] The models from the TLUSTY O- and B-star grids (including their SYNSPEC spectra) can be obtained from the TLUSTY website at `http://nova.astro.umd.edu/`

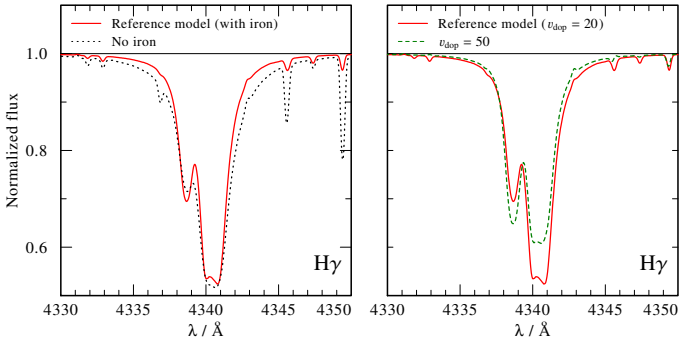

Figure 2.7.: Left panel: the spectrum around Hγ for the hydrostatically consistent supergiant test model (red solid line) is compared to a similar PoWR model calculated without iron group elements (black dotted line). Right panel: the same test model is calculated with a higher Doppler broadening velocity $v_{\rm dop}$ (green dashed line) and compared to the original.

and small scale heights (see Eq. 2.4), the PoWR spectra would be close to the TLUSTY results. To check that PoWR models of OB-type stars with negligible winds show a good agreement with the corresponding TLUSTY models, we dedicate this section to a comparison of dwarf, giant, and supergiant PoWR models with their TLUSTY counterparts, focusing on the pressure-broadened Balmer lines. In all cases, PoWR models with the consistently treated quasi-hydrostatic domain are used, i.e., those models that we referred to as type (b) above.

Since we calcuated the models used in Sect. 2.3 with "typical" O-star mass-loss rates, they are not expected to provide a very close agreement with the TLUSTY models. The discrepancies are most prominent in the Hα line for the supergiant and giant models, while small differences are also found in the other Balmer lines. In Fig. 2.8, we illustrate the effect of reducing the mass-loss rate. It is evident that the spectral appearance converges in the limit of small mass loss, and it is at this limit where we expect to obtain the closest agreement with TLUSTY models. Furthermore, the sequence of models illustrates that the absence of emission lines is not sufficient to deduce that mass loss is negligible.

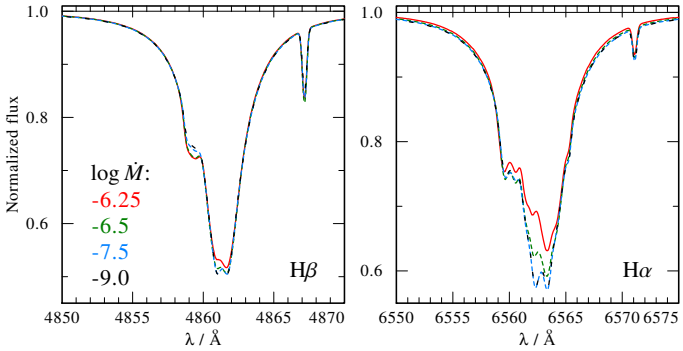

Figure 2.8.: Profiles of the Hα and Hβ lines from PoWR models with different $\dot{M}$. In the limit of low mass-loss rates, the wind effect on the spectrum becomes negligible. For an easier comparison of the line wings, the electron redistribution (see Fig. 2.9) is switched off in these simulations.

Another PoWR feature, which would hinder a comparison with the TLUSTY models, is frequency redistribution by Thomson scattering (Mihalas 1978). Given their large thermal velocities ($\sim$1000 km s^{-1}),

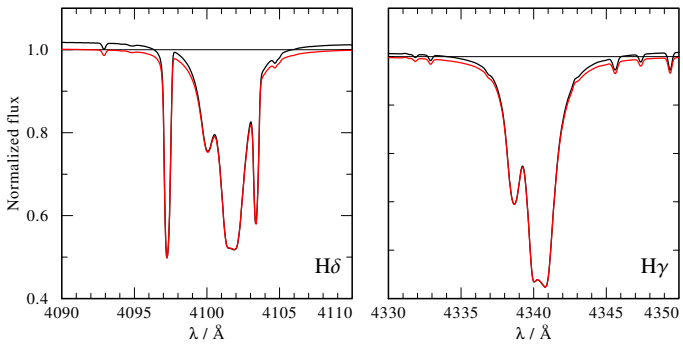

Figure 2.9.: Line profiles of Hγ and Hδ for the same supergiant PoWR model. The red line denotes the spectrum that is obtained when switching off the electron redistribution in the formal integral, while the black line indicates the "normal" output, which includes the redistribution of free electrons.

free electrons can scatter photons to significantly different wavelengths. Hence, photons that are trapped in an optically thick line core can be Doppler-shifted to the line wing or adjacent continuum, from which they can freely emerge and become visible as an excess emission. Especially at lower surface gravities and in spectral domains with a high density of spectral lines, the effect of frequency redistribution often results in a noticeable pseudocontinuum. When the synthetic flux is normalized relative to the continuum, this has the appearance of a continuum offset in the normalized spectrum. To illustrate this effect, Fig. 2.9 shows the Hδ and Hγ lines (left and right panels, respectively) for the consistent supergiant model including frequency redistribution (black solid line) and without (red solid line). Since TLUSTY does not account for this effect, we disable it for the sake of comparison. However, we stress that the importance of this effect has been demonstrated in various studies[5] (Hummer & Mihalas 1967; Auer & Mihalas 1968).

The upper, middle, and bottom panels of Fig. 2.10 show a comparison between the TLUSTY (black, dashed line) and PoWR (red, solid line) for the dwarf, giant, and supergiant models, respectively, where we compare the first four Balmer members (from left to right: Hδ, Hγ, Hβ, Hα). The PoWR model parameters are identical to those compiled in Table 2.2, but with a negligible mass-loss rate of $\log \dot{M} = -9.0\,[M_\odot\,\mathrm{yr}^{-1}]$ and a small terminal velocity of $500\,\mathrm{km\,s}^{-1}$. Furthermore, the radii of all stars were set to large values to diminish possible curvature effects and to approach a plane-parallel geometry.

It is evident that a very good agreement in the line wings is obtained between the PoWR and TLUSTY models for all three luminosity classes. In particular, the wings of the Balmer lines are barely distinguishable. Hence, the application of either models would result in practically the same surface gravity, provided that the mass loss is really negligible. Interestingly, pressure broadening in the TLUSTY O-grid models from Lanz & Hubeny (2003) uses analytical approximations to numerical calculations (cf. Hubeny et al. 1994, appendix B), while PoWR performs interpolation over pressure broadening tables (Lemke 1997) for hydrogen lines. Given the good agreement, both methods seem to be adequate for the studied parameter regime, i.e., nondegenerated stars.

While a comprehensive comparison between PoWR and TLUSTY along all spectral lines is beyond the scope of the current paper, we note that there are significant differences regarding helium and metal lines. Not only does their strength differ by up to a factor of two between TLUSTY and PoWR, but sometimes – as visible in the supergiant comparison – they may even appear in emission from one code, and absorption from the other. Because of the non-LTE conditions, even small differences in the stratification can have

[5]It may seem arbitrary to rectify the synthetic flux using the continuum before accounting for the redistribution. However, the redistributed flux varies significantly around spectral lines, while the "unredistributed continuum" is a slowly varying function of λ and therefore much more appropriate for normalization. Moreover, electron scattering contains vital information regarding the physics in the stellar atmosphere, and should not be removed by normalization.

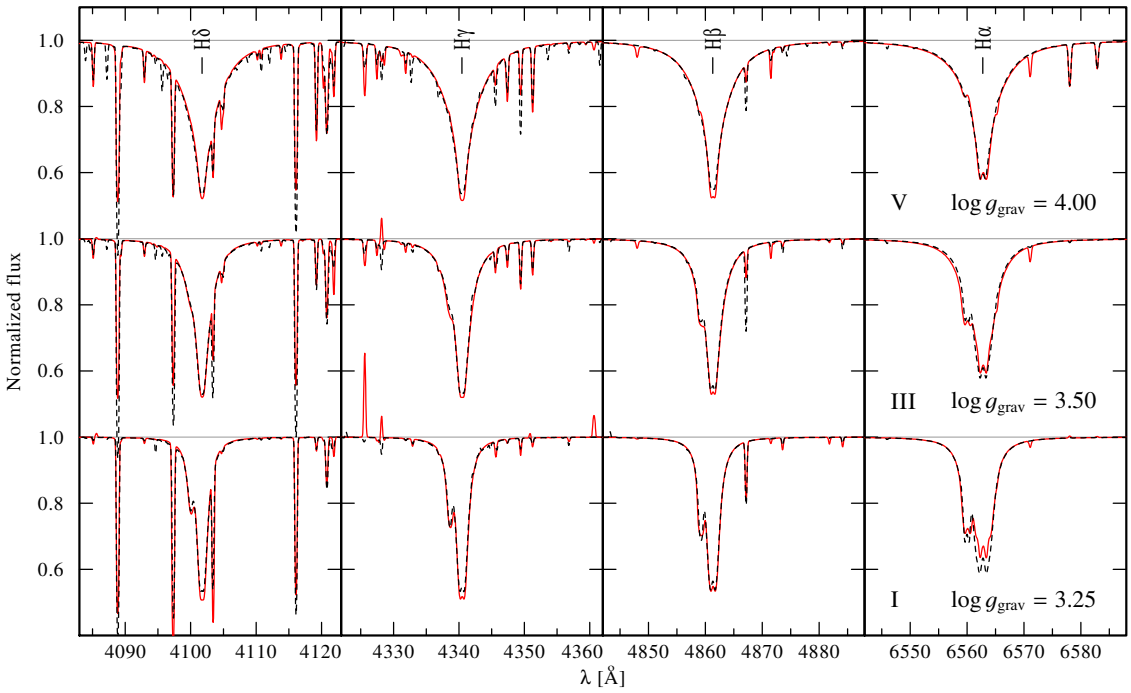

Figure 2.10.: Balmer line comparison between the PoWR models (red, solid line) and the TLUSTY models (black, dashed line) for dwarfs (upper panels), giants (middle panels), and supergiants (lower panels). The stellar parameters used in the PoWR models are as in Table 2.2, but with negligible mass-loss rates ($\log \dot{M} = -9\,[M_\odot\,\mathrm{yr}^{-1}]$), small terminal velocities ($500\,\mathrm{km\,s}^{-1}$), and large radii, to avoid wind and curvature effects.

large effects on such weak lines, e.g., between two PoWR models differing only slightly in their temperature or gravity. Indeed, we find similar discrepancies in the small lines. This can be seen in Fig. 2.4, where we compare the $\overline{\Gamma}_{\mathrm{rad}}$- and Γ_{e}-model spectra. Therefore one has to be careful deducing parameters, e.g., abundances, from only one particular line. Instead, several lines of more than one ionization stage should be compared if available.

2.5. Summary and conclusions

We present a set of stellar atmosphere models calculated with the most recent version of the PoWR code, using different approaches for the quasi-hydrostatic regime. In the limit of small mass-loss rates, we also compared the PoWR models to the plane-parallel TLUSTY atmospheres.

We conclude that a proper treatment of the quasi-hydrostatic regime is imperative for OB-type star modeling. For a consistent solution, the full radiative acceleration has to be taken into account, including line and continuum contributions.

The spectroscopic masses will be severely underestimated, by a factor of roughly 2, if models are used that account only for the radiation pressure on free electrons in the quasi-hydrostatic domain. This holds for all luminosity classes.

Omitting elements that significantly contribute to the total opacity compromises the density stratification in the quasi-hydrostatic domain, and consequently leads to an inconsistent stellar masses. Specifically neglecting important elements, such as Fe, in the models is by no means legitimate.

The effect of mass loss on the spectra of typical OB stars may seem subtle, but even small mass-loss rates can change the line profile and thus might affect deduced gravities. The absence of emission lines in

an observation does not imply negligible mass loss.

In the limit of small mass-loss rates and vanishing curvature effects, the emergent spectra of the PoWR model atmospheres generally agree very well with TLUSTY models calculated with the same stellar parameters.

2.6. acknowledgements

We would like to thank the anonymous referee for the fruitful suggestions that helped to significantly improve this paper. We would also like to thank Ivan Hubeny for the interesting and productive discussions that lead to the comparisons presented in this work. The first author of this work (A.S.) is supported by the Deutsche Forschungsgemeinschaft (DFG) under grant HA 1455/22. T.S. is grateful for financial support from the Leibniz Graduate School for Quantitative Spectroscopy in Astrophysics, a joint project of the Leibniz Institute for Astrophysics Potsdam (AIP) and the Institute of Physics and Astronomy of the University of Potsdam. A.S. would like to thank the Aspen Center for Physics and the NSF Grant #1066293 for hospitality during the invention and writing of this paper.

Chapter 3.

A coordinated X-ray and Optical Campaign of the Nearest Massive Eclipsing Binary, δ Orionis Aa: A Multiwavelength, Non-LTE spectroscopic analysis (Manuscript II)

T. Shenar, L. Oskinova, W.-R. Hamann, M. F. Corcoran, A. F. J. Pablo, N. D. Richardson, W. L. Waldron, D. P. Huenemoerder, J. Maíz Apellániz, J. S. Nichols, H. Todt, Y. Nazé, J. L. Hoffman, A. M. T. Pollock, I. Negueruela

The Astrophysical Journal, 2015, Volume 809, Issue 2, 20 pp.

Abstract

Eclipsing systems of massive stars allow one to explore the properties of their components in great detail. We perform a multi-wavelength, non-LTE analysis of the three components of the massive multiple system δ Ori A, focusing on the fundamental stellar properties, stellar winds, and X-ray characteristics of the system.

The primary's distance-independent parameters turn out to be characteristic for its spectral type (O9.5 II), but usage of the *Hipparcos* parallax yields surprisingly low values for the mass, radius, and luminosity. Consistent values follow only if δ Ori lies at about twice the *Hipparcos* distance, in the vicinity of the σ-Orionis cluster. The primary and tertiary dominate the spectrum and leave the secondary only marginally detectable. We estimate the V-band magnitude difference between primary and secondary to be $\Delta V \approx 2\overset{\mathrm{m}}{.}8$. The inferred parameters suggest the secondary is an early B-type dwarf ($\approx$ B1 V), while the tertiary is an early B-type subgiant ($\approx$ B0 IV). We find evidence for rapid turbulent velocities ($\sim 200\,\mathrm{km\,s^{-1}}$) and wind inhomogeneities, partially optically thick, in the primary's wind. The bulk of the X-ray emission likely emerges from the primary's stellar wind ($\log L_\mathrm{X}/L_\mathrm{Bol} \approx -6.85$), initiating close to the stellar surface at $R_0 \sim 1.1\,R_*$. Accounting for clumping, the mass-loss rate of the primary is found to be $\log \dot{M} \approx -6.4\,[M_\odot\,\mathrm{yr}^{-1}]$, which agrees with hydrodynamic predictions, and provides a consistent picture along the X-ray, UV, optical and radio spectral domains.

3.1. Introduction

Massive stars ($M \gtrsim 10 M_\odot$) bear a tremendous influence on their host galaxies, owing to their strong ionizing radiation and powerful stellar winds (e.g., Kudritzki & Puls 2000; Hamann et al. 2006). Yet our understanding of massive stars and their evolution still leaves much to be desired: (1) Values of mass-loss rates derived in different studies may disagree with each other by up to an order of magnitude (e.g., Puls et al. 1996; Fullerton et al. 2006; Waldron & Cassinelli 2010; Bouret et al. 2012) and often do not agree with theoretically predicted mass-loss rates (e.g., Vink et al. 2000). (2) The extent of wind inhomogeneities,

which greatly influence mass-loss rates inferred by means of spectral analyses, are still largely debated (Shaviv 2000; Owocki et al. 2004; Oskinova et al. 2007; Sundqvist et al. 2011; Šurlan et al. 2013). (3) The production mechanisms of X-ray radiation in massive stars have been a central subject of study in recent decades (Feldmeier et al. 1997; Pollock 2007) and are still far from being understood. (4) The effect of magnetic fields and stellar rotation on massive stars (e.g., Friend & MacGregor 1984; Maheswaran & Cassinelli 2009; Oskinova et al. 2011; de Mink et al. 2013; Petit et al. 2014; Shenar et al. 2014), e.g., through magnetic braking (Weber & Davis 1967) or chemical mixing (Maeder 1987), are still being investigated. (5) Lastly, stellar multiplicity seems to play a fundamental role in the context of massive stars, significantly affecting their evolution (e.g., Eldridge et al. 2013).

Several studies in the past years (e.g., Mason et al. 2009b; Maíz Apellániz 2010; Chini et al. 2012; Sana et al. 2013; Sota et al. 2014; Aldoretta et al. 2015) give direct evidence that at least half of the massive stars are found in multiple systems. Massive stars in close binary systems generally evolve differently from single stars. Such systems may experience significant tidal forces (Zahn 1975; Palate et al. 2013), mass-transfer (Pols et al. 1991), additional supernova kicks (Hurley et al. 2002), and mutual irradiation effects (Howarth 1997). Given the large binary fraction, an understanding of these processes is critical to properly model the evolution of massive stars. Fortunately, binary systems have two main advantages over single stars: First, they offer us the opportunity to empirically determine stellar masses. Second, eclipsing binary systems provide the unique opportunity to investigate different characteristics of stellar winds by taking advantage of occultation (e.g., Antokhin 2011). It is therefore insightful to analyze eclipsing multiple systems of massive stars in our Galactic neighborhood, using adequate, state-of-the-art modeling tools.

The star δ Ori A (HD 36 486, Mintaka, HIP 25 930, HR 1852) is a massive triple system (see artist's illustration in Fig. 3.1) comprised of the close eclipsing binary Aa (primary Aa1, secondary Aa2) with a 5.732 d period (Harvey et al. 1987; Harvin et al. 2002; Mayer et al. 2010), and the more distant tertiary Ab at an angular separation of $\approx 0.3''$ relative to the binary Aa with a period of ~346 yr (Heintz 1980; ESA 1997a; Tokovinin et al. 2014). The tertiary Ab has been photometrically resolved from the binary Aa in different surveys (Horch et al. 2001; Mason et al. 2009b; Maíz Apellániz 2010) and is found to contribute $\approx 25\%$ to the system's flux in the visual band. These three components are not to be confused with the more distant and significantly fainter stars δ Ori B and C at separation $33''$ and $53''$, respectively; together, these five stars comprise the multiple system δ Ori, also known as Mintaka. With a visual magnitude of $V = 2\overset{\text{m}}{.}24$ outside eclipse (Morel & Magnenat 1978), δ Ori A is one of the brightest massive multiple systems in the night sky, making it easily visible to the naked eye (it is the westmost star in Orion's belt). According to the new *Hipparcos* reduction (van Leeuwen 2007), its parallax is 4.71 ± 0.58 mas, corresponding to a distance of $d = 212 \pm 30$ pc[1]. On the other hand, the system resides in the Orion OB1b association, to which the σ-Orionis cluster belongs as well. The distance to the cluster itself is estimated to be $d \sim 380$ pc, almost a factor 2 larger than the *Hipparcos* distance (see Caballero & Solano 2008, and references therein).

This paper is a contribution to a series of papers within the framework of the δ Ori collaboration. The other papers include the analysis of high quality *Chandra* observations to explore X-ray properties (Corcoran et al. in prep. Paper I) and variability (Nichols et al. in prep. Paper II) in the system, and a complete photometric and spectrometric variabilty analysis (Pablo et al. in prep. Paper III). In this study, we focus on a non-LTE, multiwavelength spectral analysis of the three components Aa1, Aa2, and Ab, with the goal of obtaining reliable stellar and wind parameters.

δ Ori A has been repeatedly studied previously. The system, which shows clear evidence for a significant stellar wind in the optical, UV, and X-ray domains, has been assigned the spectral type O9.5 II (Walborn 1972), later refined by Sota et al. (2011) to O9.5 II Nwk, which most probably corresponds to the brigtest component: Aa1. With less confidence, the secondary Aa2 has been assigned the spectral type B0.5 III (Harvin et al. 2002). This result is questioned by Mayer et al. (2010), who argue that the secondary is too faint for this spectral type. The latter authors further suggest the spectral type O9 IV for the tertiary, and leave the secondary unclassified.

Although the stellar parameters of an eclipsing stellar system can usually be sharply constrained, much

[1]This value is not corrected for the Lutz-Kelker effect (Lutz & Kelker 1973). Maíz Apellániz et al. (2008) account for this effect and revise the distance to $d = 221$ pc. However, the difference is negligible within measurement uncertainties.

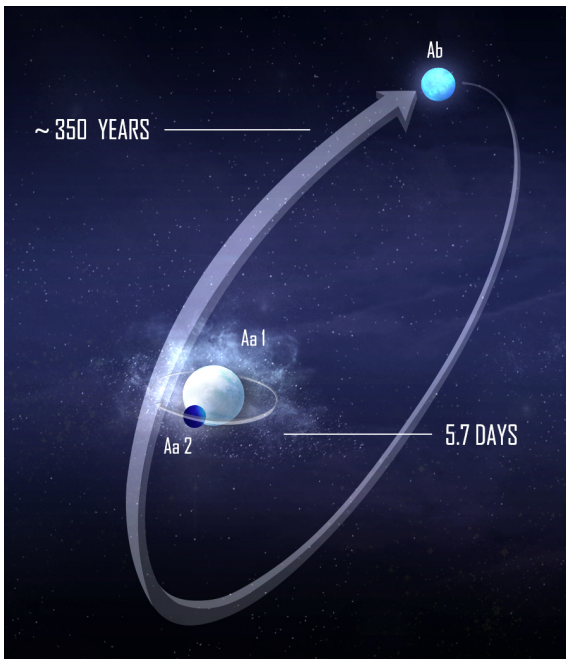

Figure 3.1.: Artist's impression of the triple system δ Ori A, as viewed from Earth. The primary (Aa1) and Secondary (Aa2) form the tight eclipsing binary of period 5.7 d. The primary shows evidence for a significant wind in all spectral domains. A third star (Ab) at an angular separation of $\approx 0.3''$ ($\sim$ 100 AU at a distance of $d = 380$ pc to Earth) orbits the system with a period of $\approx$346 yr (Tokovinin et al. 2014) and contributes roughly 25% to the total visual flux. The sizes of all three components are drawn are to scale, as inferred in this collaborative study. Their colors reflect their relative temperatures. Note that the tertiary is the second brightest companion in the system. The distance between the binary system Aa and the tertiary Ab is not to scale. Credits to Jessica Mayo

controversy is found in the literature in the case of δ Ori A. Koch & Hrivnak (1981) reported $M_1 = 23\,M_\odot$, $R_1 = 17\,R_\odot$ and $M_2 = 9\,M_\odot$, $R_2 = 10\,R_\odot$ for the primary and secondary masses and radii, respectively, as well as a V-band magnitude difference of $\Delta V_{\mathrm{Aa1Aa2}} = 1\overset{\mathrm{m}}{.}4$. Harvin et al. (2002) later inferred significantly smaller masses for the primary and secondary, $M_1 = 11.2\,M_\odot$, $M_2 = 5.6\,M_\odot$, and a smaller contribution of the secondary in the visual band: $\Delta V_{\mathrm{Aa1Aa2}} = 2\overset{\mathrm{m}}{.}5$. These results were challenged by Mayer et al. (2010), who suggested that a confusion between the secondary Aa2 and tertiary Ab led to the low masses obtained by Harvin et al. (2002). Mayer et al. (2010) inferred $R_1 = 15.6\,R_\odot$ and $R_2 = 4.8\,R_\odot$. They did not detect any contribution from the secondary Aa2 and concluded that $\Delta V_{\mathrm{Aa1Aa2}} \gtrsim 3\overset{\mathrm{m}}{.}5$. Assuming $M_1 = 25\,M_\odot$, they inferred $M_2 = 9.9\,M_\odot$. In Paper III, the secondary's radial velocity (RV) curve could not be constructed, and, for an adopted primary mass of $M_1 \approx 24\,M_\odot$, it was concluded that $M_2 = 8.5\,M_\odot$ $R_1 = 15.1\,R_\odot$, $R_2 = 5.0\,R_\odot$.

Similarly, reported values of the mass-loss rate of the primary are quite diverse: Lamers & Leitherer (1993) report $\log \dot{M}_1 = -5.97$ $[M_\odot\,\mathrm{yr}^{-1}]$ based on radio observation and $\log \dot{M}_1 = -5.92$ $[M_\odot\,\mathrm{yr}^{-1}]$ based on Hα analysis. Lamers et al. (1999) later similarly obtain $\log \dot{M}_1 = -5.7$ $[M_\odot\,\mathrm{yr}^{-1}]$ based on P Cygni profile analysis using the Sobolev plus exact integration (SEI) method. Neglecting the effects of wind inhomogeneities and porosity (Oskinova et al. 2007; Šurlan et al. 2013) on the observed X-ray spectrum, and adopting a generic O-type model, Cohen et al. (2014) derived a value of $\dot{M}_1 = -7.2$ $[M_\odot\,\mathrm{yr}^{-1}]$ from X-ray line profile fitting, more than an order of magnitude less than the previously inferred value. Indeed,

no consensus on the mass-loss rate of the primary has been reached so far.

δ Ori A has an observed X-ray luminosity of $L_X \approx 1.4 \cdot 10^{32}$ erg s^{-1} for $d = 380$ pc (Paper I). δ Ori A's X-ray properties were previously explored by Miller et al. (2002), Leutenegger et al. (2006), and Raassen & Pollock (2013). These studies generally identify the X-ray formation process to be intrinsic to the primary's wind, a result which is further supported within our collaboration. An extensive review of past X-ray observations and analyses are given by Papers I and II.

In this study, we perform a consistent non-LTE photosphere and wind analysis of the three components of the triple system δ Ori A in the optical, UV, and X-ray domains, at several orbital phases. We analyze the optical and UV spectra using the non-LTE Potsdam Wolf-Rayet (PoWR) code, which is applicable to any hot star. We further illustrate the importance of optically thin and optically thick clumps in the wind. We use the non-LTE models to simulate the effect of X-rays in the wind of the primary and derive onset radii of X-ray formation regions using ratios of forbidden and intercombination lines in the *Chandra* spectra. Finally, using the non-LTE model of the primary, we calculate synthetic X-ray line profiles and compare them to observed ones. Our results are further compared to studies of the radio emission from the system. This study thus encompasses the whole range from the X-ray domain to the radio domain.

The structure of the paper is as follows: In Sect. 3.2 we describe the observational data used. Our modeling methods and assumptions are discussed in Sect. 3.3. In Sect. 3.4, we present and discuss our results. Sect. 3.5 focuses on the effect of wind inhomogeneities on the optical, UV and X-ray spectral domains, while in Sect. 3.6 we study the X-ray radiation of the star. Lastly, in Sect. 3.7, we summarize our results.

3.2. Observational data

All spectra used in this analysis contain the contribution of the primary Aa1, secondary Aa2, and tertiary Ab. In the following, all phases given are photometric phases relative to primary minimum (occurring when the secondary occults the primary), calculated with E_0 = HJD 2456277.79 d and $P = 5.732436$ d (Paper III, and references therein).

Two of our optical spectra are of high resolution and high signal-to-noise, obtained with the NARVAL spectropolarimeter on 23-24 October 2008. These spectra were reduced with standard techniques and downloaded from the PolarBase[2] (Petit et al. 2014). The observations were carried out with the Telescope Bernard Lyot. The spectra have a S/N of 500 − 800, and correspond to phases $\phi = 0.84$ and $\phi = 0.02$.

Three additional optical spectra at phases $\phi = 0.19$, 0.38, and 0.54 were obtained on the nights of 28, 29, and 30 Dec 2012 (contemporaneous with out Chandra and MOST observations) using the CAFÉ spectrograph at the 2.2 m Calar Alto telescope as part of the CAFÉ-BEANS project, a survey that is obtaining high-resolution ($R \sim 65\,000$) multi-epoch optical spectroscopy of all bright O stars in the northern hemisphere to complement OWN, the equivalent southern hemisphere survey (Barbá et al. 2010; Sota et al. 2014). On each date, ten consecutive 30 s exposures were obtained and combined to yield spectra with S/N varying from ∼ 200 in the blue part (∼ 4500 Å) to ∼ 500 in the red part (∼ 6000 Å). The data were processed using a pipeline developed specifically for the project. The velocity stability was checked using ISM lines. More details regarding the reduction pipeline are given by Negueruela et al. (2014).

For the spectral range 1200 − 2000 Å, we make use of archival *IUE* spectra at different orbital phases (see the observation log given by Harvin et al. 2002). The spectra have a signal-to-noise (S/N) ratio of ∼ 10/pixel, and are averaged in bins of 0.1 Å. The *IUE* spectra are flux-calibrated and are rectified using the model continuum.

In the spectral range 1000 − 1200 Å, we make use of the *Copernicus* observation available in the *Copernicus* archive under the ID c025-001.u2. This observation consists of 48 co-added scans obtained between 21 and 24 November 1972.

For the spectral energy distribution (SED), we make use of U, B, V, R, I, J, H, K (Morel & Magnenat 1978), WISE (Cutri & et al. 2012), and IRAS (Moshir & et al. 1990) photometry. We further use a low-resolution, flux calibrated optical spectrum kindly supplied to us by S. Fabrika and A. Valeev (priv.

[2]http://polarbase.irap.omp.eu

com.). The spectrum was obtained with the Russian BTA telescope using the SCORPIO focal reducer, on 31 Dec 2013 in the range 3800 – 7200 Å with a spectral resolution of 6.3 Å, and corresponds to phase $\phi = 0.42$. A Hartmann mask was used to avoid saturation.

The *Chandra* X-ray spectra used in Sect. 3.6 were taken with the HEG and MEG detectors for a total exposure time of 487.7 ks. The data are thoroughly described in Papers I and II.

3.3. Non-LTE photosphere and wind modeling

3.3.1. The PoWR code

PoWR is a non-LTE model atmosphere code especially suitable for hot stars with expanding atmospheres[3]. The code consists of two main parts. In the first part, referred to as the non-LTE iteration, the co-moving frame radiative transfer in spherical symmetry and the statistical balance equations are solved in an iterative scheme under the constraint of energy conservation, yielding the occupation numbers in the photosphere and wind. The second part, referred to as the formal integration, delivers a synthetic spectrum in the observer's frame. The pre-specified wind velocity field takes the form of a β-law (Castor et al. 1975) in the supersonic region. In the subsonic region, the velocity field is defined so that a hydrostatic density stratification is approached. Line blanketing by the iron lines is treated in the superlevel approach (Gräfener et al. 2002), as originally introduced by Anderson (1989). A closer description of the assumptions and methods used in the code is given by Gräfener et al. (2002) and Hamann & Gräfener (2004).

In the non-LTE iteration, line profiles are Gaussians with a constant Doppler width $v_{\rm Dop}$. In the formal integration, the Doppler velocity is composed of depth-dependent thermal motion and microturbulence. The microturbulence $\xi(r)$ is interpolated between the photospheric microturbulence $\xi(r_{\rm ph}) = \xi_{\rm ph}$ and the wind microturbulence $\xi(r_{\rm w}) = \xi_{\rm w}$, with the radii $r_{\rm ph}$ and $r_{\rm w}$ pre-specified. Thermal and pressure broadening are accounted for in the formal integration. Turbulence pressure is also accounted for in the non-LTE iteration. Optically thin wind inhomogeneities are accounted for in the non-LTE iteration using the so-called 'microclumping' approach (Hamann et al. 1995). The density contrast between a clumped and a smooth wind with an identical mass-loss rate is described by the depth-dependent clumping factor $D(r)$ (Hamann & Koesterke 1998), where the clumps are assumed to be optically thin. Optically thick clumps, or 'macroclumps', are accounted for in the formal integration as described by Oskinova et al. (2007), where the clump separation parameter $L_{\rm mac}$ is to be specified (see Sect. 3.5).

Four fundamental input parameters define a model atmosphere of an OB type star: T_*, L, g_*, $\dot{M}$. T_* is the effective temperature of a star with luminosity L and radius R_*, as defined by the Stefan-Boltzmann relation $L = 4\pi\sigma R_*^2 T_*^4$. g_* is related to the radius R_* and mass M_* via $g_* = g(R_*) = G\,M_* R_*^{-2}$. $\dot{M}$ is the mass-loss rate of the star. The stellar radius R_* is defined at the continuum Rosseland optical depth $\tau_{\rm Ross}$=20, which is the inner boundary of our model, and which was tested to be sufficiently large. The outer boundary of the model is set to $100\,R_*$. Note that the stellar radius is generally not identical to the photospheric radius $R_{2/3}$ defined at $\tau_{\rm Ross} = 2/3$. However, usually $R_* \cong R_{2/3}$, except in cases of extreme radiation pressures (e.g., supergiants, Wolf-Rayet stars). Nevertheless, one must bear in mind that the effective temperature referring to the photospheric radius, which we denote with $T_{2/3}$ to avoid ambiguity, may slightly differ from T_*. Similarly, $g_{2/3} = g(R_{2/3})$ is the gravity at $\tau_{\rm Ross} = 2/3$. Like most studies, we specify photospheric values when compiling our results in Table 3.1, but the cautious reader should be aware of this difference when comparing with other studies.

Due to the strong radiative pressures in massive stars, one cannot measure the gravity g_* directly from their spectra, but rather the effective gravity $g_{\rm eff}$. g_* is obtained from $g_{\rm eff}$ via $g_{\rm eff} := g_* \left(1 - \overline{\Gamma}_{\rm rad}\right)$, where $\overline{\Gamma}_{\rm rad}$ is a weighted average of the ratio of total outward radiative force to inward gravitational force over the hydrostatic domain. The outward radiative force is calculated consistently in the non-LTE iteration, and includes the contribution from line, continuum, and Thomson opacities (Sander et al. 2015).

[3]PoWR models of Wolf-Rayet stars can be downloaded at http://www.astro.physik.uni-potsdam.de/PoWR.html

3.3.2. The analysis method

The analysis of stellar spectra with non-LTE model atmosphere codes is an iterative, computationally expensive process, which involves a multitude of parameters. Nevertheless, most parameters affect the spectrum uniquely. Generally, the gravity g_* is inferred from the wings of prominent hydrogen lines. The stellar temperature T_* is obtained from the line ratios of ions belonging to the same element. Wind parameters such as $\dot{M}$, v_∞, and $L_{\rm mac}$ are derived from emission lines, mainly in the UV. The luminosity L and the colour excess $E(B-V)$ are determined from the observed spectral energy distribution (SED), and from flux-calibrated spectra. The abundances are determined from the overall strengths of lines belonging to the respective elements. Finally, parameters describing the various velocity fields in the photosphere and wind (rotation, turbulence) are constrained from profile shapes and strengths. The radius R_* and spectroscopic mass M_* follow from L, T_* and g_*.

To analyze a multiple system such as δ Ori A, a model for each component star is required. As opposed to single stars, the luminosities of the components influence their contribution to the overall flux and thus affect the normalized spectrum. The light ratios of the different components therefore become entangled with the fundamental stellar parameters. Fortunately, with fixed temperatures and gravities for the secondary and tertiary components, the observational constraints provide us with the light ratios (see Sect. 3.3.3).

Methods to disentangle a composite spectrum into its constituent spectral components by observing the system at different phases have been proposed and implemented during the past few years (Bagnuolo & Gies 1991; Simon & Sturm 1994; Hadrava 1995; González & Levato 2006; Torres et al. 2011). In fact, an attempt to disentangle the spectrum of δ Ori A was pursued by Harvin et al. (2002) and Mayer et al. (2010). However, even after performing the disentanglement, the two sets of authors come to significantly different results. A disentanglement of the He I λ6878 line was performed in Paper III, but, after accounting for the contribution of the tertiary as obtained here, no clear signal from the secondary was detected. Given the very low contribution of the secondary Aa2, and having only poor phase coverage in the optical, we do not pursue a disentanglement of δ Ori A.

As a first step, the secondary and tertiary models are kept fixed. Motivated by the results of Paper III, we initially adopt $T_{2/3} \sim 25\,$kK and $\log g_{2/3} \sim 4.15\,[\mathrm{g\,cm^{-2}}]$ for the secondary. The tertiary is initially fixed with the parameters suggested by Mayer et al. (2010). With the light ratios at hand, this fixes the luminosities of Aa2 and Ab. Having fixed the secondary and tertiary models, we turn to the second step, which is an accurate analysis of the primary.

To constrain T_*, we use mostly He I and He II lines, such as He I $\lambda\lambda$4026, 4144, 4388, 4713, 4922, 5015, 6678 and He II λ4200, 4542, 5412, 6683. The prominent He II λ4686 line is found to be a poor temperature indicator (see Sect. 3.4.2). The temperature is further verified from lines of carbon, nitrogen and silicon. g_* is primarily derived from the wings of prominent Balmer and He II lines. Here we encounter the difficult problem of identifying the contribution of the tertiary to the hydrogen lines due to the pronounced wings of the Balmer lines. We therefore also made use of diagnostic lines such as C III λ5696, whose behavior heavily depends on the gravity (see Sect. 3.4.4).

$\dot{M}$ and $L_{\rm mac}$ follow from a simultaneous fitting of Hα and UV P Cygni lines. The wind parameters are checked for consistency with previous analyses of radio observations and with X-ray observations (see Sect. 3.6.3). The terminal velocity v_∞ is determined from UV resonance lines. However, v_∞ can only be determined accurately after the wind microturbulence has been deduced. The determination of the projected rotational velocity $v \sin i$ and of the inner (photospheric) and outer (wind) microturbulent velocities $\xi_{\rm ph}$ and $\xi_{\rm w}$, as well as of the macroturbulent velocity $v_{\rm mac}$, is discussed in detail in Sect. 3.4.3.

The abundances are determined from the overall strengths of lines belonging to the respective elements. We include the elements H, He, C, N, O, Mg, Al, Si, P, S, and elements belonging to the iron group (e.g., Fe, Ni, Cr etc.). With the remaining stellar parameters fixed, this is a straight-forward procedure.

The total bolometric luminosity $L = L_1 + L_2 + L_3$ is obtained by fitting the synthetic flux with the observed SED. The individual component luminosities follow from the light ratios. The color excess E_{B-V} is derived using extinction laws published by Cardelli et al. (1989) with $R_V = 3.1$, and can be very accurately determined from flux-calibrated *IUE* observations. The inferred value for A_V is consistent with those of Maíz Apellániz & Sota (in prep. 2015), who obtain a value of 0.185±0.013 mag using Tycho+Johnson+2MASS photometry and the extinction laws of Maíz Apellániz et al. (2014).

After obtaining a satisfactory model for the primary, we continue to iterate on the secondary and tertiary models by identifying small deviations between the composite synthetic and observed spectra at different orbital phases, as described in Sect. 3.4.2. This allows us to adjust the temperatures and gravities of both models, as well as of the projected rotation velocities. After improving the secondary and tertiary models, we return to the primary and adjust the model parameters accordingly. We repeat this process several times until a satisfactory fit is obtained in the UV and optical, taking hundreds of lines into account in this process.

3.3.3. Initial assumptions

Given the large number of parameters involved in this analysis, it is advisable to initially fix parameters which are constrained based on observations, previous studies, and theoretical predictions.

We adopt β=0.8 for the exponent of the β-law for all components, which is both supported by observations as well as theoretically predicted (e.g., Kudritzki et al. 1989; Puls et al. 1996). Varying this parameter in the range $0.7 - 1.5$ did not significantly effect on the resulting synthetic spectrum.

A V-band magnitude difference of $\Delta V_{\rm AaAb} = 1\overset{\rm m}{.}35$ between the binary system Aa (composed of Aa1 and Aa2) and the tertiary Ab was measured by the *Hipparcos* satellite (ESA 1997a). Horch et al. (2001) report $\Delta V_{\rm AaAb} = 1\overset{\rm m}{.}59$, obtained from speckle photometry. Mason et al. (2009b) find $\Delta V_{\rm AaAb} = 1\overset{\rm m}{.}4$ by means of speckle interferometry. Like Mayer et al. (2010), we adopt $\Delta V_{\rm AaAb} = 1\overset{\rm m}{.}4$, corresponding to the flux ratio $R_{AaAb} := F_V(Aa)/F_V(Ab) = 3.63$. As for the binary components Aa1 and Aa2, additional information regarding $\Delta V_{\rm Aa1Aa2}$ can be obtained from the visual light curve of the system δ Ori A. The secondary light curve minimum (primary star in front) has a depth $\Delta V_{\rm II.min} \approx 0\overset{\rm m}{.}055$ with an error of about $0\overset{\rm m}{.}005$. Since the secondary eclipse is partial (Paper III), the secondary minimum yields a lower limit to R_{Aa2Aa1}. One obtains after some algebra

$$R_{Aa2Aa1} \geq \frac{(R_{\rm II.min} - 1)(R_{\rm AaAb} + 1)}{R_{\rm AaAb} - R_{\rm II.min} + 1}. \tag{3.1}$$

In our case, $R_{\rm AaAb} \approx 3.63$ and $R_{\rm II.min} \approx 1.05$, and so $F_V(Aa2) \gtrsim 0.07\, F_V(Aa1)$, which in turn implies $\Delta V_{Aa1Aa2} \lesssim 2\overset{\rm m}{.}9$. It follows that the secondary Aa2 contributes *at least* 6.5% to the visual flux of the binary, and *at least* 5.1% to the total visual flux of the system. We thus initially assume $\Delta V_{Aa2Aa1} = 2\overset{\rm m}{.}8$, and further constrain this value in the spectral analysis (see Section 4.1).

In Sect. 3.4.1, we show that usage of the *Hipparcos* distance $d = 212$ pc results in extremely peculiar parameters for the primary given its spectral type, and that a much better agreement is obtained for the alternative distance of the neighboring stellar cluster σ-Orionis, $d \sim 380$ pc (see also discussion by Simón-Díaz et al. 2015). We therefore refer to both distances in the following, and discuss this issue more thoroughly in Sect. 3.4.1. We note, however, that our results can be easily scaled with the distance, should it be revised in future studies (see Sect. 3.4).

As we illustrate in Sect. 3.5, there are several indications for wind inhomogeneities (clumps) in the wind of Aa1. While clumping may already initiate at sub-photospheric layers e.g., due to sub-photospheric convection (Cantiello et al. 2009), we avoid an attempt to treat clumpiness in the optically thick layers below the photosphere. For reasons which are discussed in detail in Sect. 3.5, we adopt a depth-dependent clumping factor $D(r)$ which is fixed to 1 (no clumping) in the domain $R_* \leq r \leq 1.1\, R_*$ and reaches a maximum value of $D_{\rm max} = 10$ at $r \geq 10\, R_*$.

Due to the faintness of the secondary and tertiary, we we can only give upper limits to their mass-loss rates, and set their terminal velocities to be 2.6 times their escape velocity (Lamers & Cassinelli 1999). We further assume $\xi(r) = 10\,{\rm km\,s^{-1}}$ for the secondary, a typical value for OB type stars of luminosity classes III and lower (cf. Villamariz & Herrero 2000, and references therein). We choose to adopt an identical density contrast $D(r)$ for all three models. Finally, we do not attempt to constrain the abundances in the secondary and tertiary, but rather adopt solar values (Asplund et al. 2009). This set of assumptions should bear very little effect on the derived fundamental parameters of the three components.

Table 3.1.: Inferred stellar parameters for the multiple stellar system δ Ori A

	Aa1		Aa2		Ab	
$T_{2/3}$ [kK]	29.5±0.5		25.6±3000		28.4±1500	
$\log g_{\rm eff}$ [cm s^{-2}]	3.0±0.15		3.7		3.2±0.3	
$\log g_{2/3}$ [cm s^{-2}]	3.37±0.15		3.9		3.5±0.3	
v_∞ [km s^{-1}]	2000±100		1200		2000	
D	10		10		10	
$L_{\rm mac}$ [$R_\odot$]	$\gtrsim$0.5		-		-	
$E(B-V)$ [mag]	0.065±0.01		0.065±0.01		0.065±0.01	
A_V [mag]	0.201±0.03		0.201±0.03		0.201±0.03	
$v \sin i$ [km s^{-1}]	130±10		150±50		220±20	
$\xi_{\rm ph}$ [km s^{-1}]	20±5		10		10±5	
$\xi_{\rm w}$ [km s^{-1}]	200±100		10		10	
$v_{\rm mac}$ [km s^{-1}]	60±30		0		50±30	
H (mass fraction)	0.70±0.05		0.7		0.7	
He (mass fraction)	0.29±0.05		0.29		0.29	
C (mass fraction)	$2.4 \pm 1 \times 10^{-3}$		2.4×10^{-3}		2.4×10^{-3}	
N (mass fraction)	$4.0 \pm 2 \times 10^{-4}$		7.0×10^{-4}		7.0×10^{-4}	
O (mass fraction)	$6.0 \pm 2 \times 10^{-3}$		6.0×10^{-3}		6.0×10^{-3}	
Mg (mass fraction)	6.4×10^{-4}		6.4×10^{-4}		6.4×10^{-4}	
Al (mass fraction)	5.6×10^{-5}		5.6×10^{-5}		5.6×10^{-5}	
Si (mass fraction)	$4 \pm 2 \times 10^{-4}$		6.6×10^{-4}		6.6×10^{-4}	
P (mass fraction)	5.8×10^{-6}		5.8×10^{-6}		5.8×10^{-6}	
S (mass fraction)	3.0×10^{-4}		3.0×10^{-4}		3.0×10^{-4}	
Fe (mass fraction)	1.3×10^{-3}		1.3×10^{-3}		1.3×10^{-3}	
Adopted distance d [pc]	212	380	212	380	212	380
$\log L$ [$L_\odot$]	4.77±0.05	5.28±0.05	3.7±0.2	4.2±0.2	4.3±0.15	4.8±0.15
$\log \dot{M}$ [$M_\odot$/yr]	−6.8±0.15	−6.4±0.15	−8.5	−8.1	≤ -7.0	≤ -6.6
$M_{\rm spec}$ [$M_\odot$]	$7.5^{+3}_{-2.5}$	24^{+10}_{-8}	2.6	8.4	7.0^{+7}_{-4}	22.5^{+24}_{-14}
$R_{2/3}$ [$R_\odot$]	9.2±0.5	16.5±1	3.6±1	$6.5^{+2}_{-1.5}$	5.8±1	10.4±2
M_V [mag]	−4.47±0.13	−5.74±0.13	−1.7±0.5	−3.0±0.5	-3.2±0.4	-4.5±0.4

3.4. Results

The stellar parameters inferred for the three components are given in Table 3.1. The model of the primary includes the effect of macroclumping and X-rays, which we thoroughly discuss in Sects. 3.5 and 3.6. The upper part of the table displays parameters which, to first order, do not depend on the adopted distance. The lower part of the table denotes distance-dependent parameters. For the convenience of the reader, we

give these parameters for both "candidate" distances, $d = 212$ pc and $d = 380$ pc. Luminosities scale as $L \propto d^2$, mass-loss rates as $\dot{M} \propto d^{3/2}$, radii as $R_* \propto d$, and the mass as $M_{\rm spec} \propto d^2$. The error margins given in Table 3.1 are discussed in Sect. 3.4.4 and are based on sensitivity of our analysis to these parameters. Values without errors which are not upper bounds indicate adopted values.

The upper panel of Fig. 3.2 displays the synthetic SEDs for the models of the three components of the system. The total synthetic SED (red solid line) comprises the synthetic fluxes of the primary Aa1 (green dashed line), secondary Aa2 (gray dotted-dashed line), and tertiary Ab (pink dotted line). Recall that the tertiary is brighter than the secondary. The blue squares denote U, B, V, R, I, J, H, K, WISE, and IRAS photometry. We also plot two observed flux-calibrated spectra in the UV and optical (blue lines). The lower panels of Fig. 3.2 show the composite synthetic (red dotted line) and observed (blue line) normalized UV and optical spectra of the system. The optical spectrum and the UV spectrum in the range 1200 – 2000Å correspond to phase $\phi \approx 0.54$. The synthetic normalized spectrum consists of three models calculated for Aa1, Aa2, and Ab, shifted according to their RVs. The synthetic spectra are convolved with a Gaussian of FWHM = 0.1 Å to account for instrumental broadening, inferred from fitting of the interstellar Na I $\lambda\lambda$5890, 5896.3 lines. We do not plot the individual spectra of the three components for clarity. Note that the wavy pattern seen in the observed spectrum (e.g., in the domain 5900 – 6500 Å) is an artifact which originates in the connection of the echelle orders, not related to the stellar system.

It is evident that both the synthetic SED and normalized spectrum agree well with the observed spectrum. A good balance is obtained for all He I lines and He II lines, as well as for the metal lines. The inferred parameters for microturbulence, rotation and macroturbulence yield consistent line strengths and profiles over the whole spectral domain. The pseudo continuum formed by the iron forest in the range 1300 – 1800 Å, as well as most photospheric and wind features, are well reproduced.

The few features which are not reproduced very well are the Balmer lines, and especially Hδ. Hδ has a significantly smaller observed EW (≈ 1.85 Å) compared to the synthetic spectrum (≈ 2.35 Å). In fact, the observed EW of Hδ is somewhat smaller than typical for similar spectral types (e.g., Cananzi et al. 1993), and the question arises as to the cause. A significantly smaller gravity for the primary does not agree with the wing shape of the other Balmer and He II lines and hardly affects the EW. Reducing the hydrogen abundance of the primary implies a larger helium abundance, which is not consistent with the helium lines. Larger $\dot{M}$ values lead to very strong emission in Hα, which is not observed. The photospheric microturbulence has only negligible effect on the EW of hydrogen lines. We therefore conclude that the Balmer lines are dilluted by the light of one or both of the other components. However, the low EW of Hδ could only be reproduced when assuming very peculiar parameters for the tertiary, e.g., a very weak gravity ($\log g_{2/3} \lesssim 3.2\,[\mathrm{g\,cm^{-2}}]$), or very large mass-loss rates ($\log \dot{M} \gtrsim -5.5\ [M_\odot/\mathrm{yr}]$). Such parameters are not only hard to justify physically, but also not consistent with the remaining spectral lines. The problem is also seen, albeit to a lesser extent, in the lines Hγ and Hβ. Future observations should shed light on this peculiarity.

3.4.1. Which distance is the correct one?

It is reassuring that those fundamental stellar parameters of the primary which do not depend on the distance match well with its spectral type. Interpolating calibrations by Martins et al. (2005) to an O9.5 II class yields $T_{2/3} = 29.3$ kK and $\log g_{2/3} = 3.35\,[\mathrm{g\,cm^{-2}}]$, which agrees with our results within the error margins. The primary's nitrogen and silicon abundances are found to be slightly subsolar. It is interesting to note that Sota et al. (2011) recently added the suffix "Nwk" to the spectral type of Aa1, implying relatively weak nitrogen lines, which we confirm independently.

For $d = 380$ pc, the distance-dependent parameters agree well with calibrations by Martins et al. (2005). Interpolating to luminosity class II, calibrations by Martins et al. (2005) imply $\log L/L_\odot = 5.3$, $M = 25\,M_\odot$, $R_{2/3} = 18.2\,R_\odot$, and $M_V = -5\overset{\mathrm{m}}{.}73$ for an O9.5 II star, which is consistent with our results. Furthermore, this distance implies radii and masses for the primary and secondary which agree well with the results obtained independently in Paper III. However, very peculiar values are obtained when using the *Hipparcos* distance of $d = 212$ pc (see lower part of Table 3.1). In fact, all three components appear to be peculiar when adopting the *Hipparcos* distance. While a membership in a close binary system offers some room for deviations from standard values, this would not explain why the distant tertiary Ab should be peculiar too.

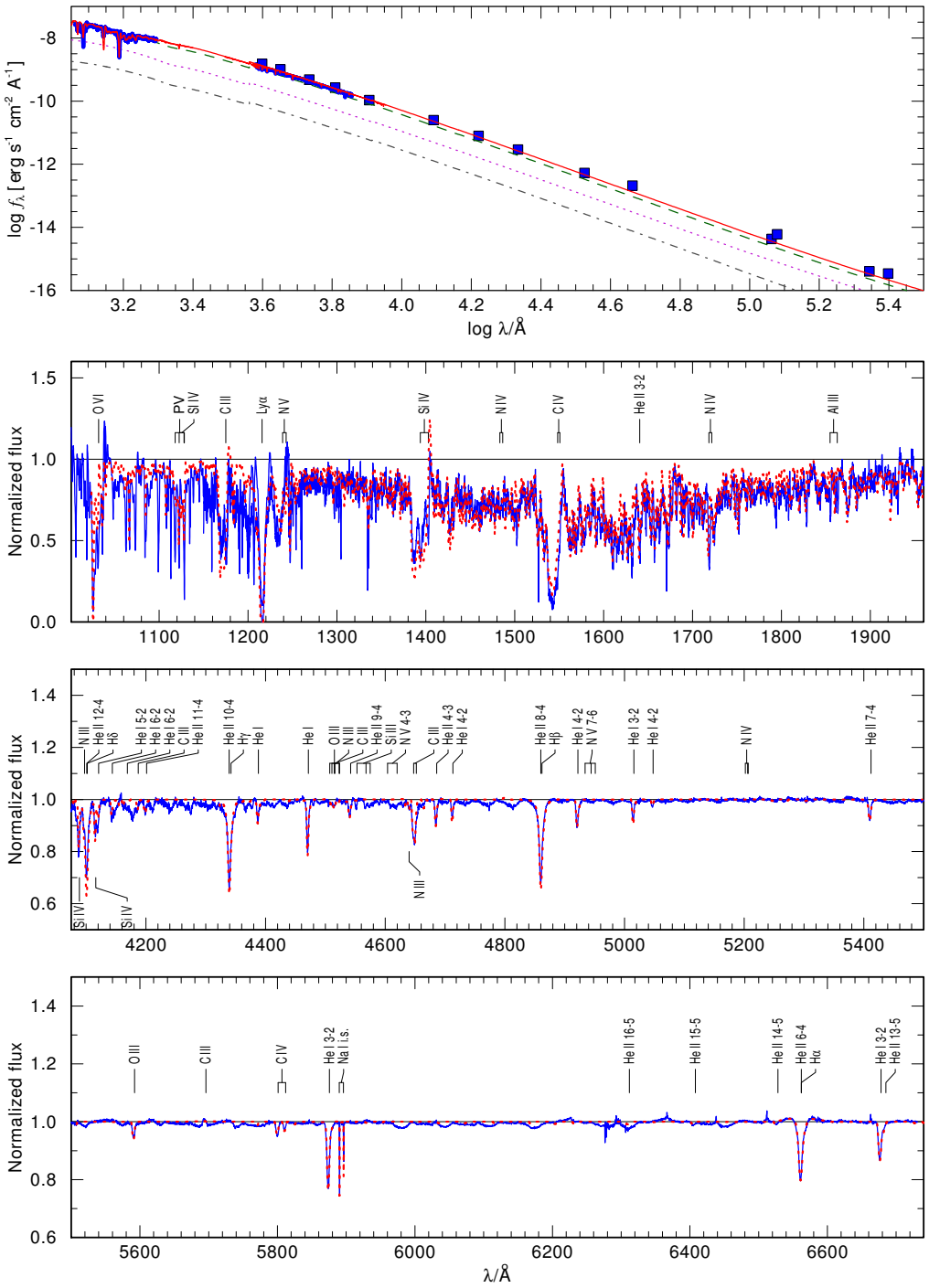

Figure 3.2.: *Upper panel:* Comparison between observations (blue squares and lines) and the total synthetic SED (red solid line), which consists of the primary (green dashed line), secondary (gray dash-dotted line), and tertiary (pink dotted line) models. *Lower panels:* Comparison between the composite synthetic (red dotted line) and observed (blue line) normalized spectra in the UV and optical. Both spectra roughly correspond to phase $\phi = 0.54$. For clarity, we refrain from showing the contributions of each component model to the normalized spectrum. The wavy pattern seen in the observed spectrum (e.g., in $\approx 6000 - 6200$ Å) is an artifact caused by connecting the echelle orders, not related to the stellar system.

The fact that distance-independent parameters are not unusual raises even more suspicion regarding the *Hipparcos* distance.

A similar discrepancy is observed other bright stars: Hummel et al. (2013) analyzed the binary system ζ Orionis A ($V = 1.79$) and inferred a distance of $d = 294 \pm 21$ pc based on an orbital analysis, and $d = 387 \pm 54$ pc based on a photometric estimate. Both these distances are significantly larger than the corresponding *Hipparcos* distance of $d = 225^{+38}_{-27}$ pc (van Leeuwen 2007), which encouraged them to discard the *Hipparcos* distance in their study. Another bright star for which the *Hipparcos* parallax implies very peculiar stellar parameters is the prototypical O supergiant ζ Puppis ($V = 2.25$); Its distance was suggested to be at least twice as large as implied by its measured parallax (Pauldrach et al. 2012; Howarth & Stevens 2014).

Returning to δ Ori A, our estimate of $d \sim 380$ pc would correspond to a parallax of $\pi \sim 2.6$ mas, deviating by $\sim 3.5\sigma$ from the newly reduced *Hipparcos* parallax of 4.71 ± 0.58 mas (van Leeuwen 2007). The probability for such a deviation to arise randomly is thus extremely small ($< 0.1\%$). Ground-based parallaxes for δ Ori A generally suffer from much larger uncertainties. For example, the Yale catalog gives $\pi = 9.7 \pm 6.7$ mas (van Altena et al. 1995). It is interesting to note that the original *Hipparcos* catalog gives a parallax of 3.56 ± 0.83 mas (ESA 1997b). In this case, the deviation could be plausibly explained as a random error, with 2.6 mas being $\sim 1\sigma$ away. While stellar multiplicity has been suggested to cause systematic errors in parallax measurements (e.g. Szabados 1997), the argument is unlikely to hold here given the different timescale of the involved orbits compared to that of the parallax measurement (which is to say, a year). However, large errors in the parallax measurement are also expected to occur in the case of very bright stars, which could lead to saturation, resulting in an inaccurate estimate of the barycenter of the point spread function. Brightness is indeed a property δ Ori A shares with the objects mentioned above. It is beyond the scope of the paper to judge whether the new *Hipparcos* reduction suffers from underestimated errors, but the fact that several bright stars show a similar pattern should encourage thorough studies on the matter.

The distance to δ Orionis is difficult to directly measure with modern techniques. The system is probably too bright for ground-based (e.g. RECONS[4]) as well as space-based instruments (e.g. the *Hubble Space Telescope*'s Fine Guidance Sensor; the *Gaia* mission). Our best hope is to obtain the RV curve of the secondary, which requires optical spectroscopy with a S/N $\gtrsim 1000$ (Paper III). Then, with a direct measure of the system parameters, follow-up long-baseline interferometry may provide the angular extent of the orbit, allowing for an orbital parallax measurement similar to that of ζ Ori A (Hummel et al. 2013). At 380 pc, the angular extent of the orbit will be on the order of 0.5 mas and thus difficult to measure, as the smallest angular separation for a binary yet resolved is 1.225 mas (Raghavan et al. 2009). However, this was done in the $K-$ band with the CHARA Array, so the resolution in the $R-$band should be sufficient to resolve the binary. Moreover, along with a light-curve analysis, and possessing *both* RV curves, one could accurately derive the masses and radii of both components, which, upon comparison with a distance-dependent spectral analysis, would supply another constraint on the distance. For now, we suggest that the *Hipparcos* distance may be underestimated, but leave the question open for future studies to resolve.

3.4.2. Constraining the parameters of Aa2 and Ab

The five columns of Fig. 3.3 depict six prominent He II and He I lines, from left to right: He II λ4686, He I λ4922, He II λ5411, He I λ5876, and the two adjacent lines He I λ6678 and He II λ6683. Each row depicts a different orbital phase, from top to bottom: $\phi = 0.02, 0.19, 0.38, 0.54, 0.84$. This time, we explicitly show the relative contributions of the primary (green dashed line), secondary (gray solid line) and tertiary (pink dotted-dashed line) to the total synthetic spectrum (red dotted line), compared to the observations at each phase (blue line). In Table 3.2, we specify the RVs with which the three components are shifted at each phase. The RVs for the primary were inferred in this study and agree very well with the RV curve of Mayer et al. (2010) and those of Paper III.

[4] www.recons.org

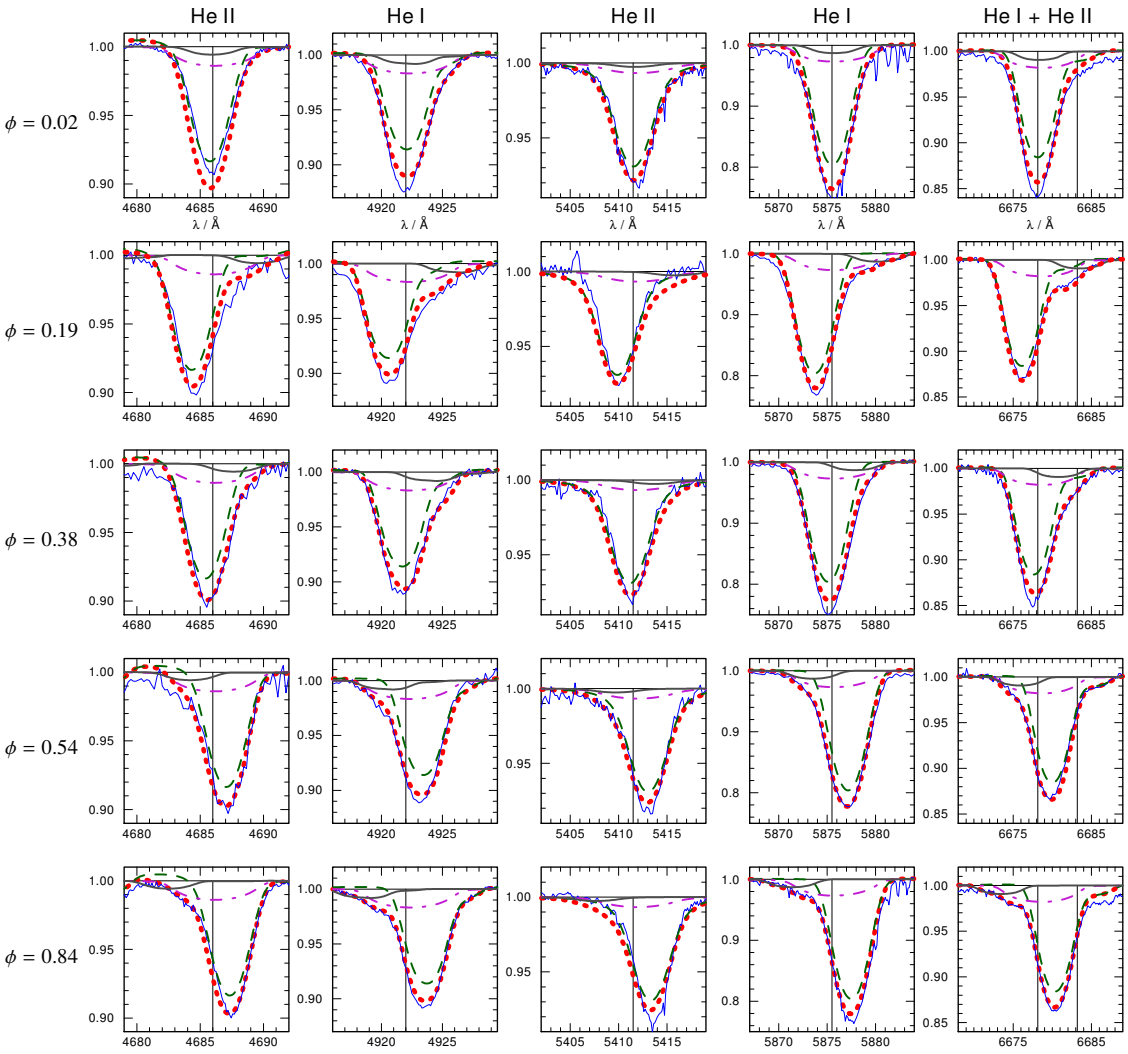

Figure 3.3.: The 25 panels show the contribution of the primary (green dashed line), secondary (gray solid line), and tertiary (pink dashed-dotted line) models to the composite synthetic spectrum (red dotted line) for six prominent helium lines and five different phases, compared with observations (blue line). The lines depicted are, from left to right, He II λ4686, He I λ4922, He II λ5411, He I λ5876, and the two adjacent lines He I λ6678 and He II λ6683. The phases are, from top to bottom, $\phi = 0.02, 0.19, 0.38, 0.54$, and 0.84. At each phase, the component models are shifted with the velocities given in Table 3.2.

The tertiary

There is a wide and shallow spectral feature which does not originate in the primary and which is constant along all orbital phases (see Figs. 3.3 and 3.4). Like Mayer et al. (2010), we identify this feature with the tertiary Ab, which is in fact the second brightest source in the system. The RV of the tertiary, which is practically constant over all phases, is also inferred independently, and agrees well with that suggested by Mayer et al. (2010).

We find that the tertiary contributes significantly more to H I lines than to He II lines. Together with the visual flux ratio implied from observations, this leads to a tertiary temperature of $T_* \sim 29.0\,\mathrm{kK}$. The gravity

Table 3.2.: Radial velocities derived/adopted for each phase in km s^{-1}

Phase	Aa1[I] 1]	Aa2[I] 2]	Ab[I] 1]
0.02	0	10	25
0.19	-92	230	25
0.38	-22	120	25
0.54	83	-100	25
0.84	105	-210	25

Notes. [(1)] Values for primary and tertiary derived in the analysis [(2)] Values for secondary adopted from Harvin et al. (2002), with the exception of phase 0.84, which is derived here.

and mass-loss of the tertiary were constrained based on the Balmer lines. As already discussed, it is very hard to identify the explicit contribution of the tertiary to these lines, and so the gravity and mass-loss of the tertiary are only roughly constrained. The parameters derived for the tertiary (cf. table 3.1) are consistent with it being a *B*0 IV type star (Habets & Heintze 1981; Schmidt-Kaler 1982)

The secondary

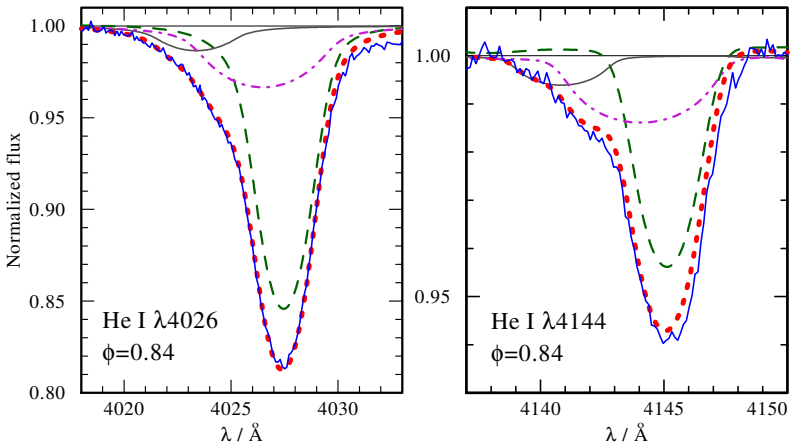

Figure 3.4.: The two panels depict two observed He I lines (blue lines) at phase $\phi = 0.84$ in which the secondary may be detectable. The different curves correspond to the primary (green dashed line), secondary (gray solid line), tertiary (pink dashed-dotted line), and total (red dotted line) synthetic spectra.

It is very hard, or perhaps impossible, to recognize any contribution from Aa2 to the spectrum. One exception might be the He I lines $\lambda\lambda$4026, 4144 at phase $\phi = 0.84$, which we show in the left and right panels of Fig. 3.4, respectively (colors and lines are as in Fig. 3.3). At this phase, the primary's RV approaches its maximum of $\sim 110\,\mathrm{km\,s^{-1}}$, and so the secondary is expected to be more easily observed. The He I λ4026 line, for example, seems to have an extended wing towards blueshifted wavelengths. The very weak He I λ4144 line is one of the few spectral lines which possibly portrays a partially isolated feature originating in the secondary. We therefore infer a RV for the secondary in this phase. For all other phases, we adopt the secondary's RVs from Harvin et al. (2002), since the secondary's lines cannot be isolated in the spectrum.

However, as Mayer et al. (2010) pointed out, it is likely that Harvin et al. (2002) confused the secondary with the tertiary, so that the secondary RVs reported by Harvin et al. (2002) are questionable.

Even without directly detecting the secondary, we can still constrain its stellar parameters. Since the light curve provides a lower limit for its visual flux (see Sect. 3.3.3), the luminosity of Aa2 cannot be arbitrarily small. Instead, to avoid too-strong line features from the secondary (which are not observed), we are forced to change other stellar parameters, e.g., T_* and $v \sin i$. The secondary's projected rotation velocity ($v \sin i \approx 150\,\mathrm{km\,s^{-1}}$) agrees with the feature shown in the right panel of Fig. 3.4, and the secondary temperature ($T \approx 26\,\mathrm{kK}$) is consistent with that obtained from the light curve analysis of the system (Paper III).

In Sect. 3.3.3 we argued that the light curve of δ Ori Aa implies that the secondary contributes at least 5.4% to total visual flux of the system. In this section, we argue that the secondary can contribute no more than this amount. In other words, our lower bound for the relative flux contribution becomes also our upper bound, and therefore $\Delta V_{\mathrm{Aa1Aa2}} \approx 2\overset{\mathrm{m}}{.}8$. Together with the temperature of the secondary, this enables us to infer an approximate value for the luminosity of the secondary. Its parameters suggest it is a $\approx$ B1 V type star (Habets & Heintze 1981; Schmidt-Kaler 1982).

3.4.3. Bulk and turbulent motions

Rotation and macroturbulence

Rotation is usually the dominant broadening mechanism of photospheric metal lines in OB type spectra, as is the case here. We infer the projected rotational velocity $v \sin i$ by convolving the synthetic spectrum with a rotation profile and comparing the line shapes to the observed spectrum. While flux convolution is a fair approximation for photospheric spectra, it does not account for the effect of limb darkening and for the extended formation regions of some lines. Accounting for rotation in the formal integration is essential for a consistent inclusion of these effects, but is computationally expensive. We therefore use the convolution method to infer $v \sin i$, and, only after obtaining the best-fit value of $v \sin i$, do we account for rotation directly in the formal integration (cf. Hillier et al. 2012; Shenar et al. 2014), assuming co-rotation up of the photosphere ($\tau_{\mathrm{Ross}} = 2/3$) and angular momentum conservation in the wind. Compared to simple flux convolution, the detailed treatment of rotation generally yields deeper lines with less elliptic profiles (e.g., Unsöld 1955) and may significantly affect the inferred abundances, projected rotation velocities, and even fundamental stellar parameters.

The effect of rotation on the spectrum is coupled to the effects of macroturbulence v_{mac}, which we model using a Radial-Tangential profile (Gray 1975; Simón-Díaz & Herrero 2007). Macroturbulence does not enter the radiative transfer per definition. Therefore, like solid body rotation, macroturbulence conserves the EWs of the lines. Typical values of $v_{\mathrm{mac}} \sim 50\,\mathrm{km\,s^{-1}}$ are reported for OB type stars (Lefever et al. 2007; Markova & Puls 2008; Bouret et al. 2012). While the origin of macroturbulence is not certain, it has been suggested to be a manifestation of collective pulsational broadening (e.g., Aerts et al. 2009). $v \sin i$ and v_{mac} are inferred simultaneously from the profile shapes of helium lines and metal lines. Not accounting for macroturbulence generally results in qualitatively different profiles from what are observed in photospheric lines (see e.g., example given by Puls et al. 2008).

Harvin et al. (2002) inferred $v \sin i = 157\,\mathrm{km\,s^{-1}}$ for the primary. While this value agrees well with the wings of prominent helium and metal lines, it leads to too-broad Doppler cores. A significantly better fit is obtained with $v_{\mathrm{mac}} = 60\,\mathrm{km\,s^{-1}}$ and $v \sin i = 130\,\mathrm{km\,s^{-1}}$. For an inclination of $i = 76°$ (Paper III) and a radius of $R = 16.5\,R_\odot$ (table 3.1), this could imply that the rotation period is approximately synchronized with the orbital period of 5.7 d.

For the tertiary, we find an optimal fit for $v \sin i = 220\,\mathrm{km\,s^{-1}}$ and $v_{\mathrm{mac}} = 50\,\mathrm{km\,s^{-1}}$, thus confirming the findings of Harvin et al. (2002) and Mayer et al. (2010) that the tertiary is a rapid rotator. For the secondary, motivated by the arguments discussed in Sect. 3.4.2, we estimate $v \sin i \sim 150\,\mathrm{km\,s^{-1}}$. We adopt $v_{\mathrm{mac}} = 0$ for the secondary, lacking any spectral lines from which it can be inferred. Any other typical values would bear no effect on our results.

Microtubulence and terminal velocity

In contrast to macroturbulence, microscopic turbulent motion enters directly into the process of radiative transfer and generally affects the EWs of spectral lines. In the non-LTE iteration, we do not specify the microturbulence explicitly, but rather the total Doppler width $v_{\rm Dop}$ of the opacity and emissivity profiles. $v_{\rm Dop}$ thus determines the resolution of the frequency grid in the non-LTE iteration. This parameter generally has a negligible effect on the obtained population numbers, with the extreme exception of the He II λ4686 line. As was already noted by Evans et al. (2004), this line reacts very strongly to changes in $v_{\rm Dop}$. We illustrate this in Fig. 3.5, where we show a segment of the optical spectrum containing the He II λ4686 line. In the figure, we depict three models corresponding to the primary calculated with parameters identical to those given in Table 3.1, but with $v_{\rm Dop}$ = 20, 40, and 60 km s^{-1} , respectively. It is evident that the He II 4686 Å line reacts remarkably strongly to $v_{\rm Dop}$. The exact origins of this effect are still under investigation (Shenar et al. in prep. 2015), but likely involve a feedback effect in the highly non-linear iterative solution of the radiative transfer problem. The remaining He II lines show a much weaker reaction in the opposite direction. Other lines hardly respond to changes of this parameter. This example shows that, overall, the choice of the parameter $v_{\rm Dop}$ is not critical for the fit, and that He II λ4686 is a poor temperature indicator. Based on this, $v_{\rm Dop}$ = 30 km/s is used in the analysis, consistent with the inferred microturbulence (see below).

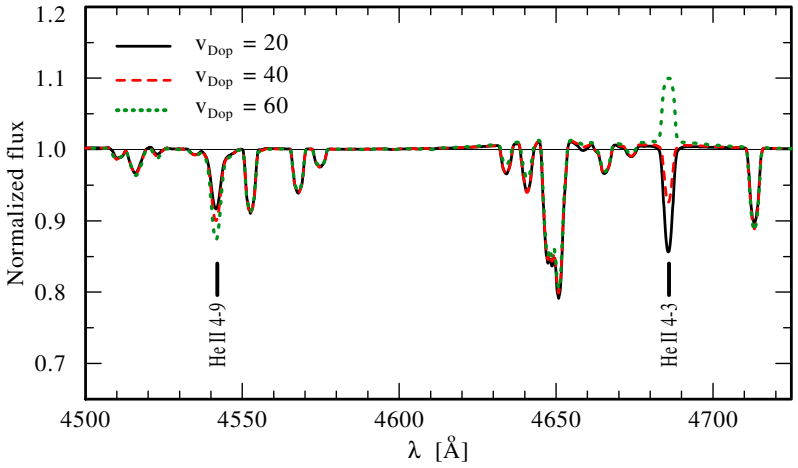

Figure 3.5.: This figure illustrates the extreme sensitivity of the He II λ4686 line to the parameter $v_{\rm Dop}$. Here we depict only the primary model, calculated with the parameters in Table 3.1, but with $v_{\rm Dop}$ = 20 km s^{-1} (black solid line), 40 km s^{-1} (red dashed line), and 60 km s^{-1} (green dotted line). The formal integration is performed with the same turbulent velocity as given in Table 3.1. Notice that most lines hardly react to this parameter.

In the formal integration, apart from including natural and pressure broadening, the Doppler width is separated into a thermal component $v_{\rm th}$, which follows the temperature stratification in the model, and a depth-dependent microturbulence component $\xi(r)$, which is assumed to be identical for all ions. As described in Sect. 3.3.1, $\xi(r)$ is interpolated between the photospheric $\xi_{\rm ph}$ and wind $\xi_{\rm w}$ turbulent velocities between two pre-specified radii, all of which are free parameters.

Values of photospheric microturbulence reported for O giants range between $\sim$ 10 km s^{-1} and 30 km s^{-1} (e.g., Gies & Lambert 1992; Smartt et al. 1997; Bouret et al. 2012). Since the photospheric microturbulence $\xi_{\rm ph}$ is rarely found to be larger than 30 km s^{-1} , its effect on the profile width is negligible compared to the effect of rotation. However, $\xi_{\rm ph}$ can have a very strong effect on the EW of spectral lines. The abundances are thus coupled to $\xi_{\rm ph}$, and wrong turbulence values can easily lead to a wrong estimation of the abundances (e.g., McErlean et al. 1998; Villamariz & Herrero 2000). To disentangle the abundances and turbulence

from, e.g., the temperature, we take advantage of the fact that different lines respond individually to changes in abundances, turbulence, and temperature, depending on their formation process. Fig. 3.6 shows an example. The left, middle, and right panels depict the He I λ5876 line as observed at phase $\phi = 0.84$ (blue line). In each panel, we show three different composite synthetic spectra (i.e. composing all three components), which were calculated with parameters identical to those given in Table 3.1, except for one stellar parameter of the primary. In the left panel, T_* is set to 29.5, 30, and 30.5 kK. In the middle panel, the helium mass fraction is set to $X_{\rm He}$ of 0.2, 0.3, and 0.4. Lastly, in the right-most panel, we set $\xi_{\rm ph}$ to 15 km s^{-1}, 20 km s^{-1}, and 25 km s^{-1}, respectively. The three composite spectra at the left and middle panels can hardly be distinguished from each other, portraying the insensitivity of the He I λ5876 line to temperature and helium abundance. In the relevant parameter domain, it is mainly $\xi_{\rm ph}$ which influences the strength of the He I λ5878 line. By considering hundreds of lines at all available orbital phases, we find that $\xi_{\rm ph} = 20$ km s^{-1} provides the best results for the primary's model. Similarly, we find that a microturbulence of 10 km s^{-1} for the tertiary yields the best global fit.

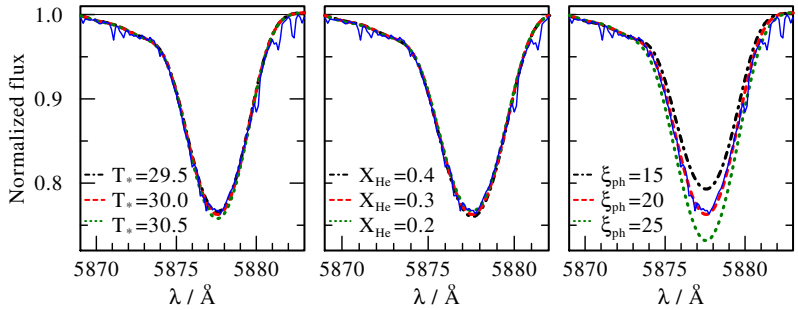

Figure 3.6.: Sensitivity of the He I λ5876 line to temperature, helium abundance, and microturbulence. The observed spectrum (blue line) at phase $\phi = 0.84$ is plotted along with three composite synthetic spectra calculated with the parameters given in Table 3.1, but with different temperature (left panel: $T = 29.5, 30, 30.5$ kK), helium abundance (middle panel: $X_{\rm He} = 0.2, 0.3, 0.4$), and photospheric microturbulence (right panel: $\xi_{\rm ph} = 15, 20, 25$ km s^{-1}) for the primary model (black dotted-dashed, red dashed, and green dotted lines, respectively).

We find evidence for a rapid increase of the turbulent velocity in the primary right beyond the sonic point. The left panel of Fig. 3.7 shows the C IV $\lambda\lambda$ 1548, 1551 resonance doublet, as observed in the *IUE* spectrum taken at phase $\phi = 0.73$. The observation shows a wide absorption trough which extends to red-shifted wavelengths, and our task is to reproduce this feature. The black dashed line depicts the composite synthetic spectrum calculated with the parameters in Table 3.1, but without an increased wind turbulence in the primary model, i.e. $\xi_{\rm w} = \xi_{\rm ph} = 20$ km s^{-1}. The absorption trough is not reproduced. Increasing the terminal velocity only affects the blue edge of the line. Varying β in the domain $0.7 - 1.5$ does not lead to any notable changes in the spectrum. The only mechanism that is found to reproduce the redshifted absorption trough is a rapid increase of the microturbulence beyond the sonic point. The red solid line was calculated like the dashed black line, but with a wind turbulent velocity of $\xi_{\rm w} = 200$ km s^{-1}. $\xi(r)$ is assumed to grow from $\xi_{\rm ph}$ at $r_{\rm in} \leq 1.1\,R_*$ to $\xi_{\rm w}$ at $r_{\rm out} \geq 2\,R_*$. At the same time, the blue absorption edge is shifted by ~ 200 km s^{-1}, thus influencing the value deduced for v_∞. The right panel of Fig. 3.7 shows the same C IV resonance doublet, as observed in three *IUE* spectra taken at phases $\phi = 0.18, 0.72, 0.98$ (black, red, and green lines, respectively). The figure illustrates the relatively small variability of this line, showing that our results do not depend on phase, and rejecting the contamination by another component as an explanation for the extended red-shifted absorption. The absorption trough is not reproduced for $r_{\rm out}$ significantly larger than $2\,R_*$, which is understandable given the need for red-shifted absorption. It is interesting to note that it is microturbulence, and not macroturbulence, which is needed to reproduce this feature. A further improvement of the line profile fit is obtained by accounting for optically thick clumps (macroclumps) in

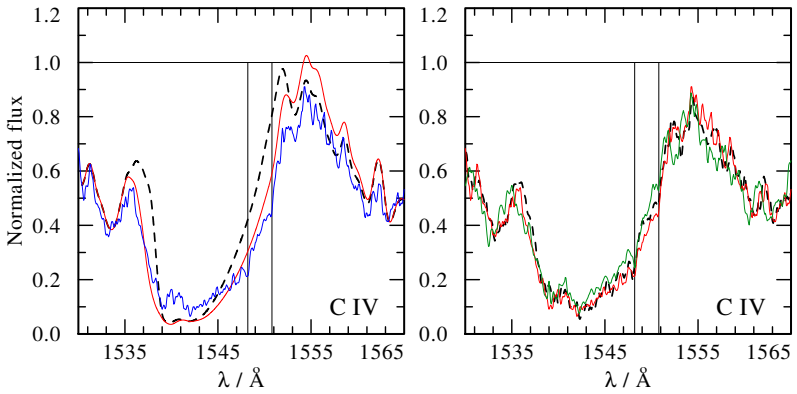

Figure 3.7.: *Left panel:* observed C IV resonance doublet at phase $\phi = 0.73$ (blue line) is compared to two synthetic composite spectra, with increased wind turbulence of $\xi_w = 200\,\mathrm{km\,s^{-1}}$ in the primary model (red solid line), and without it (black dashed line). Large microturbulent velocities beyond the sonic point are the only mechanism that can reproduce the redshifted absorption trough. Note that a further improvement of the profile is achieved by accounting for macroclumps, which are not included here. *Right panel:* Comparison of three *IUE* observations at phases $\phi = 0.18, 0.73, 0.98$ (black, red, and green lines, respectively), illustrating that the redshifted absorption trough is observed at all phases.

the wind, as we will discuss in Sect. 3.5. We do not include macroclumping at this stage in order to single out the effect of ξ_w on the line profile.

Having inferred the turbulent velocity and after accounting for clumping in the wind of the primary, it is straight-forward to derive the terminal velocity v_∞ from resonance P Cygni lines. All prominent lines in the UV imply the same value for v_∞ ($2000 \pm 100\,\mathrm{km\,s^{-1}}$).

3.4.4. Uncertainties

Since the calculation of a PoWR model atmosphere is computationally expensive, a statistical approach for error determination is virtually impossible. The errors given in Table 3.1 for each physical quantity are obtained by fixing all parameters but one and varying this parameter, estimating upper and lower limits that significantly change the quality of the fit in many prominent lines relative to the available S/N ratio. Errors for parameters which are implied from fundamental parameters via analytical relations, e.g., the spectroscopic mass, are calculated by means of error propagation. In the case of multiple systems, all models but one test model are kept fixed, and only one parameter of the test model is varied.

As mentioned in Sect. 3.4, it is very hard to constrain the gravity of the primary due to contamination by the other components. However, we took advantage of the fact that specific lines do drastically change their strength as a function of gravity. An example for such a diagnostic line, C III λ5696, is shown in the left panel of Fig. 3.8, as observed at phase $\phi = 0.02$ (blue line). Three composite spectra (i.e. including all components) are plotted, where only the $\log g_*$ of the primary is changed to 3.9 (black dotted-dashed line), 3.55 (red dashed line), and 3.2 [$\mathrm{g\,cm^{-2}}$] (green dotted line). The remaining stellar parameters are kept fixed to the values given in Table 3.1. This line only starts to portray emission when $\log g_* \sim 3.5$ [$\mathrm{g\,cm^{-2}}$]. This line also serves as a good example to why χ^2 fitting would not always suggest the best fitting model. The contribution of such a small line to the reduced χ^2 is negligible, unlike its diagnostic power. The right panel of Fig. 3.8 depicts the sensitivity of the He I line to the stellar temperature. The temperature of the primary is changed to 29.5 (black dotted-dashed line), 30 (red dashed line), and 30.5 kK (green dotted line). Most He I and He II lines react strongly to changes in the temperature and thus enable us to sharply constrain it.

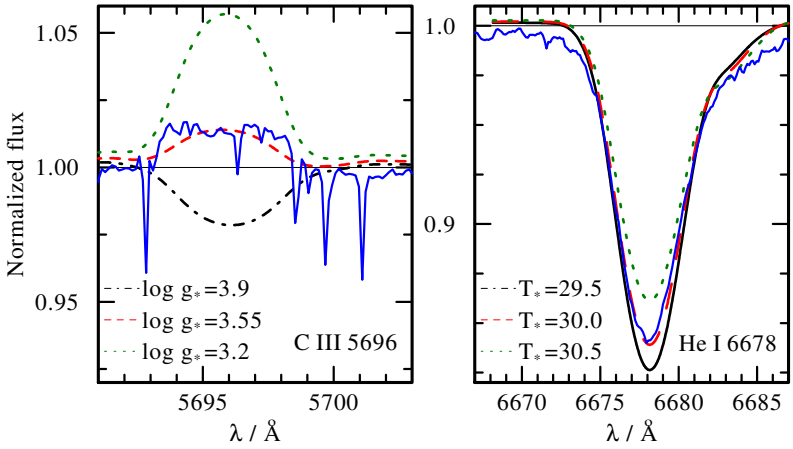

Figure 3.8.: *Left panel:* Sensitivity of C III λ5696 to gravity. The observed spectrum at phase $\phi = 0.02$ (blue line) is compared to three composite synthetic spectra calculated with the parameters given in Table 3.1, but with $\log g_*$ of the primary set to 3.9, 3.55, and 3.2 (black dotted-dashed, red dashed, and green dotted lines, respectively). *Right panel:* Sensitivity of He I λ6678 to temperature. We set the temperature of the primary to 29.5, 30.0, and 30.5 kK (black dotted-dashed, red dashed, and green dotted lines, respectively).

3.5. Inhomogeneities in the primary's wind

Evidence for wind inhomogeneities (clumping) in the winds of hot stars are frequently reported. Hillier (1984) and Hillier (1991) illustrated the effect of optically thin clumps on the electron scattering wings of Wolf-Rayet emission lines. More compelling direct evidence for clumping in the form of stochastic variability on short timescales was observed in both Wolf-Rayet (e.g., Lépine & Moffat 1999) and OB stars (Eversberg et al. 1998; Markova et al. 2005; Prinja & Massa 2010). Clump sizes likely follow a continuous distribution (e.g., power-law) which is intimately connected with the turbulence prevailing in the wind (e.g., Moffat 1994). However, since consistent non-LTE modeling of inhomogeneous stellar winds in 3D is still beyond reach, the treatment of clumping is limited to approximate approaches.

3.5.1. Microclumping

A systematic treatment of optically thin clumps was introduced by Hillier (1984) and later by Hamann & Koesterke (1998) using the so-called microclumping approach, where the population numbers are calculated in clumps which are a factor of D denser than the equivalent smooth wind. In this approach, processes sensitive to ρ, such as resonance and electron scattering, are not sensitive to clumping, and imply $\dot{M}$ directly. However, processes which are sensitive to ρ^2, such as recombination and free-free emission, are affected by clumping, and in fact only imply the value of $\dot{M}\sqrt{D}$. This enables consistent mass-loss estimations from both types of processes, and offers a method to quantify the degree of inhomogeneity in the wind in the optically thin limit.

To investigate wind inhomogeneities in the primary Aa1, we first adopt a smooth model. The four panels of Fig. 3.9 depict four "wind" lines: three UV resonance doublets belonging to Si IV, P V, and C IV ($\propto \rho$), and Hα, as the only recombination line potentially showing signs for emission ($\propto \rho^2$). In each of the four panels, four composite synthetic spectra (i.e. containing all three components) are plotted along the observation (blue line). The four models differ only in the mass-loss rate of Aa1: $\log \dot{M}$ = -5.6 (black dashed line), -6.0 (red solid line), -7.1 (green dotted line), and -8.6 [$M_\odot\,\mathrm{yr}^{-1}$] (purple dotted-dashed line). The remaining stellar parameters are identical to the ones given in Table 3.1 (for $d = 380\,\mathrm{pc}$), but with $D = 1$ for the

primary. The observations roughly correspond to phase $\phi \sim 0.8$, except in the case of the P v doublet, which is obtained from the co-added *Copernicus* data (see Sect. 3.2).

While a best fit for Hα (lower right panel in Fig. 3.9) is obtained with $\log \dot{M} \approx -6.0$ $[M_\odot\,\mathrm{yr}^{-1}]$, we note that H$\alpha$ portrays noticeable variability with time, which increases the uncertainty of the inferred mass-loss rate. Furthermore, our estimation of the mass-loss rate from Hα could be inaccurate due to underestimated contribution to the emission by either the tertiary or by wind-wind collision effect. Fortunately, the Hα mass-loss rate is supported by radio observations. Assuming a smooth wind, Lamers & Leitherer (1993) infer a mass-loss rate of $\log \dot{M} \approx -5.95$ $[M_\odot\,\mathrm{yr}^{-1}]$ based on the radio flux of the system for an adopted distance of $d = 500$ pc. This value is revised to $\log \dot{M} \approx -6.1$ $[M_\odot\,\mathrm{yr}^{-1}]$ for $d = 380$ pc, only slightly smaller than the value derived for H α in this study. Since both these processes scale as ρ^2, and since the wind is assumed to be smooth in both cases, we therefore conclude that $\log\left(\dot{M}\sqrt{D}\right) \approx -6.0\,[M_\odot\,\mathrm{yr}^{-1}]$ for the primary.

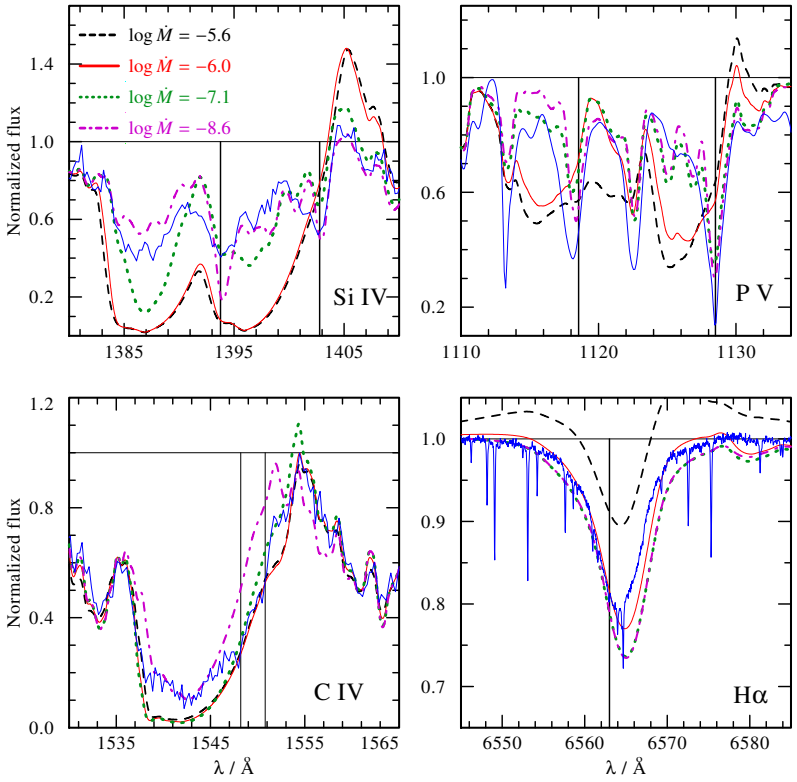

Figure 3.9.: Observed "wind" lines (blue line): The Si IV $\lambda\lambda$1394, 1408 (upper left), C IV $\lambda\lambda$1548, 1551 (lower left), and P V $\lambda\lambda$1118, 1128 (upper right) resonance doublets, and Hα (lower right), roughly at phase $\phi \sim 0.8$, except for the Copernicus data (P V) which are co-added. Each panel depicts four composite spectra with the same parameters as in table 3.1, but without clumping ($D = 1$), and with different mass-loss rates: $\log \dot{M} = -5.6, -6.0, -7.1$, and -8.6 $[M_\odot\,\mathrm{yr}^{-1}]$ (black dashed, red solid, green dotted , and purple dashed-dotted lines, respectively). The Hα and different P Cygni lines clearly imply different mass-loss rates, and cannot be fitted simultaneously.

We now turn to the UV resonance lines. The Si IV line, shown in the upper left panel of Fig. 3.9, is clearly not saturated in the observation. In the model, it remains saturated for $\log \dot{M} \geq -6.8$ $[M_\odot\,\mathrm{yr}^{-1}]$. A best fit is obtained with $\log \dot{M} \approx -7.5$ $[M_\odot\,\mathrm{yr}^{-1}]$. Together with the condition discussed in the previous paragraph, this implies $D \geq 40$; a best fit is obtained for $D \sim 1000$. The P V resonance line (upper right

panel) implies a similar mass-loss rate, and hence a similar clumping contrast. The C IV line (bottom left panel), which does not look saturated in the observation[5] , requires a much lower mass-loss rate, of the order of $\log \dot{M} \approx -8.0$ $[M_\odot\,\mathrm{yr}^{-1}]$, and as a consequence implies $D \approx 10^4$.

But are such large density contrasts physically sound? 1D and 2D time-dependent hydrodynamic simulations of line driven winds suggest typical values of $D = 4 - 10$, with $D = 20 - 100$ occurring in the most extreme cases (Owocki et al. 1988; Feldmeier et al. 1997; Runacres & Owocki 2002; Sundqvist & Owocki 2013). Evolutionary considerations support $D \sim 2 - 3$ in order to obtain sufficient mass-loss from OB type stars (e.g., Hirschi 2008). Values of $4 - 10$ are typically reported for Wolf-Rayet stars based on electron scattering wings of strong emission lines (e.g., Todt et al. 2013; Hainich et al. 2014), while larger density contrasts of the order of 20 or more are suggested for OB stars (e.g., Bouret et al. 2012) to reconcile the strong discrepancy between $\dot{M}$ values derived from P Cygni resonance lines and recombination lines. Analyses of the P V resonance doublet simultaneously with optical recombination lines (e.g., Fullerton et al. 2006) may imply clumping factors as large as 100. However, we note that the latter authors neglect the effect of porosity (Oskinova et al. 2007), and that the resulting low mass-loss rates are inconsistent with polarization studies based on electron scattering (St-Louis & Moffat 2008), which depends linearly on density. It seems therefore that the implied values for D exceed plausible limits, and that no single value for D can satisfy all emission features simultaneously.

One possibility is that the abundances, or any other fundamental parameters derived for Aa1 which may affect the formation of the UV resonance lines, are significantly inaccurate. This is unlikely, because the photospheric features, as well as the general shape of the UV iron forest, are well reproduced and do not leave room for variations. Another possibility is that one of the components, perhaps through interaction with the primary's wind, is contaminating the observation. However, there are no clear indications for a periodic variation of the UV resonance lines with phase, as could be expected in such a case. We therefore suggest that not only is the wind of Aa1 clumped, but also that the clumps are optically thick in the strong UV lines. As illustrated by Oskinova et al. (2007), the optically thickness of the clumps leads to an effective reduction of the opacity of strong UV resonance lines, and could thus enable to obtain results which are consistent over the X-ray, UV, optical, IR and radio regimes. A further indication for optically thick clumps comes from the variable EW ratio of the of the two Si IV components. A ratio of 1 is expected to occur in the extreme case where the porous wind consists of optically thick clumps and "holes" between them, while a ratio of ≈ 2 (corresponding to the ratio of oscillator strengths of the two components) should occur in the case of a homogenous wind. The EW ratio of the Si IV doublet, which is observed to be smaller than 2, could be explained by the presence of optically thick structures present in the wind (cf. Prinja & Massa 2010).

3.5.2. Macroclumping

In PoWR, macroclumping is implemented only in the formal integration, leading to an effective reduction of the opacity in strong lines. Oskinova et al. (2007) thoroughly discuss the method, and illustrate the significant effect of macroclumping in the O supergiant ζ Puppis. Šurlan et al. (2013) model the effect of macroclumps by means of 3D Monte Carlo simulations and obtain similar results. A consequence of accounting for macroclumps is the need to introduce a further parameter, L_{mac}, which specifies the separation between the clumps. The non-LTE nature of the line formation makes a simultaneous prediction of L_{mac}, D, and $\dot{M}$ practically impossible. We are therefore forced to adopt a value for one of these parameters. Since not much is known about the geometry of the clumps, we avoid prespecifying L_{mac}. Instead, we choose to adopt $D = 10$ as a compromise between $D \sim 2$ and $D \sim 100$. Motivated by hydrodynamic studies (Feldmeier et al. 1997; Runacres & Owocki 2002), we assume that the clumping initiates at $r = 1.1\,R_*$ and grows to its maximum contrast of $D = 10$ at $r \sim 10\,R_*$. Our results depend only weakly on the depth-dependence of $D(r)$.

[5] We note that the IUE observation may suffer from calibration problems, which sheds doubt on whether the C IV resonance line is unsaturated. However, the observed shape of its absorption trough suggests it is indeed unsaturated. This is evident in each of the 60 available *IUE* spectra, some even showing this more extremely. While we speculate that the line is desaturated here, our results do not depend on this strongly.

Fig. 3.10 portrays the two C IV and Si IV resonance doublets as observed at phase $\phi = 0.83$ (blue line). The black dashed line depicts the synthetic composite spectrum without the inclusion of macroclumping in the primary. The red dotted line depicts the same composite spectrum, but with $L_{\rm mac} = 0.5\,R_*$ adopted for the primary. The strong effect of macroclumping on the resonance lines is evident. The $H\alpha$ line, as well as the photospheric features, are hardly affected by the macroclumping formalism. The value $L_{\rm mac} = 0.5\,R_*$ provides a fair compromise for most wind lines, but the Si IV resonance lines in fact require larger values of the order of $L_{\rm mac} \sim R_*$. The analysis therefore suggests $L \gtrsim 0.5\,R_*$. This value should not be given too much significance, as macroclumps are treated only as a rough approximation here. Nevertheless, we accounted for the major effects expected to rise from both optically thick and optically thin clumps, so mass-loss rates are unlikely to be very different than those derived here. Future variability studies should help to further constrain the amount of inhomogeniety in the primary's wind.

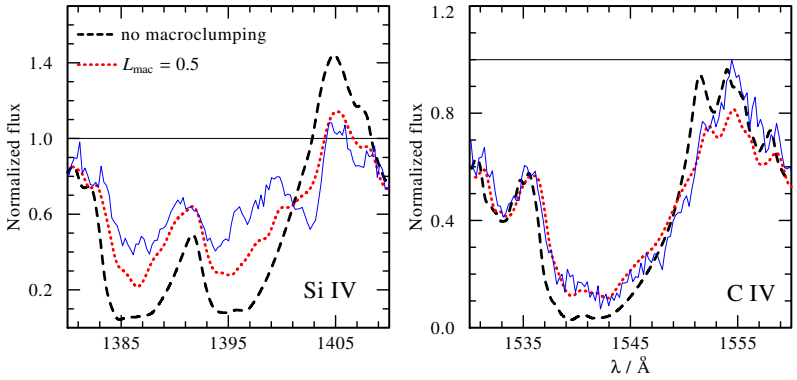

Figure 3.10.: The observed Si IV and C IV resonance doublets (left and right panels, respectively) at phase $\phi = 0.83$ (blue line) compared to the composite synthetic spectrum calculated with the parameters in Table 3.1, but without macroclumping in the primary (black dashed line), and with macroclumping using $L_{\rm mac} = 0.5\,R_*$ (dotted red line).

After assuming a clumping factor, the mass-loss rate is fairly well constrained, but still depends on the adopted distance. For the adopted distance of $d = 380$ pc, the mass-loss rate is found to be $\log \dot{M} = -6.4 \pm 0.15\,[M_\odot\,{\rm yr}^{-1}]$. Since the mass-loss rate scales as $D^{-1/2}$, we can consider the two extreme alternatives for the clumping factor $3 \leq D \leq 50$ to set lower and upper bounds for the mass-loss rate of the primary: $-6.2 \leq \log \dot{M}_1 \leq -6.8\,[M_\odot\,{\rm yr}^{-1}]$. Interestingly, Vink et al. (2000) predict $\dot{M}_{\rm Vink} = -6.48\,[M_\odot\,{\rm yr}^{-1}]$ for a star with the parameters of the primary (for $d = 380$ pc) based on hydrodynamic calculations, which is in very good agreement with our results for the adopted clumping factor of $D = 10$ (cf. Table 3.1). However, we note that Vink et al. (2000) performed their calculations for homogenous winds, and it is not clear whether their predictions would remain the same in the case of significant inhomogeneities (Muijres et al. 2011).

3.6. Where do the X-rays in δ Ori A come from?

So far, our analysis focused on the "cool" stellar wind. However, the cool wind alone cannot account for the observed X-rays in δ Ori A. It is commonly believed that X-ray emission in single stars originates in the wind due to instability of the line-driving mechanism (e.g., Feldmeier et al. 1997) or via acoustic driving from subsurface convection (Cantiello et al. 2009). In binary systems, an excess of hard X-ray flux may originate from wind-wind collisions (Williams et al. 1990; Corcoran 2003). In this section, we explore the properties of the "hot" X-ray producing component.

3.6.1. Auger ionization

The presence of strong X-ray radiation in OB type stars was hypothesized prior to the first direct X-ray observations in massive stars. Cassinelli & Olson (1979) were the first to suggest that the detection of UV resonance lines of high-ionization ions such as N v and O vi, which are observed in many O type stars, may indicate that Auger ionization (Meitner 1922; Auger 1923) plays an important role in their formation. Auger ionization occurs when very energetic photons remove an electron of an inner shell (usually the K-shell), ultimately resulting in a double ionization. The Auger effect on UV spectra has been frequently detected in studies of OB type stars (e.g., Oskinova et al. 2011).

The effect of X-rays in the wind of the primary Aa1 is evident by merely inspecting its UV spectrum. The presence of the strong UV resonance doublets O vi $\lambda\lambda$1032,1038 and N v $\lambda\lambda$1239,1243 cannot be reproduced otherwise. Indeed, an X-ray luminosity of $\approx 1.4 \cdot 10^{32}$ erg s^{-1} is reported for δ Ori A (Paper I), which corresponds to $\sim 10^{-6.87}$ times the total bolometric luminosity of the system[6]. The question remains, however, as to the origin of the X-ray radiation observed.

There are several arguments which suggest that emission from wind-wind collisions do not dominate the X-ray flux in δ Ori A. Paper II reports a relatively weak variability of the X-ray flux, which they cannot tie with certainty to phased-locked variations, in particular wind-wind collisions. The inferred value of $\log L_X/L_{Bol} \sim -6.87$ is typical for OB type stars (e.g., Pallavicini et al. 1981; Seward & Chlebowski 1982; Moffat et al. 2002; Oskinova 2005; Nazé 2009), and does not imply any excess X-ray radiation from strong wind-wind collision. Lastly, the N v $\lambda\lambda$1239,1243 resonance doublet, which clearly forms due to the X-ray radiation, is persistent throughout all available *IUE* spectra (see right panel of Fig. 3.11 below). If most X-rays originated in a collision zone which irradiated only a part of the star (whose orientation relative to the observer depended on phase), then a larger variability could be anticipated. It therefore seems plausible to assume that the X-rays originate in the wind itself.

We model the effect of X-ray radiation as described by Baum et al. (1992). The X-ray emission is assumed to originate in optically thin filaments of shocked plasma embedded in the wind. The X-ray field is characterized by the temperature T_X of the shocked plasma and the radially-constant filling factor X_{fill}, which describes the ratio of shocked to non-shocked plasma. The onset radius of shocked plasma is denoted by R_0. The X-ray emissivity $\eta_X(r)$ at each radial layer $r > R_0$ is proportional to ρ^2. In principle, the three parameters T_X, X_{fill} and R_0 are chosen such that the observed X-ray SED (Huenemoerder, priv. com.) is approximately reproduced by the synthetic X-ray SED emerging from the model, after accounting for interstellar extinction. Once the onset radius R_0 has been fixed, T_X and X_{fill} follow from the observed SED. Motivated by the f/i analysis and X-ray line modeling results (see Sects. 3.6.3 and 3.6.2), we fix the onset radius to $R_0 = 1.1\,R_*$, leading to $T_X = 3$ MK and $X_{fill} = 0.1$. These are only rough approximations to the X-ray properties in the wind (see Paper I), used to reproduce the bulk of X-ray emission observed.

The left panel of Fig. 3.11 shows the effect of including X-rays in the wind of the primary on the N v resonance doublet $\lambda\lambda$1239, 1243. The blue line depicts the *IUE* observation of this doublet at phase $\phi = 0.1$. The black dashed line plots the synthetic composite spectrum without the inclusion of X-rays. Since the temperature in the wind is far from being sufficient to populate the N v ground state, only photospheric absorption is obtained. The red solid line is obtained after the inclusion of X-rays. While the line shape is not accurately reproduced, it is clear that X-rays are required in order to reproduce the observed P Cygni N v resonance line. Note also that the line is blended with components of iron lines in the blue part, making a determination of its terminal width difficult. The right panel of Fig. 3.11 depicts three *IUE* observations at phases $\phi \sim 0.8, 0.3, 0.1$. While the N v resonance doublet shows stronger variability than most other resonance lines, the P Cygni feature is persistent and clearly visible in all 60 available *IUE* spectra.

3.6.2. f/i analysis

Spectra of He-like ions (i.e. ions with two electrons) exhibit a group of three neighboring X-ray lines referred to as resonance (r), forbidden (f), and intercombination (i) lines. A well established method to constrain the formation region of X-rays in stellar winds makes use of observed forbidden-to-intercombination (f/i)

[6] We use here the total bolometric luminosity because all components are OB type stars and are thus expected to emit X-rays proportionally to their luminosities.

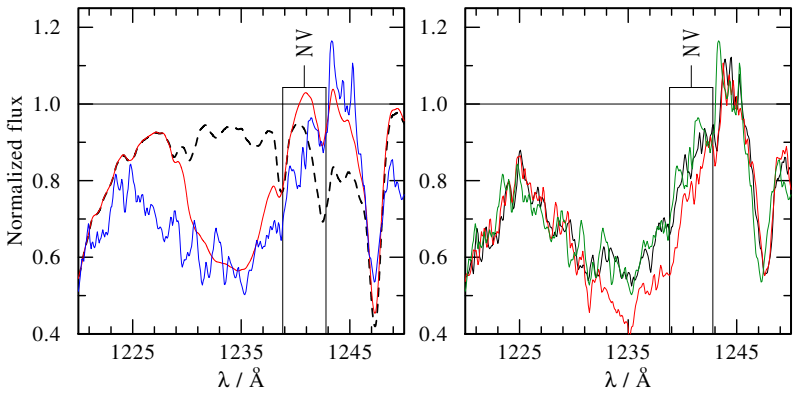

Figure 3.11.: *Left panel:* Observed N v resonance doublet at phase $\phi \sim 0.1$ (blue line) with two synthetic composite spectra, calculated with the parameters in Table 3.1, not including X-rays (black dashed line), and including X-rays (red solid line). *Right panel:* Like the right panel of Fig. 3.7, the three *IUE* observations at phases $\phi = 0.8, 0.3, 0.1$ (black, red, and green lines, respectively).

line ratios. f/i analyses were originally developed to study the solar X-ray radiation (Gabriel & Jordan 1969; Blumenthal et al. 1972), but are now also frequently used to study the X-ray emission of OB and Wolf-Rayet stars (e.g., Waldron & Cassinelli 2001; Leutenegger et al. 2006; Waldron & Cassinelli 2007). The f/i line ratio is determined by the relative population of the upper levels of the f and i lines, altered either by collisions or by photo-excitations (e.g., Porquet et al. 2001). For each helium-like ion, there are three possible transitions between the upper levels of the f and i lines, denoted in the following with indices j = 0,1,2. These transitions are typically at UV frequencies, although their exact wavelengths depend on the ion. The stronger the UV radiation field is, the smaller the f/i ratio becomes. A detailed treatment allows one to construct an equation which predicts the f/i line ratio $\mathcal{R}$ as a function of the radiative excitation rate ϕ and electron density n_e (cf. Blumenthal et al. 1972, Eq. 1c).

The interpretation of observed f/i line ratios requires some discussion. After all, what we observe is likely the X-ray radiation reaching us from an extended region where it is formed. The simplest way to interpret the observations would be to assume that the X-ray emitting gas is distributed over a thin spherical shell located at a formation radius $R_{\rm form}$, often referred to as the point-like interpretation. However, we know from detailed X-ray line fitting (see Sect 3.6.3) that the X-ray radiation must originate in an extended region. Obviously, the point-like interpretation cannot describe the whole truth. A more generalized interpretation to the observed f/i line ratios, thoroughly described by Leutenegger et al. (2006), involves the integration of the X-ray radiation emanating from a continuous range of radii. Within the assumptions of this method, it is not the formation region which is sought, but the *onset* radius R_0 of the X-ray emission. We refer the reader to studies by Gabriel & Jordan (1969), Blumenthal et al. (1972), and Leutenegger et al. (2006) for a detailed description of the methodology of both interpretations.

We do not calculate the radiative excitation rate of the upper f level by diluting the photospheric fluxes, (cf. Leutenegger et al. 2006, Eq. 2), but instead use directly the mean intensities J_ν at each radial layer, as obtained by our PoWR model. This way, we account for diffuse emission and limb darkening in a consistent manner. We include all three transitions $j = 0, 1, 2$ in the calculation, properly weighted with their respective branching ratios. The relevant wavelengths λ_j and oscillator strengths f_j are extracted from the NIST database.

Fig. 3.12 shows an example calculated for the He-like Mg xi ion. The blue dotted line depicts the f/i ratio $\mathcal{R}(r)$ predicted by the model for the point-like assumption as a function of the formation radius $R_{\rm form}$, neglecting collisional excitation. The solid horizontal line depicts the observed value of $\mathcal{R}_{\rm obs} = 0.96 \pm 0.36$ (Paper I). The shaded green area depicts the 1-σ measurement uncertainty. If the major part of the X-ray radiation originates at one radial layer, this layer will be located at $R_{\rm form} = 4.1^{+1.2}_{-1.0}\, R_*$, where the uncertainty

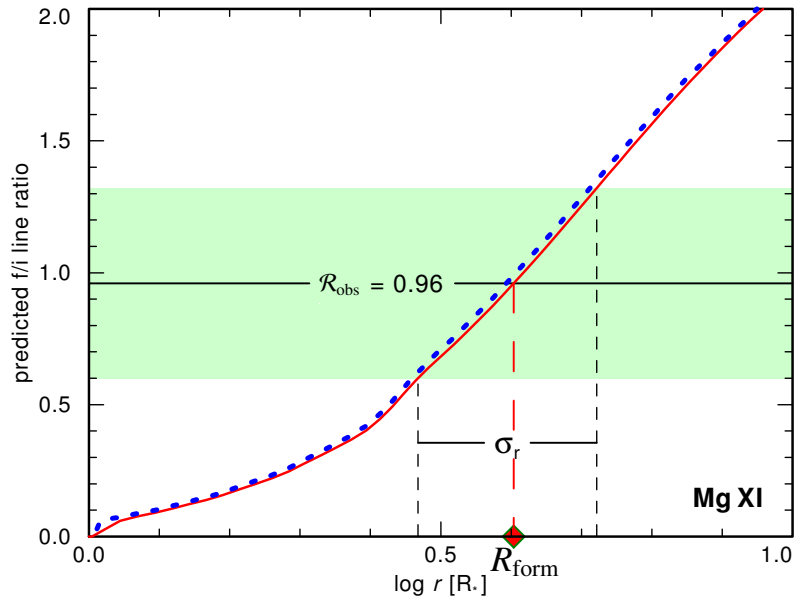

Figure 3.12.: Theoretical f/i ratio $\mathcal{R}(r)$ is plotted as a function of the X-ray formation radius (blue dotted line) for the Mg XI ion. The intersection of $\mathcal{R}(r)$ with the observed value $\mathcal{R}_{obs}$ implies the formation radius under the assumptions of the point-like approach. The error σ_r in the formation radius corresponds to 1-σ measurement uncertainties in $\mathcal{R}_{obs}$, depicted by the green shaded rectangle. The red solid line depicts $\mathcal{R}(r)$ as well, but includes the contribution of collisions assuming a full ionization and a factor 1000 density enhancement in the shocked plasma

σ_r corresponds to the measurement uncertainty. In Fig. 3.12, we also illustrate the influence of collisional excitation on $\mathcal{R}(r)$. The red solid line also plots $\mathcal{R}(r)$, but accounts for collisional excitation, assuming a full ionization and an unrealistically large factor of 1000 for the density enhancement in the shocked regions. Evidently, the contribution of collisions to the excitation of the upper f level is negligible in δ Ori A.

In Fig. 3.13, we compare the point-like interpretation with the more generalized interpretation described by Leutenegger et al. (2006) for the ion Mg XI. The red solid line depicts $\mathcal{R}(r)$, as in Fig. 3.12. The green dashed line shows the predicted f/i ratio $\overline{\mathcal{R}}(r)$ as a function of the *onset* radius R_0. Note that while both functions are depicted in the same coordinate frame, the meaning of r is different. As is evident from the figure, at the observed value of $\mathcal{R} = 0.96$, the onset radius R_0 predicted by integrating and weighting the contribution of all layers at $r > R_0$ is approximately $2.4\,R_*$.

Finally, Fig. 3.14 graphically summarizes our results for the He-like ions Si XIII, Mg XI, Ne IX, and O VII using both the point-like and generalized interpretations. The measured f/i ratio of S XV does not provide any constraints, so this ion is not included. Measured f/i values and their uncertainties are given in Paper I. Formation radii inferred for each line are indicated with red diamonds, while onset radii are indicated with blue circles. The dashed vertical lines mark the $1-\sigma$ error range corresponding to f/i measurement uncertainties. The shaded gray area in both panels depicts the optically thick region in the model, i.e. regions where photons cannot escape.

Evidently, the X-ray formation radii are different for ions with significantly different ionization potentials (e.g., Si XIII vs. O VII). This may suggest that a distribution of temperatures governs the formation radii (see e.g., Krtička et al. 2009; Hervé et al. 2013). Fig. 3.14 suggests that higher ions are formed at lower radii. This could imply that the hotter plasma is found closer to the stellar surface, while cooler plasma dominates farther out, a fact which was also pointed out by Waldron & Cassinelli (2007) from their study of a large sample of O-type X-ray spectra. The correlation between the ionization potential and location in the wind is

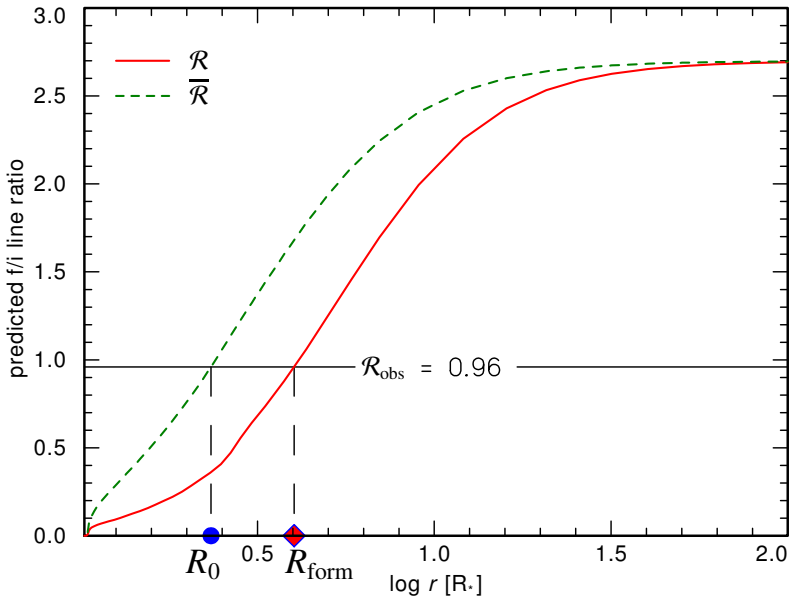

Figure 3.13.: Same as Fig. 3.12, but now accounting for an extended region of X-ray formation (green dashed line). The intersection of $\overline{\mathcal{R}}(r)$ with the observed value delivers the onset radius R_0.

no longer seen for the onset radii, which may suggest that X-rays are emitted in all He-like lines already very close to the stellar surface, independent of the element. This is in agreement with a picture based on hydrodynamic simulations, where plasma of different temperatures is present in cooling layers behind a shock front (Feldmeier et al. 1997). It is also worth noting that the formation radii roughly follow the same trend as the $\tau = 1$ surface of the cool wind, providing an independent confirmation that our analysis provides realistic values for the cool wind opacity.

3.6.3. X-ray line modeling

We now demonstrate that the high-resolution X-ray spectrum of δ Ori A can be described consistently with the cool stellar wind model obtained from the analysis of UV and optical spectra. We use the high signal-to-noise ratio X-ray spectra obtained by the *Chandra*'s HEG and MEG detectors. The observation consists of four different exposures taken at different orbital phases. A complete description of the X-ray observations and data analysis is given in Paper I. During the orbital motion, the radial velocity of the primary changes between $+114\,\mathrm{km\,s^{-1}}$ and $-78\,\mathrm{km\,s^{-1}}$, with a systemic velocity of $\gamma = 15\,\mathrm{km\,s^{-1}}$ (Paper III). It is ambiguous whether the observed X-ray Doppler shifts follow the expected orbital pattern (Paper II). Regardless, our tests show that the resulting Doppler shifts, which are comparable to the instrumental resolution and are much smaller than the wind velocity, bear a negligible effect on the modeled line profiles. We therefore neglect Doppler shifts due to orbital motion, and model the line profiles at the systemic velocity of $15\,\mathrm{km\,s^{-1}}$. For all Lα lines of H-like ions, both components of the doublet are taken into account in the model.

We analyze the X-ray spectra by simulating X-ray lines using our 2-D stochastic stellar wind code (Oskinova et al. 2004) and comparing them with observed lines. As we are interested in the line profiles, the maximum of the synthetic lines is normalized to their observed maximum. Our model is based on the assumption of a two component medium: the "cool wind" and the "hot wind". The X-ray radiation is assumed to originate in optically thin filaments evenly distributed in the hot wind component (the treatment of resonant scattering in X-ray lines is presented in Ignace & Gayley 2002). The emissivity η_X scales as ρ^2, and the filling factor is assumed to be radially constant. A more sophisticated assumption on the behavior

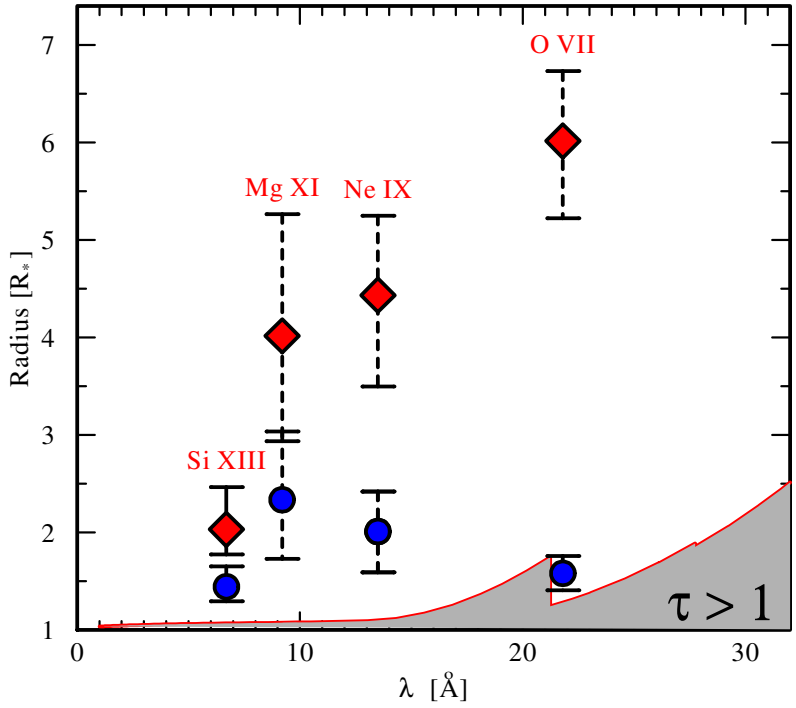

Figure 3.14.: Inferred formation radii (red diamonds) and onset radii (blue circles) of the X-ray radiation, as inferred from the four He-like ions Si XIII, Mg XI, Ne IX, and O VII. The error bars correspond to measurement uncertainties propagated into errors of the inferred radii (see Fig. 3.13). The shaded area corresponds to radii at which $\tau_{\rm Ross} \geq 1$.

of $\eta_{\rm X}$ could lead to slightly different results numerically, but should not affect our conclusions qualitatively. The X-rays are attenuated on their way to the observer due to K-shell absorption in the cool wind. Hence the X-ray propagation in the stellar wind is described by a pure absorption case of radiative transfer and is therefore relatively simple (e.g., Ignace 2001; Oskinova et al. 2004).

Macfarlane et al. (1991) demonstrated that the shape of optically thin emission lines is sensitive to the column density of the cool absorbing material: the lines become more skewed to the blue when the cool wind column density is large. They suggested using this property to measure the cool wind density. However, in clumped winds, the wind column density is reduced (Feldmeier et al. 2003), implying that the analysis of observed X-ray emission line profiles in O-type stars should account for wind clumping.

Several previous studies of X-ray emission lines in the spectra of O-type stars reported that accounting for wind clumping in the models does not improve the quality of the fit to the X-ray spectrum (e.g., Hervé et al. 2013). This is likely due to a degeneracy between the effects of mass-loss and clumping on the X-ray spectrum: one can always neglect clumping, albeit at the cost of lower estimated wind opacity. However, as we show here, the effect of clumping cannot be assumed to be negligible for the realistic mass-loss rate derived from the detailed analysis of the cool wind.

In this study, we extract the mass-absorption coefficient $\kappa_\lambda(r)$ directly from the PoWR model of the primary's cool wind. Importantly, our models include clumping and the feedback of X-ray radiation on the ionization structure of the wind and are therefore consistent. We make a simplifying assumption that the velocity field of the hot X-ray emitting plasma is the same as that of the cool X-ray absorbing wind. Thus, with the exception of the radial distribution of the hot plasma, all X-ray model parameters are determined by the non-LTE stellar atmosphere model.

The theory of X-ray transfer in clumped stellar winds was developed by Feldmeier et al. (2003) and Oskinova et al. (2004). The special case of spherical clumps was considered by Owocki & Cohen (2006).

The macroclumping formalism does not make any *ad hoc* assumptions about the size and optical depths of the cool wind clumps and is therefore suitable for effectively describing both smooth winds as well as clumped winds. This formalism further allows one to treat angle-dependent opacities, e.g., non-spherical wind clumps. A key parameter of the macroclumping formalism is the *fragmentation frequency* n_0 [s^{-1}] – the number of clumps per unit time passing through a sphere at an arbitrary radius, which does not depend on the radius due to the assumption of clump conservation. n_0 is approximately related to the average separation between clumps $L_{\rm mac}$ (see Sect. 3.5) via $L_{\rm mac}^3 \approx R_*^2 v_\infty n_0^{-1}$. Allowing for an angular-dependent opacity, e.g., flattened clumps or shell fragments, results in distinct line shapes, with flat topped line profiles in the limiting case of opaque clumps (see also Ignace et al. 2012). For each line, we consider a smooth model and a clumped model with anisotropic wind opacity (cf. Oskinova et al. 2004), assuming flattened, "pancake-like" clumps (Lépine & Moffat 1999). Comparing the observations with a grid of inhomogenious models, we find that $n_0 = 8.6 \times 10^{-5}\ s^{-1}$ provides a good compromise for several X-ray lines. This roughly corresponds to a wind flow time of $t_{\rm flow} = R_*/v_\infty \approx 1.5$ h ($n_0 \approx t_{\rm flow}^{-1}$), and to $L_{\rm mac} \sim 1\,R_*$, consistent with the lower bound $L_{\rm mac} \gtrsim 0.5$ implied from the UV and optical analysis.

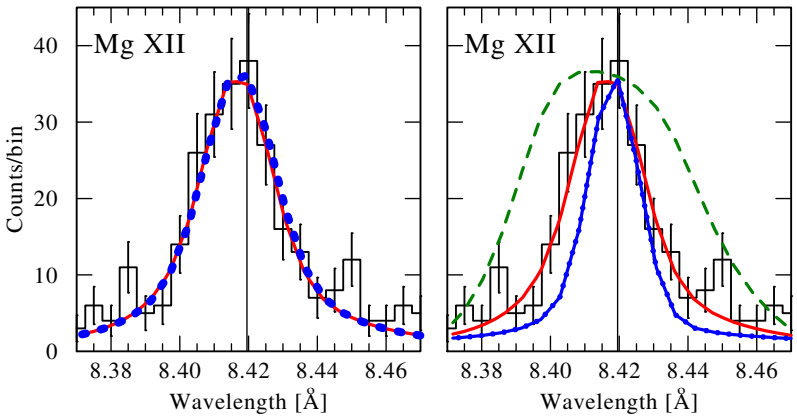

Figure 3.15.: *Left panel*: Observed co-added HEG±1 spectrum of δ Ori A centered on the Mg XII line (histogram), compared with a smooth-wind model (blue dotted line), and a clumped model (red solid line). As anticipated, clumping hardly affects the line formation at short wavelengths. *Right panel*: Again Mg XII, with three smooth models which assume X-ray onset radii of 1.01 R_* (blue dotted-solid line), 1.1 R_* (red solid line) and 1.5 R_* (green dashed line), suggesting that X-ray radiation *initiates* roughly at 1.1 R_* (for the adopted velocity law). The vertical lines indicate the rest wavelength shifted with the systemic velocity 15 km s^{-1}

The cool wind is virtually transparent at wavelengths shorter than 10 Å (see Fig. 3.14 in Sect. 3.6.2). In this case, the line shape can provide vital information regarding the velocity field and density distribution of the hot plasma. The left panel of Fig. 3.15 shows the observed Mg XII line compared with a smooth-wind model (blue dotted line) and a clumped-wind model (red solid line). The Mg XII line has the highest S/N ratio in the HEG wavelength range, and since the HEG has a superior spectral resolution (0.012 Å) compared to the MEG (0.023 Å), it is especially useful for studying the detailed shape of line profiles. Fig. 3.15 illustrates the above statement: lines at $\lambda \lesssim 10$ Å are hardly absorbed in the wind, and thus do not show any sensitivity to wind clumping. Furthermore, the good agreement between the models and the observations implies that the majority of X-rays originate in filaments co-moving with the cold wind, exhibiting the whole range of velocities up to the roughly the terminal velocity in their line profiles.

The right panel of Fig. 3.15 shows a comparison between the observed Mg XII line and three smooth-wind models that assume different onset radii for the X-ray emission: 1.01 R_* (blue dotted solid line), 1.1 R_* (red solid line), and 1.5 R_* (green dashed line). This comparison clearly illustrates that X-rays must form already very close to the stellar surface, at around 1.1 R_*. Larger onset radii result in flat-topped line profiles which

do not agree at all with the observed profiles. Smaller onset radii imply narrower lines than those observed. We note that the exact values are very sensitive to the adopted velocity law. However, the same conclusion is obtained for all our test models, where we vary the exponent of the β-law in the domain $0.5 < \beta < 1.5$: X-rays are formed in the wind, and onset radii are close to the stellar surface. Note that a small onset radius does not imply that the X-ray forms *only* close to the stellar surface.

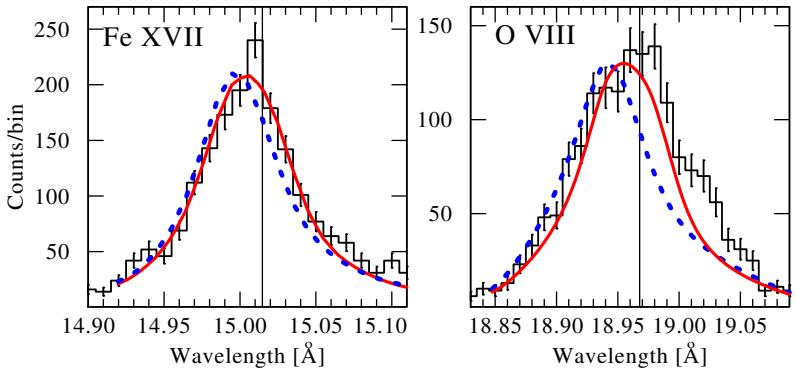

Figure 3.16.: *Left panel*: Observed co-added MEG±1 spectrum of δ Ori A centered on Fe XVII line (histogram) and two wind model lines: smooth (blue dotted line) and clumped (red solid line). The onset of X-ray emitting plasma is at $1.2\,R_*$. *Right panel*: Same as left panel, but for the O VIII line

While the effect of porosity is negligible at $\lambda \lesssim 10$ Å, it should generally be taken into account when modeling lines at longer wavelengths, where the cool wind opacity increases. Fig. 3.16 shows a comparison of the observed Fe XVII λ15.01 Å (left panel) and O VIII $\lambda\lambda$18.967, 18.972 Å (right panel) lines with models that include and neglect clumping (red solid and blue dotted lines, respectively). The wind model that neglects clumping is in poor agreement with the data, while a better agreement is reached when clumping is assumed. Nevertheless, the exact profile shape is not reproduced, especially in the case of the O VIII line. In fact, there is evidence that the widths of the X-ray lines in δ Ori A change with time (Paper II). Our tests indicate that the observed lines can be more accurately reproduced when fitted at each phase separately. To fit the global profiles, the variable line profiles would need to be averaged out. However, such a study, while interesting, is not the subject of this Paper.

To summarize, we illustrated that clumping generally plays a role in shaping the observed X-ray lines, that the line profiles suggest small onset radii of $\sim 1.1\,R_*$, and that the X-ray emitting parcels are likely coupled to the cool wind.

3.7. Summary and Conclusions

We have performed a multi-wavelength, non-LTE spectroscopic analysis of the massive δ Ori A system, which contains the visually brightest O-type eclipsing binary in the sky and a wider tertiary component. Our goal was to obtain accurate stellar parameters for the components of the system, to analyze their winds, and to gain a better understanding of the X-ray radiation emitted from the system. Three additional studies performed within the framework of the current collaboration explore the X-ray properties (Paper I) and variability (Paper II) of the system, and conduct a complete binary and optical variabilty analysis of the system (Paper III).

We conclude the following:

- Distance-independent parameters such as T_* and $\log g_*$ derived for the primary (cf. Table 3.1) are consistent with its spectral type O9.5 II. Distance-dependent parameters such as the luminosity and mass are found to be unusually low for the *Hipparcos* distance $d = 212$ pc. Typical values

($L_1 = 5.28\,L_\odot$, $M_1 = 24\,M_\odot$) are obtained for the distance $d = 380\,\mathrm{pc}$ of the neighboring cluster. These results agree well with the results reported in Paper III, suggesting that the *Hipparcos* distance is strongly underestimated.

- The secondary is marginally detectable in the composite spectrum. The V-band magnitude difference between the primary and secondary is constrained to $\Delta V_{\mathrm{Aa1Aa2}} \sim 2\overset{\mathrm{m}}{.}8$. The parameters of the secondary suggest it is a B type dwarf. The tertiary is confirmed to be a rapid rotator with $v \sin i \sim 220\,\mathrm{km\,s^{-1}}$, and its parameters correspond to an early B type or a late O type subgiant.
- Rapid turbulent velocities ($\sim 200\,\mathrm{km\,s^{-1}}$) prevail in the wind of the primary close to the stellar surface. We further find evidence for optically thick wind-inhomogeneities ("macroclumping"), affecting both strong resonance lines and X-ray lines.
- For a clumping factor of $D = 10$ and accounting for porosity, the primary's inferred mass-loss rate is $\log \dot{M} \approx -6.4\,[M_\odot\,\mathrm{yr}^{-1}]$. This value provides a consistent picture for δ Ori A along all spectral domains, from X-rays and UV to the optical and radio, and is furthermore in good agreement with hydrodynamical predictions.
- Most X-rays emerging from δ Ori A are likely intrinsic to the wind of the primary. X-ray onset radii are found to be $\sim 1.1 R_*$.

While δ Ori A gives us a precious opportunity to study stellar winds and multiple systems of massive stars, there are still questions left unanswered. Does the primary really have an exceptionally low mass, luminosity, and mass-loss rate, or is the *Hipparcos* distance significantly underestimated? Did mass-transfer occur between the primary Aa1 and the secondary Aa2? Where do the clumps in the primary wind originate, and how can they be further quantified? Why do we not clearly observe X-ray emission originating in the interaction between the primary and secondary? How did the system evolve to its current state, and how will it continue to evolve? To answer these questions, efforts should be made in obtaining high S/N optical and X-ray spectra which resolve the binary Aa from the tertiary Ab, and which enable a proper disentanglement of the system. Moreover, further studies should provide more hints regarding the correct distance of the system. Finally, variability studies of P Cygni lines in the system should provide crucial, independent constraints on the amount of inhomogeniety in the primary's wind. Answering these questions should take us one step closer to a more complete understanding of stellar winds, and of the evolution and properties of massive stars in multiple systems.

3.8. Acknowledgements

We thank our anonymous referee for constructive comments which helped to improve our paper. TS is grateful for financial support from the Leibniz Graduate School for Quantitative Spectroscopy in Astrophysics, a joint project of the Leibniz Institute for Astrophysics Potsdam (AIP) and the institute of Physics and Astronomy of the University of Potsdam. LMO acknowledges support from DLR grant 50 OR 1302 We would like to thank A. Valeev and S. Fabrika for kindly providing us with an optical spectrum of the system. We thank T. J. Henry and J. A. Caballero for fruitful discussions regarding system's distance. MFC, JSN, and WLW are grateful for support via Chandra grant GO3-14015A and GO3-14015E. AFJM. acknowledges financial aid from NSERC (Canada) and FRQNT (Quebec). JMA acknowledges support from [a] the Spanish Government Ministerio de Economía y Competitividad (MINECO) through grants AYA2010-15 081 and AYA2010-17 631 and [b] the Consejería de Educación of the Junta de Andaluc ía through grant P08-TIC-4075. Caballero NDR gratefully acknowledges his Centre du Recherche en Astrophysique du Québec (CRAQ) fellowship. YN acknowledges support from the Fonds National de la Recherche Scientifique (Belgium), the Communauté Française de Belgique, the PRODEX XMM and Integral contracts, and the 'Action de Recherche Concertée' (CFWB-Académie Wallonie Europe). JLH acknowledges support from NASA award NNX13AF40G and NSF award AST-0807477. IN is supported by the Spanish Mineco under grant AYA2012-39364-C02-01/02, and the European Union.

Chapter 4.

Measuring the stellar wind parameters in IGR J17544-2619 and Vela X-1 constrains the accretion physics in Supergiant Fast X-ray Transient and classical Supergiant X-ray Binaries (Manuscript III)

A. Giménez-García, T. Shenar, J. M. Torrejón, L. Oskinova, S. Martínez-Núñez, W.-R. Hamann, J. J. Rodes-Roca, A. González-Galán, J. Alonso-Santiago, C. González-Fernández, G. Bernabeu, A. Sander

Astronomy & Astrophysics, 2016, Volume 591, 25 pp.

Abstract

Classical Supergiant X-ray Binaries (SGXBs) and Supergiant Fast X-ray Transients (SFXTs) are two types of High-mass X-ray Binaries (HMXBs) that present similar donors but, at the same time, show very different behavior in the X-rays. The reason for this dichotomy of wind-fed HMXBs is still a matter of debate. Among the several explanations that have been proposed, some of them invoke specific stellar wind properties of the donor stars. Only dedicated empiric analysis of the donors' stellar wind can provide the required information to accomplish an adequate test of these theories. However, such analyses are scarce. To close this gap, we perform a comparative analysis of the optical companion in two important systems: IGR J17544-2619 (SFXT) and Vela X-1 (SGXB). We analyse the spectra of each star in detail and derive their stellar and wind properties. We compare the wind parameters, giving us an excellent chance of recognizing key differences between donor winds in SFXTs and SGXBs. We find that the stellar parameters derived from the analysis generally agree well with the spectral types of the two donors: O9I (IGR J17544-2619) and B0.5Iae (Vela X-1). An important difference between the stellar winds of the two stars is their terminal velocities $v_\infty = 1500 \mathrm{km\,s^{-1}}$ in IGR J17544-2619 and $v_\infty = 700\,\mathrm{km\,s^{-1}}$ in Vela X-1, which has important consequences on the X-ray luminosity of these sources. Their specific combination of wind speed and pulsar spin favours an accretion regime with a persistently high luminosity in Vela X-1, while it favours an inhibiting accretion mechanism in IGR J17544-2619. Our study demonstrates that the wind relative velocity is critical in the determination of the class of HMXBs hosting a supergiant donor, given that it may shift the accretion mechanism from direct accretion to propeller regimes when combined with other parameters.

4.1. Introduction

Within the wide zoo of High-mass X-ray Binaries (HMXBs), we find two classes of sources where a compact object, usually a neutron star, accretes matter from the stellar wind of a supergiant OB donor. These are the classical Supergiant X-ray Binaries (SGXBs) and the Supergiant Fast X-ray Transients (SFXTs). These

two groups of systems, despite hosting roughly the same type of stars, have distinctive properties when observed in the X-rays.

Supergiant X-ray Binaries are persistent sources, with an X-ray luminosity in the range $L_X \sim 10^{33-39}$ erg/s. They are often variable, showing flares and off-states that indicate abrupt changes in the accretion rate (Kreykenbohm et al. 2008; Martínez-Núñez et al. 2014). However, their variability is not as extreme as in SFXTs (Walter & Zurita Heras 2007). The dynamic range (ratio between luminosity in outburst and in quiescence) in SGXBs is $\lesssim 2$ orders of magnitude. In contrast, the dynamic range in SFXTs can reach up to six orders of magnitude in the most extreme cases such as IGR J17544-2619 (Romano et al. 2015; in't Zand 2005), analysed in this work. During quiescence, SFXTs exhibit a low X-ray luminosity of $L_X \sim 10^{32}$ erg/s (in't Zand 2005), but they spend most of their time in an intermediate level of emission of $\sim 10^{33-34}$ erg/s (Sidoli et al. 2008). They display short outbursts (~few hours), reaching luminosities up to 10^{36-37} erg/s (Sidoli 2011; Sidoli et al. 2009).

There are other sources in between SGXBs and SFXTs, the so called "intermediate SFXTs", which have a dynamic range of $\gtrsim 2$ orders of magnitude. Hence, there is no sharp border that clearly separates SGXBs and SFXTs. The categorization of SFXTs as a new class of HMXBs (Negueruela et al. 2006) was possible thanks to *INTEGRAL* observations (Sguera et al. 2005). Since then, several explanations have been proposed in order to explain their transient behavior.

Negueruela et al. (2008) suggested that the intrinsic clumpiness of the wind of hot supergiant donors, together with different orbital configurations, may explain the different dynamic ranges between SGXBs and SFXTs. If the eccentricity of SFXTs is high enough, the compact object swings between dense regions with a high probability of accreting a wind clump and flare up, and diffuse regions where this probability is low and the source is consequently faint in the X-rays. In SGXBs, the compact object would orbit in a closer and more circular trajectory, accreting matter incessantly. However, the short orbital period of some SFXTs is contradictory with this scheme (Walter et al. 2015).

Other ingredients, such as the magnetic field of the neutron star and/or the the spin period, might be important. This is supported by the monitoring of SFXTs. Tracing SFXTs for a long period, Lutovinov et al. (2013) conclude that, in SFXTs, the accretion is notably inhibited most of the time. One can invoke to the different possible configurations of accretion, co-rotation and magnetospheric radius in order to relax the extremely sharp density contrast required in the above mentioned interpretation (Grebenev & Sunyaev 2007; Bozzo et al. 2008; Grebenev 2010). The size of these radii depend on the wind, orbital, and neutron star parameters. For instance, if the magnetospheric radius is larger than the accretion radius (Bondi 1952), the inflow of matter is significantly inhibited by a magnetic barrier, resulting in a relatively low X-ray emission from the source. Under this interpretation, the physical conditions in SFXTs make them prone to regime transitions as a response to relatively modest variations in the wind properties of the donor, which cause abrupt changes in X-ray luminosity.

These changes might also be explained within the theory of quasi-spherical accretion onto slowly rotating magnetized neutron stars developed by Shakura et al. (2012). This theory describes the so-called *subsonic settling accretion regime* in detail. In slowly rotating neutron stars, the penetration of matter into the magnetosphere is driven predominantly by Rayleigh-Taylor instabilities (Elsner & Lamb 1976). When the cooling of the plasma in the boundary of the magnetosphere is not sufficiently efficient, the accretion of matter is highly inhibited and consequently the X-ray luminosity is low. On the other hand, when the cooling time is much smaller than the characteristic free-fall time ($t_{cool} \ll t_{ff}$), the instability conditions are fulfilled and the plasma easily enters the magnetosphere, triggering high X-ray luminosity. The last is achieved when the X-ray luminosity is $L_X \gtrsim 4 \cdot 10^{36}$ erg/s, and the rapid Compton cooling dominates over the radiative cooling. For the brightest flares ($L_X > 10^{36}$), Shakura et al. (2014) proposed that a magnetized wind of the donor might induce magnetic reconnection, enhancing the accretion up to the critical X-ray luminosity and triggering the suction of the whole shell by the neutron star.

We need as much information as possible about the stellar wind conditions in order to understand the different behavior of SGXBs and SFXTs. However, very few analyses of SGXBs and SFXTs have been performed so far in the ultraviolet-optical-infrared spectral range using modern atmosphere codes which include NLTE and line blanketing effects. Moreover, although the X-rays are mainly produced in the surroundings of the compact object, the analysis of X-rays observations is directly affected by the physical properties of the donor and its wind. For instance, the assumed abundances strongly affect the derived value

of one of the most important parameters in the X-rays studies: the equivalent hydrogen column density (N_H). More reliable abundances make the N_H estimations more reliable. Analysing spectra by means of line-blanked, NLTE model atmosphere codes is currently the best way to extract the stellar parameters of hot stars with winds.

In this work we analyze the optical companion of two X-ray sources: IGR J17544-2619 (SFXT) and Vela X-1 (SGXB). These sources are usually considered to be *prototypical* for their respective classes (Martínez-Núñez et al. 2014; Sidoli et al. 2009; Mauche et al. 2007). Hence, in addition to the important scientific value of studying these sources by themselves, this is an excellent opportunity to compare the donor's parameters in these two prototypical systems, and to test how well the aforementioned resolutions for the SFXT puzzle fit in with our results.

The structure of the paper is as follows. In Sect. 4.2 we describe the set of observations used in this work. In Sect. 4.3 we explain the main features of Potsdam Wolf-Rayet (PoWR) code employed in the fits. In Sect. 4.4 we detail the fit process and give the obtained results. In Sect. 4.5 we discuss several consequences arising from our results. Finally, in Sect. 4.6 we enumerate the conclusions that we find from this work.

4.2. The observations

Table 4.1.: Table of observations of IGR J17544-2619. We used $T_{90} = T_0 = T_{\phi=0} = 55924.271$ (MJD) and orbital period $P_{orb} = 4.9272$ d (Drave et al. 2014).

Instrument	Phase	Date (YYYY-MM-DD)	MJD	Exposure (s)
SpeX	0.65	2004-08-15	53232.29	60
FEROS	0.01	2005-09-30	53643.05	1470
	0.01	2005-09-30	53643.03	1470
	0.01	2005-09-30	53643.01	1470
	0.02	2005-09-30	53643.07	1470
	0.61	2005-09-28	53641.08	1470
	0.61	2005-09-28	53641.06	1470
	0.61	2005-09-28	53641.04	1470
	0.62	2005-09-28	53641.10	1470
	0.74	2005-09-09	53622.01	1470
	0.75	2005-09-09	53622.02	1470
	0.76	2005-09-09	53622.10	1470
	0.76	2005-09-09	53622.08	1470
	0.97	2005-09-15	53628.06	1470
	0.98	2005-09-15	53628.08	1470

In this study we used data from International Ultraviolet Explorer (IUE)[1], the fiber-fed extended range optical spectrograph (FEROS)[2] operated at the European Southern Observatory (ESO) in La Silla, Chile;

[1] available at https://archive.stsci.edu/iue/
[2] available at http://archive.eso.org/

Table 4.2.: Table of observations of Vela X-1. We used $T_{90} = T_0 = T_{\phi=0} = 52974.001$ (MJD) and orbital period $P_{\rm orb} = 8.964357$ d (Kreykenbohm et al. 2008).

Instrument	Phase	Date (YYYY-MM-DD)	MJD	Exposure (s)
SWP	0.05	1978-05-05	43633.62	9000
	0.07	1984-02-19	45749.32	8280
	0.08	1985-05-03	46188.67	4500
	0.09	1985-05-03	46188.75	4500
	0.09	1985-05-03	46188.81	3300
	0.10	1985-05-03	46188.86	1020
	0.10	1985-05-03	46188.92	6000
	0.10	1993-11-08	49299.55	8400
	0.14	1978-12-07	43849.51	8400
	0.17	1992-11-06	48932.56	10800
	0.22	1993-11-09	49300.55	8100
	0.28	1983-01-22	45356.80	10800
	0.28	1992-11-07	48933.57	9600
	0.29	1983-01-22	45356.91	4500
	0.29	1984-02-21	45751.31	9000
	0.33	1993-11-10	49301.55	9000
	0.40	1984-02-22	45752.36	9000
	0.40	1988-02-22	47213.55	8460
	0.41	1992-11-08	48934.72	9900
	0.45	1978-04-30	43628.21	10800
	0.46	1982-12-19	45322.52	9000
	0.46	1993-11-11	49302.71	8400
	0.49	1985-05-07	46192.36	7200
	0.50	1985-05-07	46192.47	7200
	0.51	1985-05-07	46192.58	7200
	0.52	1988-02-23	47214.54	8460
	0.52	1988-03-12	47232.54	7826
	0.53	1978-12-20	43862.03	7800
	0.53	1983-01-07	45341.09	10800
	0.55	1993-11-03	49294.56	6000
	0.60	1978-12-02	43844.71	5400
	0.61	1983-01-16	45350.77	10800
	0.66	1993-11-04	49295.55	8400
	0.71	1978-12-03	43845.69	8400
	0.73	1984-02-16	45746.31	9000
	0.74	1983-01-09	45343.01	10800
	0.75	1985-04-21	46176.77	7200
	0.76	1985-04-21	46176.86	4500
	0.77	1979-03-21	43953.77	9000
	0.77	1985-04-21	46176.99	6900
	0.79	1993-11-05	49296.71	7500
	0.84	1984-02-17	45747.32	9000
	0.85	1978-07-23	43712.49	7500
	0.90	1993-11-06	49297.73	6600
	0.97	1983-01-11	45345.10	10800
	0.97	1983-01-20	45354.07	5400
	0.97	1984-02-18	45748.49	7500
	0.98	1983-01-20	45354.13	3300
	0.99	1993-11-07	49298.54	9600
FEROS	0.68	2005-04-22	53482.05	700
	0.68	2005-04-22	53482.06	700
	0.68	2005-04-22	53482.07	700
	0.68	2005-04-22	53482.07	700
	0.68	2005-04-22	53482.09	700
	0.68	2005-04-22	53482.10	700

and the infrared (IR) spectrograph SpeX in the NASA Infrared Telescope Facility (IRTF) in Mauna Kea, Hawaii.

The IUE is provided with two spectrographs (long-wavelength in the range 1850 – 3300 Å and short-wavelength in 1150 – 2000 Å) and four cameras (prime and redundant camera, for each spectrograph). Each spectrograph can be used with either large aperture (a slot 10x20 arcsec), or small aperture (a circle 3 arcsec diameter). In addition, each spectrograph has two dispersion modes: high resolution and low resolution. High resolution mode ($\sim$ 0.2 Å) utilizes an echelle grating plus a cross-disperser. Low resolution mode ($\sim$ 6 Å) utilizes only the cross-disperser. IUE provides flux calibrated data. This is an important advantage due to two main reasons: first, we used these observations to fit the spectral energy distribution from the models, as explained below in Sect. 4.4.2; and second, we did not have to normalize the UV spectrum. As we can see in Fig. 4.10, it is not straightforward to see the actual flux level of the UV continuum, since this spectral range is almost completely covered by spectral lines. Therefore, any normalization by visual inspection would lead to significant errors. Instead, we rectified the IUE spectra using the PoWR model continuum.

FEROS is a spectrograph that yields high resolution echelle spectroscopy ($R \sim 48000$) and high efficiency ($\sim$ 20%) in the optical wavelength range (3600 – 9200 Å) (Kaufer et al. 1999). SpeX is an infrared spectrograph in the 0.8 – 5.5 μm range. Among the different modes available in this instrument, we used the 0.8 – 2.4 μm cross-dispersed mode (SXD), which yields moderate spectral resolution ($R \sim 2000$) (Rayner et al. 2003).

In Table 4.1 we present the set of observations of IGR J17544-2619. We used an observation from SpeX taken on August 8, 2004. In the ESO archive there are 14 FEROS observations of IGR J17544-2619 taken on four different dates during September 2005. There are not IUE available public observations of IGR J17544-2619.

In Table 4.2 we present the set of observations of Vela X-1. In the ESO archive there are six consecutive FEROS observations of 700s taken on April 22, 2006. For the IUE data, we used the high dispersion and large aperture observations using the short-wavelength spectrograph (1150-2000 Å) and the prime camera (SWP). There are 49 observations in the public database of the IUE following these criteria.

For each instrument, we averaged over all the available observations taking into account the exposure time in order to improve the signal-to-noise ratio. We did not take the variability of the UV spectral lines depending on the orbital phase into account, that has been reported for Vela X-1 (Sadakane et al. 1985). The variability consists on the presence of an extra absorption component in several spectral lines, specially ones belonging to Al III and Fe III , mainly at phases $\phi > 0.5$. This variability must be taken into account to interpret the full picture of the stellar wind of Vela X-1. However, in this work, we prioritized a signal-to-noise ratio as high as possible over fitting a number of phase dependent spectra with significantly lower signal-to-noise. This permits us to estimate the stellar parameters of Vela X-1 more accurately, while not affecting any of the conclusions derived in this work, as we have carefully examined.

4.3. The PoWR code

PoWR computes models of hot stellar atmospheres assuming spherical symmetry and stationary outflow. The non-LTE population numbers are calculated using the equations of statistical equilibrium and radiative transfer in the co-moving frame. Since these equations are coupled, the solution is iteratively found. Once convergence is reached, the synthetic spectrum is calculated integrating along the emergent radiation rays. The main features of the code have been described by Gräfener et al. (2002) and Hamann & Gräfener (2003a).

The basic input parameters in PoWR are the following: stellar temperature ($T_\star$), luminosity ($L_\star$), mass-loss rate ($\dot{M}$), surface gravity ($g_\star$) and chemical abundances. The chemical elements taken into account are detailed in Table 4.4. The stellar radius ($R_\star$) follows from $T_\star$ and $L_\star$ using the Stefan-Boltzmann law: $L_\star = 4\pi\sigma T_\star^4 R_\star^2$, where σ is the Stefan-Boltzmann constant. We note that, in PoWR, $R_\star$ refers to the layer where the Rosseland continuum optical depth $\tau_{\rm max} = 20$, and not to the definition of stellar radius (or photospheric radius), where $\tau_{\rm Ross} = 2/3$. Nevertheless, we will give the stellar parameters in the next sections referring to both $\tau_{\rm max} = 20$ and the $\tau_{\rm max} = 2/3$, in order to avoid any confusion (e.g., we will use

$R_\star$ for the radius at $\tau_{\max} = 20$ and $R_{2/3}$ for the radius at $\tau_{\max} = 2/3$). The surface gravity $g_\star$ and $R_\star$ imply the stellar mass ($M_\star$) via $g_\star = GM_\star R_\star^{-2}$. Instead of $g_\star$, one may specify the effective surface gravity $g_{\rm eff}$, which accurately accounts for the outward force exerted by the radiation field, as thoroughly described by Sander et al. (2015).

The density stratification in the stellar atmosphere, $\rho(r)$, is calculated from the continuity equation $\dot{M} = 4\pi r^2 v(r)\rho(r)$, given $\dot{M}$ and the radial velocity stratification $v(r)$. For $v(r)$, PoWR distinguish between two different regimes: the quasi-hydrostatic domain and the wind domain. A detailed description of the quasi-hydrostatic domain can be found in Sander et al. (2015). In the wind domain, the β-law is adopted (Castor et al. 1975):

$$v(r) = v_\infty \left(1 - \frac{r_0}{r}\right)^\beta \tag{4.1}$$

where v_∞ is the terminal velocity of the wind, $r_0 \approx R_\star$ (depending on the precise location of the connection point) and β is an input parameter typically ranging between $\beta = 0.6 - 2.0$ (Puls et al. 2008). The connection point is chosen in order to ensure a smooth transition between the two domains. The temperature stratification is calculated from the condition of radiative equilibrium (Hamann & Gräfener 2003b).

The code also permits to account for density inhomogeneities and additional X-rays from a spherically-symmetric, shock heated plasma. Density inhomogeneities are described in PoWR by means of an optional radial-dependent input parameter: the density contrast $D(r) = \rho_{cl}/\bar{\rho}$, where ρ_{cl} is the density of the clumped medium and $\bar{\rho}$ is the average density. The inter-clump medium is assumed to be empty. During the analysis, $D(r)$ is assumed to grow from $D(r_{\rm sonic}) = 1$ (smooth plasma) to a maximum value D, which is reached at the layer where the stellar wind velocity is $\mathrm{f}_{\max} \times v_\infty$. D is a free parameters derived in the analysis. $\mathrm{f}_{\max}$ has a modest influence on the spectra. We assumed $\mathrm{f}_{\max} \sim 0.6$ on the basis of this moderate effect. The X-rays are described using three parameters: the X-ray temperature $T_{\rm X}$, the filling factor $X_{\rm F}$ (i.e. the ratio between shocked to unshocked plasma), and the onset radius R_X, as described in Baum et al. (1992). In this work, we assumed $T_{\rm X} = 10^7$ K, $R_X = 1.2\,R_\star$ and $X_{\rm F} = 0.05$. The main influence of X-rays in the model is via Auger ionization, which is responsible for the appearance of resonance lines belonging to high ions such as N v and O vi in the spectra of O stars (Cassinelli & Olson 1979; Krtička & Kubát 2009; Oskinova et al. 2011). Any changes in these parameters barely affect the spectrum, as long as they they produce a similar X-ray luminosity.

During the iterative calculation of the population numbers, the spectral lines are taken to be Gaussian with a constant Doppler width of $v_{\rm Dop} = 40$ km/s; the effect of $v_{\rm Dop}$ on the spectrum is negligible for most lines (see discussion by Shenar et al. 2015). During the formal integration, the line profiles include natural broadening, pressure broadening, and Doppler broadening. The Doppler width is decomposed per element to a depth dependent thermal motion and a microturbulent velocity $\xi(r)$. The photospheric microturbulence, $\xi_{\rm ph}$, is derived in the analysis, and beyond the photosphere we assumed that it grows from $\xi = \xi_{\rm ph}$ to $\xi = 100$ km/s at the layer where the stellar wind velocity is 500 km/s. Rotational broadening is simulated via convolution with rotational profiles with a width corresponding to the projected rotational velocity $v_{\rm rot} \sin i$ (denoted by $v_{\rm rot}$ hereafter for simplicity), except for important wind lines, for which the convolution is no longer valid (see e.g. Hillier et al. 2012), and where an explicit angle-integration would be required (as described by Shenar et al. 2014). The so-called macroturbulence $v_{\rm mac}$ is accounted for by convolving the spectra with so-called Radial-Tangential profiles (Gray 1975; Simón-Díaz & Herrero 2007).

4.4. The fitting procedure

We used the PoWR code to calculate synthetic spectra and a Spectral Energy Distribution (SED) which best match the observations. The large number of free parameters, together with the long computation time for each model, do not permit the construction of a grid of models that covers the full parameter space. Instead, we attempted to identify the best-fitting model by visual inspection and systematic variation of the parameters. As an initial step, we calculate models using typical parameters of late O / early B stars. We then use specific spectral lines for each parameter as a guideline for the fit. Generally, the effective gravity $g_{\rm eff}$ is derived from the pressure-broadened wings of the Balmer lines and He II lines. The temperature $T_\star$ is derived based on line ratios belonging to different ions of the same element. The mass-loss rate $\dot{M}$, v_∞ and

D are derived from "wind-lines", with D adjusted so that a simultaneous fit is obtained for both resonance lines (which scale as ρ) and recombination lines such as Hα (which scale as ρ^2). The luminosity $L_\star$ and the reddening E_{B-V} are derived by fitting the SED to photometry and flux-calibrated spectra. We apply the reddening law by Fitzpatrick (1999). Abundances are estimated from the overall strengths of the spectral lines. The photospheric microturbulence $\xi_{\rm ph}$ is found from the strength and shape of helium lines. Finally, the parameters β, $v_{\rm rot}$ and $v_{\rm mac}$ are adopted on the basis of the shape and depth of the spectral lines, together with previous estimations found in the literature, when available. Upon adjusting the model, the whole spectral domain was examined to iteratively improve the fit. Overall, we managed to find models which satisfactorily reproduce the observed spectra and SEDs of the donors of the two systems analysed here.

We show the complete fits in Appendix A.2. The details about the fitting procedure for the two objects are given in the following subsections. The obtained parameters are summarised in Table 4.3 and the chemical abundances in Table 4.4. The parameters that do not include an error estimation in the tables are adopted following the above mentioned criteria.

Even though the optical companion in Vela X-1 is usually known as HD 77581, for the sake of simplicity we will refer to the donors with the name that is used for the X-rays sources, namely, IGR J17544-2619 and Vela X-1. Depending on the context, the reader should easily recognize whether it is the donor or the X-ray source which is being referred to.

Table 4.3.: Stellar parameters obtained from the best fit. (a) Joss & Rappaport (1984). (b) Pellizza et al. (2006). (c) Fraser et al. (2010)

Parameters	J17544-2619	Vela X-1
$\log(L_\star/L_\odot)$	5.4 ± 0.1	5.5 ± 0.1
$M_\star/M_\odot$	25.9 ± 2.0^b	21.5 ± 4.0
$R_\star/R_\odot$	20^{+4}_{-3}	28.4^a
$R_{2/3}/R_\star$	1.04	1.09
$T_\star$ (kK)	29.0 ± 1.0	25.5 ± 1.0
$T_{2/3}$ (kK)	28.5 ± 1.0	24.4 ± 1.0
$\log(g_\star$ (cgs))	3.25 ± 0.20	2.86 ± 0.10
$\log(g_{\rm eff}$ (cgs))	2.80 ± 0.20	2.35 ± 0.10
$\log(g_{\rm eff\ 2/3}$ (cgs))	2.77 ± 0.20	2.27 ± 0.10
v_∞ (km/s)	1500 ± 200	700^{+200}_{-100}
$v_{\rm esc}$ (km/s)	618 ± 75	436 ± 65
$\log(\dot{M}/(M_\odot/{\rm yr}))$	-5.8 ± 0.2	-6.2 ± 0.2
D	4	11 ± 5
$\xi_{\rm ph}$ (km/s)	25 ± 10	30 ± 10
β	0.8	1.0
$v_{\rm mac}$ (km/s)	60	80
$v_{\rm rot}$ (km/s)	160	56^c
$E_{\rm B\text{-}V}$	2.14 ± 0.10	0.77 ± 0.05
$R_{\rm V}$	2.9	3.1
d (kpc)	3.0 ± 0.2	2.0 ± 0.2

4.4.1. IGR J17544-2619

IGR J17544-2619 was first detected on September 2003 with the IBIS/ISGRI detector on board *INTEGRAL* (Sunyaev et al. 2003). It is located in the direction of the galactic center, at galactic coordinates $l = 3.24°$,

Table 4.4.: Chemical abundances derived from the best fit, in mass fraction and relative to solar abundances from Asplund et al. (2009). (a) The notation of Fe actually stands for a generic atom including iron group elements Sc, Ti, V, Cr, Mn, Co and Ni. For more details see Gräfener et al. (2002).

	IGR J17544-2619		Vela X-1	
Quemical Element	Mass Fraction	Rel. Ab.	Mass Fraction	Rel. Ab.
H	$(6.2 \pm 0.5)E-01$	0.85	$(6.5 \pm 0.5)E-01$	0.89
He	$(3.7 \pm 0.5)E-01$	1.47	$(3.4 \pm 0.5)E-01$	1.35
C	$(5.0 \pm 3.0)E-04$	0.17	$(5.0 \pm 3.0)E-04$	0.17
N	$(2.2 \pm 0.6)E-03$	2.58	$(1.8 \pm 0.6)E-03$	2.11
O	$(6.0 \pm 2.0)E-03$	0.76	$(7.0 \pm 0.2)E-03$	0.88
Si	$(7.3 \pm 2.0)E-04$	1.00	$(5.5 \pm 2.0)E-04$	0.75
S	$5.0E-04$	1.00	$5.0E-04$	1.00
P	$6.4E-06$	1.00	$6.4E-06$	1.00
Al	$5.8E-05$	1.00	$7.0E-05$	1.00
Mg	$7.0E-04$	1.00	$7.0E-04$	1.00
Fe[a]	$1.4E-03$	1.00	$1.4E-03$	1.00

$b = -0.34°$. The orbital period is ∼4.9d (Clark et al. 2009). According to *Chandra* observations, the compact object is a neutron star (in't Zand 2005). Pellizza et al. (2006) used optical and NIR observations in order to classify the optical companion as a O9Ib. *Chandra* and *Swift* observations showed that the system exhibits a high dynamic range in its X-ray variability, changing the X-ray flux by 5 orders of magnitude (in't Zand 2005; Romano et al. 2015).

Nowadays, the spin period $P_{\rm spin}$ of the hypothetical neutron star in IGR J17544-2619 is a matter of debate, given the results arising from observations taken at different times, different luminosities and different instruments. Drave et al. (2012) analysed RXTE data of the source at intermediate X-ray luminosity ($\sim 10^{33-34}$ erg/s), and reported the detection of an X-ray pulsation with $P_{\rm spin} = 71.49$s at a statistical significance of 4.37σ. Romano et al. (2015) inspected *Swift* observations of the source experiencing an extraordinarily bright outburst (peak luminosity $\sim 10^{38}$ erg/s), and reported the detection of X-ray pulsations with $P_{\rm spin} = 11.60$s at a statistical significance of about 4σ too. However, these results contrast with the analyses of *XMM-Newton* and *NuSTAR* observations performed by Drave et al. (2014) and Bhalerao et al. (2015) respectively. These authors do not find any evidence of pulsations on time scales of 1-2000s.

We have adjusted $T_\star$ of IGR J17544-2619 using different ions, mainly He I-He II and Si III-Si IV. In Fig. 4.1 we show an example of four helium lines of which the best-fit model provides a good description. Higher (lower) temperatures yield more (less) absorption than observed in the He II lines. We have used other lines of helium, silicon, nitrogen and oxygen. The vast majority of them are well described by the best-fit model, within the errors. The obtained effective temperature is compatible with the donor's spectral class O9 Ib (Martins et al. 2005).

The effective gravity $g_{\rm eff}$ was found using the hydrogen Balmer lines Hγ and Hδ. We did not use Hβ and Hα because these lines are notably affected by the stellar wind. Figure 4.2 shows a comparison of the observations with the best-fitting model for these two Balmer lines. We show that the observations are compatible with a relatively wide range of values, as also reflected in the errors given in Table 4.3.

The distance to IGR J17544-2619 is not well known, with an estimate of 2-4 kpc Pellizza et al. (2006), based on the extinction and the calibration of the absolute magnitude for O9Ib stars. In this work we improve this estimation. As a first step, we fitted the SED to photometry from the 2MASS catalogue (Cutri et al. 2003), Zacharias et al. (2012a) and Rahoui & Chaty (2008) assuming the distance to be 3 kpc. Then, we derived initial values for the luminosity of the donor and the reddening to the system.

As a second step, in order to provide more constraints on the distance, we employed a method based

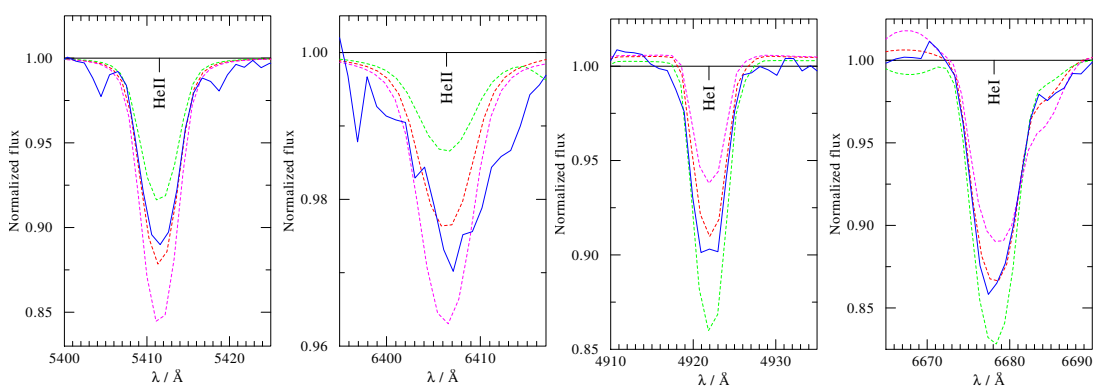

Figure 4.1.: Example of four helium lines in IGR J17544-2619, used for the estimation of $T_\star$. We show the observation (solid blue line), the best-fit model (red dashed line), a model with lower temperature of $T_\star = 28$ kK (green dashed line), and a model with higher temperature of $T_\star = 30$ kK (pink dashed line).

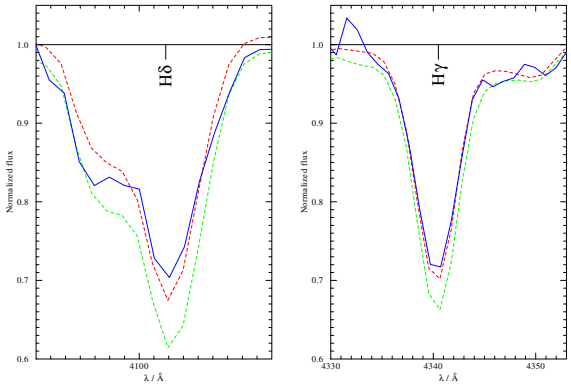

Figure 4.2.: Hγ and Hδ in IGR J17544-2619, used for the surface gravity estimation. We show the observation (solid blue line), the best-fit model (red dashed line) and a model with larger effective gravity of $\log(g_{\rm eff}) = 3.0$ in cgs units (green dashed line).

on the well constrained luminosity of Red Clump Giant stars (RCG). These stars can be isolated in a NIR colour-magnitude diagram and permit the estimation of the interstellar extinction along the line of sight (López-Corredoira et al. 2002). Due to their narrow luminosity function, the apparent magnitude of RCGs provides an estimation of the distance. Then, given a certain line of sight, a diagram of the extinction versus the distance can be derived (for more details see González-Fernández et al. 2014). For IGR J17544-2619 we employed the derived E_{J-K} from the SED fit to obtain an estimate of the distance. We note that this method is only applicable to stars in the direction of the galactic center like IGR J17544-2619, where the medium is more homogeneous and the density of RCGs is higher. Using this method, we obtain a distance of 3.0 ± 0.2 kpc (Fig. 4.3). Revised values for the luminosity and reddening are then derived. The final results of the SED fit are shown in Fig. 4.4.

From the luminosity and temperature we derive $R_\star$, which provides an upper limit to the eccentricity of the system. For the lower limit $R_\star = 17\,R_\odot$, we find $e < 0.25$. For higher eccentricities, periodic Roche-lobe overflow is expected from the orbital solution of the system (Clark et al. 2009), at odds with the X-ray behavior of the source. Given the radius of the source and the derived surface gravity, we find

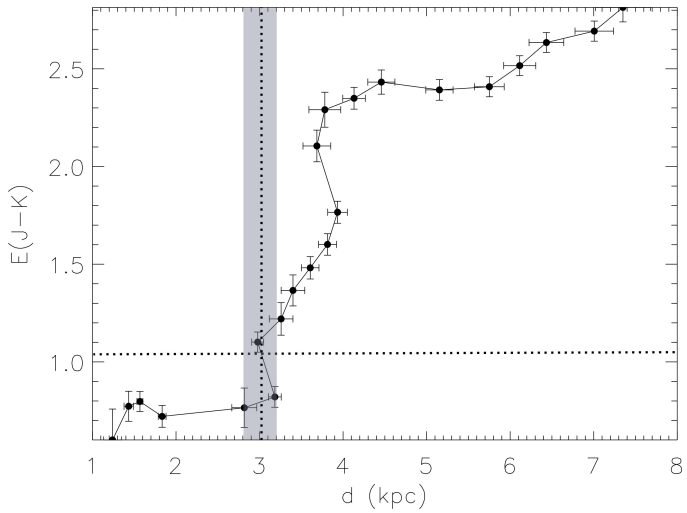

Figure 4.3.: Extinction curve in the galactic direction of IGR J17544-2619. The shaded area reflects the error in the distance estimation from the errors of estimation of the extinction and the errors in the calculation of the extinction curve.

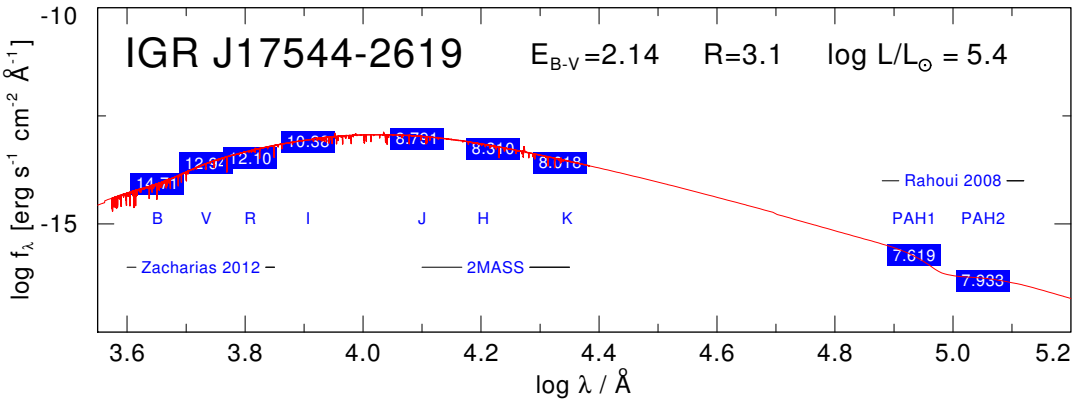

Figure 4.4.: Fit of the SED of IGR J17544-2619. In red we plot the best-fit model. We indicate the photometry values for each band in blue. The employed references are cited. The values of extinction, distance and luminosity are shown in Table 4.3.

$M_\star = 25.9\,M_\odot$. This value matches very well with the estimation of $M_\star = 25 - 28\,M_\odot$ done by Pellizza et al. (2006) based on the mass calibration with its spectral type.

The terminal velocity of the stellar wind v_∞ was derived using the P-Cygni profile of He I λ10833 Å (see Fig. 4.5). The blue wing in He I λ10833 Å is a very good indicator due to its strong sensitivity to v_∞. It is reasonably well fitted when assuming $v_\infty \simeq 1500$ km/s. Unfortunately, the emission exhibited by this line is not well reproduced by the best-fit model, as explained below.

The $\dot{M}$ and D were simultaneously adjusted by means of Hα and the P-Cygni profile of HeI λ10833 Å. Provided that the strength of emission in these recombination spectral lines varies with $\dot{M}\sqrt{D}$ (Gräfener et al. 2002), we cannot estimate $\dot{M}$ and D independently using these lines. As it is shown in Fig. 4.6, we were not able to fit all the lines at the same time. The best-fit model provides an acceptable description of Hα, but yields insufficient emission for HeI λ10833 Å. We choose the best description of Hα as the best-fit

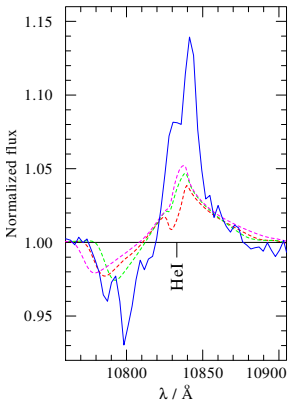

Figure 4.5.: He I at λ 10833 Å, used for the estimation of v_∞ in IGR J17544-2619 fitting the blue wing of the P-Cygni profile. We show the observation (solid blue line), the best-fit model (red dashed line), a model with $v_\infty = 1300$ km/s (green dashed line), and a model with $v_\infty = 1700$ km/s (pink dashed line).

because it provides a better fit to the overall spectrum. We note that the optical and infrared spectra were not taken at the same time, and therefore any kind of variability in the lines might produce a disagreement. However, Hα does not show such a large variability within the observations we have analysed (see Fig. 4.7).

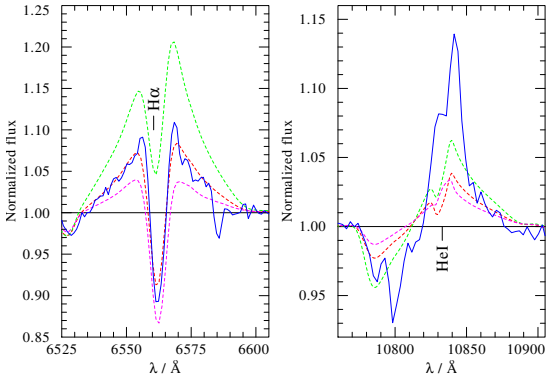

Figure 4.6.: Hα and He I λ10833Å lines for the estimation of $\dot{M}\sqrt{D}$ in IGR J17544-2619. We show the observation (solid blue line), the best-fit model (red dashed line), a model with higher $\dot{M}\sqrt{D}$ (1.35 times the best-fit value, green dashed line), and a model with lower $\dot{M}\sqrt{D}$ (0.8 times the best-fit value, pink dashed line).

Without available resonance scattering lines in the observations at hand, we cannot compare P-Cygni lines with recombination lines to deduce the clumping factor D. However, our calculations show that changing $\dot{M}$ dramatically affects the absorption spectrum in a fashion which is not related to the product $\dot{M}\sqrt{D}$. An example is shown in Fig. 4.8, where we show three models calculated with different values of $\dot{M}$ and D, but with a fixed product $\dot{M}\sqrt{D}$. Evidently, while the emission exhibited by the wings of H-α (shown in Fig. 4.8) is similar in all models, the absorption lines are strongly affected in a non-trivial manner. The reason for this unexpected behaviour is that many of the strong lines in the spectrum (e.g. the Balmer series) are formed significantly beyond the photosphere ($\tau_{\rm Ross} \approx 2/3$), where the mass-loss rate already strongly affects the density stratification via the continuity equation. Exploiting this effect, we find that

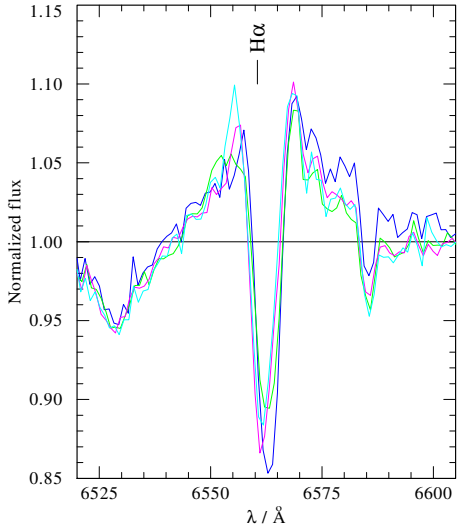

Figure 4.7.: Hα in IGR J17544-2619 at different orbital phases: $\phi \simeq$ 0.01,0.61,0.75,0.97 (blue, green, pink and turquoise solid lines respectively).

$D \approx 4$ provides the best results for the overall spectrum. However, we warn that further observations are needed to better constrain the clumping factor in this star. Nevertheless, we note that our final conclusions do not strongly depend on this factor and the implied mass-loss rate, as will be discussed in Section 4.5.

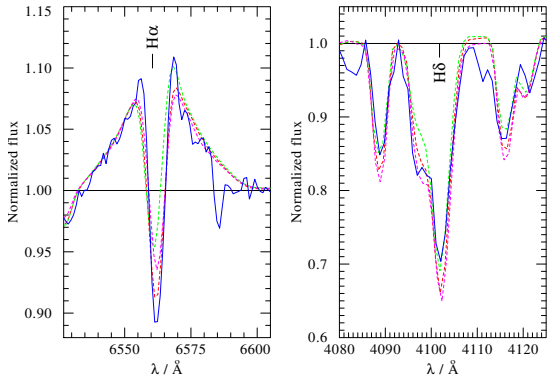

Figure 4.8.: Hα and Hδ for the estimation of $\dot{M}$ in IGR J17544-2619. We show the observation (solid blue line), the best-fit model ($\dot{M} = 10^{-5.8}\ M_\odot$/yr, $D = 4$, red dashed line), a model with higher $\dot{M}$ ($\dot{M} = 10^{-5.5}\ M_\odot$/yr, $D = 1$, green dashed line), and a model with lower $\dot{M}$ ($\dot{M} = 10^{-5.9}\ M_\odot$/yr, $D = 8$, pink dashed line). Different $\dot{M}$ values do not yield different Hα wings as long as the product $\dot{M}\sqrt{D}$ remains constant. However, we observed that other important lines like Hδ are sensitive these variations.

The chemical composition was estimated from unblended spectral lines for He, C, N, O and Si. The rest of the considered element abundances (see Table 4.4) were assumed solar following Asplund et al. (2009). The fit yielded moderate overabundance of He and N, together with underabundance of C and O. In all, there are indications of chemical evolution in the outer layers of the stellar atmosphere.

The photospheric microturbulent velocity ($\xi_{\rm ph}$) was adjusted using He I and Si IV lines. A higher $\xi_{\rm ph}$

induce stronger absorption in several spectral lines, as shown in Fig. 4.9.

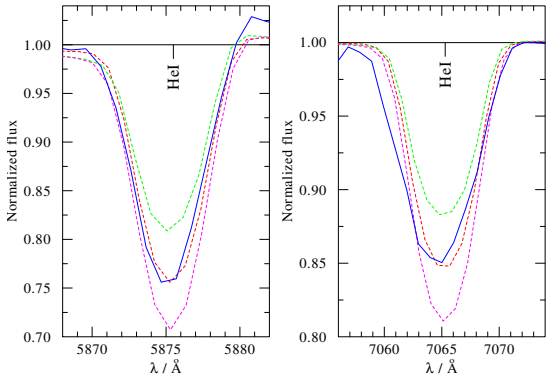

Figure 4.9.: Example of two He I lines in IGR J17544-2619, used in the $\xi_{\rm ph}$ estimation. As usual, the observation is plotted in solid blue line, and the best-fit model in red dashed line. Models with $\xi_{\rm ph}$ = 15,35 km/s are also presented (green and pink dashed lines respectively).

The $v_{\rm rot}$ and $v_{\rm mac}$ were roughly estimated using the width of the He lines. The derived projected rotational velocity is around 0.3 times the critical rotation velocity ($v_{\rm crit} = \sqrt{G\,M_\star R_\star^{-1}}$). This high rotational velocity may favour the chemical mixing, in line with the abundances derived in the fit.

To summarise, our NLTE analysis of optical and near IR spectra of IGR J17544-2619 showed that the optical O9I-type companion in this source is not peculiar and has stellar and wind parameters that are similar to other stars of the same spectral type, e.g. δ Ori (Shenar et al. 2015).

4.4.2. Vela X-1

Vela X-1 is one of the most studied HMXBs, since it is a bright source discovered in the early ages of the X-ray astronomy (Chodil et al. 1967). It is located at galactic coordinates $l = 263.06°$, $b = 3.93°$. The distance was estimated to be 1.9 ± 0.2 kpc by (Sadakane et al. 1985). The system has a moderate eccentricity of $e = 0.09$ (Bildsten et al. 1997), and orbital period $P_{\rm orb} = 8.96$ days (Kreykenbohm et al. 2008). The compact object is a neutron star that pulsates with $P_{\rm spin} = 283$s (McClintock et al. 1976). The optical companion HD 77581 (B0.5Iae) was identified by Vidal et al. (1973).

It is very likely that the wind of Vela X-1 is disturbed by the X-ray source. The photoionization produced close to the photosphere due to the intense X-ray luminosity might hinder the acceleration of the wind and generate a structure known as photoionization wake (Blondin et al. 1990; Krtička et al. 2015). This structure appears in the UV spectra as an additional absorption component at phases larger than $\phi \sim 0.5$ (Kaper et al. 1994). In addition, the hard X-rays light curves of the source in near-to-eclipse phases show asymmetries between ingress and egress, that have been interpreted as caused by the existence of this type of structure trailing the neutron star (Feldmeier et al. 1996). Moreover, a density enhancement in the line of sight during the second half of the orbit is also observed in the X-rays absorption, although the amount of absorbing material is highly variable from one orbit to another.

We derived $T_\star$ following the same procedure that we used for IGR J17544-2619. The obtained $T_{2/3}$ is similar to previous estimations: Sadakane et al. (1985) used the equivalent width (EW) of photospheric lines to estimate the effective temperature $T_{2/3} = 25000$ K; Fraser et al. (2010) used the TLUSTY code to estimate $T_{2/3} = 26500$ K.

For the fit of the SED, we used photometry from the 2MASS catalogue (Cutri et al. 2003) and the *Stellar Photometry in Johnson's 11-color system* (Ducati 2002), together with the IUE observations. We made an estimation of the reddening, distance and $R_{\rm V} \equiv A(V)/E_{B-V}$ by means of the SED fit. Then, we used the

estimation of the stellar radius $R_{2/3} = 31\,R_\odot$ from Joss & Rappaport (1984), and $T_{2/3}$ from the successive fits, in order to derive the luminosity (and the distance estimation) from the Stefan-Boltzmann law. Given that the obtained $T_{2/3}$ is very similar to previous estimations, the derived distance of 2.0 ± 0.2 is almost equal to the value d=1.9 kpc given by Sadakane et al. (1985). We show the results of the SED analysis in Fig. 4.10.

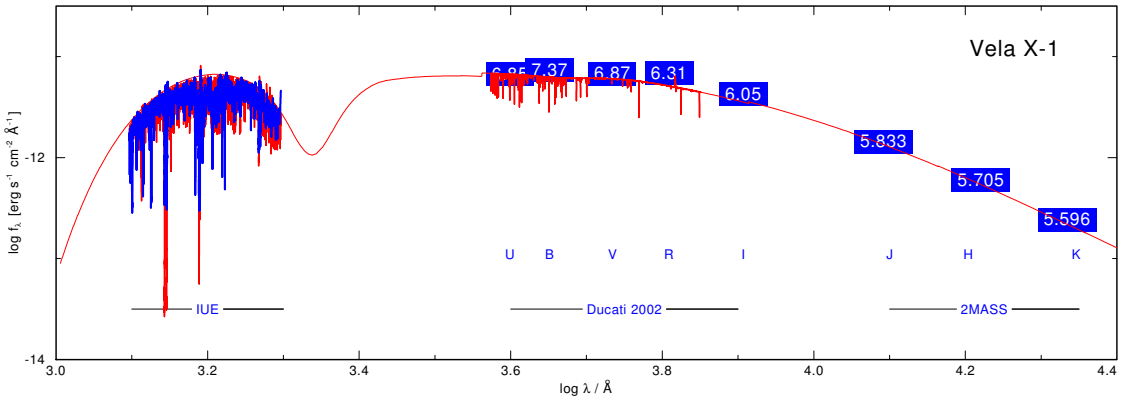

Figure 4.10.: Fit of the SED of Vela X-1. In red we plot the best fit model with the spectral lines in the domain where we have done the spectral analysis, and the continuum where we have available photometry (marked in blue). We cite the references used for the photometry. Note that the true continuum in the UV range do not correspond with the apparent continuum from the observation, due to the number of spectral lines in this domain. The employed values of extinction, distance and luminosity are shown in Table 4.3.

The estimation of g_{eff} was especially delicate in Vela X-1 because of its very low g_{eff}. A higher value beyond the error given in Table 4.3 has a strong effect in the overall spectrum and hinders a satisfying fit. The derived value enables a good fit, and it is in agreement with previous estimations (Fraser et al. 2010).

We used UV resonance lines to find v_∞. In Fig. 4.11 we show the Si IV resonance lines λ 1394,1403 Å, where the effect of v_∞ is very clear. Models with higher terminal velocities induce a shift towards the blue part of these spectral lines. The best description of the observations is achieved for v_∞ = 700 km/s. This value is in agreement with the estimation of van Loon et al. (2001): v_∞ = 600 km/s; and not too far from Watanabe et al. (2006), who estimated v_∞ = 1100 km/s using *Chandra* X-rays observations.

In contrast, it is in disagreement with the estimation of Dupree et al. (1980), namely v_∞ = 1700 km/s. These authors used a subset of the IUE observations used in this work, and considered the UV resonance lines Si IV and C IV in the X-ray eclipse phases to make their estimation. We have revisited our v_∞ estimation using only observations taken at orbital phases $\phi = 0.9 - 0.1$, in order to be able to directly compare to Dupree et al. (1980). In Fig. 4.12, we show the Si IV and C IV lines, as observed in the total averaged spectrum and the spectrum averaging over $\phi = 0.9 - 0.1$. C IV is almost the same in both cases. Then, the disagreement in the estimates of v_∞ does not come from orbital phase variations but from the omission of the impact of the X-rays in the stellar wind by Dupree et al. (1980). As we can see in Fig. 4.12, when we introduce X-rays in the models we are able to reproduce C IV without needing a high velocity, due to the significant enhancement of the population of C IV in the wind. We note that the X-ray radiation we are introducing in the models is an intrinsic radiation of the donor wind that is presumably produced in the shocks within the stellar wind itself (e.g. Krtička et al. 2009). This radiation is not coming from the neutron star, since the effects are also noticeable at eclipsing phases. The impact of the X-rays coming from the neutron star is a different and complex issue, and it has been already studied by other authors (Watanabe et al. 2006). Regarding the Si IV resonance lines, in Fig. 4.12 we show that high stellar wind velocities as derived by Dupree et al. (1980) do not fit, neither using the total averaged spectrum, neither using the

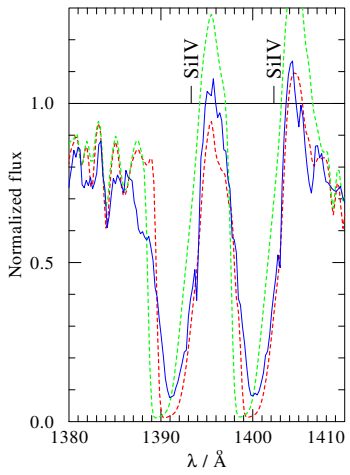

Figure 4.11.: Si IV lines used for the estimation of v_∞ in Vela X-1. It is showed the observation (blue solid line), the best-fit model (red dashed line) and a model with $v_\infty = 900$ km/s (green dashed line).

eclipsing phases spectrum.

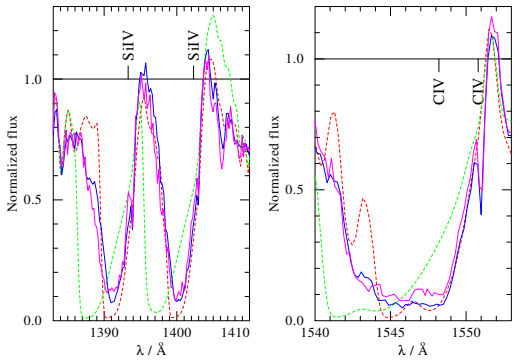

Figure 4.12.: Si IV and C IV resonance lines. We plot the total averaged spectrum (blue solid line) and the averaged spectrum over orbital phases $\phi = 0.9-0.1$ (pink solid line). We also plot the best-fit model ($v_\infty = 700$, red dashed line), and a model with $v_\infty = 1400$ km/s (green dashed line).

The value $\dot{M}\sqrt{D}$ was estimated using Hα (see Fig. 4.13). We did not find a good fit of the blue wing of the line, observed in absorption, but our model properly fits the emission in the red wing of the spectral line. Unfortunately, we do not have more optical observations covering further orbital phases in order to check whether Hα is variable. Nevertheless, previous studies of similar sources demonstrate that this might be the case: González-Galán (2015) reported the variability of Hα in the very similar B0Iaep optical companion in the SGXB system XTE J1855-026. Moreover, the shape of Hα in XTE J1855-026 at $\phi = 0$ (see Fig. 5.12 in González-Galán 2015), when the neutron star is hidden behind the optical counterpart, is strongly reminiscent of the shape that our model reproduces in Fig. 4.13. Hence, the relative disagreement between our best-fit model and our observation of Vela X-1 (taken at $\phi = 0.68$), might be produced by some kind of interaction of the neutron star with the donor and/or the stellar wind, which is not possible to model

using the assumption of spherical symmetry that PoWR employs. This disagreement might be related to similar features observed in other strong lines, as further discussed in Sect. 4.5.3.

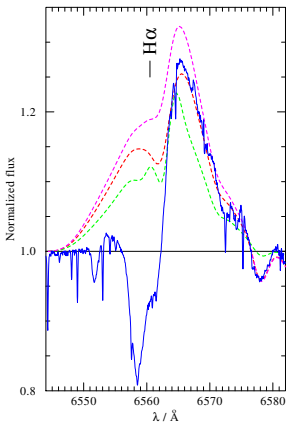

Figure 4.13.: Hα line for the estimation of $\dot{M}\sqrt{D}$ in Vela X-1. We can see the observation (blue solid line), the best-fit model (red dashed line), a model with 0.8 times the $\dot{M}\sqrt{D}$ value of the best fit (green dashed line), and a model with 1.2 times the $\dot{M}\sqrt{D}$ value of the best fit (pink dashed line).

We derived $\dot{M}$ and D from the Al III resonance lines λ1855 and λ1863Å. As we can see in Fig. 4.14, the variation of $\dot{M}$ (and consequently D) directly affect these lines. Higher (lower) $\dot{M}$ enhances (reduces) the density of the stellar wind, producing too strong (weak) absorption.

Unfortunately, other resonance lines available in the spectrum (N V, C IV and Si IV) are saturated in the models within a reasonable range of parameters around the best-fit, and consequently are not suitable for the $\dot{M}$ diagnosis. Interestingly, in contrast to the models, the N V and Si IV resonance lines are slightly desaturated in the observations (see Fig. 4.15). The origin of this phenomenon might be related to the presence of optically thick clumps (macroclumping), which directly affects the mass-loss rate estimations (Oskinova et al. 2007; Šurlan et al. 2012). Undoubtedly, its study deserves further investigation, which is beyond the scope of this work.

Based on the X-ray data analysis, Manousakis & Walter (2015) have suggested that the velocity law with the parameter $\beta = 0.5$ fits better with the X-ray light curve of the system in near-to-eclipse phases. However, a satisfying fit is not possible when we assume $\beta = 0.5$. We have tried models using $\beta = 0.5$ and adapting $\dot{M}\sqrt{D}$ in order to fit Hα. However, as shown in Fig. 4.16, Hα in our observation is not compatible with $\beta = 0.5$. As we mentioned above, Hα might suffer from important variability along the orbit. Moreover, the X-ray irradiation from the neutron star might produce variations in the stellar wind. In our opinion, this might be the cause of the apparent disagreement between the conclusions extracted from the X-rays and the optical wavebands.

The chemical composition was estimated following the same approach as it was done for IGR J17544-2619. Interestingly, we found again indications of chemical evolution in the star, given the moderate overabundance of He and N, together with the underabundance of C and O (see Table 4.4).

We adopted the value of $v_{\rm rot} \sin i = 56$ km/s derived by Fraser et al. (2010). Previous estimations pointed to much higher values around 115 km/s (Zuiderwijk 1995; Howarth et al. 1997), but such a high rotational velocity is not compatible with some of the lines that we see unblended in the optical observation (see Fig. 4.17). The rotational velocity directly affects the estimation of the neutron star mass ($M^{\rm NS}_{\rm Vela\,X\text{-}1}$) from radial velocity curves, as shown by Koenigsberger et al. (2012). If $v_{\rm rot} \sin i = 56$ km/s, it is feasible that $M^{\rm NS}_{\rm Vela\,X\text{-}1} \sim 1.5\,M_\odot$, close to the canonical value ($1.4\,M_\odot$), instead of a high mass neutron star $M^{\rm NS}_{\rm Vela\,X\text{-}1} \gtrsim 1.8\,M_\odot$, as suggested by other authors (e.g. Quaintrell et al. 2003; Barziv et al. 2001).

To summarise, our new analysis of Vela X-1 is in broad agreement with previous studies of this system.

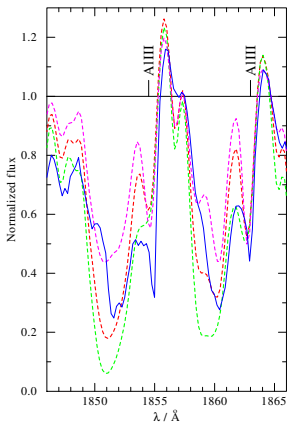

Figure 4.14.: Al III resonance lines λ1855 and λ1863Å, employed for the $\dot{M}$ estimation in Vela X-1. We show the observation (solid blue line), the best-fit model ($\dot{M} = 10^{-6.2}\ M_\odot$/yr, $D = 11$, red dashed line), a model with higher $\dot{M}$ ($\dot{M} = 10^{-5.8}\ M_\odot$/yr, $D = 2$, green dashed line), and a model with lower $\dot{M}$ ($\dot{M} = 10^{-6.3}\ M_\odot$/yr, $D = 20$, pink dashed line).

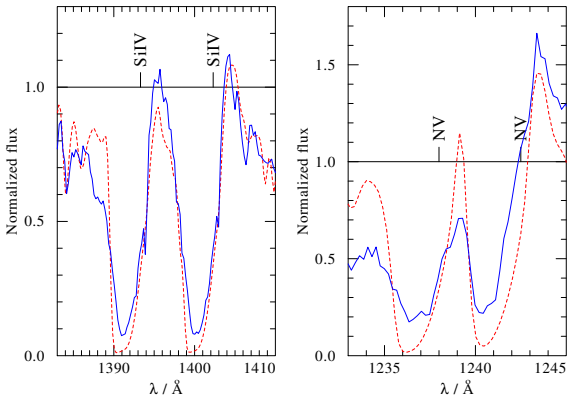

Figure 4.15.: Si IV and N V resonance lines in Vela X-1. While the observations show slight desaturation, all the models within a reasonable parameter space around the best-fit model produce saturated lines.

We find a rather low stellar wind velocity, while $\dot{M}$ is typical for the stars of its spectral type. Like other studies, we note spectral line variability in dependence with orbital phase, and attribute it to the influence of the X-rays and the compact object on the stellar wind.

The final physical parameters of the the two sources obtained in this work are shown in Table 4.3.

4.5. Discussion

4.5.1. Wind-fed accretion

In SFXTs and SGXBs, the X-ray emission is powered by the accretion of matter from the donor's wind onto the compact object. The efficiency of the conversion of the potential energy into X-ray luminosity

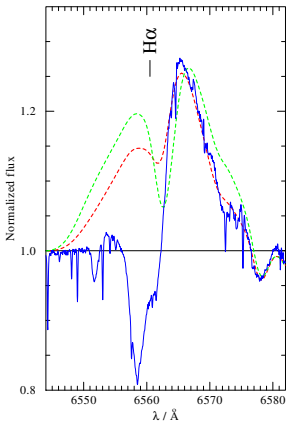

Figure 4.16.: Hα used the estimation of the parameter β in Vela X-1. We present the observation (solid blue line), the best-fit model ($\beta = 1.0$, red dashed line), and a model with $\beta = 0.5$ (green dashed line), as proposed by Manousakis & Walter (2015).

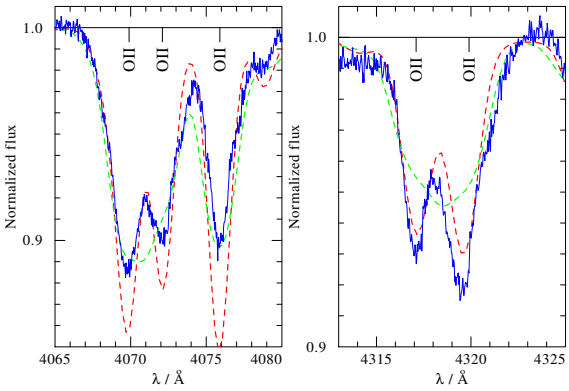

Figure 4.17.: Example of unblended lines in the spectrum of Vela X-1. In red we plot a model with $v_{\rm rot} \sin i = 56$ km/s. In green we plot a model with $v_{\rm rot} \sin i = 116$ km/s.

depends on many factors including the properties of the stellar wind, the properties of the compact object and the orbital separation.

The most efficient way of producing X-rays is the so called direct accretion: the stellar wind that is gravitationally captured by the neutron star free-falls onto the compact object. The expected luminosity is close to the accretion luminosity $L_{\rm acc}$. The following equations contain the most relevant parameters in this regime:

$$R_a = \frac{2GM_{\rm NS}}{v_{\rm rel}^2} \tag{4.2a}$$

$$f_a = \frac{R_a^2}{4a^2} \tag{4.2b}$$

$$L_{\rm acc} = f_a \frac{GM_{\rm NS}\dot{M}}{R_{\rm NS}} \tag{4.2c}$$

where R_a is the accretion radius (also called Bondi radius), that is to say, the maximum distance to the neutron star where the stellar wind is able to avoid falling onto the compact object; G is the gravitational

Parameters	J17544-2619	Vela X-1
$P_{\rm orb}$ (d)	4.9[a]	8.964357[b]
$P_{\rm spin}$ (s)	71.49[c], 11.58[d]	283.532[b]
$a \sin i$ (lt-s)	-	113.89[b]
i (deg)	-	> 73[e]
a (10^{12}cm)	2.6[j]	3.5[k]
a ($R_\star$)	1.9	1.8
e	< 0.25[a,i]	0.09[f]
B (G)	1.45[g] $\times 10^{12}$	2.6[h] $\times 10^{12}$

Notes. Parameters used in Sect. 4.5.
References: (a) Clark et al. (2009) (b) Kreykenbohm et al. (2008) (c) Drave et al. (2012) (d) Romano et al. (2015) (e) van Kerkwijk et al. (1995) (f) Bildsten et al. (1997) (g) Bhalerao et al. (2015) (h) Kreykenbohm et al. (2002) (i) this work. (j) From $P_{\rm orb}$, total mass of the system and the 3rd Kepler's law. (k) From $a \sin i$, and the average $\langle \sin i \rangle = 0.985$ over $i > 73°$.

constant; $M_{\rm NS}$ is the mass of the neutron star, which in this work is hereafter assumed to be the canonical value 1.4 $M_\odot$; R_{NS} is the radius of the neutron star, which in this work is henceforward assumed to be 12 km (Lattimer & Steiner 2014); $v_{\rm rel}$ is the velocity of the wind relative to the neutron star; f_a is the fraction of stellar wind that is gravitationally captured by the neutron star; a is the orbital distance and $L_{\rm acc}$ is the accretion luminosity, namely, the luminosity that would arise if the whole potential energy of the accreted matter is eventually transformed in X-ray luminosity.

For IGR J17544-2619, using the results of our spectral fitting, the data shown in Table 4.5.1 and assuming a circular orbit, we obtain from Eq. 4.2c:

$$L_{\rm acc} = 1.4 \cdot 10^{36} \text{ erg/s}$$

The value of $L_{\rm acc}$ is 1-2 orders of magnitude higher than the luminosity that the source exhibits most of the time: $L_{\rm X} < 5 \cdot 10^{34}$ erg/s (Bozzo et al. 2015). Most likely, some inhibition mechanism is acting in IGR J17544-2619 (Drave et al. 2014; Bozzo et al. 2008).

As a possible explanation for the variability of IGR J17544-2619 and its lower-than-expected luminosity at quiescence, Bozzo et al. (2008) discussed the application of their model to the light curve of an outburst observed by *Chandra*. This theoretical framework describes the mechanisms for the inhibition of the accretion according to the relative size of the spheres defined by $R_{\rm a}$, $R_{\rm M}$ and $R_{\rm co}$; where $R_{\rm a}$ is the already defined accretion radius, $R_{\rm M}$ is the magnetospheric radius (location where the pressure exerted by the gas equals the local magnetic pressure), and $R_{\rm co}$ is the co-rotation radius (location where the angular velocity of the neutron star equals the Keplerian velocity). These radii, in turn, depend on: $\dot{M}$, $v_{\rm rel}$, magnetic moment of the neutron star (μ), orbital separation (a) and $P_{\rm spin}$.

For simplicity, the orbital velocity of the neutron star and the eccentricity are not considered in the model by Bozzo et al. (2008). That is to say, it is assumed that $e = 0$ and $v_{\rm wind} \simeq v_{\rm rel}$, where $v_{\rm wind}$ is the stellar wind velocity in the position of the neutron star. We note that when the stellar wind velocity is not very high, this assumption might not be accurate. Indeed, the orbital velocity ($v_{\rm orb}$) in Vela X-1 is very similar to $v_{\rm wind}$ (see Table 4.5.1). In IGR J17544-2619, the orbital velocity is around the half of the stellar wind velocity. Despite these simplifications, the model provides significant insight on the explanation of the qualitative behavior of the sources with regard to their persistence or variability, as it is shown next in this section. A more accurate approach considering eccentric orbits and the orbital velocity of the compact object would be an important advance in the model, but it is out of the scope of this paper.

Nowadays, the tentative estimations of the spin period in IGR J17544-2619 ($P_{\rm spin} = 71.49$s by Drave et al. (2012) and alternatively $P_{\rm spin} = 11.58$s by Romano et al. 2015), along with the stellar wind parameters derived in this work, permit to discuss the application of the model by Bozzo et al. (2008) from a new

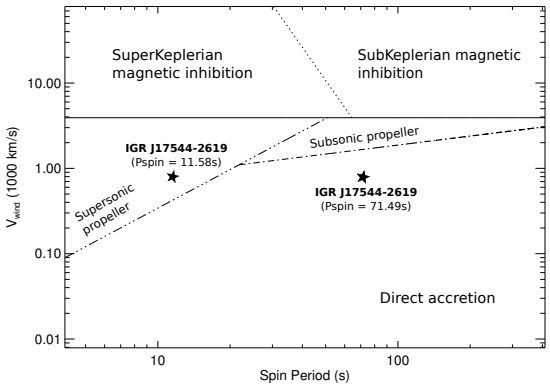

Figure 4.18.: Position of IGR J17544-2619 in the $v_{\rm wind}$-$P_{\rm spin}$ diagram for the two tentative estimations of $P_{\rm spin}$. Equations 25, 26, 27 and 28 by Bozzo et al. (2008) are represented by a solid, dotted, triple-dot-dashed and dot-dashed lines respectively.

perspective. The rest of parameters required for this section are shown in Table 4.5.1. Using those values, we can elaborate diagrams $v_{\rm wind}$-$\dot{M}$ and $v_{\rm wind}$-$P_{\rm spin}$, where the different accretion regimes occupy different domains of the space of parameters. These domains directly arise from the Eq. 25-28 by Bozzo et al. (2008).

In Fig. 4.18 we show the position of IGR J17544-2619 in the diagram $v_{\rm wind}$-$P_{\rm spin}$ for the two currently available tentative estimations of the $P_{\rm spin}$. The source lie in the direct accretion regime for $P_{\rm spin}$ = 71.49s, and in the supersonic propeller regime for $P_{\rm spin}$ = 11.58s. Hence, the shortest $P_{\rm spin}$ = 11.58s matches better with the X-ray behavior of the source and its likelihood of staying in an inhibited accretion regime.

In Fig. 4.19 we show the location of IGR J17544-2619 in the diagram $v_{\rm wind}$-$\dot{M}$. It is important to note that the position of the system in this diagram is not a fixed point due to the the intrinsic variability of the velocity and local density of the stellar wind in hot massive stars. Thus, we have plotted a red region in Fig. 4.19 showing a variability of one order of magnitude in $v_{\rm wind}$ and $\dot{M}$. That is to say, the maximum $\dot{M}$ and $v_{\rm wind}$ in the encircled region is ten times higher than the minimum $\dot{M}$ and $v_{\rm wind}$. Such a variability is fully plausible, as demonstrated by hydrodynamical simulations of radiatively driven stellar winds (e.g. Feldmeier et al. 1997). These clumps of higher density, intrinsic to stellar winds of hot stars, are sometimes invoked to explain the X-ray variability of HMXBs (Oskinova et al. 2012). As we can see in Fig. 4.19, the encircled region intersects regimes of direct accretion and inhibited accretion. Hence, it is possible that in objects like IGR J17544-2619, the abrupt changes in the wind density may lead to the switching from one accretion regime to the other. Moreover, besides the clumping of the stellar wind, the eccentricity of the orbit ($e < 0.25$) would lead to additional variations in the orbital separation (and consequently in $v_{\rm wind}$ and the density of the medium), which reinforce the intrinsic variability of the stellar wind and its capability to lead to transitions across regimes.

Considering an alternative explanation for the X-ray variability of IGR J17544-2619, Drave et al. (2014) invoked the quasi-spherical accretion model by Shakura et al. (2012). However, if the spin period is actually as short as 71.49s or 11.58s, the condition of a slowly rotating pulsar, i.e. $R_M \ll R_{co}$ (where R_M is the magnetospheric radius and R_{co} the co-rotation radius), assumed by this approach, would be debatable. Even though it raises doubts about the feasibility of applying this model, it cannot be ruled out until the spin period and the magnetic field of the neutron star are firmly constrained.

In the case of Vela X-1, we can see in Fig. 4.20 and 4.21, the source is well in the middle of the zone where direct accretion is expected. Hence, more extreme density or velocity jumps would be required to trigger any change of accretion regime. These extreme jumps are also plausible, but much more unlikely. However, they might sporadically occur and lead to a sudden decrease of the luminosity in Vela X-1.

Using the parameters shown in Table 4.5.1 and Eq. 4.2c, we obtain $L_{\rm acc} = 8.7 \times 10^{36}$ erg/s for Vela X-1. The average X-rays luminosity of the source is $\langle L_{\rm X} \rangle \simeq 4.5 \times 10^{36}$ (Sako et al. 1999). More specifically, $L_{\rm acc} \simeq 0.5 \times \langle L_{\rm X} \rangle$. This means that there is a good agreement between $L_{\rm acc}$ and $L_{\rm X}$, which implies that the direct accretion scenario can describe the way that matter is accreted in Vela X-1.

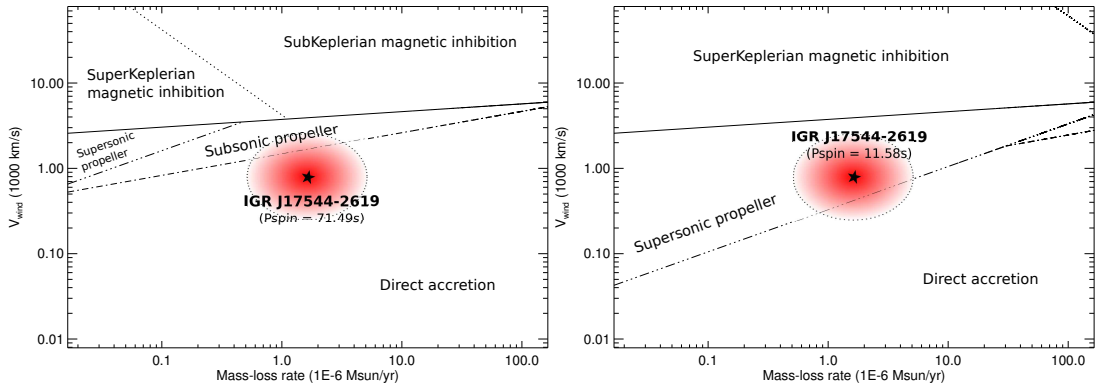

Figure 4.19.: Position of IGR J17544-2619 in the $v_{\rm wind}$-$\dot{M}$ diagram. Upper panel: diagram calculated using $P_{\rm spin}$ = 11.58s. Lower panel: diagram calculated using $P_{\rm spin}$ = 71.49s. The dashed line encircles the space within one order of magnitude of $v_{\rm wind}$ and $\dot{M}$. Equations 25, 26, 27 and 28 by Bozzo et al. (2008) are represented by a solid, dotted, triple-dot-dashed and dot-dashed lines respectively.

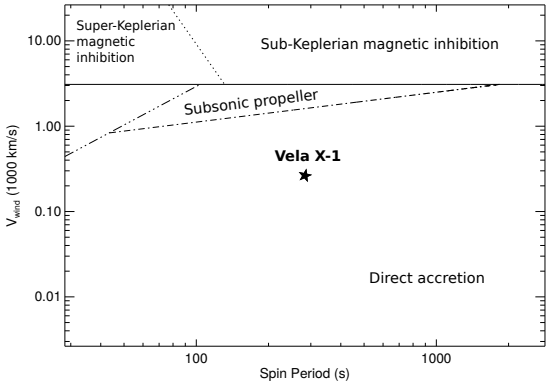

Figure 4.20.: Position of Vela X-1 in the $v_{\rm wind}$-$P_{\rm spin}$ diagram. The dashed line encircles the space within one order of magnitude of $v_{\rm wind}$ and $\dot{M}$. Equations 25, 26, 27 and 28 by Bozzo et al. (2008) are represented by a solid, dotted, triple-dot-dashed and dot-dashed lines respectively.

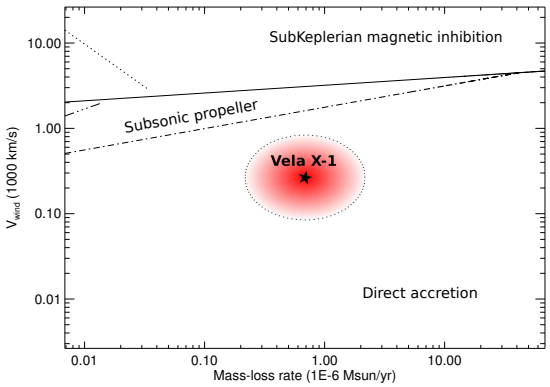

Figure 4.21.: Position of Vela X-1 in the $v_{\rm wind}$-$\dot{M}$ diagram. Equations 25, 26, 27 and 28 by Bozzo et al. (2008) are represented by a solid, dotted, triple-dot-dashed and dot-dashed lines respectively.

The framework of different accretion regimes described by Bozzo et al. (2008) is able to explain why

IGR J17544-2619 is prone to show a high X-ray variability and inhibited accretion (assuming the shortest $P_{\rm spin}$ = 11.58s), and Vela X-1 is persistently very luminous in the X-rays. As exposed in Fig. 4.19 and 4.21, the required variability in the stellar wind for a transition in the accretion regime is far lower in IGR J17544-2619 than in Vela X-1. The main ingredients that make the sources so different are the $P_{\rm spin}$ (shorter in IGR J17544-2619), and the $v_{\rm wind}$ (larger in IGR J17544-2619).

We may conjecture whether this theoretical framework can be applied to other SGXBs and SFXTs. Unfortunately there are not many sources where we can find complementary studies including dedicated analysis of the stellar wind, orbital parameters and neutron star parameters. The studies of the stellar wind are specially scarce. Besides the two sources analysed in this work, there are at least four where a comparable amount of information is available in the literature. They are IGR J11215-5952, GX 301-2, X1908+075 and OAO 1657-415. We show the diagrams $v_{\rm wind}$-$P_{\rm spin}$ and $v_{\rm wind}$-$\dot{M}$ for these sources in Appendix A.1. Again, the diagrams seem to qualitatively explain the behavior of the systems. GX 301-2, X1908+075 and OAO 1657-415 are persistent SGXBs, and they occupy regions of highly likelihood of persistent emission in the diagrams. In contrast, the likelihood of regime transitions in IGR J11215-5952 is much higher.

IGR J11215-5952 is a system with very large eccentricity and long orbital period (Romano et al. 2009). It shows recurrent flares with a period of $\sim$ 330d (Sidoli et al. 2006). Its high variability leads to its classification as a SFXT, even though the predictability of the flares is not a common feature in the rest of SFXTs. Sidoli et al. (2007) proposed that the recurrent flares might be explained by an additional equatorial component of the stellar wind combined with the highly eccentric orbit. In Figure A.1 we can see that a moderate clumpiness would lead to frequent transition regimes, and hence it would be expected a very high X-rays variability. However, the diagram shown in Figure A.1 is calculated assuming a circular orbit, which is not accurate for IGR J11215-5952. In this source, the high eccentricity of the system might be a more important factor than the clumpiness of the wind, and the transition into the direct accretion regime might be likely only during near-periastron passages, producing periodic outbursts.

Regarding other systems, the framework used here might encounter problems to explain the behavior of other SFXTs with larger $P_{\rm spin}$ such as IGR J16418-4532 ($P_{\rm spin}$ = 1212s, Sidoli et al. 2012) and IGR J16465-4507 ($P_{\rm spin}$ = 228s, Lutovinov et al. 2005). The estimation of the stellar wind parameters in these systems will be very useful to measure the extent of the applicability of the model by Bozzo et al. (2008) explaining the dichotomy between SGXBs and SFXTs. Moreover, studies of the X-rays absorption might provide an additional perspective on the issue. Giménez-García et al. (2015) studied a sample of SGXBs and SFXTs using XMM-Newton and it was observed that the SGXBs included in the sample were in general more absorbed than the SFXTs. This may suggest a more intense interaction of the X-rays radiation with the stellar wind, or, alternatively, that the neutron star orbits a more dense medium in SGXBs due to a closer orbit or a slower stellar wind of the donor.

Finally, we can compare the v_∞ and the $v_{\rm esc}$ that we obtain from the fits. In this regard, Lamers et al. (1995) collected a large dataset from hot stars with radiatively driven winds, and concluded that the ratio $v_\infty/v_{\rm esc}$ steeply decreases from $\sim$ 2.6 to $\sim$ 1.3 when going from high to low $T_{\rm eff}$ at a point near $T_{\rm eff} \simeq 21000$ K, corresponding to spectral type around B1. According to Vink et al. (1999), this drop is caused by a decrease in the line acceleration of Fe III in the subsonic part of the wind. In our case we have (see Table 4.3):

- IGR J17544-2619 (O9.5I): $v_\infty/v_{\rm esc} = 2.4^{+0.7}_{-0.5}$
- Vela X-1 (B0.5I): $v_\infty/v_{\rm esc} = 1.6^{+0.8}_{-0.4}$

These values follow the trend observed and described by Lamers et al. (1995). We suggest that it might be the reason why IGR J17544-2619 shows higher v_∞ than Vela X-1. The action of the X-rays can also make an important impact in the velocity of the stellar wind, as shown by Karino (2014). However, this effect is probably local, since we do not observe important differences in the terminal velocity between eclipsing and non-eclipsing orbital phases in Vela X-1. Secondary features like asymmetries or additional absorption components in the spectral lines, which might be related to the effect of the X-rays in the stellar wind, are described and discussed below in Sect. 4.5.3.

4.5.2. Evolutionary tracks

In Fig. 4.22 we show the position of Vela X-1 and IGR J17544-2619 in the Hertzprung-Russell Diagram (HRD), and the evolutionary tracks from the Geneva Stellar Models (Ekström et al. 2012). The two stars lie on the theoretical track of a star with initial mass $\sim 25-30\,M_{\odot}$. In IGR J17544-2619 the spectroscopic mass obtained from the fits is compatible with the evolutionary mass. Vela X-1 shows certain overluminosity, since its spectroscopic mass is lower than the evolutionary mass. Nevertheless, the mass of the star obviously decreases along its lifetime due to the stellar wind and possible mass transfer episodes. These phenomena might have been stronger or longer in Vela X-1 compared to IGR J17544-2619.

The overabundance of helium and nitrogen arising from the fits in the two stars might trigger an increase in luminosity following the scaling relation $L \propto \mu^{\alpha}$, where μ is the average mean molecular weight and $\alpha > 1$ (Langer 1992). Then, we expect certain overluminosity in both sources. However, as already mentioned, the overluminosity is more noticeable in Vela X-1. In all, the sources seem to be in a different evolutionary stage or to have experienced a different evolutionary history.

The chemical evolution of the donors might have been driven by episodes of important mass transfer in the past, given the close orbits of the systems, enhancing the helium and nitrogen abundances due to the accretion of chemically enriched material (Langer 2012). Moreover, Roche-lobe overflow stages induce important spin-up in the mass gainer (Packet 1981), inducing further chemical enrichment because of rotational mixing. This scenario is supported by the observation of other HMXBs where indications of nitrogen enhancement are also observed (González-Galán et al. 2014).

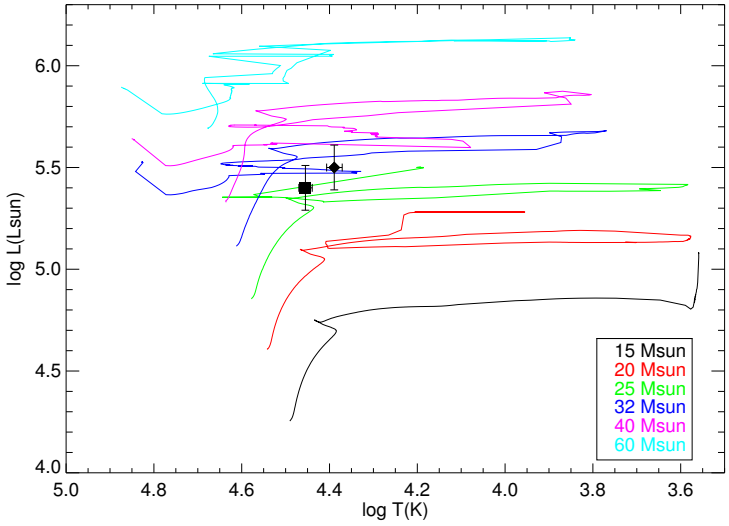

Figure 4.22.: Evolutionary tracks from the Geneva Stellar Models with solar abundances and rotation. The positions of IGR J17544-2619 (square) and Vela X-1 (diamond) are overplotted.

4.5.3. Asymmetries in spectral lines of Vela X-1

Some of the lines in the spectrum of Vela X-1 show clear asymmetries that are not possible to reproduce with spherically symmetric models like PoWR (see Fig. 4.23). This striking feature is specially noticeable for He I lines, but it is also observed in C, N, O or Si, whenever the lines are strong enough.

Asymmetries in spectral lines were also reported by Martínez-Núñez et al. (2015) in hydrogen lines of the infrared spectrum of X1908+75, a SGXB. A natural explanation for the discrepancy between models

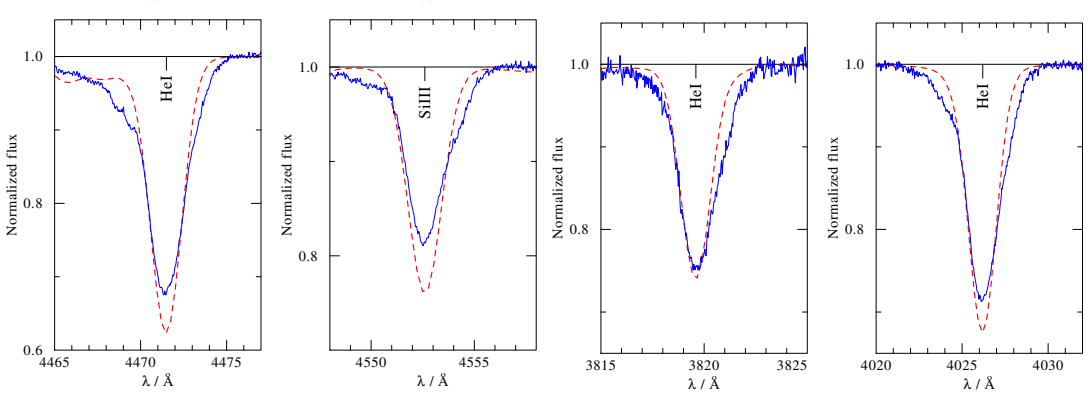

Figure 4.23.: Example of four spectral lines showing notable asymmetries: He I λ3820, 4026, 4471 Å, and Si III λ4553 Å.

and observations is the departure of the donor and/or the surrounding medium from the spherical symmetry. This departure may be triggered by tidally induced effects and the persistent X-ray irradiation of the stellar wind and the stellar surface. In this regard, Koenigsberger et al. (2012) showed that tidal effects would produce asymmetries in the line profiles.

The observed asymmetries might be related to the additional absorption that we observe in the blue part of other important lines, with special attention to Hα, Hβ, Hγ and Si IV λ 1394,1403 Å (see Fig. 4.24). Assuming that the absorption is produced by an independent component of matter moving at certain velocity, it is striking that the involved velocities required for explaining such a blueshif are different depending on the lines: $\sim 200 - 300$ km/s in Hα, Hβ and Hγ, ~ 1000 km/s in the Si IV resonance lines.

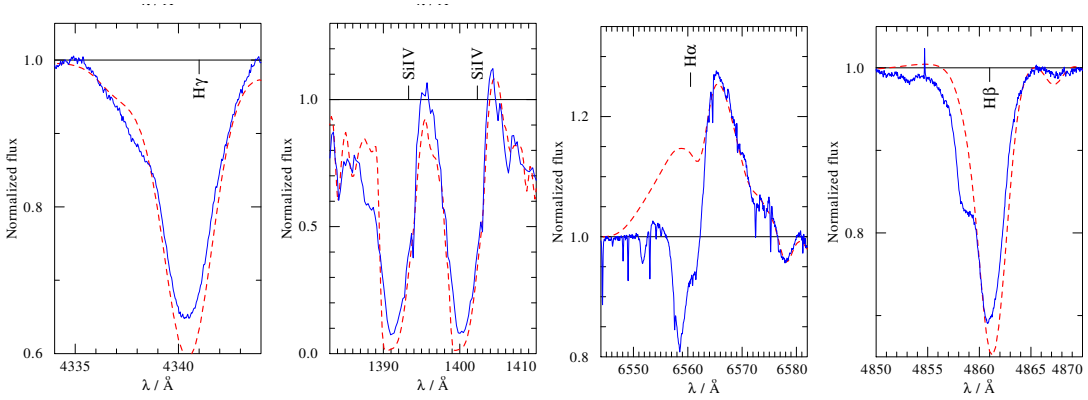

Figure 4.24.: Hα, Hβ, Hγ and Si IV λ1394,1403 Å. The observations (blue solid line) shows an additional blueshifted component that we are not able to reproduce with the models (red dashed line).

In any case, we note that these asymmetries and additional absorption features have not been observed in IGR J17544-2619. Hence, the physical cause at work is playing a significantly more important role in Vela X-1 than in IGR J17544-2619. This fact suggests that the interaction of the X-ray source with the stellar wind might be fundamental for understanding these asymmetries, given that the X-rays are on average more intense in Vela X-1. Indeed, if we compare the wind mechanic luminosity $L_{\rm mech} = \dot{M}\, v_\infty^2/2$ to the X-ray luminosity $L_{\rm X}$ we obtain:

- IGR J17544-2619: $L_{\rm mech} \simeq 10^{36}$ erg/s. That is to say, at least two orders of magnitude higher than the usual X-ray luminosity of the source.
- Vela X-1: $L_{\rm mech} \simeq 10^{35}$ erg/s. Namely, about one order of magnitude lower than the X-ray luminosity of the source in quiescence.

Hence, there is a fundamental difference in the ratio $L_{\rm mech}/L_{\rm X}$. The X-rays are much more powerful with respect to the stellar wind in Vela X-1 rather than in IGR J17544-2619. We suggest that this fact might be related to the asymmetries that we observe in the spectral lines of Vela X-1, but not in IGR J17544-2619.

4.6. Summary and conclusions

We have performed a detailed analysis of the donors of the HMXBs IGR J17544-2619 and Vela X-1, using the code PoWR that computes models of hot stellar atmospheres. We found the luminosity, extinction, stellar mass, stellar radius, effective temperature, effective surface gravity, terminal velocity of the stellar wind, mass-loss rate, clumping factor, micro and macro-turbulent velocity, rotational velocity and chemical abundances.

The estimation of the above mentioned parameters has implications on other physical parameters of the system: the derived stellar radius of IGR J17544-2619 implies an upper limit in the eccentricity of the source: $e < 0.25$. The rotational velocity derived for Vela X-1 implies that the mass of the neutron star might be $M^{\rm NS}_{\rm Vela\,X\text{-}1} \sim 1.5\,M_{\odot}$, close to the canonical value ($1.4\,M_{\odot}$).

The donors of IGR J17544-2619 and Vela X-1 are similar in many of the parameters that physically characterise them and their spectrum. Moreover, they are also comparable in the eccentricity and orbital separation. However, in the context of accretion regimes described by Bozzo et al. (2008), their moderate differences in the stellar wind velocity and the $P_{\rm spin}$ of the neutron star lead to a very different accretion regimes of the sources, which qualitatively explain their completely different X-ray behavior. After analysing other sources with sufficient information available in the literature, we have observed that the same theoretical framework is valid to qualitatively explain their X-ray behavior. Further explorations addressing the estimation of the stellar wind properties of the donors in SGXBs and SFXTs, complemented with $P_{\rm spin}$ measurements in SFXTs, will be necessary to confirm whether the conclusions exposed here can be extrapolated to additional members of these groups of HMXBs.

In summary, this study shows that the wind terminal velocity play a decisive role in determining the class of HMXB hosting a supergiant donor. While low stellar wind velocity facilitates direct steady accretion in SGXBs, the high wind velocity and velocity jumps can easily shift the accretion mechanism from direct accretion to propeller regimes in SFXTs. This effects might be enhanced by other factors such as the eccentricity of the sources. We conclude that this is one of the mechanisms responsible for these two major sub-classes of HMXBs with supergiant donors.

Acknowledgments. The work of AG-G has been supported by the Spanish MICINN under FPI Fellowship BES-2011-050874 associated to the project AYA2010-15431. T.S. is grateful for financial support from the Leibniz Graduate School for Quantitative Spectroscopy in Astrophysics, a joint project of the Leibniz Institute for Astrophysics Potsdam (AIP) and the Institute of Physics and Astronomy of the University of Potsdam. This work has been partially supported by the Spanish Ministry of Economy and Competitiveness project numbers ESP2013-48637-C2-2P and ESP2014-53672-C3-3-P, the Generalitat Valenciana project number GV2014/088 and the Vicerectorat d'Investigació, Desenvolupament i Innovació de la Universitat d'Alacant under grant GRE12-35. We wish to thank Thomas E. Harrison for his important contribution to the paper reducing the SpeX data. We also thank S. Popov for a very useful discussion. The authors gratefully acknowledge the constructive comments on the paper given by the anonymous referee. SMN thanks the support of the Spanish Unemployment Agency, allowing her to continue her scientific collaborations during the critical situation of the Spanish Research System. The authors acknowledge the help of the International Space Science Institute at Bern, Switzerland, and the Faculty of the European Space Astronomy Centre. A.S. is supported by the Deutsche Forschungsgemeinschaft (DFG) under grant HA 1455/26. Some of the data presented in this paper were obtained from the Multimission Archive at the Space Telescope Science Institute (MAST). STScI is operated by the Association of Universities for Research in Astronomy, Inc., under NASA contract NAS5-26555. Support for MAST for non-HST data is provided by the NASA Office of Space Science via grant NAG5-7584 and by other grants and contracts. This

publication makes use of data products from the Two Micron All Sky Survey, which is a joint project of the University of Massachusetts and the Infrared Processing and Analysis Center/California Institute of Technology, funded by the National Aeronautics and Space Administration and the National Science Foundation.

Chapter 5.

The Tarantula Massive Binary Monitoring: II. First SB2 orbital and spectroscopic analysis for the Wolf-Rayet binary R 145 (Manuscript IV)

T. Shenar, R. N. D. Richardson, D. Sablowski,R. Hainich, A. F. J. Moffat, H. Todt, H. Sana, W.-R. Hamann, L. M. Oskinova, A. Sander, F. Tramper, N. Langer, A. Z. Bonanos, S. E. de Mink, G. Gräfener, P. A. Crowther, J. S. Vink, L. A. Almeida, A. de Koter, R. Barbá, A. Herrero, C. J. Evans, K. Ulaczyk

Astronomy & Astrophysics, 2017, Volume 598, 16 pp.

Abstract

We present the first SB2 orbital solution and disentanglement of the massive Wolf-Rayet binary R 145 ($P = 159$ d) located in the Large Magellanic Cloud. The primary was claimed to have a stellar mass greater than 300 $M_\odot$, making it a candidate for the most massive star known. While the primary is a known late type, H-rich Wolf-Rayet star (WN6h), the secondary could not be so far unambiguously detected. Using moderate resolution spectra, we are able to derive accurate radial velocities for both components. By performing simultaneous orbital and polarimetric analyses, we derive the complete set of orbital parameters, including the inclination. The spectra are disentangled and spectroscopically analyzed, and an analysis of the wind-wind collision zone is conducted.

The disentangled spectra and our models are consistent with a WN6h type for the primary, and suggest that the secondary is an O3.5 If*/WN7 type star. We derive a high eccentricity of $e = 0.78$ and minimum masses of $M_1 \sin^3 i \approx M_2 \sin^3 i = 13 \pm 2\,M_\odot$, with $q = M_2/M_1 = 1.01 \pm 0.07$. An analysis of emission excess stemming from a wind-wind collision yields a similar inclination to that obtained from polarimetry ($i = 39 \pm 6°$). Our analysis thus implies $M_1 = 53^{+40}_{-20}$ and $M_2 = 54^{+40}_{-20}\,M_\odot$, excluding $M_1 > 300\,M_\odot$. A detailed comparison with evolutionary tracks calculated for single and binary stars, as well as the high eccentricity, suggest that the components of the system underwent quasi-homogeneous evolution and avoided mass-transfer. This scenario would suggest current masses of $\approx 80\,M_\odot$ and initial masses of $M_{\mathrm{i},1} \approx 105$ and $M_{\mathrm{i},2} \approx 90\,M_\odot$, consistent with the upper limits of our derived orbital masses, and would imply an age of ≈ 2.2 Myr.

5.1. Introduction

There are ever growing efforts to discover the most massive stars in the Universe (e.g., Massey & Hunter 1998; Bonanos et al. 2004; Schnurr et al. 2008a; Bestenlehner et al. 2011; Tramper et al. 2016). Because of their extreme influence on their environment, understanding the formation, evolution, and death of massive stars is imperative for a multitude of astrophysical fields. Establishing the upper mass limit for stars is one of the holy grails of stellar physics, laying sharp constraints on the initial mass function (Salpeter 1955; Kroupa 2001) and massive star formation (Bonnell et al. 1997; Oskinova et al. 2013a). Current estimates

for an upper mass limit range from $\approx 120\,M_\odot$ (e.g., Oey & Clarke 2005) to $\gtrsim 300\,M_\odot$ (e.g., Crowther et al. 2010; Schneider et al. 2014a; Vink 2015).

However, the only reliable method to weigh stars is by analyzing the orbits of stars in binaries (Andersen 1991; Torres et al. 2010). This is especially crucial for massive Wolf-Rayet (WR) stars, whose powerful winds make it virtually impossible to estimate their surface gravities. Fortunately, massive stars ($M \gtrsim 8\,M_\odot$) tend to exist in binary or multiple systems (Mason et al. 2009b; Maíz Apellániz 2010; Oudmaijer & Parr 2010; Sana et al. 2012, 2014; Sota et al. 2014; Aldoretta et al. 2015).

Primarily due to mass-transfer, the evolutionary path of a star in a binary can greatly deviate from that of an identical star in isolation (Paczynski 1973; Langer 2012; de Mink et al. 2014). The impact and high frequency of binarity make binaries both indispensable laboratories for the study of massive stars, as well as important components of stellar evolution. Hence, it is imperative to discover and study massive binary systems in the Galaxy and the Local Group.

R 145 (RMC 145, BAT99 119, HDE 269928, Brey 90, VFTS 695) is a known massive binary situated in the famous Tarantula nebula in the Large Magellanic Cloud (LMC), about 19 pc away from the massive cluster R 136 in projection (see Fig. 5.1). The system's composite spectrum was classified WN6h in the original BAT99 catalog (Breysacher et al. 1999), which, according to this and past studies (e.g., Schnurr et al. 2009, S2009 hereafter), corresponds to the primary. The primary thus belongs to the class of late WR stars which have not yet exhausted their hydrogen content, and is likely still core H-burning.

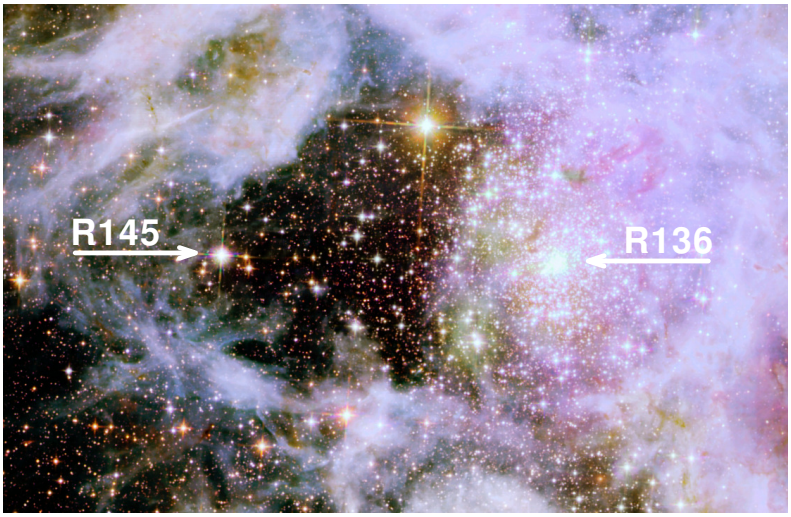

Figure 5.1.: The area of sky around R 145 (Credit: NASA, ESA, E. Sabbi, STScI). The image is obtained using the Hubble Space Telescope's (HST) WFC3 and ACS cameras in filters which roughly overlap with the I, J, and H bands. The image size is $\approx 2.5' \times 1.7'$. North is up and east to the left. The arrows indicate the positions of R 145 and the star cluster R 136. The distance between R 145 and R 136 is $\approx 1.3'$ or in projection ≈ 19 pc

The system was speculated to host some of the most massive and luminous stars in the Local Group. Erroneously assuming a circular orbit, Moffat (1989) detected a periodic Doppler shift with a period of $P = 25.17$ d, concluding R145 to be an SB1 binary. A significantly different period of 158.8 ± 0.1 d was later reported by S009, who combined data from Moffat (1989) with their own and found a highly eccentric system. S009 could not derive a radial velocity (RV) curve for the secondary. However, they attempted to estimate the secondary's RV amplitude by looking for "resonance" velocity amplitudes which would strengthen the secondary's features in a spectrum formed by co-adding the spectra in the secondary's frame of reference, under the assumption that the secondary is mainly an absorption-line star moving in anti-phase to the primary star. Combined with an orbital inclination of $i = 38° \pm 9$ they derived, their

results tentatively implied that the system comprises two incredibly massive stars of ≈ 300 and ≈ 125 $M_\odot$, making it potentially the most massive binary system known. For comparison, binary components of similar spectral type typically have masses ranging from ≈ 50 to ≈ 100 $M_\odot$ (e.g., WR 22, Rauw et al. 1996; WR 20a, Bonanos et al. 2004, Rauw et al. 2004; WR 21a, Niemela et al. 2008, Tramper et al. 2016; HD 5980, Koenigsberger et al. 2014; NGC 3603-A1, Schnurr et al. 2008a); masses in excess of 300 $M_\odot$ were so far only reported for putatively single stars (e.g., Crowther et al. 2010) based on comparison with evolutionary models.

With such high masses, signatures for wind-wind collisions (WWC) are to be expected (Moffat 1998). WWC excess emission can be seen photometrically as well as spectroscopically, and can thus also introduce a bias when deriving RVs. WWC signatures do not only reveal information on the dynamics and kinematics of the winds, but can also constrain the orbital inclination, which is crucial for an accurate determination of the stellar masses. Polarimetry offers a further independent tool to constrain orbital inclinations of binary systems (Brown et al. 1978). Both approaches are used in this study to constrain the orbital inclination i. For high inclination angles, photometric variability due to photospheric/wind eclipses can also be used to constrain i (e.g., Lamontagne et al. 1996). At the low inclination angle of R 145 (see Sects. 5.4 and 5.7, as well as S2009), however, eclipses are not expected to yield significant constraints.

Using 110 high-quality Fibre Large Array Multi Element Spectrograph (FLAMES) spectra (Sect. 5.2), we are able to derive for the first time a double-lined spectroscopic orbit for R 145. We identify lines which enable us to construct a reliable SB2 RV curve (Sect. 5.3). The majority of the spectra were taken as part of the VLT FLAMES-Tarantula survey (VLTS, Evans et al. 2011) and follow up observations (PI: H. Sana). The study is conducted in the framework of the Tarantula Massive Binary Monitoring (TMBM) project (see Almeida et al. in prep., paper I hereafter).

The RVs of both components are fitted simultaneously with polarimetric data to obtain accurate orbital parameters (Sect. 5.4). In Sect. 5.5, we disentangle the spectrum to its constituent spectra. Using the disentangled spectra, an XSHOOTER spectrum, and additional observational material, we perform a multiwavelength spectroscopic analysis of the system using the Potsdam Wolf-Rayet (PoWR) model atmosphere code to derive the fundamental stellar parameters and abundances of both stars (Sect. 5.6). An analysis of WWC signatures is presented in Sect. 5.7. A discussion of the evolutionary status of the system in light of our results is presented in Sect. 5.8. We conclude with a summary in Sect. 5.9.

5.2. Observational data

The FLAMES spectra (072.C-0348, Rubio; 182.D-0222, Evans; 090.D-0323, Sana; 092.D-0136, Sana) were secured between 2004 and 2014 with the FLAMES instrument mounted on the Very Large Telescope (VLT), Chile, partly in the course of two programs: the VLT FLAMES Tarantula Survey (Evans et al. 2011) and the TMBM project. They cover the spectral range 3960 – 4560 Å, have a typical S/N ratio of 100, and a resolution of $R \approx 8000$ (see paper I for more information). The spectra are rectified using an automated routine which fits a piecewise first-order polynomial to the apparent continuum, and are cleaned from cosmic events using a self-written Python routine.

For the spectral analysis, we use an XSHOOTER (Vernet et al. 2011) spectrum (085.D-0704, PI: Sana) taken on 22 April 2010 ($\phi \approx 0.5$, i.e. apastron, with the phase calculated using the ephemeris given in Table 5.1 in Sect. 5.4). The spectrum covers the range 3000 – 25000 Å. It has S/N ≈ 100 and a resolving power of $R \approx 7500$ in the spectral range 5500 – 10000 Å and $R \approx 5000$ in the ranges 3000 – 5500 Å and 10000 – 25000 Å. It is rectified by fitting a first-order polynomial to the apparent continuum. A segment of the spectrum is shown in Fig. 5.2.

We make use of two high-resolution (HIRES), flux-calibrated International Ultraviolet Explorer (IUE) spectra available in the IUE archive. The two spectra (swp47847, PM048, PI: Bomans; swp47836, PM033, PI: de Boer) were obtained on 08 and 10 June 1993 at roughly $\phi = 0.7$ and are thus co-added to enhance the S/N. The co-added spectrum has a resolving power of $R \approx 10000$ and S/N ≈ 10. The spectrum is rectified using the composite PoWR model continuum (see Sect. 5.6).

Linear polarimetry was obtained between 1988 and 1990 at the 2.15-m "Jorge Sahade" telescope of the Complejo Astronómico El Leoncito (CASLEO) near San Juan, Argentina, with the Vatican Observatory

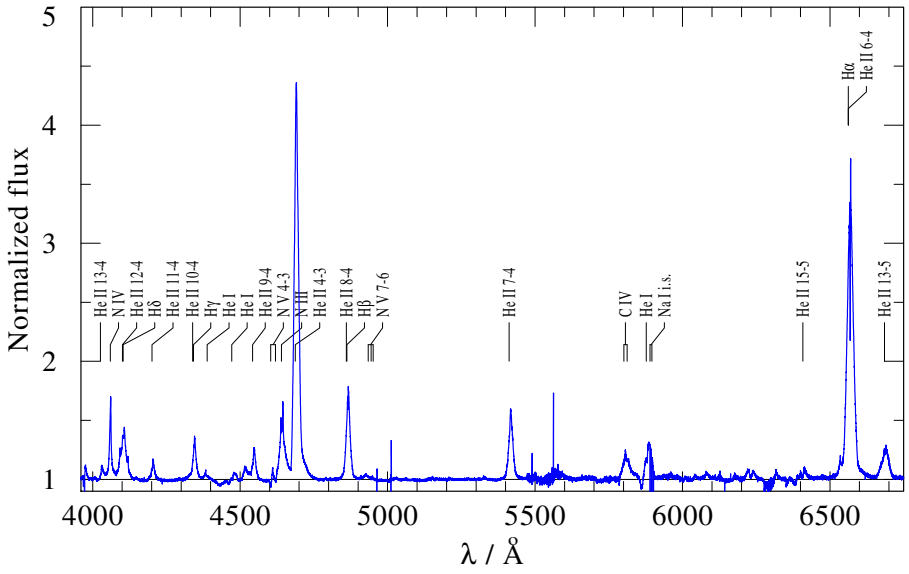

Figure 5.2.: Segment of the XSHOOTER spectrum of R 145.

Polarimeter (VATPOL, Magalhaes et al. 1984) and at the European Southern Observatory (ESO)/Max-Planck-Gesellschaft (MPG)-2.2m telescope at La Silla, Chile, with Polarimeter with Instrumentation and Sky COmpensation (PISCO, Stahl et al. 1986). The data were obtained and originally used by S2009, where more details can be found.

5.3. SB2 orbit construction

As discussed in the introduction, R145 is a known SB1 binary. However, no previous studies could unambiguously isolate the secondary in the spectrum. Thanks to the moderate resolution, high S/N of the archival FLAMES spectra, we are now able to detect spectral features which belong solely to the secondary and thus construct an SB2 orbit for the system.

Figure 5.3 shows two FLAMES spectra taken shortly before and after periastron ($\phi = 1$), where the RV differences are most extreme. It is readily seen that almost all spectral features shift in the same direction, i.e. they stem primarily from one component, the primary. However, a closer inspection reveals that the secondary contributes to the N IV λ4058 emission and to some absorption features seen on top of He II and Balmer lines. Most importantly, the Si IV emission doublet at $\lambda\lambda$4089, 4116 moves in pure antiphase to the majority of the available spectral features, implying that the Si IV lines stem from the secondary alone. A zoom-in of Fig. 5.3 which focuses on the N IV λ4058 spectral region and a neighboring member of the Si IV doublet is shown in Fig. 5.4, where we also plot a spectrum taken close to apastron ($\phi \approx 0.5$).

To measure the RVs of the components in the individual FLAMES spectra, we perform a 1D cross-correlation algorithm to different spectral features in all available spectra. We tried two types of templates to cross-correlate with: a Gaussian, and the observations themselves. Both methods resulted in comparable values, although the Gaussians resulted in a worse fit quality, and are therefore omitted here.

We first used one of the FLAMES spectra as a template to cross-correlate with. A calibration of the template to the restframe using rest wavelengths λ_0 is known to lead to systematic errors since the barycenter of emission lines rarely coincides with λ_0. Thus, to calibrate the template, we cross-correlated specific features with two preliminary PoWR models (see Sect. 5.6) calculated for the primary and secondary. We used the relatively symmetric and isolated N IV λ4058 line and Si IV doublet to calibrate the templates of the primary and secondary, respectively. Note that, while the calibration to the restframe depends to a certain extent on our PoWR models, this only affects the systemic velocity V_0, and *not* the remaining orbital

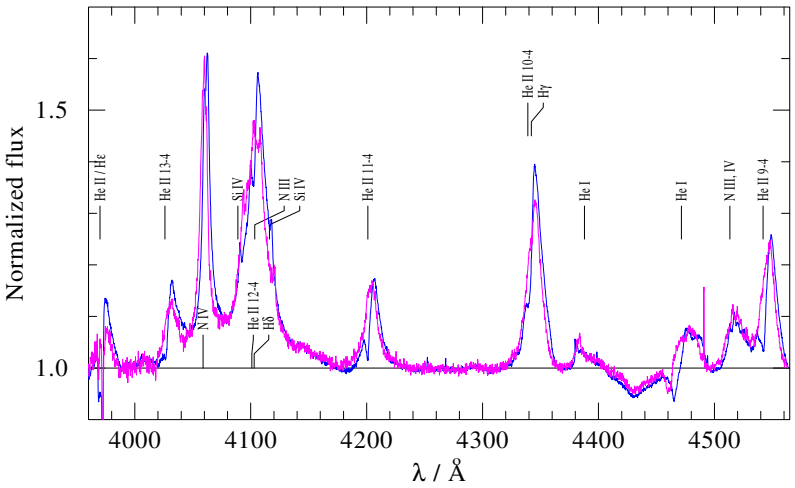

Figure 5.3.: Two FLAMES spectra taken slightly before ($\phi = -0.03$) and after ($\phi = 0.07$) periastron passage (extreme velocity amplitudes).

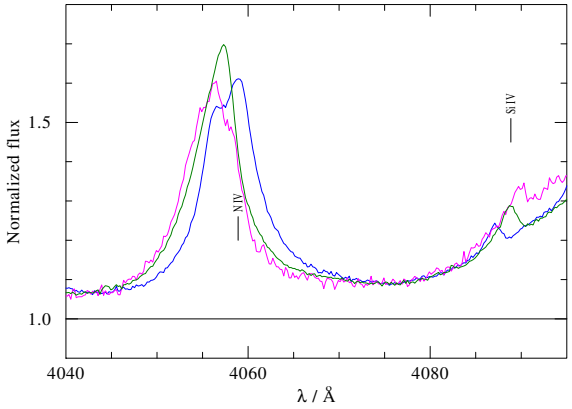

Figure 5.4.: Zoom-in of Fig. 5.3 showing the N IV and Si IV lines moving in anti-phase. A FLAMES spectrum at $\phi \approx 0.5$ is also shown (green). The primary dominates the N IV line, while the Si IV lines originate solely in the secondary. The spectra are shifted by the systemic LMC velocity of 270 km s^{-1} .

parameters.

Once the two template spectra are calibrated, we cross-correlate them against the individual FLAMES spectra, identifying the RV with the maximum of the cross-correlation function. For the primary, we measured RV shifts using the lines N IV λ4058, He II λ4200, He II λ4542, and Hγ. The secondary contributes to all these lines, but its contribution is significantly smaller due to its lower mass-loss rate, and, judging by the cross-correlation fits, we do not expect that it should influence the derived RVs. For the secondary, the Si IV doublet offers the most reliable way to track the secondary's motion, although the weak N III λ4379 line also shows a clear antiphase behavior, and was therefore measured for RVs. The Si IV lines, which are blended with the Hδ line, were rectified relatively to the contribution of the underlying Hδ emission for a more accurate derivation of the RVs.

With the preliminary velocities at hand, we created "master templates" for the primary and secondary by shifting the individual FLAMES spectra to the rest frame and co-adding them. We then used these master templates to perform a new cross-correlation with the individual observations. The newly derived

RVs differed only slightly from the previous ones and generally show less scatter. Errors on the RVs are estimated to be 10 km s^{-1} for the primary and 5 km s^{-1} for the secondary.

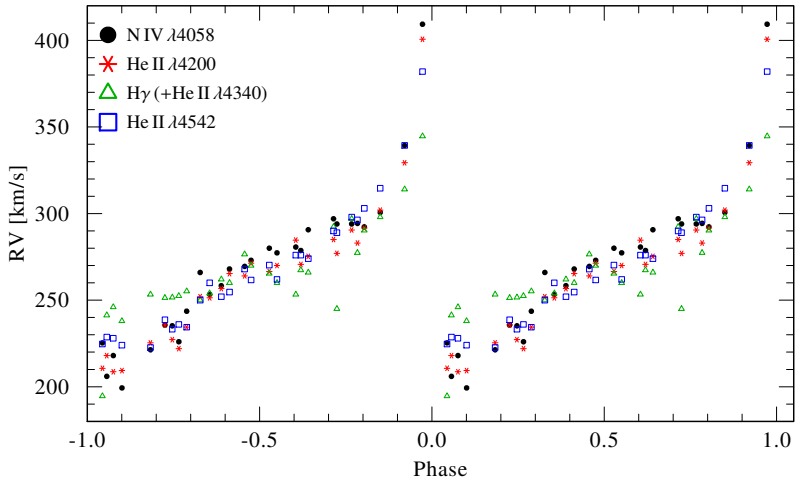

Figure 5.5.: RVs for the primary component plotted over phase as measured for selected lines (see text).

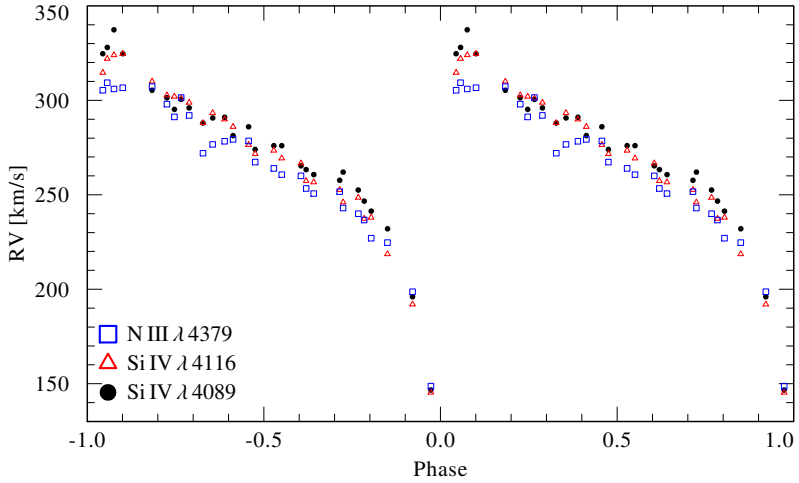

Figure 5.6.: As Fig. 5.5, but for the secondary.

The derived RVs for the primary and secondary as a function of phase are shown in Figs. 5.5 and 5.6. The phase is calculated relative to our final orbital solution (Table 5.1). The measured RVs for the N IV (primary) and Si IV lines (secondary) are listed in Table B.1. The points are binned at intervals of 0.01 on phase (note that often three FLAMES spectra were secured in a single observing night, cf. Table B.1).

From Fig. 5.5, it is evident that N IV λ4058 and the He II λ4200 and λ4542 lines predict similar RVs, with N IV showing a slightly larger velocity amplitude. In contrast, Hγ (+ He II λ4340) shows significantly more scatter and a phase-dependent deviation from the other lines. As we will show in Sect. 5.7, the reason is likely a contamination of Hγ by WWC, as well as its large formation radii. The preliminary PoWR model for the primary (see Sect. 5.6) suggests that the He II lines form a few stellar radii away from the stellar surface, as opposed to the N IV line, which forms about $\approx$ 0.1 stellar radii away. This implies that the N IV line is more likely to represent the motion of the WR primary, and is therefore used for the orbital fitting.

As for the secondary, we use the Si IV doublet. PoWR models calculated for the secondary (see Sect. 5.6) suggest that it forms very close to the stellar surface ($\approx 0.05\,R_*$ above the stellar surface), and should be very reliable for measuring the secondary's RVs. The two Si IV components agree well with each other and show a typical scatter of $\sigma \approx 7\,\mathrm{km\,s^{-1}}$ (Fig. 5.6). For the final RVs of the secondary, we average the results of these two lines.

In principle, we can derive orbital parameters using these velocities. However, the data only cover a few orbits and suffer from large gaps between them. We therefore combine old velocity measurements obtained by Moffat (1989) and S2009 for the primary with our datasets to assemble the longest possible time series, hence to obtain P with the highest possible accuracy. We note that the older velocities portray a significant systematic shift compared to the velocities derived here. This is mostly due to the different restframe calibration method used here. When performing the fitting, we therefore also fit for the systematic shifts for both sets of velocities. The SB1 fitting procedure is performed through a modified Fourier technique (Gosset et al. 2001) using the results of a Fourier analysis as a guess value for the initial period.

From the SB1 fit, we derive the period $P_{\mathrm{orb}} = 158.760 \pm 0.017\,\mathrm{d}$, the epoch of periastron passage $T_0[\mathrm{MJD}] = 56022.4 \pm 0.8$, the RV amplitude of the primary $K_1 = 78 \pm 3\,\mathrm{km\,s^{-1}}$, the eccentricity $e = 0.75 \pm 0.01$, and and the argument of periastron $\omega = 61 \pm 1^\circ$. Since the older velocities suffer from significantly larger errors, we do not adopt all orbital parameters derived, but only the period, which benefits significantly from the $\approx 30\,\mathrm{yr}$ of coverage. We do not find evidence for apsidal motion in the system. In the next section, we analyze the polarimetric data simultaneously with the FLAMES data to better determine the orbital parameters and the orbital inclination. Note that the assumption here is that the period change due to mass-loss from the system is negligible during these 30 years. Since roughly $10^{-4.3}\,M_\odot$ are lost from the system each year (see Sect. 5.6), approx. $\Delta M_{\mathrm{tot}} = 0.001\,M_\odot$ were lost within 30 yr. The period change within 30 years can be estimated via $P_{\mathrm{i}}/P_{\mathrm{f}} = (M_{\mathrm{tot,\,f}}/M_{\mathrm{tot,\,i}})^2$ (Vanbeveren et al. 1998). Assuming $M_{\mathrm{tot}} = 100\,M_\odot$ for an order-of-magnitude estimate, we obtain a difference in the period which smaller than our error, and thus negligible.

5.4. Simultaneous polarimetry and RV fitting

Fitting the polarimetric data simultaneously with the RV data enables us to lay tighter constraints on the orbital parameters. Furthermore, as opposed to an RV analysis, polarimetry can yield constraints on the inclination i. As the orbital masses scale as $M_{\mathrm{orb}} \propto \sin^3 i$, knowing i is crucial.

The polarimetric analysis is based on ideas developed by Brown et al. (1978, 1982), later corrected by Simmons & Boyle (1984). A similar analysis for the system was performed by S2009. As such, light emitted from a spherically-symmetric star is unpolarized. While Thomson scattering off free electrons in the stellar wind causes the photons to be partially linearly polarized, the total polarization measured in the starlight cancels out if its wind is spherically-symmetric. However, when the light of a star is scattered in the wind of its binary companion, the symmetry is broken, and some degree of polarization is expected. The degree of polarization depends on the amount and geometry of the scattering medium, which depends on the properties of the wind (e.g., mass-loss) and on the orbital phase.

In our case, the dominant source of free electrons would clearly be the wind of the primary WR star (see also Sect. 5.6), although some of the primary's light may also be scattered in the wind of the secondary star. We first assume that only the wind of the primary contributes to the polarization, given its dominance over that of the secondary. We will later relax this assumption. Following Robert et al. (1992), the Stokes parameters $U(\phi)$ and $Q(\phi)$ can be written as the sum of the (constant) interstellar polarizations U_0, Q_0 and ϕ-dependent terms:

$$\begin{aligned} U(\phi) &= U_0 + \Delta Q(\phi)\sin\Omega + \Delta U(\phi)\cos\Omega \\ Q(\phi) &= Q_0 + \Delta Q(\phi)\cos\Omega - \Delta U(\phi)\sin\Omega, \end{aligned} \tag{5.1}$$

where Ω is the position angle of the ascending node, and $\Delta Q(\phi)$, $\Delta U(\phi)$ (in the case of spherically-symmetric winds) are given by

Table 5.1.: Derived orbital parameters

Parameter	Value
$P_{\rm orb}$ [days]	158.760 (fixed[a])
T_0 [MJD]	56022.6 ± 0.2
K_1 [km s^{-1}]	96 ± 3
K_2 [km s^{-1}]	95 ± 4
e	0.788 ± 0.007
$\omega[^\circ]$	61 ± 7
$M_{\rm orb,\,1} \sin^3 i\ [M_\odot]$	13.2 ± 1.9
$M_{\rm orb,\,2} \sin^3 i\ [M_\odot]$	13.4 ± 1.9
$a_1 \sin i\ [R_\odot]$	302 ± 10
$a_2 \sin i\ [R_\odot]$	299 ± 10
V_0 [km s^{-1}]	270 ± 5
$\Omega\ [^\circ]$	62 ± 7
$i\ [^\circ]$	39 ± 6
τ_*	0.10 ± 0.01
Q_0	-2.13 ± 0.02
U_0	0.58 ± 0.02
γ	0.87 ± 0.07
$M_{\rm orb,\,1}\ [M_\odot]$	53^{+40}_{-20}
$M_{\rm orb,\,2}\ [M_\odot]$	54^{+40}_{-20}
$a_1\ [R_\odot]$	480^{+90}_{-65}
$a_2\ [R_\odot]$	475^{+100}_{-70}

Notes. Derived orbital parameters from a simultaneous fit of the FLAMES RVs and the polarimetry. The period is fixed to the value found from the SB1 fitting using all published RVs for the primary (see Sect. 5.3)
[(a)] Fixed to the period derived in Sect. 5.3.

$$\begin{aligned} \Delta U(\phi) &= -2\tau_3(\phi)\cos i \sin(2\lambda(\phi)) \\ \Delta Q(\phi) &= -\tau_3(\phi)\left[\left(1+\cos^2 i\right)\cos(2\lambda(\phi)) - \sin^2 i\right]. \end{aligned} \tag{5.2}$$

Here, $\lambda(\phi) = \nu(\phi)+\omega-\pi/2$ is the longitude of the scattering source (primary) with respect to the illuminating source (secondary). ν is the true anomaly, ω is the argument of periastron. τ_3 is the effective optical depth of the scatterers (see eqs. 4,5 in Robert et al. 1992) which scales with the (constant) total optical depth τ_* of the primary star (see Moffat et al. 1998). St.-Louis et al. (1988) assumed that $\tau_3(\phi) = \tau_*\,(a/D(\phi))^\gamma$, where $D(\phi)$ is the separation between the companions, and γ is a number of the order of unity. Brown et al. (1982) showed that $\gamma \approx 2$ in the case of a wind which is localized closely to the primary's stellar surface. However, this need not be the case for WR stars.

The free parameters involved in the polarimetry fitting are therefore $\Omega, i, \tau_*, Q_0, U_0$, and γ, as well as the orbital parameters P, ω, and e. One may generalize this model easily if both companions possess winds which can significantly contribute to the total polarization. In this case, τ_* is the sum of optical depths of both stars, weighted with the relative light ratios (see Eq. 2 in Brown et al. 1982). The formalism may

be therefore implemented here, with the only consequence that τ_* relates to the mass-loss rates of both companions.

The simultaneous fitting of the FLAMES RVs and the polarimetric data is performed through a χ^2 minimization algorithm, with a relative weight given to the RV and polarimetric data chosen so that both types of data have a similar contribution to the total χ^2. Best fit RV and Q/U curves are shown in Figs. 5.7 and 5.8. During the fitting procedure, the period is fixed to the value inferred from the combined RV sample (see Sect. 5.3). The corresponding best-fitting parameters are given in Table 5.1.

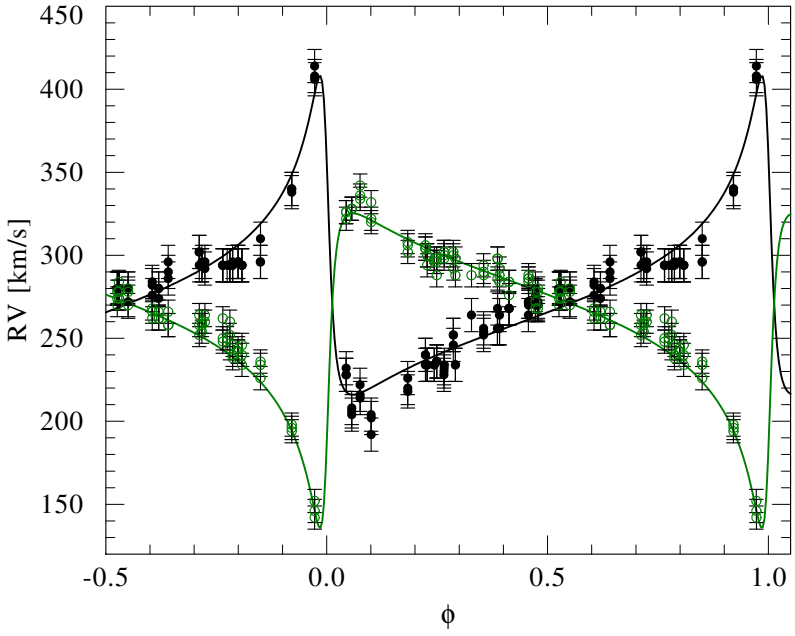

Figure 5.7.: Orbital solution plotted against the measured RVs for the N IV λ4058 line (primary, black stars) and the averaged velocities of the Si IV $\lambda\lambda$4089, 4116 doublet (secondary, green triangles)

The inclination found in this study is very similar to that reported by S2009, which is not surprising given that we make use of the same polarimetric data. We note that clumps in the wind can generally enhance the scattering and may therefore lead to an overestimation of the inclination. The eccentricity is found to be larger, $e = 0.788 \pm 0.007$ as opposed to $e = 0.70 \pm 0.01$ found by S2009. This also affects the remaining orbital parameters (cf. Table 5 in S2009). Most importantly, the orbital masses found here are much lower, $\approx 55^{+40}_{-20}\,M_\odot$ for each component compared to $M_1 \gtrsim 300$ and $M_2 \gtrsim 125$ which were inferred by S2009. The reason for this discrepancy is the improved derivation of K_2 in our study. While we cannot supply a definitive reason for the erroneous derivation of K_2 by S2009, we suggest that it may be related to the fact that the secondary exhibits emission features as well as a blue-shifted absorption. Furthermore, the spectra used in the latter study are of significantly lesser quality compared with the FLAMES spectra.

The masses derived here are in much better agreement with the brightness of the system, as discussed by S2009. While the masses obtained here are close to the lower limit of what would be expected for these spectral types, as measured from eclipsing systems (e.g., Rauw et al. 2004; Bonanos et al. 2004; Schnurr et al. 2008b; Koenigsberger et al. 2014), they are not inconsistent, especially considering the errors. Moreover, given the bias of the polarimetric fitting towards higher inclination angles (e.g., Aspin et al. 1981; Wolinski & Dolan 1994), the masses derived here are likely underestimated.

From Fig. 5.1, it is evident that the binary R 145 is located outside the dense, massive cluster R 136. The projected separation between the system and the cluster is only ≈ 20 pc, which, accounting for an age of ≈ 2 Myr (cf. Table 5.3), implies an average velocity of a mere $\approx 10\,\mathrm{km\,s^{-1}}$. The derived systemic velocity (cf. Table 5.1), which is comparable to the LMC mean velocity, would be consistent with a slow runaway

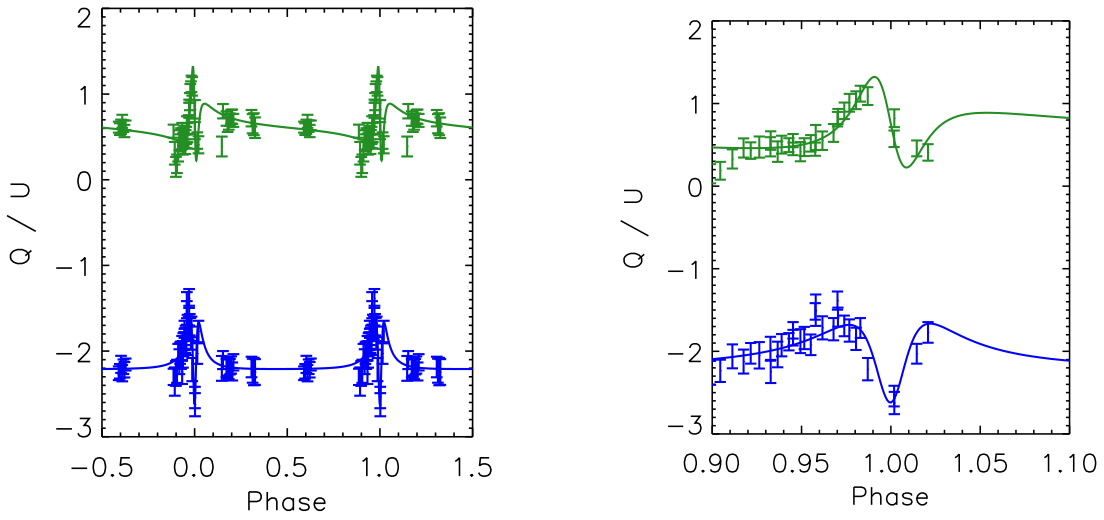

Figure 5.8.: Our polarimetric solution for Q (blue) and U (green) plotted against measured polarimetric data. The right panel is a zoom-in of the left panel around periastron passage

ejected due to dynamical interactions within the cluster, as claimed for VFTS 682 (Banerjee et al. 2012). Alternatively, it may have formed in situ in the halo of the massive cluster R 136.

5.5. Spectral disentanglement

Using the orbital parameters given in Table 5.1 as an initial guess, we apply the disentanglement code Spectangular (Sablowski & Weber, 2016, A&A, submitted) to the FLAMES spectra. The code performs the disentangling on a set of spectra in the wavelength domain rather than in the Fourier space (Hadrava 1995). Disentangling is coupled to an optimisation algorithm on the orbital parameters. Hence, it provides revised orbital parameters and the separated component spectra.

It has been shown by Hadrava et al. (2009) that the disentangling can be successful as long as the line-profile variability is small compared to a mean profile and the orbital motion. However, these conditions are hardly met by the system under study, both due to the intrinsic variability of WR stars (e.g., due to clumping) as well as due to WWC. Indeed, we find that the orbital solution severely depends on the spectral domains used and the initial solution assumed. We therefore adopt the orbital parameters obtained in Sect. 5.4. In contrast, the resulting disentangled spectra are hardly influenced by the different solutions. We are therefore confident that the disentangled spectra obtained here represent well the true spectra well, except in cases where the lines are heavily contaminated by variability.

With no eclipses in the system, it is impossible for the disentanglement procedure to provide the light ratio of the primary and secondary components. The adopted light ratio influences the strength of the lines in the disentangled, rectified spectra. Based on a calibration with equivalent widths (EWs) of putative single stars (see below), we estimate the light ratio to be $F_{v,2}/F_{v,\mathrm{tot}} = 0.55 \pm 0.1$, where F_v is the visual flux in the Smith v band. This ratio is assumed for the rectified disentangled spectra, shown in Fig. 5.9.

The disentangled spectrum of the primary is consistent with it being of WN6h type. We compared the spectrum with two WN6h spectra in the LMC: BAT99 30 and BAT99 31. The adopted light ratio results in EWs of the He II lines which agree well with the two latter objects, but also results in an EW of the He I λ4471 line which is about three times larger, suggesting a strong He I excess in the system, likely originating in WWC (see Sect. 5.7).

The spectrum of the secondary is suggestive of a so-called slash star (Crowther & Walborn 2011).

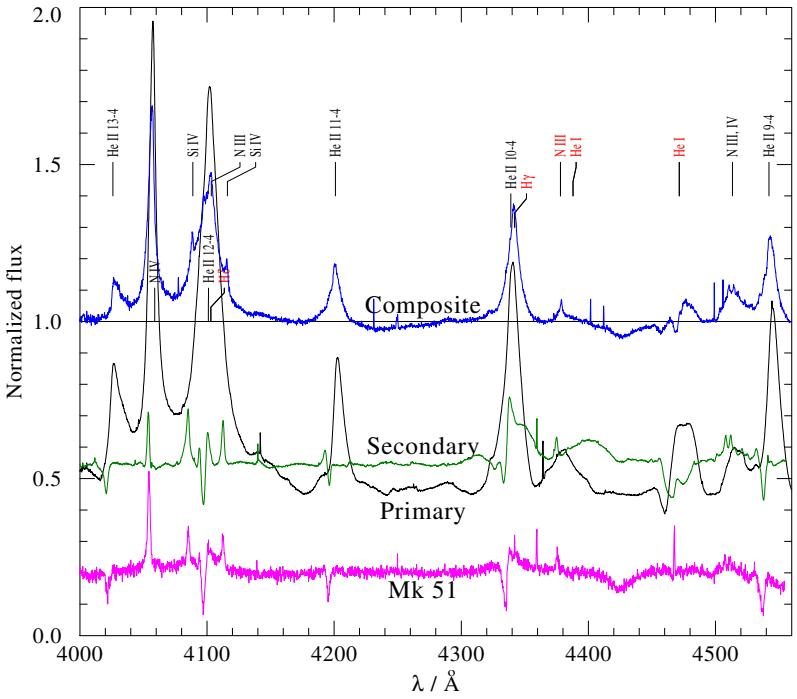

Figure 5.9.: The disentangled normalized spectra of the primary (black) and secondary (green), shifted to their relative light ratio. A composite FLAMES spectrum ($\phi \approx 0.5$) is shown for comparison (blue), as well as an observed normalized spectrum of Mk 51 for comparison with the secondary, shifted by -0.8 for clarity.

Unfortunately, the FLAMES spectra do not include diagnostic lines which are important for the classification (e.g., Hβ, N v $\lambda\lambda$4603,4619 and N III $\lambda\lambda\lambda$4634,4640,4642). Moreover, some lines, marked in red in Fig. 5.9, are strongly affected by WWC (see Sect. 5.7). This is especially significant for the secondary's spectrum, which generally shows weaker features compared to the primary. Especially the shape and strength of the lines in the range 4000 – 4200 Å is suggestive of an O3.5 If*/WN7 star, for which the star Melnick 51 (Mk 51) is a prototype. For comparison, we plot in Fig. 5.9 an observed normalized FLAMES spectrum of Mk 51 (P. Crowther, priv. com.). The Si IV doublet is stronger in R 145 than observed for MK51, and the N IV line weaker. However, the derived model and parameters for the secondary (see Sect. 5.6) are suggestive of the spectral class O3.5 If*/WN7. We therefore adopt this spectral class in this study. The light ratio adopted here is also chosen so that the EWs of the majority of the Balmer and He II lines agree with this spectral type (see Fig. 5.9).

5.6. Spectral analysis

The disentangled spectra, together with the high-quality XSHOOTER spectrum and the complementary UV and photometric data, enable us to perform a spectral analysis of both components. The spectral analysis is performed with the Potsdam Wolf-Rayet[1] (PoWR) model atmosphere code, applicable to any hot star (e.g., Shenar et al. 2015; Todt et al. 2015; Giménez-García et al. 2016). The code iteratively solves the co-moving frame, non-local thermodynamic equillibrium (non-LTE) radiative transfer and the statistical balance equations in spherical symmetry under the constraint of energy conservation, yielding the occupation numbers in the photosphere and wind. By comparing the output synthetic spectra to observed

[1]PoWR models of Wolf-Rayet stars can be downloaded at http://www.astro.physik.uni-potsdam.de/PoWR.html

spectra, fundamental stellar parameters are derived. A detailed description of the assumptions and methods used in the code is given by Gräfener et al. (2002) and Hamann & Gräfener (2004). Only essentials are given here.

A PoWR model is defined by four fundamental stellar parameters: the effective temperature T_*, the surface gravity g_*, the stellar luminosity L, and the mass-loss rate $\dot{M}$. The effective temperature T_* is given relative to the stellar radius R_*, so that $L = 4\,\pi\,\sigma\,R_*^2\,T_*^4$. R_* is defined at the model's inner boundary, fixed at mean Rosseland optical depth of $\tau_{\rm Ross} = 20$ (Hamann et al. 2006). The outer boundary is set to $R_{\rm max} = 1000\,R_*$. The gravity g_* relates to the radius R_* and mass M_* via the usual definition: $g_* = g(R_*) = G\,M_* R_*^{-2}$. We cannot derive g_* here because of the negligible effect it has on the wind-dominated spectra, and fix it to the value implied from the orbital mass.

Table 5.2.: Derived physical parameters for R 145

Parameter	Primary	Secondary
Spectral type	WN6h	O3.5 If*/WN7
T_* [K]	50000 ± 3000	43000 ± 3000
$\log L\,[L_\odot]$	6.35 ± 0.15	6.33 ± 0.15
$\log R_{\rm t}\,[R_\odot]$	1.05 ± 0.05	1.50 ± 0.15
v_∞ [km s^{-1}]	1200 ± 200	1000 ± 200
$R_*\,[R_\odot]$	20^{+6}_{-5}	26^{+9}_{-7}
$D\,[R_\odot]$	10 ± 0.3 dex	10 ± 0.3 dex
$\log \dot{M}\,[M_\odot\,{\rm yr}^{-1}]$	−4.45 ± 0.15	−4.9 ± 0.3
$v \sin i$ [km s^{-1}]	< 200	< 150
$v_{\rm rot}$ [km s^{-1}]	< 350	< 270
$X_{\rm H}$ (mass fraction)	0.4 ± 0.1	0.5 ± 0.2
$X_{\rm C}/10^{-4}$ (mass fraction)	0.8 ± 0.3	0.7 ± 0.4
$X_{\rm N}/10^{-3}$ (mass fraction)	8 ± 4	8 ± 4
$X_{\rm O}/10^{-4}$ (mass fraction)	$\lesssim 1$	$\lesssim 1$
$X_{\rm Si}/10^{-4}$ (mass fraction)	7 (fixed)	7 ± 3
$M_{\rm v}$[mag]	−7.21 ± 0.25	−7.43 ± 0.25
$M_{\rm V}$[mag]	−7.15 ± 0.25	−7.30 ± 0.25
$M_{\rm MLR,hom}[M_\odot]$	101^{+40}_{-30}	109^{+60}_{-40}
$M_{\rm MLR,He\text{-}b}[M_\odot]$	55^{+15}_{-12}	54^{+15}_{-12}
E_{B-V} [mag]	0.34 ± 0.01	
A_V [mag]	1.4 ± 0.2	

The chemical abundances of the elements included in the calculation are prespecified. Here, we include H, He, C, N, O, Si, and the iron group elements dominated by Fe. The mass fractions $X_{\rm H}$, $X_{\rm C}$, and $X_{\rm N}$, and $X_{\rm Si}$ are derived in this work. Based on studies by Korn et al. (2000) and Trundle et al. (2007), we set $X_{\rm Fe} = 7 \cdot 10^{-4}$. Lacking any signatures associated with oxygen, we fix $X_{\rm O} = 5 \cdot 10^{-5}$ for both components. Values larger than 10^{-4} lead to spectral features which are not observed.

Hydrostatic equilibrium is assumed in the subsonic velocity regime (Sander et al. 2015), from which the density and velocity profiles follow, while a β-law (Castor et al. 1975) with $\beta = 1$ (e.g., Schnurr et al. 2008b) is assumed for the supersonic regime, defined by the β exponent and the terminal velocity v_∞. Optically thin clumps are accounted for using the microclumping approach (Hillier 1984; Hamann & Koesterke 1998), where the population numbers are calculated in clumps which are a factor of D denser than the

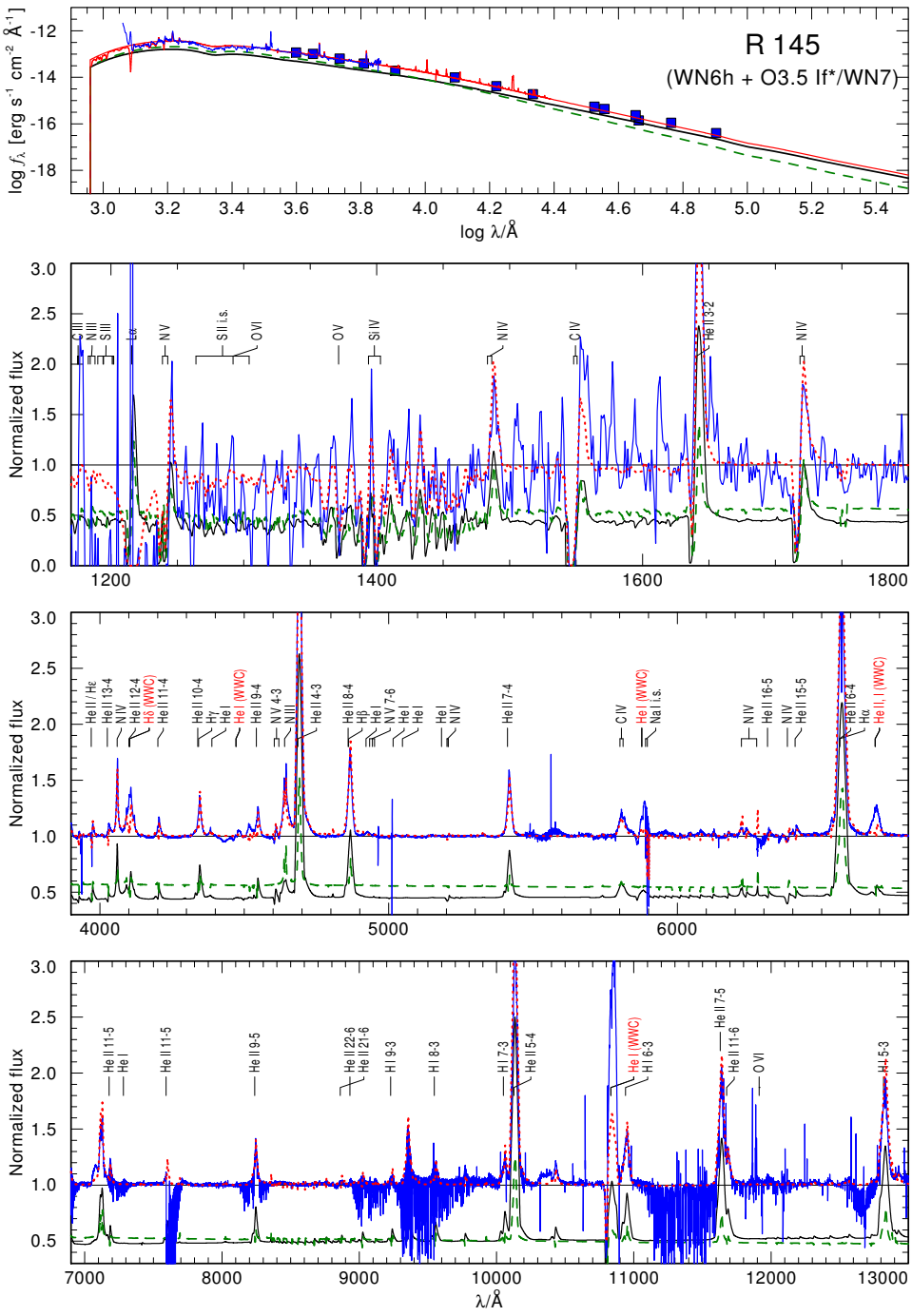

Figure 5.10.: Comparison between observed (blue squares and lines) SED (upper panel) and the normalized IUE and XSHOOTER spectra (lower panel) and the synthetic composite spectrum (red dotted line). The composite spectrum is the sum of the primary (black solid line) and secondary (green dashed line). The observed and modelled spectra in the UV are binned at 1Å for clarity. Lines which are strongly affected by WWC are marked with red idents.

equivalent smooth wind ($D = 1/f$, where f is the filling factor). Because optical WR spectra are dominated by recombination lines, whose strengths increase with $\dot{M}\sqrt{D}$, it is customary to parametrize their models using the so-called transformed radius (Schmutz et al. 1989),

$$R_t = R_* \left[\frac{v_\infty}{2500\,\mathrm{km\,s^{-1}}} \Big/ \frac{\dot{M}\sqrt{D}}{10^{-4}\,M_\odot\,\mathrm{yr}^{-1}} \right]^{2/3}, \tag{5.3}$$

defined so that EWs of recombination lines of models with given abundances, T_*, and R_t are approximately preserved, independently of L, $\dot{M}$, D, and v_∞.

The effective temperature of the primary is derived mainly based on the ionisation balance of N III, N IV, and N V lines. For the secondary, the weakness of associated He I lines, as well as the presence of a strong N III component and a weak N IV component constrain T_*. Once the temperatures and light ratio (see Sect. 5.5) are constrained, mass-loss rates (or transformed radii) can be determined. For the primary, this is straightforward, while for the secondary, this can only be done approximately. The terminal velocity v_∞ is determined primarily from P-Cygni lines in the UV. Clumping factors are determined using electron scattering wings, primarily of He II λ4686. Hydrogen content is derived based on the balance of the Balmer series (He II + H) to pure He II lines. The remaining abundances are derived from the overall strengths of their associated lines.

The luminosity and reddening follow from a simultaneous fit to available photometry, adopting a distance of 50 kpc (Pietrzyński et al. 2013). We use U photometry from Parker et al. (1992), BVRI photometry from Zacharias et al. (2012b), JHK and IRAC photometry from the compilation of Bonanos et al. (2010), and WISE photometry from Cutri & et al. (2013). The reddening is modelled using the reddening law published by (Howarth 1983). In the latter, we find $R_V = 4.0 \pm 0.5$ is most consistent in reproducing the complete photometry, comparable to other stars in 30 Dorados (Maíz Apellániz et al. 2014), and we therefore fix $R_V = 4$ and fit for E_{B-V}. Maíz Apellániz et al. (2014) derived new laws for the 30 Dor region, but since the difference between these laws and older ones are negligible in the reddening regime involved here (see figures 11 and 12 in the latter paper) - especially for the purpose of this study - these new laws are not implemented here.

The nitrogen abundance is found to be about a factor of two larger in both components compared to the typical LMC values (cf. Hainich et al. 2014), mostly due to the strong N III doublet at ≈ 4640 Å. Furthermore, to reproduce the Si IV doublet originating in the secondary, it is necessary to set X_{Si} to an abundance comparable to the Galactic one ($\approx$ two times larger than typical LMC abundance, cf. Trundle et al. 2007). Since X_{Si} is not expected to change throughout the stellar evolution, we assume that silicon was initially overabundant, and fix the same value for the primary. Unfortunately, the poor quality of the UV data does not enable us to determine the abundance of the iron group elements. Because of the relatively large associated errors, we refrain from interpreting this apparent overabundance.

A comparison of the best-fitting models to the observed spectral energy distribution (SED) and normalized spectra is shown in Fig. 5.10. Note that the composite spectrum strongly underpredicts low-energy transitions such as He I lines. We will show in Sect. 5.7 that these lines are expected to be strongly contaminated by WWC. The derived stellar parameters are listed in Table 5.2, where we also give the Smith and Johnson absolute magnitudes M_v and M_V, as well as the total extinction A_V. We also give upper limits derived for the projected and actual rotation velocity $v \sin i$ and v_{rot} for both components, as derived by comparing lines formed close to the stellar surface (N IV λ4058, Si IV doublet) to synthetic spectra which account for rotation in an expanding atmosphere, assuming co-rotation up to $\tau_{Ross} = 2/3$ and angular momentum conservation beyond (cf. Shenar et al. 2014). Given the low inclination angle, these only lay weak constraints on the actual rotation velocities v_{rot} of the stars. Errors are estimated from the sensitivity of the fit quality to variations of stellar parameters, or via error propagation.

Table 5.2 further gives stellar masses which are based on mass-luminosity relations calculated by Gräfener et al. (2011) for homogeneous stars. The relations depend on L and X_H alone. $M_{MLR,\,hom}$ assumes the derived value of X_H in the core, i.e. a homogeneous star. $M_{MLR,\,He\text{-}b}$ assumes $X_H = 0$, i.e. the relation for pure He stars, which is a good approximation if the hydrogen rich envelope is of negligible to moderate mass (see discussion by Gräfener et al. 2011). If indeed $M_{orb} \approx 55\,M_\odot \approx M_{MLR,\,He\text{-}b}$, as is implied from Tables 5.1 and 5.2, the stars are likely already core He-burning. However, this is very unlikely to be true for

the secondary given its spectral type and luminosity. Rather, the orbital masses are likely underestimated due to an overestimated inclination (e.g., Aspin et al. 1981), and may in fact be more similar to $M \approx 80 - 90\,M_{\odot}$, which is consistent with the upper boundary of our errors (see further discussion in Sect. 5.8).

Within errors, the derived physical parameters are in good agreement with the spectral types of the primary and secondary (cf. Crowther & Walborn 2011; Hainich et al. 2014). Bestenlehner et al. (2014) and Hainich et al. (2014) both analyzed R 145 assuming a single component, which explains why they derive a luminosity in excess of $\log L = 6.5\,[L_{\odot}]$, about $0.2 - 0.3$ dex higher than found here for the primary. Hainich et al. (2014) found a comparable effective temperature to that found for the primary in our study, while Bestenlehner et al. (2014) found a significantly lower temperature of 40 kK (comparable to the secondary), which is a consequence of associating strong features stemming partially from the secondary (e.g., strong N III lines) with the primary. Similarly, the mass-loss rates derived here are different than in the previous studies because they did not account for line dilution and adopted wrong luminosities. Given the careful binary analysis performed here, we are inclined to believe that our results represent the system much more accurately than previous studies.

5.7. Variability and wind-wind collision

Our results from the previous sections imply that both binary components in R145 have significant stellar winds. In this case, it is expected that a cone-shaped wind-wind collision (WWC) zone would form, its tip situated along the line connecting the centers of both stars at the point where the dynamical pressures of the two outflows equalize (Stevens et al. 1992; Moffat 1998). The temperatures at the immediate vicinity of the collision zone can reach a few 10^7 K. The plasma rapidly cools and emits radiation as it streams outwards along the cone.

Observationally, the emission takes on two forms. On the one hand, WWC leads to excess emission which can be seen photometrically, either in X-rays (Cherepashchuk 1976; Corcoran et al. 1996) or in non-thermal radio, infra-red and optical (e.g., Williams et al. 1997). On the other hand, WWC emission can also be spotted spectroscopically on top of prominent emission lines in the optical, as the plasma cools off via recombination (e.g., Rauw et al. 1999; Hill et al. 2000; Sana et al. 2001). A spectroscopic analysis of the excess emission arising from the WWC zone can place strong constraints on the kinematics and inclination of the system (Luehrs 1997). The overall strength of the emission is expected to reach a maximum at periastron. In the adiabatic case, an inverse proportion with the separation D between the stars is predicted (Usov 1992). A sharper scaling ($\propto D^{-n}$, $n > 1$) is expected in highly radiative cases.

In Fig. 5.11, we show V- and I-band light-curve of R 145 (K. Ulaczyk, private communication) obtained with the OGLE-III shallow survey (Ulaczyk et al. 2012), phased with the ephemeris in Table 5.1. One can see a clear indication of excess emission during periastron passage. Possible mechanisms which could cause a phase-dependent variability include wind eclipses, ellipsoidal deformations (e.g., Soszynski et al. 2004), and WWC. Wind eclipses are expected to cause a dip as the components align along the line of sight (phases 0.01 and 0.82), and while the outliers seen in Fig. 5.11 around these phases could indicate a wind eclipse, the data points are too sparse to tell. Ellipsoidal deformations could play a role, although it is unclear whether they are expected to be important for spectra which are wind-dominated. However, the emission excess seen during periastron is most easily explained by WWC. Given the sparseness of the data, however, we refrain from modelling the light-curve.

To study the spectroscopic variability, we calculated the EWs of several lines in all 110 FLAMES spectra to check for periods present in the dataset. Figure 5.12 shows the EWs plotted versus phase, binned on intervals of $\Delta\phi = 0.01$. It is evident that lines associated with "cooler" ions such as He I, N III, and Balmer lines show a clear increase of the emission near periastron ($\phi = 0$). This behavior is not seen at all in the He II λ4200 and N IV λ4058 lines, but is seen in the He II λ4541 line, possibly because it is blended with an N III component.

In Fig. 5.13, we plot the same data points as in Fig. 5.12 for Hγ, but include three curves which correspond to functions of the form $A_1 + B_1\,D^{-1}(\phi)$, $A_2 + B_2\,D^{-2}(\phi)$, and $A_3 + B_3\,D^{-\alpha}(\phi)$ with the constants $A_{\rm i}$, $B_{\rm i}$, and α chosen to minimize the sum of the squared differences χ^2. When leaving the exponent α as a free parameter, we obtain $\alpha \approx 0.25$. A similar test for N III λ4378 line results in $\alpha \approx 1$, while for the He II λ4541

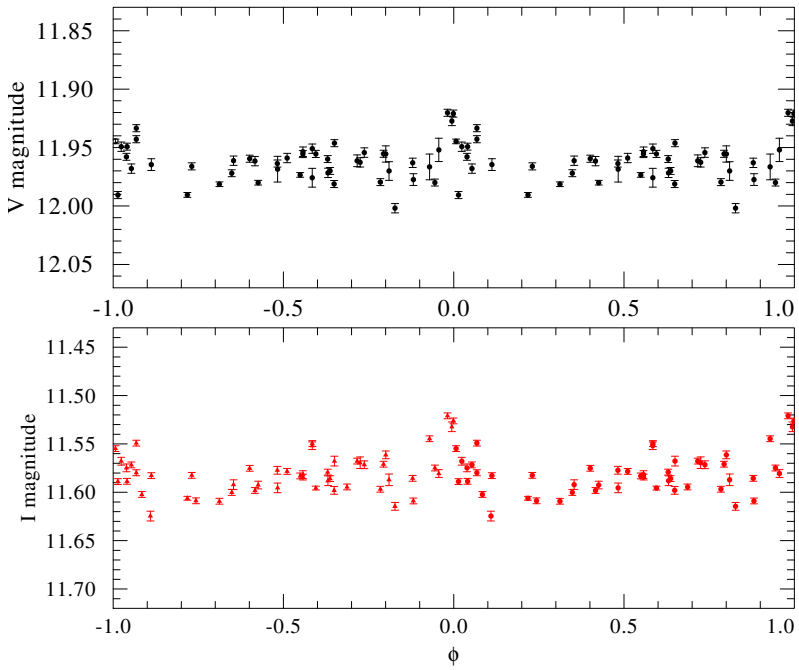

Figure 5.11.: Phased OGLE-III V- and I-band light-curve of R 145

line, we obtain $\alpha \approx 1.2$. Given the intrinsic scatter in the EWs and the poor coverage during periastron, we cannot exclude the $1/D$ adiabatic dependence predicted by Usov (1992).

We checked for the presence of periodic signals on the EWs of the lines shown in Fig. 5.12. In most cases, we find significant detections of periods which agree with the orbital period. The remaining periods are found to be insignificant. In Fig. 5.14, a periodogram (Scargle 1982; Horne & Baliunas 1986) is shown as an example. The most prominent peak appears for a period of 158.9 ± 0.8 days, in very good agreement with the orbital period found (cf. Table 5.1). The occurrence of further apparently significant peaks is caused primarily by spectral leakage due to the unevenly spaced data (Horne & Baliunas 1986), as we confirmed by subtracting the main signal and constructing a second periodogram. We find a marginal detection of a further period of $P_2 \approx 21$ d, which may be related to stochastic variability in the system, but could also be spurious.

Figure 5.15 shows dynamic spectra calculated for three prominent lines: He I λ4471, H γ, and He II λ4200. The He I image is especially striking. There is a clear pattern of emission excess traveling from $\approx -600\,\mathrm{km\,s^{-1}}$ at $\phi \approx 0$ to $\approx 300\,\mathrm{km\,s^{-1}}$ at $\phi \approx 0.7$, and back again. This velocity amplitude clearly does not stem from the motion of the stars, which trace a different RV pattern and move at amplitudes of $\approx 100\,\mathrm{km\,s^{-1}}$. In fact, the emission pattern is fully consistent with a rotating WWC cone, as suggested by Luehrs (1997). Also interesting are the two strong absorption dips seen close to periastron, which likely occur when the cone arms tangentially sweep along the line of sight, thereby instantaneously increasing the optical depth.

To proceed with a more quantitative analysis of the WWC zone, we follow the simple argumentation by Hill et al. (2000). Typically, very strong emission lines are needed for a quantitative analysis of WWC. However, our FLAMES spectra do not contain these lines. The most suitable line for the analysis is found to be He I λ4471. Due to its weakness, only a rough analysis can be made here. The basic model predicts the dependence of the full width half maximum (FW) of the emission excess profile and its mean RV as a function of orbital phase ϕ. FW(ϕ) and $\overline{\mathrm{RV}}(\phi)$ can be written as

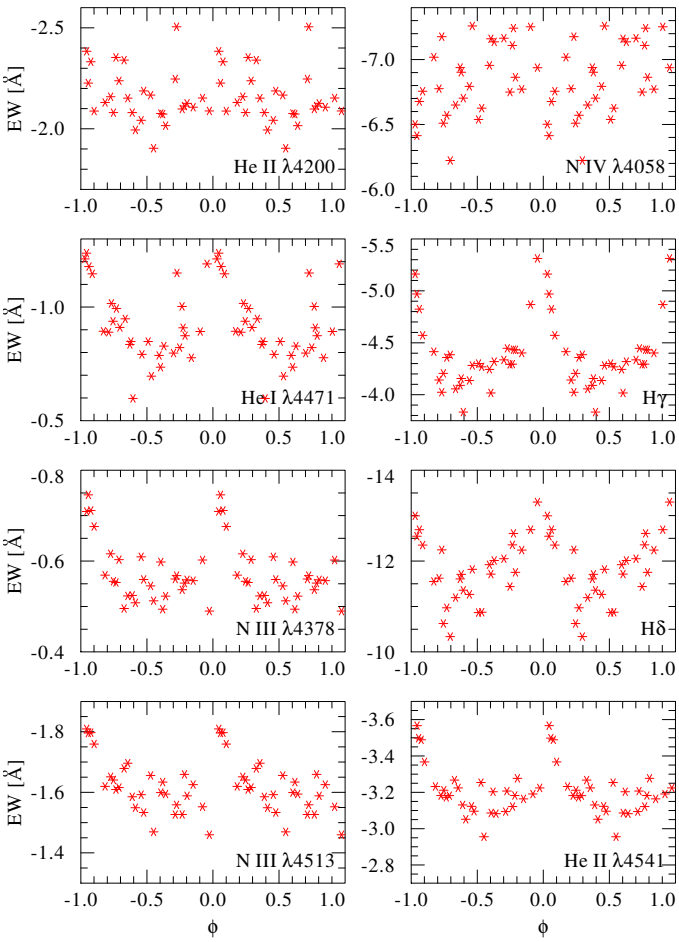

Figure 5.12.: EWs as a function of orbital phase ϕ measured for selected lines in the FLAMES spectra, binned at $\Delta\phi = 0.01$ intervals.

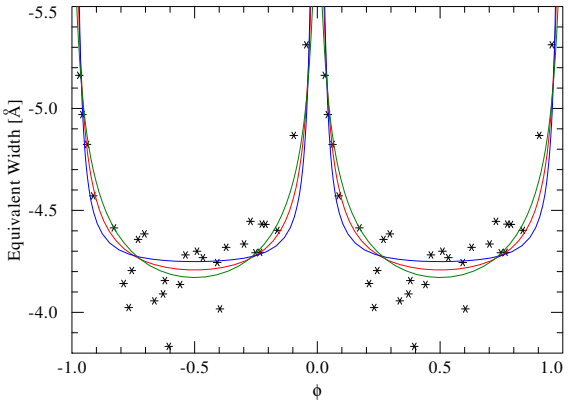

Figure 5.13.: Fits of the form $A_1 + B_1\, D^{-2}$ (blue curve), $A_2 + B_2\, D^{-1}$ (red curve), and $A_3 + B_3\, D^{-\alpha}$ (green curve) to the data points describing the EW as a function of phase ϕ for the line Hγ.

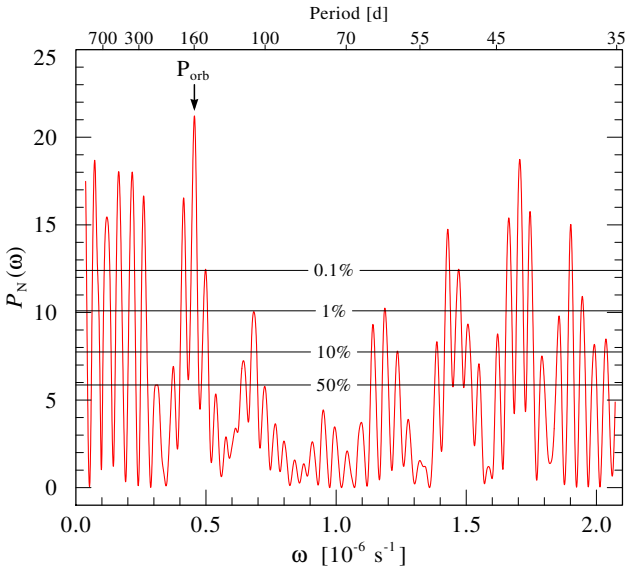

Figure 5.14.: Periodogram of the EWs of the Hδ line. The periodogram was calculated from $\omega = 2\pi/T$ to $\omega = \pi N_0/T$ with a spacing $0.1/T$, where N_0 is the number of data points and T the total time of the observation. Various false-alarm probability levels are marked.

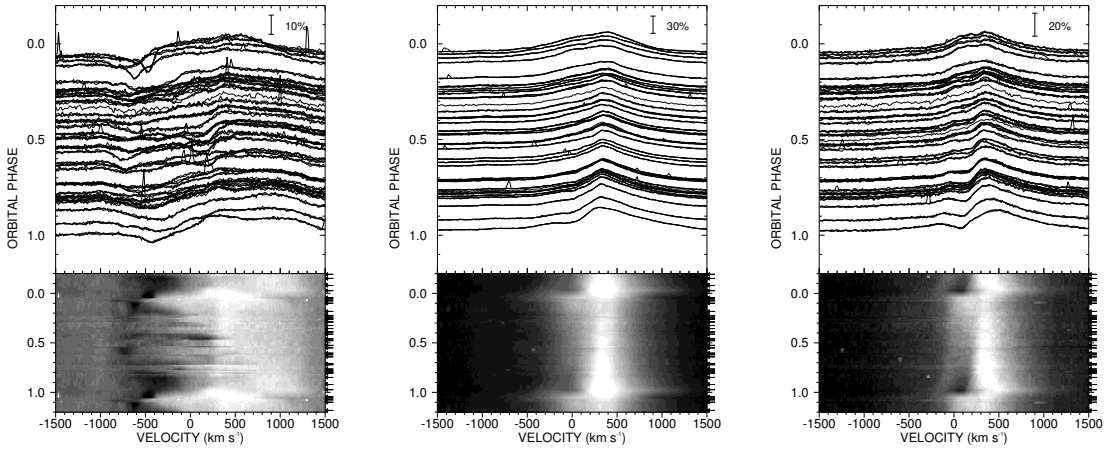

Figure 5.15.: Dynamic FLAMES spectra of He I λ4471 (left), Hγ (center), He II λ4200 (right)

$$\begin{aligned} \mathrm{FW}(\phi) &= C_1 + 2\,v_{\mathrm{str}}\,\sin\theta\sqrt{1-\sin^2 i\cos^2(\phi-\delta\phi)} \\ \overline{\mathrm{RV}}(\phi) &= C_2 + v_{\mathrm{str}}\cos\theta\sin i\cos(\phi-\delta\phi)\,, \end{aligned} \tag{5.4}$$

where C_1 and C_2 are constants, v_{str} is the streaming velocity of the shocked gas, θ is the opening angle of the cone, i is the orbital inclination, and $\delta\phi$ is a phase shift introduced due to Coriolis forces (see figure 6 in Hill et al. 2000).

An unbiased measurement of FW and RV could not be performed because of the low S/N of the line. Instead, the blue and red "edge" velocities of the emission excess, v_{b} and v_{r}, were estimated directly from the gray-scale plot shown in Fig. 5.15, from which FW and $\overline{\mathrm{RV}}$ were calculated via $\mathrm{FW}(\phi) = v_{\mathrm{r}}(\phi) - v_{\mathrm{b}}(\phi)$ and $\overline{\mathrm{RV}}(\phi) = 0.5\,(v_{\mathrm{b}}(\phi) + v_{\mathrm{r}}(\phi))$. The stream velocity can be deduced from the position of the strong absorption

dips around $\phi \approx 0$, seen at approximately 600 km s^{-1}. Accounting for the systemic velocity of the system (≈ 300 km s^{-1}), we fix $v_{\rm str} = 900$ km s^{-1}. The value found here is slightly lower than the terminal velocity of the primary ($v_\infty \approx 1200$ km s^{-1}), as is expected.

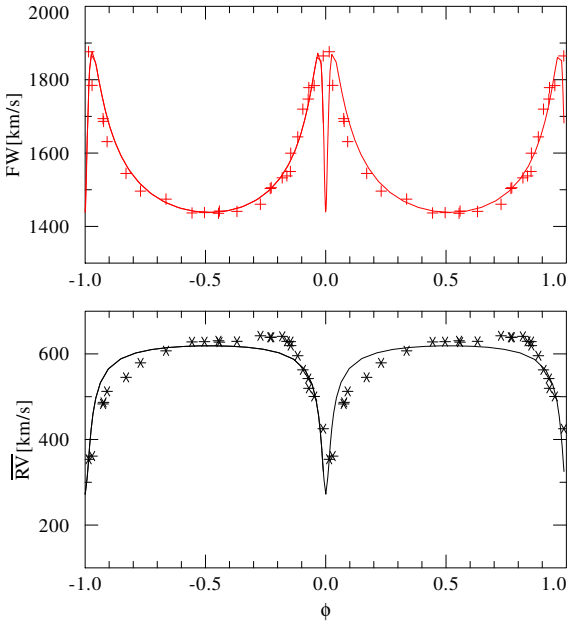

Figure 5.16.: Measured FW(ϕ) and $\overline{\rm RV}(\phi)$ of the WWC emission excess profiles compared to their best-fitting models

Having fixed $v_{\rm str}$, we look for a set of parameters C_1, C_2, θ, i, and $\delta\phi$ which minimize χ^2. For this purpose, a standard python routine (lmfit) is used. Our measurements of FW and $\overline{\rm RV}$, compared with the best-fitting solutions, are shown in Fig. 5.16. We find $C_1 = 150 \pm 30$ km s^{-1}, $C_2 = 450 \pm 20$ km s^{-1}, $\theta = 73 \pm 6°$, $i = 40 \pm 5°$, and $\delta\phi = 8 \pm 3°$. The errors given here are strongly underestimated, as the true error lies in the measurement technique of the velocities and the simplified model.

It is immediately apparent that both our polarimetric analysis as well as the WWC analysis deliver almost identical inclinations. Admittedly, the value obtained here is biased by the method of measuring $v_{\rm b}$ and $v_{\rm r}$, and should be therefore only be seen as a further confirmation, rather as an independent derivation of i. It is also interesting to consider the opening angle θ. Usov (1995) showed that the opening angle can be calculated from

$$\theta = 2.1\left(1 - \frac{\eta^{2/5}}{4}\right)\eta^{1/3}, \tag{5.5}$$

where $\eta = \dot{M}_2 v_{\infty,2} / \left(\dot{M}_1 v_{\infty,1}\right)$ is the wind momentum ratio of both companions. Adopting our derived values from Table 5.2, we find $\eta = 0.48$, which yields $\theta = 76°$, in agreement with our results.

WWC may also manifest itself via powerful X-ray emission (Rauw & Naze 2015, and references therein). However, the presence of strong X-ray emission is not a necessary attribute of a colliding wind binary. Oskinova (2005) demonstrated that, on average, the ratio between stellar bolometric and X-ray luminosity ($\log L_{\rm X}/L_{\rm bol} \approx -7$) is similar among Galactic massive binary and single stars, not without exceptions (e.g., Eta Car, Corcoran et al. 1995). R 145 was detected by *Chandra* X-ray observatory (X-ray source designation CXOU J053857.06-690605.6, Townsley et al. 2014). The observations were taken over a period of 9 days around $T = 53760.7$ [MJD], corresponding to $\phi \approx 0.75$. Using $E_{\rm B-V}$ from Table 2 to estimate the interstellar neutral hydrogen column density, the observed count rate, and the median energy of the X-ray photons (Townsley et al. 2014), the X-ray luminosity of R 145 in the 0.2-12 keV band is $L_{\rm X} \approx 2 \times 10^{33}$ erg s^{-1}. This

corresponds to[2] $\log L_X/L_{bol,tot} \approx -6.9$. Thus, R 145 is not an especially luminous X-ray source, albeit it may be somewhat harder than a typical single star, as observed in other massive binaries (e.g., Nazé et al. 2011). Overall, the X-ray luminosity of R 145 is similar to that of other detected massive stars in the LMC (e.g., Naze et al. 2014)

The components of R 145 follow a highly eccentric orbit. Therefore, modulations of the X-ray emission with orbital phases are expected. Previous snap-shot observations are not suitable for detecting such orbital modulations. Dedicated monitoring X-ray observations of R 145 should provide the required information about energetic processes in its interacting stellar winds.

5.8. The evolution of the system

We now exploit the rich information derived here to constrain the evolutionary path of R 145. Unfortunately, despite using high-quality data in this study, the derived orbital masses suffer from large uncertainties (cf. Table 5.1). This is mainly due to the small inclination angle $i = 39°$, at which even a modest formal error of $6°$ translates to an error of $\approx 50\%$ in the mass. Moreover, due to non-linear biases, the value of i obtained is likely overestimated. Another hindrance is that the FLAMES spectra poorly cover the periastron passage (see Fig. 5.7). Nevertheless, the masses of both components could be derived to an unprecedented precision, and set important constraints on the system.

The first question that comes to mind is whether the stars in this system have interacted in the past via mass-transfer. To see whether the stars may currently be interacting via mass-transfer, we calculate the Roche lobe radii using the Eggelton approximation (Eggleton 1983). Using the semi major axis a, one finds $R_{RLOF,1} \approx R_{RLOF,2} \approx 360\,R_\odot$. At closest approach (periastron), the distance between the stars is $(1-e)\,a$, and the Roche lobe radii would be $R_{RLOF,1} \approx R_{RLOF,2} \approx 80\,R_\odot$. Thus, even at closest approach, the stars are safely within their Roche lobes (cf. Table 5.2).

This, however, does not imply that the system had not interacted in the past. Although the primary is likely still core H-burning, It cannot be excluded that the primary exhibited larger radii in the past. How compact the primary was throughout its evolution is strongly related to how homogeneous it was. Stars undergoing quasi-homogeneous evolution (QHE) tend to maintain much higher temperatures throughout their evolution and therefore remain relatively compact (e.g., Brott et al. 2011). Homogeneity is typically enhanced in stellar evolution codes by adopting large initial rotation velocities, which induce chemical mixing (Meynet & Maeder 2005; Heger & Langer 2000). Very massive stars may also be close to homogeneous simply due to their large convective cores and strong mass-loss rates (e.g., Gräfener et al. 2011; Vink et al. 2015). If the primary underwent QHE, mass-transfer was likely avoided in the system. Otherwise, mass-transfer had likely occurred in the system. Note that the fact that the system is highly eccentric is indicative that no mass-transfer has occurred, since RLOF tends to circularize an orbit (Hurley et al. 2002).

To gain more insight on this question, we compare the observables derived here to a set of evolutionary tracks calculated for single stars. We use tracks calculated by Brott et al. (2011) and Köhler et al. (2015) for initial masses in the range $5 \leq M_i \leq 500\,M_\odot$ and initial rotational velocities $0 \leq v_{rot,\,i} \lesssim 500\,\mathrm{km\,s^{-1}}$ at a metallicity of $Z = 0.0047$ ("Bonn" tracks hereafter), as well as tracks calculated with the BPASS[3] (Binary Population and Spectral Synthesis) code by Eldridge et al. (2011) and Eldridge & Stanway (2012) for homogeneous and non-homogeneous single stars with $5 \leq M_i \leq 150\,M_\odot$ and $Z = 0.004$ (BPASS tracks hereafter).

Finding the initial parameters and age which best reproduce the properties of both components according to the Bonn tracks is done most easily with the BONNSAI[4] Bayesian statistics tool (Schneider et al. 2014b). The disadvantage of the Bonn tracks is that they do not include the post core H-burning phase, which is why we also use the BPASS tracks, which include the full evolutionary path. While the secondary is almost certainly core H-burning given its spectral type, this cannot be considered certain for the WR primary,

[2]Note that we compare with the total bolometric luminosity of the system because both stars are expected to intrinsically emit X-rays.

[3]bpass.auckland.ac.nz

[4]The BONNSAI web-service is available at www.astro.uni-bonn.de/stars/bonnsai

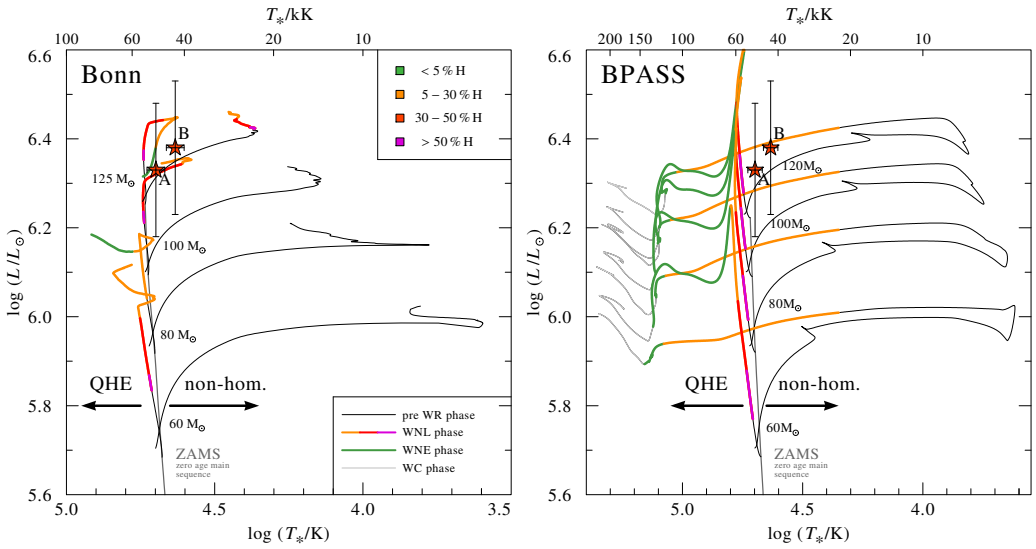

Figure 5.17.: The HRD positions of the primary (A) and secondary (B) components of R 145 compared to Bonn (left panel) and BPASS (right panel) evolutionary tracks calculated for (near-)homogeneous and non-homogeneous evolution for LMC metallicities. See text for details

although its properties and spectral type imply that it is likely core H-burning as well (e.g., Hainich et al. 2014).

Fig. 5.17 shows the Hertzsprung-Russell diagram (HRD) positions of the primary (A) and secondary (B) components of R 145 compared to a selected number of Bonn (left panel) and BPASS (right panel) evolutionary tracks. The colors code the amount of surface hydrogen content (see legend). We include both QHE models as well as non-homogeneous models. For the Bonn tracks, QHE is reached via high initial rotation rates; the tracks shown in Fig. 5.17 are calcualted for $v_{\mathrm{rot,\,i}} \approx 350\,\mathrm{km\,s^{-1}}$. The QHE BPASS tracks assume full homogeneity a priori; rotation is not considered in the BPASS code. Note that the QHE Bonn tracks are not fully homogeneous.

We first use the BONNSAI tool to find the initial parameters which best reproduce the observables T_*, L, X_{H}, and M_{orb} of the primary, accounting for the errors as found in this study. As could be anticipated, only tracks with large initial rotations ($v_{\mathrm{rot,\,i}} \gtrsim 350\,\mathrm{km\,s^{-1}}$) can reproduce its HRD position (see left panel of Fig. 5.17); the non-homogeneous tracks terminate at low temperatures and do not return to high temperatures because hydrogen is then exhausted in the core. To obtain a consistent set of initial parameters for the secondary, we use the BONNSAI tool again to compare with the secondary's observables, but this time, we also use the primary's age (and associated errors), as obtained from the BONNSAI tool. The resulting initial masses and age (as derived for the primary) are shown in Table 5.3. The Table also gives the current masses and hydrogen content of both components as predicted from the best-fitting evolutionary track. We note that the initial rotations obtained by the BONNSAI tool for the primary and secondary are $v_{\mathrm{rot,\,i}} = 410$ and $340\,\mathrm{km\,s^{-1}}$, respectively, while the predicted current rotational velocities are 240 and $260\,\mathrm{km\,s^{-1}}$. The current velocities are thus marginally consistent with the upper bounds given in Table 5.2.

A similar procedure is performed with the BPASS tracks. We use a χ^2 minimization algorithm to find the best-fitting homogeneous and non-homogeneous tracks and ages which reproduce the properties of the primary (see eq. 3 in Shenar et al. 2016). Once a track and age for the primary is inferred, we repeat the procedure for the secondary, adopting the primary's age an an associated error estimate which is based on the grid spacing. The corresponding initial parameters, ages, and current mass and surface hydrogen content, are given in Table 5.3. Because the BPASS tracks cover the whole evolution of the star, appropriate solutions can be found for the non-homogeneous case as well (see also right panel of Fig. 5.17). In Table 5.3,

we also give the maximum radius $R_{\mathrm{max,\,1}}$ reached by the primary throughout its evolution. This should give an indication to whether or not the primary has exceeded its Roche lobe radius in the past.

Both the Bonn tracks and the BPASS tracks imply very similar initial parameters and ages in the QHE case for both components. The tracks reproduce the observables reasonably well (compared to the errors), but the current masses predicted by the evolutionary tracks ($\approx 80-90\,M_\odot$) are larger than the orbital masses derived here ($\approx 55\,M_\odot$). Such masses would be obtained at an inclination of $\approx 33°$, which is roughly consistent with our formal error on i given in Table 5.1. The QHE scenario would therefore suggest that the actual masses are $\approx 80-90\,M_\odot$ per component. For the non-QHE scenario, only the BPASS tracks can place meaningful constraints. In this scenario, the properties of the primary are reproduced when the evolutionary tracks "return" from the red to the blue, and He-core burning initiates. This scenario is consistent with much lower current masses, closer to those derived here. However, significant discrepancy is obtained for the hydrogen content. More importantly, a comparison between the maximum radius reached by the primary and the Roche lobe implies that, assuming the non-homogeneous tracks, the primary overfilled its Roche lobe in the past. Note that the separation increases with time due to mass-loss, making mass-transfer inevitable in the non-homogeneous case. In this scenario, binary interaction therefore has to be accounted for.

Table 5.3.: Comparison with best-fitting evolution tracks

	Bonn		BPASS		
	non-hom.[a]	QHE[b]	non-hom.	QHE[c]	Binary[d]
$M_{\mathrm{i,1}}$ $[M_\odot]$	-	105 ± 20	100 ± 20	100 ± 20	120 ± 20
$M_{\mathrm{i,2}}$ $[M_\odot]$	-	91 ± 15	90 ± 20	90 ± 20	80 ± 20
$M_{\mathrm{cur,1}}$ $[M_\odot]$	-	77^{+30}_{-15}	48 ± 10	96	58
$M_{\mathrm{cur,2}}$ $[M_\odot]$	-	78^{+20}_{-10}	52 ± 10	85	113
Age [Myr]	-	2.3 ± 0.4	3.1 ± 0.3	2.1 ± 0.4	2.8 ± 0.4
$X_{\mathrm{H,1}}$ (mass fr.)	-	0.3 ± 0.1	0.1 ± 0.1	0.4 ± 0.1	0.1 ± 0.1
$X_{\mathrm{H,2}}$ (mass fr.)	-	$0.74^{+0}_{-0.25}$	0.1 ± 0.1	0.5 ± 0.1	-
$R_{\mathrm{max,\,1}}$ $[R_\odot]$	-	40	1500[e]	20	-

Notes. Initial parameters and predictions of best-fitting evolution tracks calculated for single stars experiencing homogeneous/non-homogeneous evolution. [(a)] Solution does not exist because the tracks terminate after exhaustion of H in the core (see Fig. 5.17). [(b)] QHE in the Bonn tracks is reached via an initial rotation velocity of $\approx 350\,\mathrm{km\,s^{-1}}$ for both components, which best-reproduces the observables. [(c)] These tracks are fully homogeneous a-priori; rotation is not accounted for in the BPASS tracks. [(d)] The tracks are identical to the non-homogeneous tracks, but include mass-transfer. The initial parameters defining the best-fitting track are $M_{\mathrm{i,1}} = 120\,M_\odot$, $q_{\mathrm{i}} = 0.7$, and $P_{\mathrm{i}} = 100\,\mathrm{d}$ [(e)] This value exceeds the Roche lobe radius of the primary by far, rendering this (single-star) solution inappropriate.

For this purpose, we used a set of tracks calculated with version 2.0 of the BPASS code (Eldridge et al. 2008) for $Z = 0.004$ which are non-homogeneous and account for mass-transfer. Each track is defined by an initial period P_{i}, an initial mass ratio $q_{\mathrm{i}} = M_{\mathrm{i,\,2}}/M_{\mathrm{i,\,1}}$, and an initial mass for the primary $M_{\mathrm{i,1}}$, calculated at intervals of 0.2 on $0 < \log P\,[\mathrm{d}] < 4$, 0.2 on $0 < q_{\mathrm{i}} < 0.9$, and $10 - 20\,M_\odot$ on $10 < M_{\mathrm{i,1}} < 150\,M_\odot$. The tracks do not include the hydrogen abundance of the secondary, so only a comparison with the primary's X_{H} is possible.

To find the track which best reproduces the observables, we use a χ^2 minimization algorithm (see eq. 4 in Shenar et al. 2016). We account here for T_*, L, M_{orb} for both components, X_{H} for the primary, the current period P, and the current mass-ratio $q = M_2/M_1 = K_1/K_2$. Note that we include the mass ratio because it has a much smaller formal error ($q = 1.01 \pm 0.07$), as opposed to the actual masses.

The parameters of the best fitting binary track are given in the last column of Table 5.3. Even the best fitting track results in a mass ratio of almost 2. The reason is that in all relevant tracks, RLOF from the primary to the secondary occurs, which tends to result in mass ratios significantly different than 1. The binary track also fails to reproduce the large hydrogen mass fraction inferred for the primary. Binary evolution tracks therefore do poorly in reproducing the system's observables.

To summarize, it appears that the system has evolved quasi-homogeneously, similarly to HD 5980 (Koenigsberger et al. 2014). This would suggest current masses of $\approx 80\,M_\odot$ and initial masses of $M_1 \approx 105\,M_\odot$ and $M_2 \approx 90\,M_\odot$. Admittedly, one may argue that it is unlikely for both stars to be born with initial rotational velocities in excess of $300\,\mathrm{km\,s^{-1}}$ (e.g., Ramírez-Agudelo et al. 2015), which are required for the QHE case judging by the Bonn tracks. However, as noted above, homogeneity can also be a quality which characterizes very massive stars by virtue of their large convective cores and strong mass-loss (Gräfener et al. 2011). Hence, the rotation which is needed for the BONN tracks may serve as a proxy for QHE rather than point at the actual physical mechanism responsible for homogeneity.

In Shenar et al. (2016), we argued that the majority of binaries in the Small Magellanic Cloud are not consistent with the QHE scenario. We suggested that tidal interaction could have slowed down the stellar rotations and thus suppressed the mixing. Since the separation of the components in R 145 is very large, however, tidal forces may be less important here (e.g., Hurley et al. 2002), except, perhaps, during periastron passage.

Assuming QHE indeed took place, there is no obvious reason to expect that the components would interact via RLOF in the future. This would be the case if the secondary would overfill its Roche lobe, which is currently hard to predict. It is possible that tidal forces would slowly suppress the mixing of the secondary, which would imply that it may reach the radii necessary to overfill its Roche lobe. Otherwise, the two stars are probably destined to become an eccentric double black hole system. With the help of fortunate kicks during core-collapse, the system could become close enough to merge within a Hubble time, emitting a gravitational wave event like those recently observed with LIGO (Abbott et al. 2016; Marchant et al. 2016).

5.9. Summary

We have performed an exhaustive analysis of the very massive system BAT99 119 (R 145) in the LMC, which was part of the Tarantula Massive Binary Monitoring (TMBM) campaign. Using high-quality FLAMES spectra, we detected and resolved for the first time lines from the secondary component and derived a first SB2 orbital solution for the system. The composite FLAMES spectral were disentangled to the constituent spectra of both components, and a spectral analysis was performed to derive the physical parameters of the components. This enabled us to confirm the primary's spectral type as WN6h, and to infer for the first time a spectral type for the secondary: O3.5 If*/WN7. A polarimetric analysis, as well as a WWC analysis, helped constrain the inclination of the system. Finally, a comparison with evolutionary tracks was conducted.

The system was previously speculated to host the most massive stars known ($M_1 > 300\,M_\odot$, S2009). From our orbital + polarimetric analysis, we derive $q = M_2/M_1 = 1.01 \pm 0.07$ and masses $M_1 \approx M_2 \approx 55^{+40}_{-20}\,M_\odot$. Thus, although the masses suffer from large uncertainties, we can exclude masses larger than $100\,M_\odot$ in the system.

We find clear evidence for WWC in the system. Interestingly, the signature of WWC is only clear in low-ionization transitions. We could only perform a rough quantitative spectroscopic analysis of the WWC spectral features because of the absence of very strong lines which are affected by WWC. The resulting inclination ($i = 40°$) is consistent with that obtained from polarimetry $i = 39°$), and the half opening angle ($\theta = 76°$) is consistent with the mass-loss rates and terminal velocities derived from the spectral analysis.

A comparison with quasi homogeneous and non-homogeneous Bonn and BPASS evolutionary tracks, the latter accounting for mass transfer as well, implies that quasi-homogeneous evolution (QHE) best describes the system. In this scenario, the components remain compact throughout their evolution and do not fill their Roche lobes. Non-homogeneous evolution would imply mass transfer, and this in turn leads to mass ratios which are very different than found here (≈ 1), which is why we can exclude non-homogeneous evolution

to a high degree of certainty. The high eccentricity found in this study ($e \approx 0.8$) is in line with the fact that the components did not interact via RLOF, which would tend to circularize the system. However, QHE is only consistent if the current masses are $\approx 80 - 90\,M_{\odot}$, which is roughly the upper limit of our derived orbital masses. In any case, the initial masses of the stars are found to be $M_{1,\,\mathrm{i}} \approx 105$ and $M_{2,\,\mathrm{i}} \approx 90\,M_{\odot}$.

Future spectroscopic and polarimetric observations are strongly encouraged to obtain more spectral phase coverage during periastron passage, which would constrain the orbital fit further and reduce uncertainties. A phase coverage of the red optical spectrum, as well as X-ray light curves, would be highly helpful in analyzing the WWC region to a much larger degree of accuracy, enabling an accurate derivation of the inclination, and a detailed study of WWC in this important system.

5.10. Acknowledgements

TS is grateful for financial support from the Leibniz Graduate School for Quantitative Spectroscopy in Astrophysics, a joint project of the Leibniz Institute for Astrophysics Potsdam (AIP) and the institute of Physics and Astronomy of the University of Potsdam. AFJM is grateful for financial aid from NSERC (Canada) and FQRNT (Quebec). NDR is grateful for postdoctoral support by the University of Toledo and by the Helen Luedke Brooks Endowed Professorship.

Chapter 6.

Wolf-Rayet stars in the Small Magellanic Cloud: Analysis of the binaries (Manuscript V)

T. Shenar, R. Hainich, H. Todt, A. Sander, W.-R. Hamann, A. F. J. Moffat, J. J. Eldridge, H. Pablo, L. M. Oskinova, N. D. Richardson

Astronomy & Astrophysics, 2016, Volume 591, 25 pp.

Abstract

Massive WR stars are evolved massive stars characterized by strong mass-loss. Hypothetically, they can form either as single stars or as mass donors in close binaries. About 40% of the known WR stars are confirmed binaries, raising the question as to the impact of binarity on the WR population. By performing a spectral analysis of all multiple WR systems in the SMC, we obtain the full set of stellar parameters for each individual component. Mass-luminosity relations are tested, and the importance of the binary evolution channel is assessed. The spectral analysis is performed with the PoWR model atmosphere code by superimposing model spectra that correspond to each component. Evolutionary channels are constrained using the BPASS evolution tool. Significant Hydrogen mass fractions (0.1 - 0.4) are detected in all WN components. A comparison with mass-luminosity relations and evolutionary tracks implies that the majority of the WR stars in our sample are not chemically homogeneous. The WR component in the binary AB 6 is found to be very luminous ($\log L \approx 6.3[L_\odot]$) given its orbital mass ($\approx 10\,M_\odot$), presumably because of observational contamination by a third component. Evolutionary paths derived for our objects suggest that Roche lobe overflow had occurred in most systems, affecting their evolution. However, the implied initial masses are large enough for the primaries to have entered the WR phase, regardless of binary interaction. Together with the results for the putatively single SMC WR stars, our study suggests that the binary evolution channel does not dominate the formation of WR stars at SMC metallicity.

6.1. Introduction

Stars with initial masses $M \gtrsim 20\,M_\odot$ may reach the Wolf-Rayet (WR) phase, which is characterized by strong stellar winds and hydrogen depletion, at a late stage of their evolution as they approach the Eddington limit (Conti 1976). There are two prevalent channels for a star to do so. On the one hand, the powerful radiation-driven winds of massive stars can peel off their hydrogen-rich layers, which leads to the typical emission line WR spectrum (Castor et al. 1975; Cassinelli 1979). On the other hand, mass donors in binary systems may shed copious amounts of mass during Roche lobe overflow (RLOF), approaching the Eddington limit owing to severe mass-loss (e.g. Paczynski 1973). Several studies (e.g. Maíz Apellániz 2010; Sota et al. 2011; Sana et al. 2012; Chini et al. 2012; Aldoretta et al. 2015) give direct evidence that at least half of all massive stars are binaries. Among the WR stars, about 40 % are confirmed binaries (van der Hucht 2001). It is inevitable that some of these systems contain interacting companions. Sana et al. (2013) estimate that roughly half of the O-type stars will interact with a companion via mass transfer during their

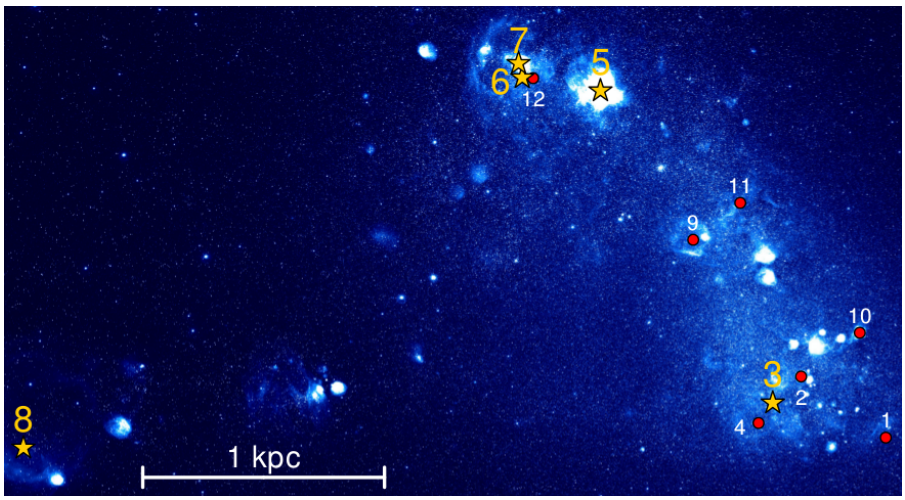

Figure 6.1.: Narrow band O [III] nebular emission image of the SMC (Smith et al. 2005) with all known WR stars marked. Yellow stars correspond to confirmed binary systems.

lifetime, and recent studies invoke binary interaction to explain a multitude of phenomena (e.g. Vanbeveren et al. 2007; Richardson et al. 2011; Langer 2012; de Mink et al. 2013). Yet the impact of binarity on the WR population remains debated (e.g. Vanbeveren et al. 1998; Crowther 2007).

Binaries are not only important from an evolutionary standpoint- they further enable one to deduce stellar parameters to an accuracy unattainable for single stars. For instance, if the orbital inclination i and both radial velocity (RV) curves can be obtained, the companions' masses can be accurately calculated from Newtonian dynamics. This method is indispensable in the case of WR stars, whose masses are otherwise difficult to determine. Knowledge of these masses provides a critical test not only of stellar evolution models, but also of mass-luminosity relations (MLRs) for WR stars (Langer 1989; Gräfener et al. 2011). Studies of wind-wind collisions (WWC) in massive binaries have proven fruitful for obtaining orbital inclinations (Luehrs 1997; Moffat 1998; Reimer & Reimer 2009). These types of wind collisions were also suggested to be prodigious X-ray sources (Cherepashchuk 1976; Prilutskii & Usov 1976), which was fully confirmed by subsequent observations and modeling efforts (e.g. Stevens et al. 1992; Zhekov 2012; Rauw & Naze 2015), and yielding important physical constraints on WR binaries.

Hence, there are various reasons why a spectroscopic and photometric analysis of WR binaries is essential for the study of massive stars. Despite this, binaries have often been left out in previous spectroscopic studies of WR stars (e.g. Hamann et al. 2006; Sander et al. 2012; Hainich et al. 2014) because of the complexity involved in their analysis. This paper begins to bridge the gap by presenting a systematic analysis of WR binaries.

An interesting test case for the impact of binarity on WR stars is offered by investigating low metallicity environments. Since the mass-loss rate $\dot{M}$ scales with surface opacity originating in metals, it is expected to decrease with decreasing surface metallicity Z (Kudritzki et al. 1987; Puls et al. 2000; Vink et al. 2000). For WR stars, recent empirical studies suggest $\dot{M} \propto Z$ (e.g. Nugis et al. 2007; Hainich et al. 2015). The smaller Z is, the harder it is for a single star to develop the stellar wind necessary to become a WR star. Standard stellar evolution models predict that, at solar metallicity, initial masses of $M_{\rm i} \gtrsim 20\,M_{\odot}$ are sufficient for single stars to reach the WR phase, while at Small Magellanic Cloud (SMC) metallicity, masses of at least $\sim 45\,M_{\odot}$ are required (Meynet & Maeder 2005). The frequency of single WR stars is thus expected to decrease with Z. In contrast, the frequency of WR stars formed via RLOF is not a priori expected to depend on Z.

Motivated by such predictions, Foellmi et al. (2003b), Foellmi, Moffat, & Guerrero (2003a, FMG hereafter), Schnurr et al. (2008b), and Bartzakos et al. (2001a) conducted a large spectroscopic survey in the Small and Large Magellanic Cloud (SMC and LMC, respectively) with the goal of measuring the

binary fraction in their respective WR populations. The LMC and SMC are both known to have a subsolar metallicity: a factor $\sim 1/3$ and $\sim 1/7$ solar, respectively (Dufour et al. 1982; Larsen et al. 2000). Following the reasoning of the previous paragraph, it is expected that the fraction of WR stars formed via RLOF will be relatively large in the LMC, and even larger in the SMC. Bartzakos et al. (2001a) made use of stellar evolution statistics published by Maeder & Meynet (1994) to predict that virtually *all* WR stars in the SMC are expected to have been formed via RLOF. Similar predictions remain even with the most recent generation of stellar evolution codes (e.g. Georgy et al. 2015). It was therefore surprising that FMG measured a WR binary fraction in the SMC of $\sim 40\,\%$, consistent with the Galactic fraction, revealing a clear discrepancy between theory and observation which must be explained.

Table 6.1.: Overview of the known WR stars in the SMC and their binary status

Object	Spectral Type	V [mag]	Status	K_1 [km s^{-1}]	K_2 [km s^{-1}]	P [d]	i [°][a]	e
SMC AB 1	WN3ha	15.1	-	-	-	-	-	-
SMC AB 2	WN5ha	14.2	-	-	-	-	-	-
SMC AB 3[b]	WN3h + O9	14.5	SB2	144	-	10.1	57^{+33}_{-29} [c]	0.09
SMC AB 4	WN6h	13.3	-	-	-	-	-	-
SMC AB 5[d]	(WN6h+WN6-7)+(O+?)	11.1	SB3[e]	214	200	19.3	86^{+1}_{-1} [f]	0.27
SMC AB 6	WN4 + O6.5I:	12.3	SB2	290	66	6.5	57^{+33}_{-12} [g]	0.1
SMC AB 7[h]	WN4 + O6I(f)	12.9	SB2	196	101	19.6	68^{+22}_{-15} [g]	0.07
SMC AB 8[i]	WO4 + O4V	12.8	SB2	176	55	16.6	40^{+10}_{-3}	0
SMC AB 9	WN3ha	15.2	Uncertain	43	-	34.2	-	0.22
SMC AB 10	WN3ha	15.8	-	-	-	-	-	-
SMC AB 11	WN4ha	15.7	-	-	-	-	-	-
SMC AB 12[j]	WN4(?)	15.5	-	-	-	-	-	-

Notes. All entries adopted from FMG unless otherwise specified. Stars analyzed here are denoted with large fonts.
[a] Errors on i are subject to realistic constraints on the O-companion mass (see text) [b] Although AB 3 is an SB2 binary, FMG could not measure K_2 because of the secondary's faintness [c] i corresponds to a mean value (see text) [d] Spectral type of the primary variable (WN3/11), but WN6h (FMG) corresponds to the most recent spectra used here. All other entries adopted from Koenigsberger et al. (2014), and references therein [e] i.e. three out of the four components are apparent in the available spectra [f] Adopted from Perrier et al. (2009) [g] i calibrated against secondary's spectral type (see text) [h] Orbital parameters adopted from Niemela et al. (2002), whose solution is more accurate than that presented by FMG (FMG) [i] Moffat et al. (1990), St-Louis et al. (2005), and references therein [j] Massey et al. (2003)

Hainich et al. (2015, paper I hereafter) conducted a spectral analysis of the putatively single WR stars in the SMC. In the present paper, we perform a non-local thermodynamic equilibrium (non-LTE) spectral analysis of the WR binary systems. Having derived the full set of parameters for all components of each system, we test current MLRs, and deduce evolutionary paths for each system.

The paper is structured as follows: Sects. 6.2 and 6.3 give an overview of our sample and the observational data used. In Sect. 6.4, we describe the assumptions and methods involved in the spectral analysis. In Sect. 6.5, we give the full set of stellar parameters derived, while Sect. 6.6 contains a thorough discussion and interpretation of our results. A summary of our results is found in Sect. 6.7. The appendices include a detailed description on the properties and analysis of our objects (A), their evolutionary paths (B), and their spectral fits (C).

6.2. The sample

There are 12 WR stars currently known in the SMC (Massey et al. 2014). Fig. 6.1 marks the positions of the known SMC WR stars on a narrow band image of the O [III] nebular emission line. Five out of the 12 stars are in confirmed binary or multiple systems based on their RV curves (FMG), marked with yellow stars in Fig. 6.1. As in paper I, we follow the name scheme SMC AB # (sometimes simply AB #), as introduced by Azzopardi & Breysacher (1979). Table 6.1 gives an overview on the 12 WR stars currently known in the SMC and their binary status. All but one are WN (nitrogen rich) stars; the WO (oxygen rich) primary in AB 8 is the exception. For the binary systems, we give the two velocity amplitudes K_1 and K_2, periods P, orbital inclinations i, and eccentricities e, if known. For the quadruple system AB 5, the orbital parameters refer to the short period WR + WR binary within the system.

The adopted orbital inclination angles i heavily affect the deduced orbital masses $M_{\rm orb}$ ($M_{\rm orb} \propto \sin^3 i$). The inclinations of AB 5 and 8 could be constrained in other studies thanks to photospheric/wind eclipses. Since i is the only free parameter determining the orbital masses in the case of AB 6 and 7, we use calibrations by Martins et al. (2005) to fix their inclinations so that the secondary's orbital mass agrees with its spectral type[1]. With both i and K_2 unknown in the case of AB 3, we fix i to its mean statistical value so that $\sin^3 i = \left\langle \sin^3 i \right\rangle = 3\,\pi/16$, and adjust K_2 to calibrate the secondary's mass against its spectral type.

In all systems, we conservatively assume an uncertainty of no more than a factor two in the secondary's orbital mass, and assume the realistic constraints $15\,M_\odot \leq M_{\rm O} \leq 70\,M_\odot$ and $M_{\rm WR} \geq 5\,M_\odot$ for the O and WR stars in the sample, respectively (e.g. Martins et al. 2005; Crowther 2007). If additional constraints on i are known from other studies, they are considered as well. This restricts i to a corresponding value range.

The binary candidate SMC AB 9 (cf. Table 6.1) is omitted from this analysis. The star was already analyzed as a single star in paper I because of the absence of any spectral features which could be associated with a companion in its spectrum. For the same reason, we treat SMC AB 5 (HD 5980) as a triple system, and not a quadruple. None of the spectral features are clearly associated with the fourth component, whose existence is anticipated based on a periodic variability of the absorption lines associated with the third component (Breysacher et al. 1982; Koenigsberger et al. 2014).

6.3. Observational data

6.3.1. Spectroscopic data

For three systems (AB 3, 6, and 7), we use normalized, low-resolution spectra (FWHM $\approx 2.8 - 6.7$ Å) obtained by FMG in the spectral range of 3900–6800 Å between the years 1998 and 2002. Detailed information on the instrumentation used and the data reduction can be found in FMG. To obtain a relatively high Signal-to-Noise ratio (S/N) of about $100 - 150$, spectra taken at different binary phases were co-added in the frame of the primary. Although the reduced spectra used by FMG for RV studies are available for download, the online data suffer from obvious wavelength calibration problems for reasons that we could not trace. The original data could not be retrieved. Due to this and the poor S/N of the original spectra, we make use only of the co-added spectra in this study. Co-adding the spectra in the frame of the WR star causes the companion's spectral features (an O star in these systems) to smear. Its lines would thus appear broader and shallower than they should, although their equivalent width remains conserved. To account for this effect, we convolve the companion's model with a box function of the width $K_1 + K_2$ when comparing to these spectra. Given the low resolution of the spectra, this effect is of secondary importance. If possible, auxiliary spectra were used to derive parameters which are sensitive to the line profile.

For all of our targets, we downloaded flux calibrated spectra taken with the International Ultraviolet Explorer (IUE) covering the spectral range $1200 - 2000$ Å from the MAST archive. When available, high resolution spectra are preferred, binned at intervals of 0.05 Å to achieve an S/N$\approx$ 15. Otherwise, low resolution spectra are used (FWHM $\approx$ 6 Å, S/N $\approx$ 20). Low resolution, flux calibrated IUE spectra in the range $2000 - 3000$ Å are not used for detailed spectroscopy because of their low S/N ($\approx 5 - 10$), but

[1] While the calibration depends on Z, the effect of metallicity on the spectral type-mass calibration is smaller than the typical errors given here

rather to cover the spectral energy distribution (SED) of the targets. Optical low resolution spectra taken by Torres-Dodgen & Massey (1988) are also used for the SEDs of our targets. Flux calibrated, high resolution Far Ultraviolet Spectroscopic Explorer (FUSE) spectra covering the spectral range 960 – 1190 Å are also retrieved from the MAST archive and binned at 0.05 Å to achieve an S/N ≈ 30, except for AB 3, for which no usable FUSE spectra could be obtained. The IUE and FUSE spectra are normalized with the reddened model continuum.

For AB 5, we use auxiliary flux calibrated, high resolution (FWHM ≈ 0.02 Å) spectra taken in 2009 during primary eclipse ($\phi = 0$) with the STIS instrument mounted on the Hubble Space Telescope (HST) covering the spectral range 1150 – 1700 Å, with S/N ≈ 30 (Koenigsberger et al. 2010). The spectra are also normalized using the model continuum. Unfortunately, no out-of-eclipse UV spectra taken after the year 1999 are available in the archives. For this system, we also retrieved several high resolution spectra taken in 2005 with the Fiber-Fed Extended Range Optical Spectrograph (FEROS) mounted on the MPI 2.2 m telescope at La Silla, covering the spectral range 3750 – 9200 Å at a resolution of FWHM ≈ 0.1 Å and S/N ≈ 40. The data were reduced and used by Foellmi et al. (2008), where more information can be found. Additionally, we use a spectrum created by co-adding several spectra at phase $\phi = 0$ to achieve a S/N ≈ 200, made available by Foellmi et al. (2008).

For AB 8, we make use of a reduced, flux calibrated spectrum with a resolution of FWHM ≈ 0.2 Å and S/N ≈ 100 taken with the X-shooter spectrograph mounted on ESO's Very Large Telescope (VLT), covering the range 3000 – 25000 Å (Vernet et al. 2011). The reduced spectrum was kindly supplied to us by F. Tramper (see Tramper et al. (2013) for details).

The dates and ID numbers of all spectra used here are given in the figures showing them. Phases are calculated with ephemeris given by FMG, except for AB 8 and 5, where the ephemeris given by St-Louis et al. (2005) and Koenigsberger et al. (2014) are used, respectively. The spectral resolution is accounted for by convolving the models with corresponding Gaussians to mimic the instrumental profile.

6.3.2. Photometric data

Aside from flux-calibrated data, we use for all stars analyzed here *JHK* and IRAC photometry from Bonanos et al. (2010). If available, we also use their *UBVRI* magnitudes. For AB 5, we use the *U* and *BVR* magnitudes from Torres-Dodgen & Massey (1988) and Zacharias et al. (2005), respectively; For AB 6, we use UBV magnitudes from Mermilliod (1995); for AB 8, we use the UBV magnitudes from Massey (2002) and *I* magnitude given by the DENIS Consortium (2005). For all stars, we use WISE magnitudes from Cutri & et al. (2013).

6.4. Non-LTE spectral modeling of WR binaries

6.4.1. The PoWR code

PoWR is a non-LTE model atmosphere code especially suitable for hot stars with expanding atmospheres[2]. The code iteratively solves the co-moving frame radiative transfer and the statistical balance equations in spherical symmetry under the constraint of energy conservation. A more detailed description of the assumptions and methods used in the code is given by Gräfener et al. (2002) and Hamann & Gräfener (2004). By comparing synthetic spectra generated by the code to observations, a multitude of stellar parameters can be derived.

The inner boundary of the model, referred to as the stellar radius R_*, is defined at the Rosseland optical depth $\tau_{\rm Ross}$=20, where LTE can be safely assumed. In the subsonic region, the velocity field is defined so that a hydrostatic density stratification is approached (Sander et al. 2015). In the supersonic region, the pre-specified wind velocity field $v(r)$ generally takes the form of the β-law (Castor et al. 1975)

$$v(r) = v_\infty \left(1 - \frac{r_0}{r}\right)^\beta . \tag{6.1}$$

[2]PoWR models of Wolf-Rayet stars can be downloaded at http://www.astro.physik.uni-potsdam.de/PoWR.html

Here, v_∞ is the terminal velocity, and $r_0 \approx R_*$ is a constant determined so as to achieve a smooth transition between the subsonic and supersonic regions.

Beside the velocity law and chemical composition, four fundamental input parameters are needed to define a model atmosphere: the effective temperature T_*, the surface gravity g_*, the mass-loss rate $\dot{M}$, and the stellar luminosity L. The effective temperature relates to R_* and L via the Stefan-Boltzmann law: $L = 4\pi\sigma R_*^2 T_*^4$. The gravity g_* relates to the radius R_* and mass M_* via the usual definition: $g_* = g(R_*) = G M_* R_*^{-2}$. For the vast majority of WR models, the value of g_* bears no significant effects on the synthetic spectrum, which originates primarily in the wind. The outer boundary is taken to be $R_{\max} = 100\,R_*$ for O models and $1000\,R_*$ for WR models, which were tested to be sufficient.

During the iterative solution, the line opacity and emissivity profiles at each radial layer are Gaussians with a constant Doppler width $v_{\rm Dop}$. This parameter is set to 30 and $100\,\mathrm{km\,s^{-1}}$ for O and WR models, respectively. In the formal integration, the Doppler velocity is decomposed to depth-dependent thermal motion and microturbulence $\xi(r)$. We assume $\xi(r)$ grows with the wind velocity up to $\xi(R_{\max}) = 0.1\,v_\infty$, and set $\xi(R_*) = 20\,\mathrm{km\,s^{-1}}$ for O models and $100\,\mathrm{km\,s^{-1}}$ for WR models, respectively (e.g. Hamann et al. 2006; Bouret et al. 2012; Shenar et al. 2015). We assume a macroturbulent velocity of $30\,\mathrm{km\,s^{-1}}$ for all O components (e.g. Markova & Puls 2008; Bouret et al. 2012), accounted for by convolving the profiles with radial-tangential profiles (e.g. Gray 1975; Simón-Díaz & Herrero 2007).

It has become a consensus that winds of massive stars are not smooth, but rather clumped (Moffat et al. 1988; Lépine & Moffat 1999; Markova et al. 2005; Oskinova et al. 2007; Prinja & Massa 2010; Šurlan et al. 2013). An approximate treatment of optically thin clumps using the so-called microclumping approach was introduced by Hillier (1984) and systematically implemented by Hamann & Koesterke (1998), where the population numbers are calculated in clumps which are a factor of D denser than the equivalent smooth wind ($D = 1/f$, where f is the filling factor).

Because optical WR spectra are dominated by recombination lines, it is customary to parametrize their models using the so-called transformed radius (Schmutz et al. 1989),

$$R_{\rm t} = R_* \left[\frac{v_\infty}{2500\,\mathrm{km\,s^{-1}}} \Big/ \frac{\dot{M}\sqrt{D}}{10^{-4}\,M_\odot\,\mathrm{yr^{-1}}} \right]^{2/3}, \tag{6.2}$$

defined such that equivalent widths of recombination lines of models with given $R_{\rm t}$ and T_* are approximately preserved, independently of L, $\dot{M}$, D, and v_∞. While $R_{\rm t}$ has the dimensions of length, it should be thought of as an integrated volume emission measure per stellar surface area.

6.4.2. Assumptions

PoWR models are limited to spherical symmetry, which obviously breaks down in the case of close binary systems. Firstly, the stars are deformed into a tear-like shape due to tidal forces. Secondly, non-spherical manifestations resulting from binary interaction, such as WWC cones or asymmetrical accretion flows, may occur in binary systems. While such phenomena may be significant or even dominant in the case of specific lines (e.g. Bartzakos et al. 2001b), they typically amount to flux variations of the order a few percent (e.g. Hill et al. 2000; Palate et al. 2013), with the possible exception of AB 5 (see Appendix C.1).

The detailed form of the velocity field in the wind domain can affect spectral features originating in the wind. WR models are therefore more sensitive to the velocity law than O-star models. The finite disk correction predicts a β-law (Eq. 6.1) in the case of OB-type stars with $\beta = 0.8$ (e.g. Kudritzki et al. 1989), which we adopt for the O-star models. This value is consistent with analyses of clump propagation in O-type stars (e.g. Eversberg et al. 1998). As for WR stars, there are several empirical studies which suggest that the β exponents in the outer winds of WR stars with strong winds are in excess of four (Lépine & Moffat 1999; Dessart & Owocki 2005). On the other hand, β values of the order of unity are found for hydrogen rich WR stars (Chené et al. 2008), which describes most of our sample. For the WR components, we thus always assume the usual β-law with $\beta = 1$.

The data do not always enable us to derive the chemical abundances for each element, in which case we assume the following. For the O companions, we adopt H, C, N, O, Mg, Si, and Fe mass fractions as derived for B stars in the SMC by Korn et al. (2000), Trundle et al. (2007), and Hunter et al. (2007):

$X_{\rm H} = 0.73$, $X_{\rm C} = 2.1 \cdot 10^{-4}$, $X_{\rm N} = 3.26 \cdot 10^{-5}$, $X_{\rm O} = 1.13 \cdot 10^{-3}$, $X_{\rm Mg} = 9.9 \cdot 10^{-5}$, $X_{\rm Si} = 1.3 \cdot 10^{-4}$, and $X_{\rm Fe} = 3 \cdot 10^{-4}$. We scale the mass fractions of the remaining metals to 1/7 solar, in accordance with the ratio of the solar metallicity (Asplund et al. 2009) to the average SMC metallicity (Trundle et al. 2007): $X_{\rm Ne} = 1.8 \cdot 10^{-4}$, $X_{\rm Al} = 7.6 \cdot 10^{-6}$, $X_{\rm P} = 8.3 \cdot 10^{-7}$, $X_{\rm S} = 4.4 \cdot 10^{-5}$. The same mass fractions are adopted for WR models, except for $X_{\rm H}$, which is derived in each case, and the CNO mass fractions, which are adopted as in paper I: $X_{\rm C} = 2.5 \cdot 10^{-5}$, $X_{\rm N} = 1.5 \cdot 10^{-3}$, $X_{\rm O} = 1.0 \cdot 10^{-6}$.

A longstanding problem is assessing the density contrast in clumps and their stratification in the atmosphere. Here, $D(r)$ is assumed to be depth-dependent, increasing from 1 (smooth wind) at the base of the wind to a maximum value D (e.g. Owocki et al. 1988). Quite generally, allowing $D(r)$ to be depth-dependent yields more symmetric, less "self-absorbed" line profiles, as illustrated in Fig. C.1 in the appendix. It is found that a depth dependent clumping factor which initiates from $D(R_*) = 1$ at the base of the wind and grows proportionally to the wind velocity to the value $D(r) = D$ at $v(r) \geq 0.5\, v_\infty$ provides a good agreement with the observations, which tend to exhibit symmetric profiles. The maximal value D can be roughly constrained for each WR star (see Sect. 6.4.3), and is treated as a free parameter. We note that other studies suggest clumping may already initiate at the photosphere (e.g. Cantiello et al. 2009; Torrejón et al. 2015). Clumping factors for the O companions, which cannot be deduced from the available spectra, are fixed to $D = 10$, supported by hydrodynamical simulations (Feldmeier et al. 1997). When the companions' mass-loss rates cannot be constrained, we adopt them from hydrodynamical predictions by Vink et al. (2000).

We adopt a distance of $d = 62$ kpc to the SMC (Keller & Wood 2006). The reddening towards our objects is modeled using a combination of the reddening laws derived by Seaton (1979) for the Galaxy, and by Gordon et al. (2003) for the SMC. As in paper I, we assume an extinction of $E_{B-V} = 0.05$ for the Galactic component (Sect. 4.3 in paper I) and fit for the total extinction, adopting $R_{\rm V} = 3.1$.

6.4.3. The analysis method

The non-LTE analysis of spectra, even in the case of single stars, is an iterative and computationally expensive process. Generally, g_* is inferred from the wings of photospheric H and He II absorption lines. The effective temperature T_* is inferred from the line ratios of ions belonging to the same element, mostly He lines for the O stars, and mostly metal lines for WR stars. Wind parameters such as $\dot{M}$ (or $R_{\rm t}$) and v_∞ are derived from recombination and P Cygni lines. If possible, the maximum density contrast D is derived from electron-scattering wings. The luminosity L and total extinction E_{B-V} are determined by fitting the combined spectral energy distribution (SED) of the models to the photometric measurements. The abundances are determined from the overall strengths of lines belonging to the respective elements. Finally, the projected rotation velocity $v \sin i$ is constrained from profile shapes. For the O companions, this is done by convolving the models with appropriate rotation profiles. For the WR stars, if the resolution and S/N enable such an analysis, we derive upper limits for rotation by applying a 3D integration scheme, assuming co-rotation up to $\tau_{\rm Ross} = 2/3$ (Shenar et al. 2014).

To analyze a multiple system, models for each of its components are required. Ideally, one would disentangle the composite spectrum to its constituent spectra by observing the system at different phases (e.g. Bagnuolo & Gies 1991; Hadrava 1995; Marchenko & Moffat 1998). Unfortunately, our data are not adequate for this purpose. Moreover, spectral disentangling does not yield direct information regarding the light ratios unless the stellar system is eclipsing. Since we work with composite spectra, our task is therefore to combine models in such a way that the composite spectrum and SED are reproduced. An example is shown in Figs. 6.3 and 6.2, where a comparison between the SED and observed rectified spectra of the binary system SMC AB 6 and our best fitting models is shown, respectively.

As opposed to single stars, the luminosities of the components influence their relative contribution to the flux and thus the synthetic normalized spectrum. The light ratios of the different components therefore become entangled with the fundamental stellar parameters, and it is not trivial to overcome the resulting parameter degeneracy. The analysis of composite spectra thus consists of the following steps:

- *Step 1:* Based on line ratios and previous studies (e.g. spectral types), preliminary models for the O and WR companions are established. If necessary, the spectra are shifted to account for

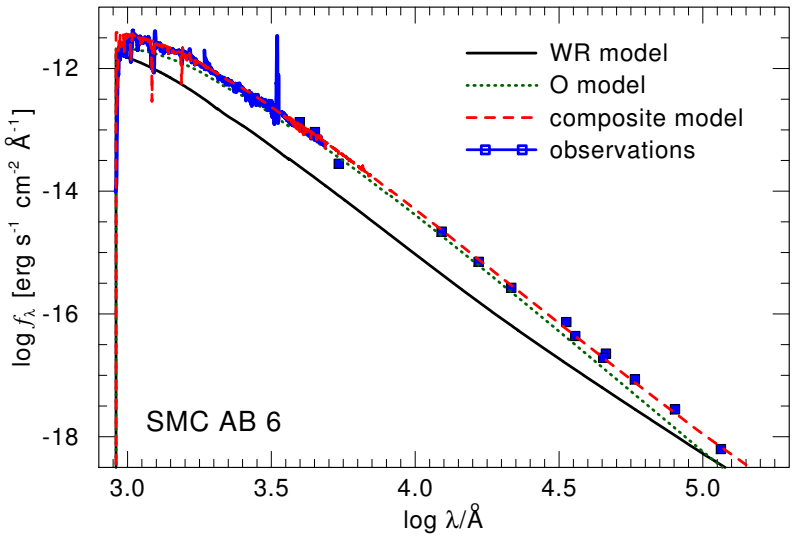

Figure 6.2.: The observed SED of AB 6 (blue lines and squares) compared to the synthetic SED (red dashed line), which is the sum of the WR (black solid line) and O (green dotted line) models.

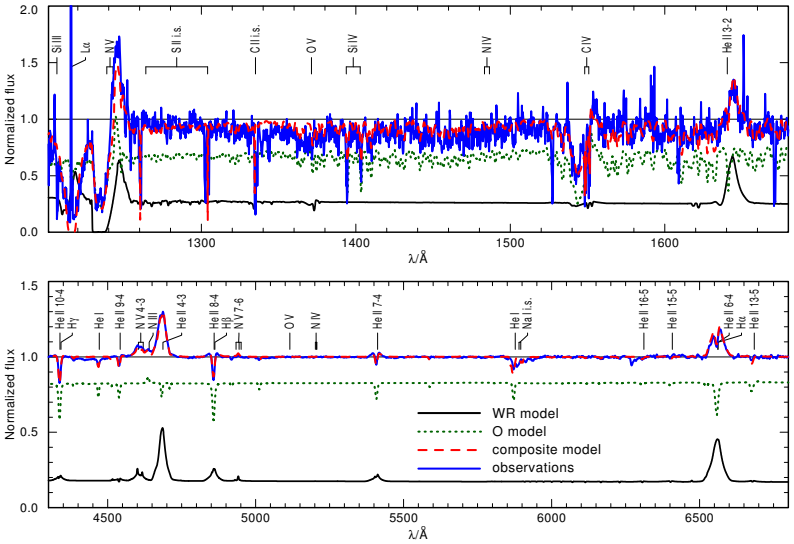

Figure 6.3.: A comparison between IUE (ID:sp41784, $\phi = 0.47$) and optical (co-added, FMG) rectified spectra of SMC AB 6 (blue ragged line) and the composite synthetic spectrum (red dashed lines). The composite model is the sum of the WR (black solid line) and O (green dotted line) models. The relative offsets of the model continua correspond to the light ratio between the two stars. Note that the light ratios are different in the optical and UV due to the different temperatures of both components.

systemic/orbital motion.

- *Step 2:* The light ratios are derived (or constrained) by identifying absorption features which can be clearly associated with the O companion and which are preferably not sensitive to variations of its physical parameters. While identifying the WR lines is usually easier, their strengths strongly

depend on the mass-loss rate and thus do not enable one to determine the light ratios independently.

- *Step 3:* The luminosity of one of the companions and the reddening of the system are adjusted to fit the available photometry. Since the light ratio is known/constrained, the luminosity of the companion follows.
- *Step 4:* $\dot{M}$ (or R_t), D, and v_∞ are adjusted for the WR model based on the strengths of its lines.
- *Step 5:* If needed, the parameters of the WR and O models are further refined. If any wind lines can be associated with the O companion, its wind parameters are adjusted.
- *Step 6:* With the refined models, steps 2 - 5 are repeated until no significant improvement to the fit of prominent lines (at a few percent level) can be achieved.

The set of spectral lines most diagnostic for the analysis generally depends on the system. In Fig. 6.4, we show an example for two photospheric features which originate in the secondary beyond doubt, and which greatly help to deduce the light ratio in the case of SMC AB 6: the P v $\lambda\lambda$ 1118, 1128 resonance doublet (left panel) and the strong C III multiplet at $\approx \lambda$1176 (right panel). Optical He lines as well as the spectral type imply $30 < T_* < 40$ kK for the secondary. A careful comparison of O star models in this temperature range reveals that these lines are insensitive to temperature and gravity variations. We thus conclude that the relative strength of such lines in the normalized spectrum is affected primarily by the light ratio. The features imply a similar light ratio of $F(\mathrm{O})/F(\mathrm{WR}) \sim 2$ in the FUSE domain, and agree with the other features in the available spectra, e.g. sulfur lines. While this method is sensitive to the adopted abundances, X_P and X_S should remain fairly constant (e.g. Bouret et al. 2012) throughout the stellar evolution. A multitude of lines is used for each system to reduce the probability for a systematic deviation.

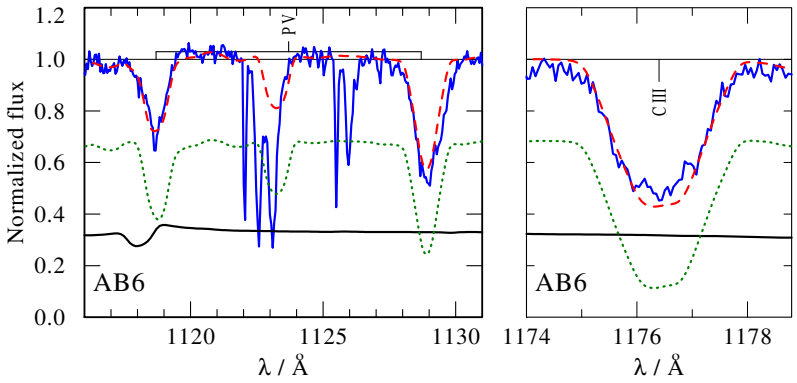

Figure 6.4.: A comparison between the rectified FUSE observation of AB 6 (ID:X0150102000, $\phi = 0.44$, blue ragged line) and the composite synthetic spectrum (red dashed line) for the P v $\lambda\lambda$ 1118, 1128 resonance doublet and the C III multiplet at $\sim \lambda$1176. The WR and O models are depcited by a black solid line and green dotted line, respectively. The narrow absorption features originate in the interstellar medium (ISM).

Another robust way for determining the light ratios is offered by high resolution P Cygni line profiles. An example is shown in the left and right panels of Fig. 6.5. The left panel shows a high resolution HST spectrum of the C IV resonance doublet of the quadruple system AB 5, taken at $\phi \cong 0$ during an eclipse of the secondary (B) by the primary (A). The spectrum clearly shows a P Cygni absorption consisting of two contributions originating in the primary and tertiary (C). As Georgiev et al. (2011) already demonstrated, the strength of the "step" observed in the C IV doublet is influenced by the components' light ratio. The different terminal velocities of stars A and C cause the more extended part of the line to appear unsaturated. The right panel shows the N v resonance doublet $\lambda\lambda$ 1239, 1243 for the WO binary AB 8, which clearly originates in the O companion and which is typically saturated in observations of single O stars with strong

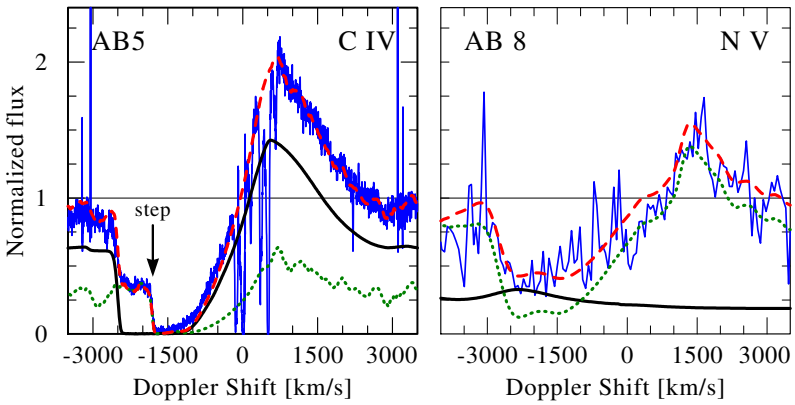

Figure 6.5.: Same as Fig. 6.4, but showing the observed C IV $\lambda\lambda$ 1548, 1551 resonance doublet in AB 5 (HST, ID:ob2na1020, $\phi \cong 0$, left panel) and the observed N V resonance doublet $\lambda\lambda$ 1239, 1243 in AB 8 (IUE, ID:sp07623, $\phi = 0.79$, right panel) in velocity space relative to the respective blue components of each doublet. Colors are as in Fig. 6.4.

winds (e.g. Walborn 2008; Bouret et al. 2012), but is not saturated here because of light dilution by the WO component. Such features give sharp constraints on the light ratios.

WR stars are almost always devoid of pure photospheric features and so their surface gravities cannot be determined via spectral analysis. Their gravities are fixed to $G\,M_{\rm orb}\,R_*^{-2}$ throughout the analysis, after R_* has been determined, but we note that the appearance of the WR spectra calculated here are virtually independent of $\log g$. Determining the gravity of the secondaries proved to be a hard task, leading to large errors in $\log g$. As described in Sect. 6.3, the co-added optical spectra of AB 3, 6, and 7 suffer from low resolution and a smearing of the companion's features. However, while the profiles of the Balmer and He II lines cannot be studied in detail because of the quality of the spectra, their equivalent widths grow with increasing $\log g_*$, which enabled its rough estimation.

In Appendix C.1, we give an overview on each analyzed system, supply a thorough documentation of the analysis, and highlight spectral features of notable interest.

6.5. Results

Table 6.2 summarizes the stellar parameters derived for the components of the five systems analyzed. The spectral fits are available in Appendix C.3 (Figs. C.3 to C.8). The Table also includes the temperatures and radii at $\tau_{\rm Ross} = 2/3$, H, C, N, O abundances, Johnson V magnitudes, projected and equatorial rotation velocities $v \sin i$ and $v_{\rm eq}$, total reddenings E_{B-V} and extinctions A_V, and Roche lobe radii $R_{\rm RL}$, calculated from the orbital masses using the Eggleton approximation (Eggleton 1983). We also give several types of stellar masses: $M_{\rm H\text{-}b}$ and $M_{\rm He\text{-}b}$ are derived for WR stars from MLRs calculated by Gräfener et al. (2011) for chemically homogeneous core H- and He-burning stars, respectively (see Sect. 6.6.1). $M_{\rm g} = G^{-1}\,g_*\,R_*^2$ is inferred from the derived surface gravity. Finally, $M_{\rm orb}$ denotes the orbital masses, calculated from the orbital parameters given in Table 6.1.

Uncertainties for the fundamental stellar parameters are estimated by examining the sensitivity of the fits to changes in the corresponding parameters. These include errors on T_*, $\log g_*$, $\log L$, $\log R_{\rm t}$, v_∞, D, $E_{\rm B-V}$, $v \sin i$ and abundances. Error propagation is used for the remaining parameters. Errors on $\dot{M}$ include only errors on $R_{\rm t}$. Errors on $M_{\rm orb}$ are dominated by errors on i (cf. Table 6.1), except for AB 5, where the uncertainty on the orbital solution dominates (Koenigsberger et al. 2014).

Table 6.2.: Inferred stellar parameters for the SMC WR binaries

	AB3		AB5			AB6		AB7		AB8	
Component	A	B	A	B	C	A	B	A	B	A	B
Spectral type[a]	WN3h	O9	WN6h	WN6-7	O	WN4	O6.5 I	WN4	O6 I(f)	WO4	O4 V
T_* [kK]	78^{+5}_{-5}	30^{+5}_{-5}	45^{+5}_{-5}	45^{+10}_{-7}	34^{+3}_{-3}	80^{+15}_{-10}	37^{+3}_{-3}	105^{+20}_{-10}	36^{+3}_{-3}	141^{+60}_{-20}	45^{+5}_{-5}
$T_{2/3}$ [kK]	77^{+5}_{-5}	30^{+3}_{-5}	43^{+5}_{-5}	43^{+10}_{-7}	33^{+3}_{-3}	78^{+15}_{-10}	37^{+3}_{-3}	98^{+20}_{-10}	35^{+3}_{-3}	115^{+10}_{-10}	44^{+5}_{-5}
$\log g_*$ [cm s^{-2}][b]	4.3	$3.9^{+0.3}_{-0.3}$	3.5	3.5	$3.2^{+0.2}_{-0.2}$	3.7	$3.5^{+0.2}_{-0.2}$	4.7	$3.6^{+0.2}_{-0.2}$	5.1	$4.0^{+0.3}_{-0.3}$
$\log L$ [$L_\odot$]	$5.93^{+0.05}_{-0.05}$	$4.5^{+0.2}_{-0.2}$	$6.35^{+0.10}_{-0.10}$	$6.25^{+0.15}_{-0.15}$	$5.85^{+0.10}_{-0.10}$	$6.28^{+0.10}_{-0.10}$	$5.90^{+0.10}_{-0.10}$	$6.10^{+0.10}_{-0.10}$	$5.50^{+0.10}_{-0.10}$	$6.15^{+0.10}_{-0.10}$	$5.85^{+0.10}_{-0.10}$
$\log R_t$ [$R_\odot$]	$1.07^{+0.05}_{-0.05}$	-	$1.15^{+0.05}_{-0.05}$	$1.3^{+0.1}_{-0.1}$	-	$1.2^{+0.1}_{-0.1}$	-	$0.75^{+0.10}_{-0.10}$	-	$0.40^{+0.05}_{-0.05}$	-
$v_\infty/10^3$ [km s^{-1}]	$1.5^{+0.1}_{-0.1}$	$2.0^{+0.5}_{-0.5}$	$2.2^{+0.2}_{-0.2}$	$2^{+0.5}_{-0.5}$	$1.65^{+0.1}_{-0.1}$	$2.2^{+0.2}_{-0.2}$	$2.0^{+0.2}_{-0.2}$	$1.7^{+0.2}_{-0.2}$	$1.5^{+0.3}_{-0.3}$	$3.7^{+0.3}_{-0.3}$	$3.2^{+0.3}_{-0.3}$
R_* [$R_\odot$]	5^{+1}_{-1}	7^{+6}_{-3}	24^{+10}_{-7}	22^{+15}_{-10}	24^{+8}_{-6}	7^{+3}_{-2}	22^{+7}_{-5}	$3.4^{+1.2}_{-1.2}$	14^{+5}_{-3}	2^{+1}_{-1}	14^{+6}_{-4}
$R_{2/3}$ [$R_\odot$]	5^{+1}_{-1}	7^{+6}_{-3}	26^{+10}_{-7}	23^{+15}_{-10}	25^{+8}_{-6}	7^{+3}_{-2}	22^{+7}_{-5}	$4.0^{+1.4}_{-1.4}$	15^{+5}_{-3}	3^{+1}_{-1}	15^{+6}_{-4}
D	10^{+10}_{-5}	10	40_{-20}	10	10	10^{+10}_{-5}	10	10^{+10}_{-5}	10	40_{-20}	10
$\log \dot{M}$ [$M_\odot$ yr^{-1}][c]	$-5.3^{+0.1}_{-0.1}$	-8.0	$-4.5^{+0.1}_{-0.1}$	$-4.5^{+0.3}_{-0.3}$	-5.9	$-5.1^{+0.2}_{-0.2}$	-5.8	$-5.0^{+0.2}_{-0.2}$	$-7.0^{+0.3}_{-0.5}$	$-4.8^{+0.1}_{-0.1}$	$-6.1^{+0.5}_{-0.3}$
$v \sin i$ [km s^{-1}]	-	200^{+100}_{-100}	< 300	< 400	120^{+30}_{-30}	-	150^{+50}_{-50}	-	150^{+30}_{-30}	-	120^{+20}_{-20}
$v_{\rm eq}$ [km s^{-1}][d]	-	240^{+300}_{-140}	< 300	< 400	120^{+30}_{-30}	-	180^{+100}_{-80}	-	160^{+70}_{-30}	-	190^{+40}_{-60}
$M_{V,\rm John}$ [mag]	$-4.4^{+0.2}_{-0.2}$	$-3.6^{+0.5}_{-0.5}$	$-7.1^{+0.3}_{-0.3}$	$-6.8^{+0.4}_{-0.4}$	$-6.7^{+0.3}_{-0.3}$	$-5.15^{+0.3}_{-0.3}$	$-6.65^{+0.3}_{-0.3}$	$-4.4^{+0.3}_{-0.3}$	$-5.7^{+0.3}_{-0.3}$	$-4.9^{+0.3}_{-0.3}$	$-5.9^{+0.3}_{-0.3}$
$X_{\rm H}$ (mass fr.)[e]	$0.25^{+0.05}_{-0.05}$	0.73	$0.25^{+0.05}_{-0.05}$	$0.25^{+0.20}_{-0.20}$	0.73	$0.4^{+0.1}_{-0.1}$	0.73	$0.15^{+0.05}_{-0.05}$	0.73	$0^{+0.15}$	0.73
$X_{\rm C}/10^{-5}$ (-||-)[e]	2^{+1}_{-1}	21	3^{+1}_{-1}	3^{+2}_{-2}	21	3^{+1}_{-1}	21	3^{+1}_{-1}	21	$0.30^{+0.05}_{-0.05} \cdot 10^5$	21
$X_{\rm N}/10^{-3}$ (-||-)[e]	4^{+2}_{-2}	0.03 (| 1[f])	2.5^{+1}_{-1}	2.5^{+1}_{-1}	0.03	3^{+1}_{-1}	0.03 (| 0.3[f])	2^{+1}_{-1}	0.03 (| 0.3[f])	0	0.03
$X_{\rm O}/10^{-5}$ (-||-)[e]	5.5	110	5.5	5.5	110	5.5	110	5.5	110	$0.3^{+0.1}_{-0.1} \cdot 10^5$	110
E_{B-V} [mag]	$0.18^{+0.01}_{-0.01}$			$0.08^{+0.02}_{-0.02}$		$0.065^{+0.01}_{-0.01}$		$0.08^{+0.01}_{-0.01}$		$0.07^{+0.01}_{-0.01}$	
A_V [mag]	$0.56^{+0.03}_{-0.01}$			$0.25^{+0.06}_{-0.06}$		$0.20^{+0.03}_{-0.03}$		$0.25^{+0.03}_{-0.03}$		$0.22^{+0.03}_{-0.03}$	
$M_{\rm H-b}$ [$M_\odot$][g]	46^{+7}_{-6}	-	83^{+20}_{-16}	73^{+42}_{-25}	-	101^{+30}_{-23}	-	51^{+13}_{-10}	-	-	-
$M_{\rm He-b}$ [$M_\odot$][g]	29^{+2}_{-2}	-	54^{+9}_{-9}	47^{+13}_{-10}	-	49^{+9}_{-7}	-	37^{+6}_{-5}	-	40^{+7}_{-6}	-
$M_{\rm g}$ [$M_\odot$]	-	13^{+70}_{-10}	-	-	34^{+64}_{-22}	-	54^{+97}_{-34}	-	30^{+55}_{-19}		70^{+210}_{-52}
$M_{\rm orb}$ [$M_\odot$][h]	20^{+80}_{-15}	20^{+20}_{-5}	61^{+10}_{-10}	66^{+10}_{-10}	-	9^{+7}_{-3}	41^{+29}_{-16}	23^{+13}_{-5}	44^{+26}_{-9}	19^{+3}_{-8}	61^{+14}_{-25}
$R_{\rm RL}$[$R_\odot$][i]	25^{+29}_{-6}	25^{+11}_{-6}	58^{+4}_{-4}	60^{+4}_{-4}	-	14^{+3}_{-2}	28^{+9}_{-7}	40^{+8}_{-3}	54^{+13}_{-6}	33^{+3}_{-5}	57^{+7}_{-12}

Notes. All entries but spectral types, $M_{\rm orb}$, and $R_{\rm RL}$ are derived in this study unless otherwise stated. Values without errors are adopted.
[a] References as in Table. 6.1 [b] Fixed for WR components using $M_{\rm orb}$ and R_* (see Sect. 6.4.3) [c] unconstrained entries adopted from Vink et al. (2000). [d] Equatorial rotation velocity calculated assuming alignment of the orbital and rotational axes. [e] Entries without errors are fixed to typical SMC abundances (see Sect. 6.4.2) [f] Alternative values in parentheses obtained when assuming the N III λ4640 emission originates in the O component (see Appendix C.1) [g] Obtained from MLRs by Gräfener et al. (2011) (see Sect. 6.6.1) [h] Based on orbital parameters given in Table 6.1 [i] Calculated via the Eggleton approximation (Eggleton 1983) assuming the orbital parameters given in Table 6.1

6.6. Discussion

6.6.1. Comparison with mass-luminosity relations

The surface of WR stars remains hidden behind their stellar winds, rendering a determination of their masses via photospheric absorption lines or astroseismological methods difficult. The only method to estimate the masses of single WR stars is by using mass-luminosity relations (MLRs, e.g. Langer 1989; Gräfener et al. 2011). Clearly, these relations need to be calibrated with model-independent methods for measuring stellar masses. Binary systems offer the most reliable method to "weigh" stars using simple Newtonian dynamics, given that the required observables (K_1, K_2, P, i, and e) are known.

We now compare theoretical MLRs published by Gräfener et al. (2011) to the luminosities and orbital

masses inferred for the WR primaries in our sample[3]. The relations are calculated for the simplified case of chemically homogeneous stars. In these relations, $\log L$ is given as a second order polynomial in $\log M$ (see Eqs. 9 and 10 in Gräfener et al. 2011), where the coefficients depend on the hydrogen mass fraction $X_{\rm H}$. In these relations, if $X_{\rm H} > 0$, the star is assumed to be core H-burning. Otherwise, it is assumed to be core He-burning.

For a star with a given luminosity, the largest possible mass predicted by theory is obtained for chemically homogeneous, hydrogen burning stars (Eq. 11 in Gräfener et al. 2011). Lower masses are obtained if the star has a He-burning core. Gräfener et al. (2011) argue that the MLR derived for pure helium stars (Eq. 13 in Gräfener et al. 2011) should give a good approximation for the masses of evolved, He-burning WR stars. However, if the contribution of shell H-burning to the luminosity is significant, a given luminosity can be supported by a yet smaller mass. The most strict lower bound on the mass at a given luminosity is given by the classical Eddington limit calculated for a fully ionized atmosphere (including only electron scattering).

Fig. 6.6 compares the theoretical predictions of the MLRs to the empirically derived $(M_{\rm orb}, \log L)$ coordinates for the WR companions. The Eddington limit, calculated for a fully ionized helium atmosphere, is also plotted. Langer (1989) also provides calculations for homogeneous stars with a vanishingly small helium abundance, which may be more suitable for the WO component in AB 8. Since these calculations predict a very similar relation to the MLR calculated for pure He-stars (the latter predicting slightly lower luminosities for a given mass), we omit the corresponding MLR from Fig. 6.6 for clarity.

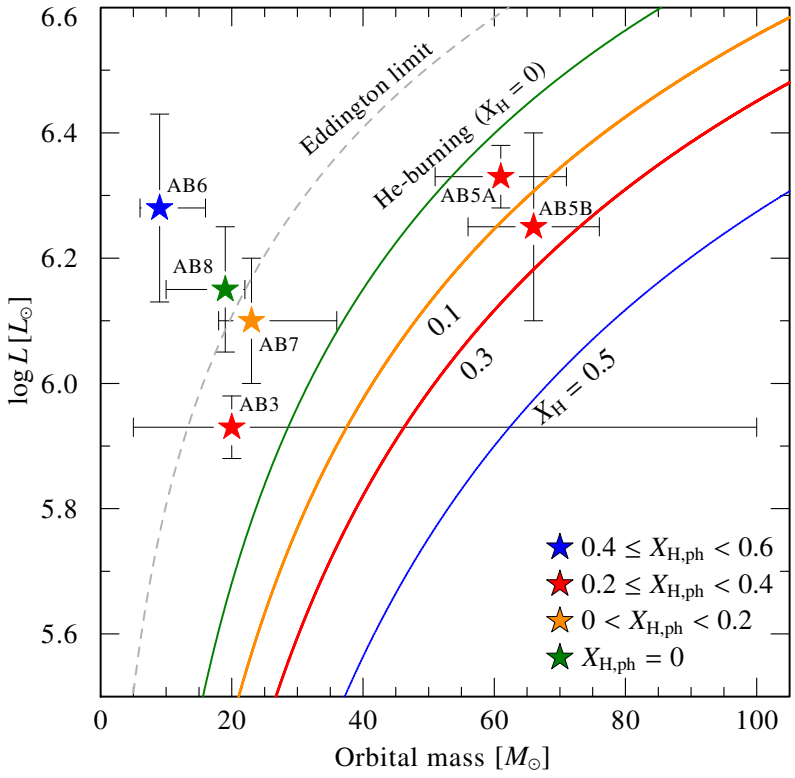

Figure 6.6.: The positions of the WR components on a $M - \log L$ diagram (symbols) compared to MLRs calculated for homogeneous stars (Gräfener et al. 2011), depicted by solid curves. The colors correspond to the hydrogen content (see legend). The Eddington limit calculated for a fully ionized helium atmosphere is also plotted (gray dashed line).

[3]We note that while these relations were calculated at solar metallicity, the influence of the metallicity is negligible (G. Gräfener, priv. com.)

Both massive WR components of AB 5 are located between MLRs calculated with $X_{\rm H,core} = 0$ and 0.3. This suggests that these stars may still be core H-burning, although both could coincide with the relation for He-burning stars within errors. Since the WR components of AB 3, 7, 6, and 8 are of early spectral type, which are understood to be core He-burning stars, we can expect them to lie on the MLR for pure He-stars, or, if a significant fraction of the luminosity originates in shell burning, between this relation and the Eddington limit[4]. As is apparent in Fig. 6.6, these stars do lie above the pure He-star MLR, suggesting that they are indeed core helium burning. The WR component in AB 3 is poorly constrained due to the large error on $M_{\rm orb}$. Since all analyzed WN components show signatures of hydrogen in their atmospheres, this suggests that the majority of WR stars in our sample are not chemically homogeneous. Taken at face value, their offsets from the MLR calculated for pure helium stars suggests the presence of shell H-burning (or shell He-burning in the case of AB 8).

While the WR component of AB 7 is located below the Eddington limit, that of AB 8 (WO) slightly exceeds it. The internal structure of WO stars is poorly understood and hard to model (N. Langer, priv. com.). Regardless, it should not be possible for the star to exceed the Eddington limit, unless significant departures from spherical symmetry occur already in the stellar interior (e.g. Shaviv 2000). However, considering the given errors on $\log L$ and $M_{\rm orb}$, there is no clear discrepancy in the case of AB 8.

The only star in the sample for which a clear inconsistency is obtained is the WR component of the shortest-period binary in our sample, AB 6. The star clearly exceeds its Eddington limit, which immediately implies that the derived luminosity and/or the orbital mass are incorrect. Furthermore, we find a significant amount of hydrogen ($\approx 40\%$) in its atmosphere, which is not expected for highly evolved, He-burning stars. In Sect. 6.6.4, we discuss possible reasons for this discrepancy, and argue that the orbital mass derived for the WR companion is most likely wrong. It is therefore omitted when considering the evolutionary status of the system in the next sections.

6.6.2. Evolutionary status: avoiding mass-transfer due to homogeneous evolution

Given the short orbital periods of our objects, it seems likely that the primaries underwent a RLOF phase before becoming WR stars. However, rapid initial equatorial rotation in excess of $400\,{\rm km\,s^{-1}}$ (Heger et al. 2000; Brott et al. 2011) may lead to quasi-chemically homogeneous evolution (QCHE). A star experiencing QCHE maintains higher effective temperatures and thus much smaller radii throughout its evolution, and may therefore avoid overfilling its Roche lobe during the pre-WR phase.

In paper I, we argued that the properties of the single SMC WR stars are compatible with QCHE. Yet tidal forces in binaries act to synchronize the axial rotation of the components with the orbital period (Zahn 1977). In binaries of extremely short periods ($\lesssim 2\,{\rm d}$), synchronization can maintain, or even enforce, near-critical rotation of the components (e.g. de Mink et al. 2009; Song et al. 2016). However, none of the binaries in our sample portray such short orbital periods, and we find no evidence for a significant increase of the orbital period throughout their evolution (see Sect. 6.6.3). In our sample, tidal interactions are rather expected to have slowed down the stellar rotation. For example, for an O star of $10 - 20\,R_\odot$ (a typical main sequence WR progenitor), synchronization with the period of AB 5 (19.3 d) would imply a rotational velocity of only 50-100 $\rm km\,s^{-1}$. Even for AB 6, the shortest period binary in our sample (6.5 d), synchronization implies $150 - 300\,{\rm km\,s^{-1}}$, which is insufficient to induce QCHE.

Synchronization timescales $\tau_{\rm sync}$ involve much uncertain physics. Hurley et al. (2002) give some estimates for binary stars with a mass ratio $q = 1$ and for initial masses up to $M_{\rm i} = 10\,M_\odot$. They show that for stars with $M_{\rm i} > 1\,M_\odot$ (i.e. stars with radiative envelopes), separations of the order of $10\,R_*$ ensure a synchronization timescale $\tau_{\rm syn}$ which is smaller than the main sequence timescale $\tau_{\rm MS}$, with the ratio $\tau_{\rm syn}/\tau_{\rm MS}$ virtually independent of the mass. Since the systems analyzed here are characterized by separations of a few R_*, tidal interactions are expected to have greatly lowered the initial rotation rates.

[4]We note that, at a given temperature, the spectral types of WR stars in the SMC tend to appear "earlier" than their Galactic counterparts (e.g. Crowther & Hadfield 2006). Seemingly early type stars in the SMC could therefore still be core H-burning.

Table 6.3.: Initial parameters and ages derived from single-star tracks assuming inhomogeneous evolution for the primary

	Inhomogeneous primaries, single-star tracks									
SMC AB	3		5		6		7		8	
$M_{1,\,\mathrm{i}}[M_\odot]^a$	50		100		80		70		80	
Age [Myr]^a	4.6		3.0		3.4		3.7		3.6	
$R_{\mathrm{max},\,1}[R_\odot]^a$	1800		1200		2000		2100		2000	
$M_{\mathrm{i},\,2}[M_\odot]^b$	15		100		46		35		50	
$v_{\mathrm{rot,\,i},\,2}[\mathrm{km\,s^{-1}}]^b$	230		-		170		160		130	
$\log\left(T_1^{\mathrm{E}}/T_1^{\mathrm{O}}\right)$	-0.01	(0.03)	-0.01	(0.05)	-0.01	(0.06)	-0.02	(0.04)	0.09	(0.15)
$\log\left(L_1^{\mathrm{E}}/L_1^{\mathrm{O}}\right)$	-0.08	(0.08)	-0.04	(0.13)	-0.16	(0.15)	-0.07	(0.12)	-0.09	(0.13)
$M_1^{\mathrm{E}} - M_1^{\mathrm{O}}$	2	(50)	-13	(14)	-	-	8	(14)	8	(10)
$X_{\mathrm{H},1}^{\mathrm{E}} - X_{\mathrm{H},1}^{\mathrm{O}}$	-0.03	(0.05)	<u>-0.11</u>	(0.05)	<u>-0.25</u>	(0.1)	-0.03	(0.05)	0.00	(0.05)

Notes. The upper part of the table gives the initial parameters and age defining the best-fitting single star tracks assuming a non-homogeneous evolution, as derived by the BPASS and BONNSAI tools, as well as the maximum radius reached by the primary throughout the evolution, $R_{\mathrm{max},\,1}$. The lower part gives $\mathrm{E}_n - \mathrm{O}_n$ as obtained from the best-fitting BPASS track, along with corresponding σ_n values in parentheses (see Sect. 6.6.2). Underlined values denote deviations which exceed 2σ.
$^{(a)}$ Obtained from the BPASS stellar evolution code $^{(b)}$ Obtained from the BONNSAI stellar evolution tool, except for AB 5, where the BPASS code was used (see text)

Table 6.4.: Initial parameters and ages derived from single-star tracks assuming homogeneous evolution for the primary

	Homogeneous primaries, single-star tracks									
SMC AB	3		5		6		7		8	
$M_{\mathrm{i},\,1}[M_\odot]^a$	50		70		100		50		70	
Age [Myr]^a	4.5		3.4		2.2		5.4		4.6	
$R_{1,\,\mathrm{max}}[R_\odot]^a$	10		13		19		10		13	
$M_{\mathrm{i},\,2}{}^b$	15		70		55		No solution		40	
$v_{\mathrm{rot\,i},\,2}{}^b$	230		-		170		No solution		410	
$\log\left(T_1^{\mathrm{E}}/T_1^{\mathrm{O}}\right)$	<u>-0.12</u>	(0.03)	<u>0.13</u>	(0.05)	<u>-0.13</u>	(0.06)	0.01	(0.06)	0.09	(0.15)
$\log\left(L_1^{\mathrm{E}}/L_1^{\mathrm{O}}\right)$	0.06	(0.08)	-0.13	(0.13)	0.05	(0.16)	-0.08	(0.12)	-0.08	(0.13)
$M_1^{\mathrm{E}} - M_1^{\mathrm{O}}$	28	(80)	6	(11)	-	-	10	(10)	8	(10)
$X_{\mathrm{H},1}^{\mathrm{E}} - X_{\mathrm{H},1}^{\mathrm{O}}$	-0.03	(0.05)	-0.01	(0.05)	-0.03	(0.1)	<u>-0.15</u>	(0.05)	0.00	(0.05)

Notes. Same as Table 6.3, but assuming homogeneous evolution (for footnotes, see Table 6.3).

To test whether single-star evolutionary tracks can explain the observed properties of our objects, we compare the primaries' T_*, L, M_{orb}, and X_{H} with evolutionary tracks for single stars with initial masses between 20 $M_\odot$ and 120 $M_\odot$ calculated at a metallicity of $Z = 0.004$ with the BPASS[5] (Binary Population and Spectral Synthesis) stellar evolution code (Eldridge et al. 2008, Eldridge et al. in prep.), which can treat

[5] bpass.auckland.ac.nz

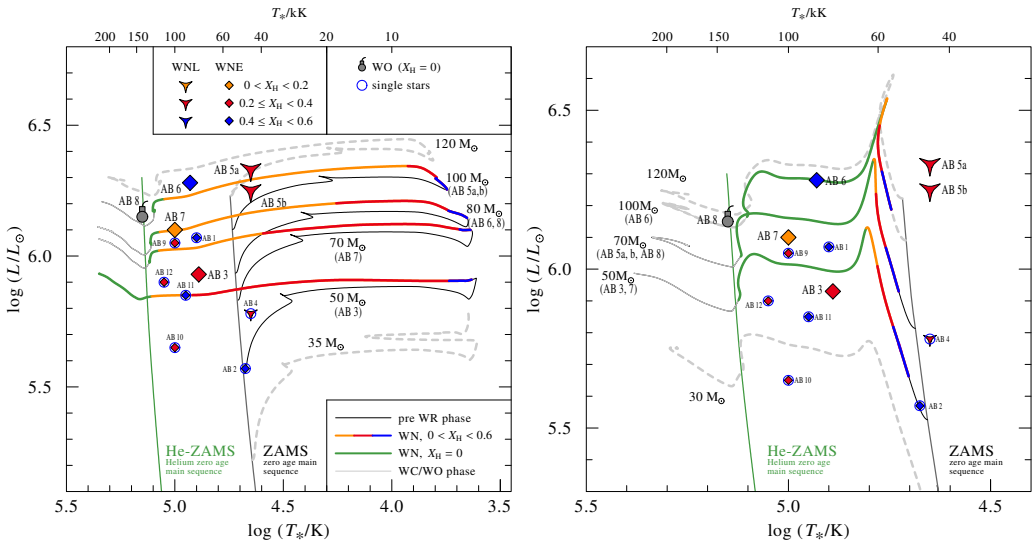

Figure 6.7.: The HRD positions of the all known single (paper I) and binary (this paper) SMC WR stars. The big symbols correspond to the binaries analyzed here, while circled smaller symbols correspond to putatively single stars. Plotted are evolutionary tracks (Eldridge et al. 2008) calculated for single stars at a metallicity of $Z = 0.004$ assuming no mixing (left panel) and chemically homogeneous evolution (right panel). The colors and symbols code the hydrogen abundance and WR type, as described in the legend. The WR phase is defined at $X_H < 0.6$. Tracks which correspond to the solutions found are shown in color.

both single and binary stars. We use two sets of tracks, one calculated assuming no chemical mixing, and the other calculated assuming a homogeneous evolution (Eldridge et al. 2011; Eldridge & Stanway 2012). For each WR star in our sample, we look for a track defined by M_i, and for an age t, which reproduce the observed quantities T_*, L, M_{orb} and X_H as good as possible, in the sense of minimizing the sum

$$\chi^2(M_i, t) = \sum_{n=1}^{4} \left(\frac{O_n - E_n(M_i, t)}{\sigma_n} \right)^2 , \tag{6.3}$$

where $O_n \in \{\log T_*, \log L, M_{orb}, X_H\}$ are the inferred values for the considered observables, and $E_n(M_i, t)$ are the corresponding predictions of the evolutionary track defined by the initial mass M_i at age t. Only in the case of AB 6, we ignore the WR component's orbital mass because of its clear inconsistency with the derived stellar luminosity (see Sects. 6.6.1 and 6.6.4). Since the tracks evolve non linearly, we avoid interpolation over the grid. Instead, we define $\sigma_n = \sqrt{\Delta_n^2 + \delta_n^2}$, where Δ_n is half the n'th parameter's grid spacing, and δ_n is the corresponding error given in Table 6.2. In the case of asymmetrical errors in Table 6.2, we assign δ_n according to whether $O_n > E_n$ or $O_n < E_n$. By minimizing χ^2, we infer initial masses and ages for the primaries in the cases of no mixing and homogeneous evolution. Conservative uncertainties on the ages are constrained from the adjacent tracks in the vicinity of the solution (typically 0.2 Myr).

As a second step, we test whether the ages derived are consistent with the current evolutionary status of the secondary, assuming still that no interaction has occurred between the companions. For this purpose, we use the BONNSAI[6] Bayesian statistics tool (Schneider et al. 2014b). The tool interpolates over detailed evolutionary tracks calculated by Brott et al. (2011) for stars of initial masses up to 60 $M_\odot$ and over a wide range of initial rotation velocities $v_{rot,i}$. Using T_*, L, M_{orb}, $v \sin i$ derived for the secondary, as well as the age derived for the primary (along with their corresponding errors), the algorithm tests whether a model

[6]The BONNSAI web-service is available at www.astro.uni-bonn.de/stars/bonnsai

exists which can reproduce the secondary's properties at the derived age at a 5% significance level. In case no such model was found, we verified this is not a consequence of the uncertain evolution of $v_{\rm eq}$ by lifting the $v \sin i$ constraint. For AB 5, we use the BPASS tracks to check consistency with the secondary, since its mass is not covered by the BONNSAI tool.

Tables 6.3 and 6.4 show the initial masses $M_{\rm i,1}$ and ages inferred for the primaries in the cases of inhomogeneous/homogeneous evolution. The Tables also give the maximum radius reached by the primary along the best-fitting track, $R_{\rm max,\,1}$. If consistent solutions for the secondaries are found by the BONNSAI tool, the secondaries' initial masses $M_{\rm i,\,2}$ and rotations $v_{\rm rot,\,i}$, as obtained from the BONNSAI tool, are given. Tables 6.3 and 6.4 also gives the differences $\mathrm{O}_n - \mathrm{E}_n$ for each of the primary's parameters, where we also include σ_n values. While all solutions provided by the BONNSAI reproduce the observed properties of the secondaries at a 5% significance level (Schneider et al. 2014b), they do not do so equally well. However, since this is merely a consistency test for single-star evolution, we do not present a detailed description of the BONNSAI fit quality, which can be recovered online by the interested reader.

The two panels of Fig. 6.7 show the positions of the complete SMC WR population in a $\log L - \log T_*$ diagram (HRD), as derived in paper I and in this study. The left panel includes BPASS tracks for the primaries calculated assuming no mixing, while the right panel includes BPASS tracks assuming homogeneous evolution. The obtained solutions are highlighted in color. Note that the HRD contains only partial information regarding the fit quality (see Tables 6.3 and 6.4). For clarity, we do not include error bars in Fig. 6.7.

From this test, it seems that QCHE is not consistent with AB 3, 6, and 7. For example, the T_* predicted by the track best fitting AB 3 deviates by 4σ from our measurement. For AB 7, not only the hydrogen content is underpredicted, but also, the age is not consistent with the secondary's stellar parameters. Based on our results, QCHE does not seem consistent with AB 5 either, since the temperature of the primary is overpredicted by more than 2σ. However, Koenigsberger et al. (2014) manage to explain the evolutionary status of AB 5 by assuming non-interacting companions experiencing QCHE. This discrepancy occurs because of the lower value inferred for T_* in this work compared to that used by Koenigsberger et al. (2014). Indeed, WWC in AB 5 may be responsible for a systematic uncertainty on T_* (see Appendix C.1). Of all systems, only AB 8 is compatible with homogeneous evolution.

The tracks which do not include mixing generally show a better agreement. However, the primary stars in this set of evolutionary tracks reach radii which greatly exceed their Roche lobe radii (cf. Table 6.3). If the systems did not undergo QCHE, there is little doubt that their companions have interacted via mass-transfer. In the next section, we account for this effect by considering binary evolution models.

6.6.3. Evolutionary status: assessing binary effects

We would now like to compare the HRD positions of the binary systems to evolutionary tracks which account for binary interaction. modeling the evolution of binaries is difficult, because on top of the complex physics involved in the evolution of single stars, the effects of tidal interaction and mass-transfer have to be accounted for. While codes exist which account for these effects simultaneously (e.g. Cantiello et al. 2007), there are no corresponding grids of tracks available. Here, we make use of evolutionary tracks calculated with Version 2.0 of the BPASS code, which accounts for mass-transfer. The tracks do not include rotationally induced mixing or tidal interaction. However, as discussed in Sect. 6.6.2, mixing should be negligible for the majority of our objects. If mixing does become important in a binary system, its components will likely avoid RLOF, as can be inferred from the small radii maintained by the homogeneous models (cf. Table 6.4). In this case, the solutions found from the single-star, chemically homogeneous evolutionary tracks should be adequate to describe the system.

Each binary track is defined by a set of three parameters: the initial mass of the primary $M_{\rm i,1}$, the initial orbital period $P_{\rm i}$, and the mass ratio $q_{\rm i} = M_{\rm i,2}/M_{\rm i,1}$. The tracks are calculated at intervals of 0.2 on $0 < \log P\,[\mathrm{d}] < 4$, 0.2 on $0 < q_{\rm i} < 0.9$, and at unequal intervals of $10 - 30\,M_\odot$ on $10 < M_{\rm i,1} < 150\,M_\odot$. Again, we use a χ^2 minimization algorithm to find the best-fitting track for each system. However, this time we consider eight different observables, thus leading to

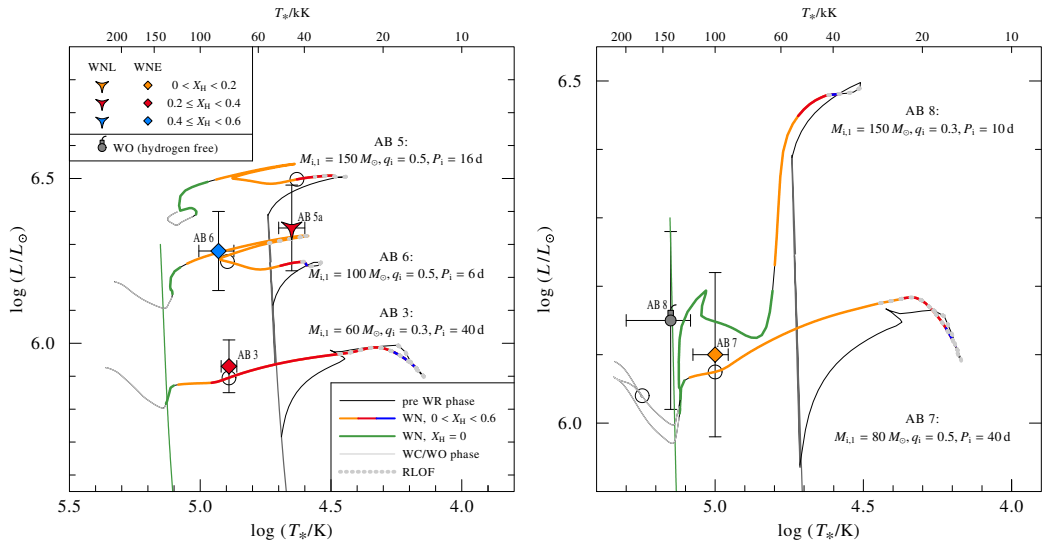

Figure 6.8.: The two panels show the derived HRD positions of the WR components compared to the binary evolution tracks which best reproduce the set of eight observables (see text). The tracks shown correspond to the primary component. Colors are as in Fig. 6.7. The circles denote the best-fitting position (ages) along the tracks. RLOF phases are marked with dotted gray lines.

$$\chi^2\left(P_\mathrm{i}, q_\mathrm{i}, M_{\mathrm{i},1}, t\right) = \sum_{n=1}^{8}\left(\frac{\mathrm{O}_n - \mathrm{E}_n\left(P_\mathrm{i}, q_\mathrm{i}, M_{\mathrm{i},1}, t\right)}{\sigma_n}\right)^2, \tag{6.4}$$

where $\mathrm{O}_n \in \{\log T_1, \log L_1, \log T_2, \log L_2, M_{\mathrm{orb},1}, M_{\mathrm{orb},2}, \log P,\ X_{\mathrm{H},1}\}$ are the measured values for the considered observables, and $\mathrm{E}_n\left(P_\mathrm{i}, q_\mathrm{i}, M_{\mathrm{i},1}, t\right)$ are the corresponding predictions of the evolutionary track defined by P_i, q_i, and $M_{\mathrm{i},1}$ at time t. σ_n is defined as in Eq. 6.3.

The two panels in Fig. 6.8 show the best-fitting evolutionary tracks corresponding to the primary components along with their HRD positions. The circles correspond to the current positions (ages) derived. We stress, however, that the HRD illustrates only three of the eight observables which were fit here. In Table 6.5, we give the set of initial parameters defining the best-fitting tracks and ages found for each system, along with the differences $\mathrm{O}_n - \mathrm{E}_n$ and the corresponding uncertainties σ_n. Evidently, we manage to find tracks which reproduce the eight observables within a 2σ level for all systems except AB 6. An evolutionary scenario which includes mass-transfer thus appears to be consistent with AB 3, 5, 7, and 8, although AB 8 was also consistent with QCHE. In Appendix C.2, we give a thorough description of the evolution of each system as given by the corresponding best-fitting track.

The solution for AB 5 overpredicts the components' masses by almost 2σ, and is generally very sensitive to the weighting of the different observables (e.g. small changes in σ_n). However, we believe this is simply a result of the grid spacing (see Appendix C.2). A greater challenge lies in explaining the similar hydrogen abundances of the two components The BPASS code does not follow the hydrogen abundance of the secondary, but since the two components were born with quite different masses in the derived solution (150 and 75 $M_\odot$), it is unlikely that they would evolve to a state of significant hydrogen depletion simultaneously. A conceivable resolution within the framework of binary evolution could involve the secondary losing much of its hydrogen envelope by undergoing a non-conservative RLOF, but this would likely require some fine tuning of the initial conditions. The QCHE scenario thus appears more natural in the case of AB 5, as proposed by Koenigsberger et al. (2014). However, it is not clear whether this scenario is consistent with the presence of tidal forces in the system. We discuss this system thoroughly in Appendix C.2.

As for AB 6, even when omitting the primary's orbital mass in the fitting procedure, we obtain a $\approx 2.5\sigma$ discrepancy in the hydrogen abundance, which is found to be lower in the evolutionary track. However, our

Table 6.5.: Comparison with the best fitting binary evolutionary tracks

SMC AB	3		5		6		7		8	
$M_{\rm i,1}[M_\odot]$	60		150		100		80		150	
$q_{\rm i}(M_{\rm i,2}/M_{\rm i,1})$	0.3		0.5		0.5		0.5		0.3	
$P_{\rm i}$[d]	40		16		6		40		10	
Age [Myr]	3.9		2.6		3.0		3.4		3.0	
$\log\left(T_1^{\rm E}/T_1^{\rm O}\right)$	0.00	(0.03)	-0.02	(0.05)	-0.01	(0.06)	-0.02	(0.08)	0.09	(0.15)
$\log\left(L_1^{\rm E}/L_1^{\rm O}\right)$	-0.03	(0.08)	0.16	(0.13)	-0.03	(0.16)	-0.03	(0.12)	-0.11	(0.13)
$\log\left(T_2^{\rm E}/T_2^{\rm O}\right)$	0.08	(0.09)	-0.02	(0.07)	0.04	(0.08)	0.08	(0.08)	-0.06	(0.08)
$\log\left(L_2^{\rm E}/L_2^{\rm O}\right)$	0.09	(0.33)	-0.17	(0.26)	-0.16	(0.28)	0.03	(0.28)	-0.22	(0.27)
$M_1^{\rm E} - M_1^{\rm O}$	6	(50)	26	(18)	-	-	11	(14)	7	(10)
$M_2^{\rm E} - M_2^{\rm O}$	-2	(16)	31	(18)	30	(30)	-1	(14)	10	(20)
$\log\left(P^{\rm E}/P^{\rm O}\right)$	0.11	(0.10)	-0.07	(0.10)	0.02	(0.1)	0.03	(0.1)	0.02	(0.10)
$X_{\rm H,1}^{\rm E} - X_{\rm H,1}^{\rm O}$	-0.03	(0.05)	-0.03	(0.05)	<u>-0.25</u>	(0.1)	-0.01	(0.05)	0.00	(0.05)

Notes. The upper part of the table gives the parameters defining the best fitting evolutionary track and corresponding ages. The lower part gives E − O for each parameter, with corresponding σ values in parentheses. Underlined values denote deviations which exceed 2σ.

tests show that this discrepancy is lifted when using tracks which assume a lower metallicity ($Z = 0.002$), i.e. this is a direct result of the uncertain mass-loss rates during the WR phase. Moreover, the BPASS binary models do not evolve the secondary in detail and therefore do not include the secondary overfilling its Roche lobe to transfer material back to the primary, as was reported for other stars (e.g. Groh et al. 2008). Such a process could contribute to the large amount of hydrogen detected in the WR star, although one would need to account for the secondary (which is observed to be an O-type supergiant) not entering the WR phase as a result of mass-loss during RLOF.

All binary solutions found go through a RLOF phase before the primary reaches the WR phase, which could already be anticipated given the large radii reached by the primaries after leaving the main sequence (cf. Table 6.3). As discussed in Appendix C.2, RLOF typically removes $\approx 30\,M_\odot$ from the primary, at times partially accreted by the secondary. Mass transfer thus appears to be crucial for the detailed evolution of the systems which do not experience QCHE.

Despite the importance of mass-transfer, our results indicate that binary interaction does not contribute to the existing number of WR stars in the SMC. In Sect. 6.1, we argued that it is a priori expected that the majority (if not all) of the SMC WR population would stem from binary evolution, which generally enables WR stars to form at lower initial masses ($M_{\rm i} \gtrsim 20\,M_\odot$) compared with single stars ($M_{\rm i} \gtrsim 45\,M_\odot$). And yet, the initial masses of the primaries are found to be in excess of $60\,M_\odot$. This means that all WR components had large enough initial masses to become WR stars *regardless* of binary effects.

It is conceivable that the limit of $M_{\rm i} \approx 45\,M_\odot$ for SMC stars to become WR stars is an overestimation, as it strictly holds for non-homogeneous stars. This limit can decrease to $\approx 20\,M_\odot$ if homogeneous evolutionary tracks are considered (cf. Fig. 6.7). Regardless, it is unclear why no WR binaries with intermediate-mass (20 - 40 $M_\odot$) primary progenitors are found. Since the initial mass function strongly favors the formation of lower mass stars (Kroupa 2001), one would expect to see at least some WR binaries originating from intermediate-mass progenitors. The only WR stars in the SMC which imply intermediate-mass progenitors are the putatively single stars AB 2 and 10. As showed in Paper I, their HRD positions can be reproduced by assuming QCHE. Alternatively, they could stem from binary evolution. While the lack of confirmed companions sheds doubts on this scenario, post-RLOF binaries would often appear as single stars due to

their small typical velocity amplitudes and/or the large brightness contrast of the companions (de Mink et al. 2014). The apparent lack of detected WR stars which are a direct result of binary interaction could thus be due to an observational bias.

Various studies (e.g. Packet 1981; Shara et al. 2015) suggest that the secondary should be spun up to near-critical rotation velocities as a consequence of mass accretion during the primary's RLOF. Interestingly, all O-companions are found to have $v_{\rm eq}$ values above the average for single O stars ($\approx 100\,{\rm km\,s^{-1}}$, e.g. Penny 1996; Ramírez-Agudelo et al. 2013), yet none of them are near critical ($\approx 500\,{\rm km\,s^{-1}}$). The fact that the O companions rotate with velocities above average implies that RLOF may have occurred, but the fact that they are sub-critical challenges this scenario. A resolution could lie in tidal interactions and/or mass-loss, which together lead to a rapid loss of angular momentum. Alternatively, the spin up during RLOF may be overestimated.

6.6.4. The strange case of AB 6

The system SMC AB 6 stands out as very enigmatic. In Sect. 6.6.1, we showed that the luminosity and orbital mass inferred for the WR component of AB 6 imply that it greatly exceeds its Eddington limit within errors. This means one or more of the following: (a) The parameters derived for the system in this paper, most importantly $\log L$, are incorrect; (b) The orbital mass derived by FMG is incorrect.

In Appendix C.1, we thoroughly describe how the components' luminosities are derived. One caveat is that the method relies on the adopted abundances. Since we use different elements (C, S, P), and since not all are expected to change with evolution, a systematic deviation is unlikely. Furthermore, the light ratio cannot be very different than derived here, since a reduction of the WR luminosity would imply an unrealistic increase of the companion's luminosity (e.g. Martins et al. 2005). However, a third component could contaminate the spectra. quite a few examples exist for false analyses of triple systems which were considered to be binary (e.g. Moffat & Seggewiss 1977). The immediate neighborhood of AB 6 is crowded with luminous stars and unresolved sources, which increases the probability for a third component contributing to the total light of the system. A third component could lead to a smaller luminosity for the WR component, although it would be hard to account for the ≈ 1 dex downwards revision in $\log L$ which would be necessary to compensate for the discrepancies.

Another possibility is that the orbital mass is incorrect. To obtain a mass which fits more reasonably with our results, an inclination of $\sim 30^\circ$ would be required. However, assuming that the mass ratio derived by FMG is correct, such an inclination would also imply a mass of $\sim 170\,M_\odot$ for the O companion, which is unrealistic. Alternatively, it is possible that the actual mass ratio is different: The RV curve of the O component in AB 6 shown by FMG is based on noisy data points obtained from the motion of the absorption features in the low resolution optical spectra. A larger RV amplitude for the O star could lead to a larger orbital mass for the WR component. Moreover, a potential third source would not only affect the derived luminosities, but could also affect the RV measurements of the other two components (see e.g. Moffat & Seggewiss 1977; Mayer et al. 2010).

Although this short-period binary is a potential candidate for unique behavior patterns, its properties, as given here, are impossible to explain within the frame of binary evolution. This peculiar system should clearly be subject to further studies.

6.7. Summary

This study presented a systematic spectroscopic analysis of all five confirmed WR multiple systems in the low metallicity environment of the SMC. Together with Paper I, this work provides a detailed non-LTE analysis of the complete SMC WR population. We derived the full set of stellar parameters for all components of each system, and obtained important constraints on the impact of binarity on the SMC WR population.

Mass-luminosity relations (MLRs) calculated for homogeneous stars (Gräfener et al. 2011) reveal a good agreement for the very massive components of SMC AB 5 (HD 5980). Because of the errors on $\log L$ and $M_{\rm orb}$, it is difficult to tell whether these stars are core H-burning or He-burning, although their derived

positions are more consistent with core H-burning. The remaining WN stars in our sample show higher luminosities than predicted by the MLR calculated for pure He stars, implying core He-burning and shell H-burning (shell He-burning for the WO component in AB 8). This is consistent with the fact that all WN components show traces for hydrogen in their atmospheres ($0.1 < X_{\rm H} < 0.4$).

The WO component in AB 8 is found to slightly exceed its Eddington limit, but this is likely a consequence of the errors on $\log L$ and $M_{\rm orb}$. The small orbital mass ($\approx 10\,M_\odot$) and high luminosity ($\log L \approx 6.3\,[L_\odot]$) inferred for the WR component of AB 6 imply that it greatly exceeds its Eddington limit, which is clearly unphysical. We believe that the most likely resolution is an underestimation of the orbital mass, possibly because of a third component contaminating the spectrum of the system, which could also affect the derived luminosity. Overall, the positions of the WR stars in our sample on the $M - L$ diagram (Fig. 6.6), together with the derived atmospheric chemical compositions, suggest that the stars are not chemically homogeneous, with the possible exception of AB 5.

A comparison of the observed properties of each system to evolutionary tracks calculated with the BPASS and BONNSAI tools for chemically homogeneous/non-homogeneous single stars suggests that chemically homogeneous evolution (QCHE) is not consistent with four of the five systems analyzed (AB 3, 5, 6, and 7). In the case of AB 5, this is a direct result of the temperature derived in this study, which could be biased by the effects of wind-wind collisions (WWC), hindering us from a definite conclusion in its case. There are good reasons to believe that the components of AB 5 did in fact experience QCHE, but not without open problems (see Sect. 6.6.3 and Appendix C.2). The case of AB 8 is uncertain, as QCHE can explain its evolutionary state, although it is not a necessary assumption. This stands in contrast to the putatively single SMC WR stars, which are generally better understood if QCHE is assumed. The difference presumably stems from tidal synchronization, inhibiting an efficient chemical mixing in the stars. We showed that, if QCHE is avoided, the components of all our analyzed systems had to have interacted via mass-transfer in the past.

Mass-transfer in binaries is found to strongly influence the detailed evolution of the SMC WR binaries, significantly changing and redistributing the total mass of the system. That said, stellar winds too play a significant role in determining the final masses of the components, which stresses the importance of accurate mass-loss calibrations in evolutionary codes.

Despite the importance of mass-transfer, initial masses derived for the primaries are in excess of $60\,M_\odot$, well above the lower limit for single stars to enter the WR phase at SMC metallicity. Put differently, it seems that the primaries would have entered the WR phase regardless of binary effects. This suggests that the existing number of WR stars in the SMC is not increased because of mass transfer, in agreement with the fact that the observed WR binary fraction in the SMC is 40 %, comparable with the MW. No WR binaries are found with intermediate-mass ($20 - 40\,M_\odot$) progenitors, although their existence is predicted by stellar evolution models. Since post-RLOF systems tend to appear as single stars, this could be due to an observational bias.

The sample clearly suffers from low number statistics, and so any general claims put forth in this paper should be taken with caution. Our understanding of binary effects on the evolution of massive stars is expected to improve in the near future, as the sample of analyzed WR binaries will continue to grow. Meanwhile, our results should serve as a beacon for stellar evolution models aiming at reproducing the observed statistical properties of the plethora of massive stellar objects, to which WR stars belong.

6.8. Acknowledgements

We thank our anonymous referee for their constructive comments. TS is grateful for financial support from the Leibniz Graduate School for Quantitative Spectroscopy in Astrophysics, a joint project of the Leibniz Institute for Astrophysics Potsdam (AIP) and the institute of Physics and Astronomy of the University of Potsdam. LMO acknowledges support from DLR grant 50 OR 1302. AS is supported by the Deutsche Forschungsgemeinschaft under grant HA 1455/26. AFJM is grateful for financial support from NSERC (Canada) and FRQNT (Québec). JJE thanks the University of Auckland for supporting his research. JJE also wishes to acknowledge the contribution of the NeSI high-performance computing facilities and the staff at the Centre for eResearch at the University of Auckland. We thank F. Tramper for providing us a

reduced spectrum of AB 8. TS acknowledges helpful discussions with G. Gräfener and N. Langer. This research made use of the SIMBAD and VizieR databases, operated at CDS, Strasbourg, France.

Chapter 7.

Discussion

Below, we discuss the results obtained here and their consequences in the broad context of massive star evolution.

7.1. Establishing the PoWR code as a general analysis tool for hot stars

A reliable interpretation of the spectra of massive stars is impossible without the usage of model atmospheres. The Potsdam Wolf-Rayet (PoWR) code used here was originally designed for the analysis of WR stars (Hamann & Gräfener 2004). While this implies that it can solve non-LTE radiative transfer in expanding atmospheres, the treatment of the hydrostatic layers of stars was originally very approximate. Prior to the updates introduced in Chapter 2, hydrostatic balance was achieved by accounting for gravity and radiation pressure on free electrons (Thomson scattering) alone. However, as we illustrate in Chapter 2, a significant part of the radiation stems from bound-bound transitions belonging to the different metallic species in the stellar atmosphere, implying that the radiation force was strongly underestimated. While the approximate treatment of the quasi-hydrostatic layers is justified for wind-dominated WR stars, this is not the case for OB-type stars, which typically exhibit both photospheric as well as wind features. The code thus had to be updated and tested on O stars and binaries before the analysis of WR binaries could initiate.

The accurate calculation of the radiative pressure impacts the determination of the stellar gravity via pressure broadening. An upwards revision of the radiation pressure results in an upwards revision of the gravities, and hence of stellar masses, derived in spectral analyses. This has great implications on the so-called mass-discrepancy problem, which stems from a disagreement between spectroscopic and orbital masses (Herrero et al. 1992; Repolust et al. 2004; Massey et al. 2012). In the new version of the PoWR code which resulted from this study, radiation pressure is accurately accounted for in a manner which is, to our knowledge, more advanced than any other model atmosphere code for expanding atmospheres which currently exists.

Another important update which was implemented during this work is the inclusion of a depth-dependent microturbulence $\xi(r)$ during the formal integration. Prior to this update, a single Doppler velocity v_{Dop} was adopted for all radii, independent of the element. The spectra of OB-type stars allow the observer to explore both the hydrostatic layers as well as their winds, implying that their spectra can probe regions up to $100\,R_*$ above the stellar surface. The turbulence is expected to vary over this spatial scale. Instead of being constant, the Doppler velocity in the new version of the PoWR code is calculated for an ion of mass m in the form $v_{\mathrm{Dop}}(m,r) = \sqrt{v_{\mathrm{th}}^2(m,r) + \xi^2(r)}$, where $v_{\mathrm{th}}^2 = 2kT(r)/m$, k is the Boltzmann constant, T is the temperature, and ξ is a user-specified microturbulence term.

The TLUSTY code (Lanz & Hubeny 2003) is commonly used for the analysis of OB-type stars. While it cannot account for stellar winds, it is considered the most advanced and intricate tool for the analysis of stellar photospheres of massive stars. To test and benchmark the new updates included in the code, we performed extensive comparisons between the PoWR and TLUSTY codes, focusing on pressure broadening of the hydrogen Balmer lines. We find a very good agreement between both codes when including the new treatment of radiation pressure. However, we also illustrate that the usage of TLUSTY can cause systematic errors for stars with significant winds, even if the wind is not immediately apparent in the spectral line considered.

The eclipsing triple system δ Ori A (Chapter 3) served as an excellent test-case for the updated PoWR code, and resulted in important physical constraints regarding the wind structure of massive stars, as well as the formation physics of X-rays in massive stars. Eclipsing binaries serve as key calibrators for stars. A careful spectroscopic and photometric analysis of eclipsing binaries allows the derivation of the light ratio, masses, and radii to accuracies unattainable otherwise. Eclipses are also of great importance for the study of stellar winds. By probing the variation of the system's light with orbital phase, constraints on the structure and properties of the winds can be obtained.

The system δ Ori A comprises an eclipsing massive binary (Aa1 + Aa2, $P \sim 6$ d) and a massive tertiary O star (Ab) orbiting the binary approximately every 350 years. Given the mass of the primary star, the system will likely evolve into a WR binary. Previous studies derived suspiciously small masses Aa1 and Aa2 which are hard to reconcile with their spectral classes. Like the majority of massive O stars, δ Ori A emits a significant amount of X-ray radiation (e.g., Pallavicini et al. 1981; Oskinova 2005). Its proximity to Earth made the acquisition of high-quality X-ray spectra using the Chandra satellite possible. Although X-rays are ubiquitous among massive stars, it is still not understood where and how these X-rays form. The main hypotheses include intrinsic shocks in the stellar wind induced by line driving instability (Feldmeier et al. 1997) or acoustic driving induced by subsurface convection (Cantiello et al. 2009). Massive binaries can also show excess emission stemming from wind-wind collisions (WWC), although this is not always the case (Oskinova 2005). As X-rays are commonly used to derive mass-loss rates (Oskinova et al. 2007; Sundqvist et al. 2012), understanding the physics behind their formation is of great importance. The major goal of this study and the associated papers (Corcoran et al. 2015; Nichols et al. 2015; Pablo et al. 2015; Shenar et al. 2015) is to take advantage of the eclipsing nature of the system to constrain the formation region of X-rays in massive stars.

To achieve this goal, a full spectroscopic analysis of the atmospheres of all three components in the system is required. This includes the separation of the observed spectra to three contributions associated with the three components of the systems. Such analyses were rarely done before. Through this study, we revised previous parameters derived for the system, and were able to show that the small masses derived by Harvin et al. (2002) for Aa1 and Aa2 were a result of confusing Aa2 with the tertiary, Ab (see also Mayer et al. 2010). We performed a detailed analysis of the wind and clumping properties of the three components, by which we illustrated the potential importance of optically thick clumps (macroclumping), often neglected in analyses of massive stars (Oskinova et al. 2007). We showed that the X-ray, UV, and optical spectra can be explained simultaneously when adopting moderate clumping factors ($D \approx 10$) when accounting for porosity. This implies a reduction of the mass-loss rates by a factor ≈ 3 compared to those obtained for homogeneous wind. This is significantly less than the factor $\approx 5 - 10$ suggested by other studies (Fullerton et al. 2006; Bouret et al. 2012). If this indeed generally holds for OB-type stars, this would have far-reaching implications on stellar evolution models.

To interpret the X-ray observations in light of our results, we performed a quantitative analysis of several ratios of forbidden and intercombination lines (f/i) in the X-ray spectrum. These ratios can give sharp constrains on the formation region of X-rays (Blumenthal et al. 1972; Leutenegger et al. 2006). The analysis took advantage of the model atmospheres generated for the system. We found that the X-ray observations implied formation radii which are significantly larger than the stellar radius, i.e. our findings seem to support intrinsic wind shocks as an explanation for the emission of X-rays. This is supported by the lack of a clear phase-dependent variability signature in the X-ray light curve (Nichols et al. 2015), since, in this case, the X-ray emitting volume is much larger than the column eclipsed by the secondary. We were not able to recognize clear evidence for wind-wind collision in the system.

Compared to the intrinsic X-ray radiation of massive stars, high mass X-ray binaries (HMXBs) exhibit X-ray luminosities which are orders of magnitude higher. The X-ray emission is associated with accretion of matter by a compact object such as a neutron star (NS) or a black hole (BH). These objects are divided into subcategories depending on the properties of their X-ray emission: Supergiant X-ray binaries (SGXBs) are persistent X-ray sources, while the X-ray emission of supergiant fast X-ray transients (SFXTs) is strongly time-dependent. Why both types of objects have such distinct behavior in the X-ray band when they both host supergiant donors is still under intense debate (e.g. Negueruela et al. 2008; Walter et al. 2015).

In the study presented in Chapter 4, we examined whether the dichotomy between the two HMXB classes can be explained by the distinct properties of their donor stars. For this purpose, we performed an analysis of

two prototypical systems: Vela X-1 (SGXB) and IGR J17544-2679 (SFXT), both consisting of a supergiant primary and a pulsar secondary. The donor stars in these systems have a similar spectral type, and the systems have comparable (nearly circular) orbital parameters, making the extreme difference in their X-ray properties most intriguing. The donor stars were analyzed using the PoWR code, allowing the derivation of all relevant stellar parameters for both systems.

We found two decisive differences between the two systems analyzed. First, the terminal velocities of the donor stars differ by approx. a factor of two. Second, the pulsar spins are significantly different in both systems. The terminal velocity and spin period are critical quantities which influence the accretion process. If the spin of the pulsar is large enough, or if the wind velocity is large enough, accretion would be partially inhibited ("Supersonic propeller") and would cause a strong variability of the X-ray emission observed on Earth. Otherwise, for spin periods and terminal velocities which are small enough, accretion happens continuously and without interruption. The parameters derived in our study imply that the prototypical SFXT system (IGR J17544-2679) is in fact experiencing a supersonic propeller accretion, while the prototypical SGXB system experiences direct accretion (see Fig. 4.18). Crucial for this new realization was the accurate derivation of the terminal velocities of both stars, which was shown in our study to be erroneous in previous publications.

Hence, the studies presented in Chapters 2, 3, and 4 probed different aspects of the winds and binary interaction in massive stars, resulting in many important constraints, and establishing the PoWR tool as adequate for the analysis of many types of hot stars.

7.2. Comparing derived orbital masses and luminosities with theoretical mass-luminosity relations

It is known that a tight relation exists between the luminosity and the mass of stars. While these so called mass-luminosity relations (MLRs) for main sequence stars are well constrained, they are less certain for massive, evolved stars. While most stars obey a sharp power law of the form $L \propto M^{\alpha}$, $3 \lesssim \alpha \lesssim 4$, the luminosities of massive stars scale approx. linearly with the mass. Such MLRs are used to derive current masses for stars with a known luminosity in cases where binary methods cannot be applied. Especially for wind-ridden stars such as WR stars, MLRs remain the only method to estimate the current stellar mass. However, MLRs strongly depend on the structure of the star, which is not necessarily known. Thus, establishing an empirical relation between L and M is essential to test and calibrate published theoretical MLRs. A comparison between the two can yield important constraints on the structure and evolution of massive stars.

Langer (1989) and Gräfener et al. (2011) published theoretical MLRs for chemically homogeneous massive stars. To which degree stars are homogeneous is still under much debate (e.g. Hainich et al. 2014; Koenigsberger et al. 2014; Shenar et al. 2016). Possible mechanisms which may induce chemical homogeneity include rotation (Heger & Langer 2000) and convection combined with mass-loss (e.g. Gräfener et al. 2011). MLRs heavily depend not only on L, but also on the hydrogen content X_{H} in the star. At a given mass, hydrogen depleted stars produce more luminosity than hydrogen rich stars due to their increased mean molecular weight.

In Chapter 5, we performed an extensive analysis of the WR binary R 145. This binary, situated in the Tarantula nebula in the LMC, was claimed to host the most massive stars known (Schnurr et al. 2009). As finding the most massive stars is one of the most desired goals of stellar physics, studying this system is of great importance for the research of the initial mass function and star formation (e.g. Gallagher et al. 1996). In our study (Chapter 5), performed in the framework of the Tarantula Massive Binary Monitoring (TMBM) project, we derived the first SB2 orbit of the system, and were thus able to derive accurate minimum masses ($M \sin^3 i$) for both components. The orbital inclination i could be derived from a polarimetric analysis, as well as by analyzing the WWC shocked region. We found $M_1 \approx M_2 \approx 55^{+40}_{-20}$, implying that the primary is not as extremely massive as claimed in the past. The composite spectra were disentangled to obtain normalized spectra for each component, the components were classified, and a spectral analysis was performed with the PoWR tool. Comparing our results to MLRs and evolutionary tracks suggests that the stars evolved in a quasi homogeneous fashion, reminiscent of HD 5980 in the SMC.

All known WR binaries in the SMC were analyzed in Chapter 6. One of the goals of the study was to compare the luminosities and orbital masses of WR stars to published MLRs (see Fig. 6.6). If the luminosities and orbital masses were accurate, and if the WR stars were homogeneous, one would expect the stars to lie on their corresponding relations. This is only roughly the case for the massive components of HD 5980 (SMC AB 5). The remaining WR stars in our sample lie above their corresponding relations, i.e. they show an excess luminosity given their mass. At least for some of these objects, the errors cannot be blamed for this discrepancy, unless they were underestimated in our study. We therefore concluded that the majority of WR stars in our sample are, in fact, not chemically homogeneous. This stands in contrast with the single WR stars in the SMC (Hainich et al. 2015). We argue this is potentially a consequence of tidal interaction in the binaries which, with time, slowed down the stellar rotation and suppressed the chemical mixing.

7.3. The impact of binarity on Wolf-Rayet stars

In the introduction and in Chapter 6, we stated that WR stars are understood to form in two possible channels. The first involves an intrinsic loss of the H-rich layers via stellar winds, perhaps combined with powerful eruptive phenomena. The second involves mass-transfer via RLOF in a binary system. Originally, binarity was believed to be the main mechanism which led to the formation of H-poor WR stars (Paczyński 1967). It later became clear that radiation pressure is powerful enough to drive the winds necessary to enable massive stars to rid themselves of their hydrogen envelopes (Castor et al. 1975; Conti 1976), which caused a certain disinterest for the binary evolution channel. However, with the mass-loss rates revised downwards by factors of ≈ 3 or more, it is not as clear today whether mass-loss via stellar winds alone can explain the number of H-free WR stars observed (e.g. Vanbeveren et al. 1998; Smith 2014). Moreover, the realization that binarity is extremely common among massive stars strongly increases the likelihood that mass-transfer plays a decisive role in the formation of WR stars.

To gain insights on the impact of binarity on WR stars, we draw on our results from Chapter 6, which are based on a spectral analysis of all known WR binaries in the SMC. Combining these with results obtained for the single WR stars in the SMC (Hainich et al. 2015), we can learn much about the impact of binarity on WR stars. The study of the SMC WR population is critical for three main reasons: 1) The known distance and low reddening along the SMC line of sight are extremely helpful for deriving key parameters such as the luminosity with small associated errors. 2) The SMC WR sample is allegedly complete (i.e., we know all WR stars in the SMC, e.g. Massey et al. 2014), and 3) Binarity is expected to dominate the formation of WR stars especially at the low metallicity environment of the SMC ($Z \approx 1/10 Z_{\odot}$).

Based on observed populations of WR and O stars and existing evolutionary models by Maeder & Meynet (1994), Bartzakos et al. (2001a) and Foellmi et al. (2003a) argued that virtually *all* WR stars in the SMC are theoretically expected to be the products of binary evolution. It thus came by surprise that the WR binary fraction does not seem to be larger in the SMC compared to the Galaxy ($\approx 40\%$, van der Hucht 2001; Foellmi et al. 2003a). However, this result alone is not conclusive, both due to the small size of the SMC sample, as well as due to observational biases which may hamper the detection of binaries. By performing a systematic spectral analysis of the binaries in the SMC, we wish to assess whether binarity played a decisive role in forming the known SMC WR stars. We wish to address this question from three different standpoints:

- **Did binarity dominate/contribute to the formation of known WR stars?** As discussed above, it is a theoretical prediction that the majority, if not all, of the known WR stars in the SMC would be the product of binary evolution. Based on our study, the short answer to this question is: no, binarity did not contribute significantly to the formation of known WR stars.

  We find that, in order to reproduce the properties of the known WR sample in the SMC, high initial masses ($\gtrsim 60\,M_{\odot}$) are necessary. Such stars are expected to evolve into WR stars as single stars almost independently of the mass-loss recipe adopted. While there are few candidate WR binaries where binarity might have been involved in their formation (e.g., the putative single stars SMC AB 2 and AB 10, or the stripped WO primary in AB 8, see Chapter 6), binarity does not seem to

be necessary for the formation of the known WR stars in the SMC. This is in agreement with the fact that the WR binary fraction in the SMC is similar to that of our Galaxy, but is in apparent contradiction with the theoretical prediction that binaries should dominate the formation of WR stars in the SMC.

Taken at face value, this apparent contradiction between theory and observations has several possible resolutions. The "theoretical" prediction that virtually all WR stars in the SMC should stem from binary evolution (Bartzakos et al. 2001a; Foellmi et al. 2003a) is a straightforward comparison involving two non-straightforward numbers: The observed ratio of WR to O stars, and the predicted ratio of WR to O stars (as predicted from evolutionary models). By comparing these two ratios, the expected frequency of O stars which become WR stars via RLOF in binaries, designated with ϕ (see Maeder & Meynet 1994), can be estimated.

Thus, there are two possible sources for errors here: Either the observed populations of WR and O stars are incomplete, or evolutionary models are not accurate enough to correctly predict WR/O ratios. Admittedly, similar results are obtained when comparing observed ratios to different evolutionary models (see discussion in Chapter 6). This could imply that evolutionary tracks are lacking either the necessary accuracy (e.g., in the adopted initial mass function) or a physical ingredient (e.g., eruptive processes). A first resolution is thus the inaccuracy/incompleteness of current generation of stellar evolution tracks. The other question is whether the observed ratio of WR to O stars is the true one. This will be discussed below.

While our results apply solely for the SMC sample, one is inclined to generalize them to all known WR stars. The reason is that, as discussed above, binarity is expected to play an increasingly more important role in the formation of WR stars at low metallicity environments. Thus, if binarity is found to be unimportant for the formation of WR stars in the SMC ($Z \approx 1/10 Z_{\odot}$), it should not be more important in our Galaxy. It could, however, be more important in environments of even smaller metallicities, such as the very first galaxies.

To summarize, except of distinct examples, we found no evidence that the binary channel dominates the formation of known WR stars. This, however, does not mean that binarity has no impact on the WR population as such.

- **Does binarity have a significant impact on known WR stars in the SMC?** The fact that binarity is not directly related to the formation of the known WR stars in the SMC does not mean that it does not influence it. In fact, a quantitative comparison with binary evolutionary tracks suggest that the majority of systems likely interacted via mass-transfer. Typically, $20-30\,M_{\odot}$ were transferred/lost in the process. We note that the mass-transfer almost always occurred while/after the primary entered the WR phase (cases B/C mass transfer).

  Whether or not RLOF occurred strongly depends on the degree of homogeneity in the star. homogeneous stars generally retrain much smaller radii throughout their evolution and may therefore avoid overfilling their Roche lobes. Generally, the faster a star is rotating, the more homogeneous it becomes (Heger & Langer 2000; Brott et al. 2011). While this is not conclusive, we find indications that tidal synchronization may have been active in slowing down the rotation velocities in the majority of WR binaries in the SMC. A detailed comparison with evolutionary models suggests that a quasi chemically homogeneous evolution (QCHE) is more consistent for the single WR stars rather than for the WR binaries. A possible reason is that the stars in the known SMC binaries lost angular momentum due to tidal friction and therefore lost their initial rotation more rapidly, which in turn implies less mixing.

  Hence, we find evidence that binarity had an important influence on the known WR stars in the SMC, even though it is not crucial for their formation. However, did we really discover all WR stars in the SMC, i.e., is the WR sample in the SMC really complete? If it is not, one may still wonder:

- **Does binarity dominate/contribute to the formation of WR stars?** This is the most general formulation of our research question. Note the omission of the word "known". The question becomes identical to the first question posed above if the WR sample in the SMC is complete. However, there are good reasons to believe that this does not need to be the case.

While O stars are rather difficult to hide because of their extreme luminosities and brightness in the visual, WR stars in binaries can be tricky to detect, because they are often fainter than O stars in the visual due to their high temperatures (large bolometric corrections). Especially in binaries, O stars can easily dominate over WR stars. Hence, there may be many more WR binaries in the SMC which have not been detected simply because of the faintness of the WR component.

The line of argumentation above implicitly assumes that the products of mass-transfer via RLOF have the appearance of WR stars (see Sect. 1.4). Indeed, several systems exist where RLOF has almost certainly occurred, and where the mass donor has the appearance of a WR star, such as V444 Cyg (Vanbeveren et al. 1998) or HD 45166 (Groh et al. 2008). However, this does not prove that all mass donors in binaries which have shed enough mass would retrain the appearance of WR stars.

To summarize, it is still not conclusive whether galaxies such as the SMC abundantly host many undiscovered WR binaries that appear as single O stars by virtue of the WR companion's relative faintness. It is of utmost importance to plan future surveys which would scan the SMC for the existence of such systems.

The caveat of drawing conclusions from this study alone is the size of the sample: In total, there are 12 WR stars known in the SMC, 5 of which are binaries. We are therefore limited by small number statistics, as often the case when dealing with exotic objects. This study is in many ways a first step towards a systematic analysis of WR binaries. Indeed, a comprehensive analysis of the much larger LMC binary sample is currently underway (Shenar et al. in prep.).

Chapter 8.

Summary

This thesis sets as a goal to quantify the impact of binarity (i.e., the presence of a companion star) on massive stars. The fact that massive stars are key drivers of galactic evolution renders this goal fundamentally important. For this purpose, massive binary systems in the Local Group, including OB-type binaries, high mass X-ray binaries (HMXBs), and Wolf-Rayet (WR) binaries, were investigated by means of spectral, orbital, and evolutionary analyses.

Four fundamental facts urged this study: 1) Owing to the enormous leap forward in observational astronomy, we now know that the majority of massive stars reside in binary systems. Hence, *binarity is common*. 2) Recent studies suggest that, during their lifetime, more than half the massive stars will interact with a companion via mass-transfer during Roche lobe overflow (RLOF), occurring when the atmosphere of a star is no longer gravitationally bound to it by virtue of the gravitational pull of its companion. Through mass-transfer, *Binarity can dramatically alter the evolutionary course of massive stars.* 3) The reduction of wind mass-loss rates $\dot{M}$ in recent decades, prompted by accounting for non-homogeneous (clumped) winds, tremendously affects evolutionary models of massive stars. With reduced mass-loss rates, single stars appear to be insufficient to quantitatively account for the different stellar populations observed. *Binarity thus seems to be a necessary component in the grand scheme of stellar evolution*. 4) Binaries offer the only reliable way to measure stellar masses of massive stars, and eclipsing binaries can be used to study the structure of stellar atmospheres, i.e., *binaries are indispensable diagnostic tools*.

WR stars are found in a relatively short-lived, evolved phase in the life of massive stars, where core helium burning is typically assumed to take place. Understanding WR stars, characterized by strong, radiatively driven winds ($-5 \lesssim \log \dot{M}[M_\odot/\mathrm{yr}] \lesssim -4$) and hydrogen deficiency, is of central importance. Their powerful stellar winds and ionizing radiation, as well as their potential final fate as Supernovae (SNe), mean that WR stars shape their environments, chemically and energetically enriching the surrounding interstellar matter, thereby driving the evolution of their host galaxies. Moreover, as potential progenitors of exotic objects as SNe type Ib/c and γ-ray bursts (GRBs), WR stars are considered a crucial link connecting the formation and death of massive stars. Hydrogen-poor WR stars are believed to form via two possible channels: by intrinsic wind mass-loss of their progenitor (O-type) stars, or by RLOF in binaries. The relative weight of these formation channels, as assessed by the astrophysical community, is being constantly re-evaluated in light of new evidence. The high frequency of binarity has led to a revived interest in the binary formation channel, with some studies going as far as suggesting that binarity may dominate the formation of WR stars.

The most direct way to gain insights regarding the impact of binarity on WR stars is to analyze known WR binaries, typically comprising a WR primary and an OB-type secondary. The spectral analyses in this thesis were performed with the non-LTE Potsdam Wolf-Rayet (PoWR) model atmosphere code. Prior to this thesis, PoWR was used primarily for the analysis of the wind-dominated WR stars, but lacked the necessary accuracy for the analysis of photospheric OB-type spectra. The updates introduced in the PoWR code for this purpose are described in Chapter 2. The most important update involves the accurate calculation of the radiation pressure in the quasi-hydrostatic layers, which, instead of accounting for electron scattering only, now accounts for all bound-bound, bound-free, and free-free transitions of the atomic species considered. Moreover, a depth dependent microturbulence was implemented, important for the analysis of stars portraying both photospheric and wind features. The updated PoWR code is now benchmarked against the widely used code TLUSTY and includes, to our knowledge, the most advanced treatment of the hydrostatic layers among model atmosphere codes that account for stellar winds.

The eclipsing OB-type triple system δ Ori A served as an intriguing test-case for the new version of

the PoWR code (Chapter 3), and provided insights regarding the formation of X-rays in massive stars. Through a multiwavelength spectral analysis, we were able to derive stellar parameters which are consistent with the system's characteristics, resolving a long-lasting discrepancy between the orbital masses and the spectroscopic masses of the system's components. We illustrated the potential importance of optically thick clumps in the wind, which in turn affect the derived mass-loss rates. By performing an analysis of forbidden and intercombination X-ray lines, we were able to constrain the formation region of the X-rays in the system. Based on our results, we concluded that the X-rays form in the primary's wind (e.g., via intrinsic shocks), and not at the stellar surface.

HMXBs, which consist of a non-degenerate mass-donor and an accreting compact object, serve as rare examples for systems where RLOF is believed to take place. The analysis of OB-type mass-donors in two prototypical HMXBs, Vela X-1 and IGR J17544-2619 (Chapter 4), resulted in fundamental conclusions regarding the dichotomy of two basic classes of HMXB. The reason for their distinct X-ray behavior has been somewhat of a mystery given the similar spectral type of the donors and the orbital characteristics of both systems. In our study, we found that the wind of the mass-donor in Vela X-1 has a terminal velocity which is significantly smaller than previously inferred. The lower terminal velocity favors a persistent accretion by the compact object in the system, hence the persistently high X-ray luminosity. The terminal velocity derived for IGR J17544-2619, on the other hand, suggests that the accretion occurs in the "propeller regime", where the neutron star can only accrete at distinct intervals, explaining the discontinuous behavior of the X-rays in the system. The study thus resolved an important dilemma regarding the contrasting behavior of both prototypical HMXBs.

The WR binary R 145 in the Large Magellanic Cloud (LMC) was claimed to host the most massive star known ($M \gtrsim 300\,M_{\odot}$). Determining the upper stellar mass limit is a holy grail of stellar physics, laying sharp constraints on the initial mass function and stellar formation. In Chapter 5, we performed an exhaustive analysis of R 145, including an orbital, polarimetric, and spectral analysis, as well as an analysis of the wind-wind collision region. We showed that, contrary to previous claims, the primary's mass is $\approx 55\,M_{\odot}$. By disentangling the composite spectrum, we derived spectral types for both components, and showed that RLOF was likely avoided. These facts have a great impact on our understanding of how massive stars evolve.

Equipped with the necessary tools, all known WR binaries in the Small Magellanic Cloud (SMC) were analyzed (Chapter 6). Due to its low metallicity content ($Z \approx 1/10 Z_{\odot}$), the SMC offers an extremely interesting test-case for the impact of binarity on WR stars. Stellar winds of stars in the SMC are much weaker on average when compared to Galactic stars of the same mass. This means that it is much harder for a single star to eject its hydrogen rich envelope and enter the WR phase. In contrast, the binary formation channel is (to first order) Z-insensitive. In fact, the theoretical prediction is that virtually *all* WR stars in the SMC should be formed via mass-transfer in binaries. Surprisingly, we find that binarity was not important for the formation of the known WR stars in the SMC, as their derived initial masses are large enough to enable them to enter the WR phase via intrinsic mass-loss. This either points towards a strong observational bias, suggesting that hydrogen-stripped stars abundantly exist in the SMC but were so far not detected (e.g., because they are dominated by a bright companion), or that current evolutionary models lack sufficient accuracy or important physical ingredients. Furthermore, a comparison between empirical masses and luminosities derived for the WR primaries, along with theoretical mass-luminosity relations, yielded important constraints on the structure and evolution of the SMC WR stars, suggesting a non-homogeneous structure for the majority of He-burning WR stars in binaries, potentially due to tidal interaction.

To summarize, this thesis thoroughly investigates important aspects concerning the binarity of massive stars, quantitatively assessing the impact of mass-transfer on their evolution. Current theoretical models, modern observational data, and state-of-the-art analysis tools are brought together to illustrate the immense diagnostic potential of binaries for the study of stellar atmospheres and winds, X-ray formation, mass-luminosity relations, stellar structure, and stellar evolution. Our primary conclusion is that, contrary to expectation, mass-transfer was not important for the formation of the majority of known WR stars in the SMC. We were able to gain insights regarding the structure of massive stars, concluding that most core He-burning WR stars in SMC binaries are not chemically homogeneous, unlike putatively single WR stars in the SMC. This greatly constrains evolutionary models of massive stars at low metallicity. This thesis not only provides new insights regarding massive binaries, but also establishes and tests advanced methods for

their analysis, e.g., spectral disentangling and consistent binary spectroscopic analysis . In many ways, this is only the first step in the long journey which lies ahead, paving the road for the urgent analyses of massive binaries in the Local Group which will be conducted in the near future. Meanwhile, the constraints put forth in this thesis should serve as a beacon for evolutionary models of massive stars and binaries which attempt to account for the plethora of stellar objects which populate our Universe.

Bibliography

Abbott, B. P., Abbott, R., Abbott, T. D., et al. 2016, Physical Review Letters, 116, 061102
Aerts, C. 2014, ArXiv e-prints 1407.6479
Aerts, C., Puls, J., Godart, M., & Dupret, M.-A. 2009, A&A, 508, 409
Aldoretta, E. J., Caballero-Nieves, S. M., Gies, D. R., et al. 2015, AJ, 149, 26
Andersen, J. 1991, A&A Rev., 3, 91
Anderson, L. S. 1989, ApJ, 339, 558
Antokhin, I. I. 2011, Bulletin de la Societe Royale des Sciences de Liége, 80, 549
Aspin, C., Simmons, J. F. L., & Brown, J. C. 1981, MNRAS, 194, 283
Asplund, M., Grevesse, N., Sauval, A. J., & Scott, P. 2009, ARA&A, 47, 481
Auer, L. H. & Mihalas, D. 1968, ApJ, 153, 923
Auger, P. 1923, C.R.A.S., 177, 169
Azzopardi, M. & Breysacher, J. 1979, A&A, 75, 120
Bagnuolo, Jr., W. G. & Gies, D. R. 1991, ApJ, 376, 266
Banerjee, S., Kroupa, P., & Oh, S. 2012, ApJ, 746, 15
Barbá, R. H., Gamen, R., Arias, J. I., et al. 2010, in Revista Mexicana de Astronomia y Astrofisica Conference Series, Vol. 38, Revista Mexicana de Astronomia y Astrofisica Conference Series, 30–32
Barnstedt, J., Staubert, R., Santangelo, A., et al. 2008, A&A, 486, 293
Bartzakos, P., Moffat, A. F. J., & Niemela, V. S. 2001a, MNRAS, 324, 18
Bartzakos, P., Moffat, A. F. J., & Niemela, V. S. 2001b, MNRAS, 324, 33
Barziv, O., Kaper, L., Van Kerkwijk, M. H., Telting, J. H., & Van Paradijs, J. 2001, A&A, 377, 925
Baum, E., Hamann, W.-R., Koesterke, L., & Wessolowski, U. 1992, A&A, 266, 402
Beals, C. S. 1929, MNRAS, 90, 202
Belczynski, K., Bulik, T., Mandel, I., et al. 2013, ApJ, 764, 96
Bestenlehner, J. M., Gräfener, G., Vink, J. S., et al. 2014, A&A, 570, A38
Bestenlehner, J. M., Vink, J. S., Gräfener, G., et al. 2011, A&A, 530, L14
Bhalerao, V., Romano, P., Tomsick, J., et al. 2015, MNRAS, 447, 2274
Bildsten, L., Chakrabarty, D., Chiu, J., et al. 1997, ApJS, 113, 367
Blondin, J. M., Kallman, T. R., Fryxell, B. A., & Taam, R. E. 1990, ApJ, 356, 591
Blumenthal, G. R., Drake, G. W. F., & Tucker, W. H. 1972, ApJ, 172, 205
Bonanos, A. Z., Lennon, D. J., Köhlinger, F., et al. 2010, AJ, 140, 416
Bonanos, A. Z., Stanek, K. Z., Udalski, A., et al. 2004, ApJ, 611, L33
Bondi, H. 1952, MNRAS, 112, 195
Bondi, H. & Hoyle, F. 1944, MNRAS, 104, 273
Bonnell, I. A., Bate, M. R., Clarke, C. J., & Pringle, J. E. 1997, MNRAS, 285, 201
Bouret, J.-C., Hillier, D. J., Lanz, T., & Fullerton, A. W. 2012, A&A, 544, A67
Bozzo, E., Falanga, M., & Stella, L. 2008, ApJ, 683, 1031
Bozzo, E., Romano, P., Ducci, L., Bernardini, F., & Falanga, M. 2015, Advances in Space Research, 55, 1255
Breysacher, J., Azzopardi, M., & Testor, G. 1999, A&AS, 137, 117
Breysacher, J., Moffat, A. F. J., & Niemela, V. S. 1982, ApJ, 257, 116
Brott, I., Evans, C. J., Hunter, I., et al. 2011, A&A, 530, A116
Brown, J. C., Aspin, C., Simmons, J. F. L., & McLean, I. S. 1982, MNRAS, 198, 787
Brown, J. C., McLean, I. S., & Emslie, A. G. 1978, A&A, 68, 415
Caballero, J. A. & Solano, E. 2008, A&A, 485, 931
Cananzi, K., Augarde, R., & Lequeux, J. 1993, A&AS, 101, 599
Cantiello, M., Langer, N., Brott, I., et al. 2009, A&A, 499, 279

Cantiello, M., Yoon, S.-C., Langer, N., & Livio, M. 2007, A&A, 465, L29
Cardelli, J. A., Clayton, G. C., & Mathis, J. S. 1989, ApJ, 345, 245
Cassinelli, J. P. 1979, ARA&A, 17, 275
Cassinelli, J. P. & Olson, G. L. 1979, ApJ, 229, 304
Castor, J. I., Abbott, D. C., & Klein, R. I. 1975, ApJ, 195, 157
Chené, A.-N., Moffat, A. F. J., & Crowther, P. A. 2008, in Clumping in Hot-Star Winds, ed. W.-R. Hamann, A. Feldmeier, & L. M. Oskinova, 163
Cherepashchuk, A. M. 1976, Soviet Astronomy Letters, 2, 138
Chini, R., Hoffmeister, V. H., Nasseri, A., Stahl, O., & Zinnecker, H. 2012, MNRAS, 424, 1925
Chodil, G., Mark, H., Rodrigues, R., Seward, F. D., & Swift, C. D. 1967, ApJ, 150, 57
Cidale, L. S. & Ringuelet, A. E. 1993, ApJ, 411, 874
Clark, D. J., Hill, A. B., Bird, A. J., et al. 2009, MNRAS, 399, L113
Cohen, D. H., Wollman, E. E., Leutenegger, M. A., et al. 2014, MNRAS, 439, 908
Conti, P. S. 1976, in Proc. 20th Colloq. Int. Ap. Liége, university of Liége, p. 132, 193–212
Corcoran, M. F. 2003, in IAU Symposium, Vol. 212, A Massive Star Odyssey: From Main Sequence to Supernova, ed. K. van der Hucht, A. Herrero, & C. Esteban, 130
Corcoran, M. F., Nichols, J. S., Pablo, H., et al. 2015, ApJ, 809, 132
Corcoran, M. F., Rawley, G. L., Swank, J. H., & Petre, R. 1995, ApJ, 445, L121
Corcoran, M. F., Stevens, I. R., Pollock, A. M. T., et al. 1996, ApJ, 464, 434
Crowther, P. A. 2007, ARA&A, 45, 177
Crowther, P. A. & Hadfield, L. J. 2006, A&A, 449, 711
Crowther, P. A., Schnurr, O., Hirschi, R., et al. 2010, MNRAS, 408, 731
Crowther, P. A. & Walborn, N. R. 2011, MNRAS, 416, 1311
Cutri, R. M. & et al. 2012, VizieR Online Data Catalog, 2311, 0
Cutri, R. M. & et al. 2013, VizieR Online Data Catalog, 2328, 0
Cutri, R. M., Skrutskie, M. F., van Dyk, S., et al. 2003, VizieR Online Data Catalog, 2246, 0
de Jager, C., Nieuwenhuijzen, H., & van der Hucht, K. A. 1988, A&AS, 72, 259
de Mink, S. E., Cantiello, M., Langer, N., et al. 2009, A&A, 497, 243
de Mink, S. E., Langer, N., Izzard, R. G., Sana, H., & de Koter, A. 2013, ApJ, 764, 166
de Mink, S. E., Sana, H., Langer, N., Izzard, R. G., & Schneider, F. R. N. 2014, ApJ, 782, 7
DENIS Consortium. 2005, VizieR Online Data Catalog, 2263, 0
Dessart, L. & Owocki, S. P. 2005, A&A, 432, 281
Drave, S. P., Bird, A. J., Sidoli, L., et al. 2014, MNRAS, 439, 2175
Drave, S. P., Bird, A. J., Townsend, L. J., et al. 2012, A&A, 539, A21
Drechsel, H., Haas, S., Lorenz, R., & Gayler, S. 1995, A&A, 294, 723
Ducati, J. R. 2002, VizieR Online Data Catalog, 2237, 0
Dufour, R. J., Shields, G. A., & Talbot, Jr., R. J. 1982, ApJ, 252, 461
Dupree, A. K., Gursky, H., Black, J. H., et al. 1980, ApJ, 238, 969
Eggleton, P. P. 1983, ApJ, 268, 368
Ekström, S., Georgy, C., Eggenberger, P., et al. 2012, A&A, 537, A146
Eldridge, J. J., Fraser, M., Smartt, S. J., Maund, J. R., & Crockett, R. M. 2013, MNRAS, 436, 774
Eldridge, J. J., Izzard, R. G., & Tout, C. A. 2008, MNRAS, 384, 1109
Eldridge, J. J., Langer, N., & Tout, C. A. 2011, MNRAS, 414, 3501
Eldridge, J. J. & Stanway, E. R. 2012, MNRAS, 419, 479
Elsner, R. F. & Lamb, F. K. 1976, Nature, 262, 356
ESA, ed. 1997a, The HIPPARCOS and TYCHO Catalogues (ESA-SP 1200; Noordwijk: ESA)
ESA. 1997b, VizieR Online Data Catalog, 1239, 0
Evans, C. J., Crowther, P. A., Fullerton, A. W., & Hillier, D. J. 2004, ApJ, 610, 1021
Evans, C. J., Taylor, W. D., Hénault-Brunet, V., et al. 2011, A&A, 530, A108
Eversberg, T., Lepine, S., & Moffat, A. F. J. 1998, ApJ, 494, 799
Feldmeier, A., Anzer, U., Boerner, G., & Nagase, F. 1996, A&A, 311, 793
Feldmeier, A., Oskinova, L., & Hamann, W.-R. 2003, A&A, 403, 217
Feldmeier, A., Puls, J., & Pauldrach, A. W. A. 1997, A&A, 322, 878

Fitzpatrick, E. L. 1999, PASP, 111, 63
Foellmi, C., Koenigsberger, G., Georgiev, L., et al. 2008, Rev. Mexicana Astron. Astrofis., 44, 3
Foellmi, C., Moffat, A. F. J., & Guerrero, M. A. 2003a, MNRAS, 338, 360
Foellmi, C., Moffat, A. F. J., & Guerrero, M. A. 2003b, MNRAS, 338, 1025
Fraser, M., Dufton, P. L., Hunter, I., & Ryans, R. S. I. 2010, MNRAS, 404, 1306
Friend, D. B. & MacGregor, K. B. 1984, ApJ, 282, 591
Fullerton, A. W., Massa, D. L., & Prinja, R. K. 2006, ApJ, 637, 1025
Gabriel, A. H. & Jordan, C. 1969, MNRAS, 145, 241
Gallagher, J. S., Mould, J. R., de Feijter, E., et al. 1996, ApJ, 466, 732
Gayley, K. G., Owocki, S. P., & Cranmer, S. R. 1997, ApJ, 475, 786
Georgiev, L., Koenigsberger, G., Hillier, D. J., et al. 2011, AJ, 142, 191
Georgy, C., Ekström, S., Hirschi, R., et al. 2015, ArXiv e-prints
Gerke, J. R., Kochanek, C. S., & Stanek, K. Z. 2015, MNRAS, 450, 3289
Gies, D. R. & Lambert, D. L. 1992, ApJ, 387, 673
Giménez-García, A., Shenar, T., Torrejón, J. M., et al. 2016, A&A, 591, A26
Giménez-García, A., Torrejón, J. M., Eikmann, W., et al. 2015, A&A, 576, A108
González, J. F. & Levato, H. 2006, A&A, 448, 283
González-Fernández, C., Asensio Ramos, A., Garzón, F., Cabrera-Lavers, A., & Hammersley, P. L. 2014, ApJ, 782, 86
González-Galán, A. 2015, ArXiv e-prints
González-Galán, A., Negueruela, I., Castro, N., et al. 2014, A&A, 566, A131
Gordon, K. D., Clayton, G. C., Misselt, K. A., Landolt, A. U., & Wolff, M. J. 2003, ApJ, 594, 279
Gosset, E., Royer, P., Rauw, G., Manfroid, J., & Vreux, J.-M. 2001, MNRAS, 327, 435
Gräfener, G. & Hamann, W.-R. 2005, A&A, 432, 633
Gräfener, G. & Hamann, W.-R. 2008, A&A, 482, 945
Gräfener, G., Koesterke, L., & Hamann, W.-R. 2002, A&A, 387, 244
Gräfener, G. & Vink, J. S. 2013, A&A, 560, A6
Gräfener, G., Vink, J. S., de Koter, A., & Langer, N. 2011, A&A, 535, A56
Gray, D. F. 1975, ApJ, 202, 148
Grebenev, S. A. 2010, ArXiv e-prints
Grebenev, S. A. & Sunyaev, R. A. 2007, Astronomy Letters, 33, 149
Grevesse, N. & Sauval, A. J. 1998, Space Sci. Rev., 85, 161
Groh, J. H., Georgy, C., & Ekström, S. 2013, A&A, 558, L1
Groh, J. H., Oliveira, A. S., & Steiner, J. E. 2008, A&A, 485, 245
Guerrero, M. A. & Chu, Y.-H. 2008, ApJS, 177, 216
Habets, G. M. H. J. & Heintze, J. R. W. 1981, A&AS, 46, 193
Hadrava, P. 1995, A&AS, 114, 393
Hadrava, P., Šlechta, M., & Škoda, P. 2009, A&A, 507, 397
Hainich, R., Pasemann, D., Todt, H., et al. 2015, A&A, 581, A21
Hainich, R., Rühling, U., Todt, H., et al. 2014, A&A, 565, A27
Hamann, W.-R. 1981, A&A, 93, 353
Hamann, W.-R. & Gräfener, G. 2003a, A&A, 410, 993
Hamann, W.-R. & Gräfener, G. 2003b, A&A, 410, 993
Hamann, W.-R. & Gräfener, G. 2004, A&A, 427, 697
Hamann, W.-R., Gräfener, G., & Liermann, A. 2006, A&A, 457, 1015
Hamann, W.-R. & Koesterke, L. 1998, A&A, 335, 1003
Hamann, W.-R., Koesterke, L., & Wessolowski, U. 1995, A&A, 299, 151
Harvey, A. S., Stickland, D. J., Howarth, I. D., & Zuiderwijk, E. J. 1987, The Observatory, 107, 205
Harvin, J. A., Gies, D. R., Bagnuolo, Jr., W. G., Penny, L. R., & Thaller, M. L. 2002, ApJ, 565, 1216
Heger, A., Fryer, C. L., Woosley, S. E., Langer, N., & Hartmann, D. H. 2003, ApJ, 591, 288
Heger, A. & Langer, N. 2000, ApJ, 544, 1016
Heger, A., Langer, N., & Woosley, S. E. 2000, ApJ, 528, 368
Heggie, D. C. 1975, MNRAS, 173, 729

Heintz, W. D. 1980, ApJS, 44, 111
Herrero, A., Kudritzki, R. P., Vilchez, J. M., et al. 1992, A&A, 261, 209
Hervé, A., Rauw, G., & Nazé, Y. 2013, A&A, 551, A83
Hill, G. M., Moffat, A. F. J., St-Louis, N., & Bartzakos, P. 2000, MNRAS, 318, 402
Hillier, D. J. 1984, ApJ, 280, 744
Hillier, D. J. 1987, ApJS, 63, 965
Hillier, D. J. 1991, A&A, 247, 455
Hillier, D. J. 2003, in Astronomical Society of the Pacific Conference Series, Vol. 288, Stellar Atmosphere Modeling, ed. I. Hubeny, D. Mihalas, & K. Werner, 199
Hillier, D. J., Bouret, J.-C., Lanz, T., & Busche, J. R. 2012, MNRAS, 426, 1043
Hillier, D. J. & Miller, D. L. 1998, ApJ, 496, 407
Hirschi, R. 2008, in Clumping in Hot-Star Winds, ed. W.-R. Hamann, A. Feldmeier, & L. M. Oskinova, 9
Horch, E., Ninkov, Z., & Franz, O. G. 2001, AJ, 121, 1583
Horne, J. H. & Baliunas, S. L. 1986, ApJ, 302, 757
Howarth, I. D. 1983, MNRAS, 203, 301
Howarth, I. D. 1997, The Observatory, 117, 335
Howarth, I. D., Siebert, K. W., Hussain, G. A. J., & Prinja, R. K. 1997, MNRAS, 284, 265
Howarth, I. D. & Stevens, I. R. 2014, MNRAS, 445, 2878
Hubeny, I., Heap, S. R., & Altner, B. 1991, ApJ, 377, L33
Hubeny, I., Hummer, D. G., & Lanz, T. 1994, A&A, 282, 151
Hubeny, I. & Lanz, T. 1995, ApJ, 439, 875
Hummel, C. A., Rivinius, T., Nieva, M.-F., et al. 2013, A&A, 554, A52
Hummer, D. G. 1963, MNRAS, 125, 461
Hummer, D. G. & Mihalas, D. 1967, ApJ, 150, L57
Hummer, D. G. & Seaton, M. J. 1963, MNRAS, 125, 437
Hunter, I., Dufton, P. L., Smartt, S. J., et al. 2007, A&A, 466, 277
Hurley, J. R., Tout, C. A., & Pols, O. R. 2002, MNRAS, 329, 897
Hutchings, J. B., Crampton, D., Cowley, A. P., & Thompson, I. B. 1984, PASP, 96, 811
Ignace, R. 2001, ApJ, 549, L119
Ignace, R. & Gayley, K. G. 2002, ApJ, 568, 954
Ignace, R., Oskinova, L. M., & Foullon, C. 2000, MNRAS, 318, 214
Ignace, R., Waldron, W. L., Cassinelli, J. P., & Burke, A. E. 2012, ApJ, 750, 40
in't Zand, J. J. M. 2005, A&A, 441, L1
Joss, P. C. & Rappaport, S. A. 1984, ARA&A, 22, 537
Kaper, L., Hammerschlag-Hensberge, G., & Zuiderwijk, E. J. 1994, A&A, 289, 846
Kaper, L., van der Meer, A., & Najarro, F. 2006, A&A, 457, 595
Karino, S. 2014, PASJ, 66, 34
Kaufer, A., Stahl, O., Tubbesing, S., et al. 1999, The Messenger, 95, 8
Keller, S. C. & Wood, P. R. 2006, ApJ, 642, 834
Kippenhahn, R. & Weigert, A. 1967, ZAp, 65, 251
Koch, R. H. & Hrivnak, B. J. 1981, ApJ, 248, 249
Koenigsberger, G., Georgiev, L., Hillier, D. J., et al. 2010, AJ, 139, 2600
Koenigsberger, G., Moreno, E., & Harrington, D. M. 2012, A&A, 539, A84
Koenigsberger, G., Morrell, N., Hillier, D. J., et al. 2014, AJ, 148, 62
Koesterke, L. & Hamann, W.-R. 1995, A&A, 299, 503
Köhler, K., Langer, N., de Koter, A., et al. 2015, A&A, 573, A71
Korn, A. J., Becker, S. R., Gummersbach, C. A., & Wolf, B. 2000, A&A, 353, 655
Kreykenbohm, I., Coburn, W., Wilms, J., et al. 2002, A&A, 395, 129
Kreykenbohm, I., Wilms, J., Coburn, W., et al. 2004, A&A, 427, 975
Kreykenbohm, I., Wilms, J., Kretschmar, P., et al. 2008, A&A, 492, 511
Kroupa, P. 2001, MNRAS, 322, 231
Krtička, J., Feldmeier, A., Oskinova, L. M., Kubát, J., & Hamann, W.-R. 2009, A&A, 508, 841
Krtička, J. & Kubát, J. 2009, MNRAS, 394, 2065

Krtička, J., Kubát, J., & Krtičková, I. 2015, A&A, 579, A111
Kubát, J. 2001, A&A, 366, 210
Kubát, J., Puls, J., & Pauldrach, A. W. A. 1999, A&A, 341, 587
Kudritzki, R. P., Pauldrach, A., & Puls, J. 1987, A&A, 173, 293
Kudritzki, R. P., Pauldrach, A., Puls, J., & Abbott, D. C. 1989, A&A, 219, 205
Kudritzki, R.-P. & Puls, J. 2000, ARA&A, 38, 613
Lamers, H. J. G. L. M., Haser, S., de Koter, A., & Leitherer, C. 1999, ApJ, 516, 872
Lamers, H. J. G. L. M. & Leitherer, C. 1993, ApJ, 412, 771
Lamers, H. J. G. L. M., Maeder, A., Schmutz, W., & Cassinelli, J. P. 1991, ApJ, 368, 538
Lamers, H. J. G. L. M., Snow, T. P., & Lindholm, D. M. 1995, ApJ, 455, 269
Lamers, J. G. L. M. H. & Cassinelli, J. P. 1999, Stellar Winds (Cambridge University Press)
Lamontagne, R., Moffat, A. F. J., Drissen, L., Robert, C., & Matthews, J. M. 1996, AJ, 112, 2227
Langer, N. 1989, A&A, 210, 93
Langer, N. 1992, A&A, 265, L17
Langer, N. 2012, ARA&A, 50, 107
Lanz, T. & Hubeny, I. 2003, ApJS, 146, 417
Larsen, S. S., Clausen, J. V., & Storm, J. 2000, A&A, 364, 455
Lattimer, J. M. & Steiner, A. W. 2014, ApJ, 784, 123
Laycock, S., Zezas, A., Hong, J., Drake, J. J., & Antoniou, V. 2010, ApJ, 716, 1217
Lefever, K., Puls, J., & Aerts, C. 2007, A&A, 463, 1093
Lefèvre, L., Marchenko, S. V., Lépine, S., et al. 2005, MNRAS, 360, 141
Lemke, M. 1997, A&AS, 122, 285
Lépine, S. & Moffat, A. F. J. 1999, ApJ, 514, 909
Leutenegger, M. A., Paerels, F. B. S., Kahn, S. M., & Cohen, D. H. 2006, ApJ, 650, 1096
Levine, A. M., Rappaport, S., Remillard, R., & Savcheva, A. 2004, ApJ, 617, 1284
López-Corredoira, M., Cabrera-Lavers, A., Garzón, F., & Hammersley, P. L. 2002, A&A, 394, 883
Lorenzo, J., Negueruela, I., Castro, N., et al. 2014, A&A, 562, A18
Lubow, S. H. & Shu, F. H. 1975, ApJ, 198, 383
Lucy, L. B. & Solomon, P. M. 1970, ApJ, 159, 879
Luehrs, S. 1997, PASP, 109, 504
Lutovinov, A., Revnivtsev, M., Gilfanov, M., et al. 2005, A&A, 444, 821
Lutovinov, A. A., Revnivtsev, M. G., Tsygankov, S. S., & Krivonos, R. A. 2013, MNRAS, 431, 327
Lutz, T. E. & Kelker, D. H. 1973, PASP, 85, 573
Macfarlane, J. J., Cassinelli, J. P., Welsh, B. Y., et al. 1991, ApJ, 380, 564
Maeder, A. 1987, A&A, 178, 159
Maeder, A., Georgy, C., & Meynet, G. 2008, A&A, 479, L37
Maeder, A. & Meynet, G. 1994, A&A, 287, 803
Maeder, A. & Meynet, G. 1996, A&A, 313, 140
Magalhaes, A. M., Benedetti, E., & Roland, E. H. 1984, PASP, 96, 383
Maheswaran, M. & Cassinelli, J. P. 2009, MNRAS, 394, 415
Maíz Apellániz, J. 2010, A&A, 518, A1
Maíz Apellániz, J., Alfaro, E. J., & Sota, A. 2008, ArXiv e-prints
Maíz Apellániz, J., Evans, C. J., Barbá, R. H., et al. 2014, A&A, 564, A63
Manousakis, A. & Walter, R. 2015, ArXiv e-prints
Marchant, P., Langer, N., Podsiadlowski, P., Tauris, T., & Moriya, T. 2016, ArXiv e-prints
Marchenko, S. V. & Moffat, A. F. J. 1998, ApJ, 499, L195
Markova, N. & Puls, J. 2008, A&A, 478, 823
Markova, N. & Puls, J. 2014, ArXiv e-prints
Markova, N., Puls, J., Scuderi, S., & Markov, H. 2005, A&A, 440, 1133
Martínez-Núñez, S., Sander, A., Gímenez-García, A., et al. 2015, A&A, 578, A107
Martínez-Núñez, S., Torrejón, J. M., Kühnel, M., et al. 2014, A&A, 563, A70
Martins, F., Mahy, L., Hillier, D. J., & Rauw, G. 2012, A&A, 538, A39
Martins, F., Schaerer, D., & Hillier, D. J. 2002, A&A, 382, 999

Martins, F., Schaerer, D., & Hillier, D. J. 2005, A&A, 436, 1049
Mason, A. B., Clark, J. S., Norton, A. J., et al. 2012, MNRAS, 422, 199
Mason, A. B., Clark, J. S., Norton, A. J., Negueruela, I., & Roche, P. 2009a, A&A, 505, 281
Mason, B. D., Hartkopf, W. I., Gies, D. R., Henry, T. J., & Helsel, J. W. 2009b, AJ, 137, 3358
Massey, P. 2002, VizieR Online Data Catalog, 2236, 0
Massey, P. & Hunter, D. A. 1998, ApJ, 493, 180
Massey, P., Morrell, N. I., Neugent, K. F., et al. 2012, ApJ, 748, 96
Massey, P., Neugent, K. F., Hillier, D. J., & Puls, J. 2013, ApJ, 768, 6
Massey, P., Neugent, K. F., Morrell, N., & Hillier, D. J. 2014, ApJ, 788, 83
Massey, P., Olsen, K. A. G., & Parker, J. W. 2003, PASP, 115, 1265
Mauche, C. W., Liedahl, D. A., Akiyama, S., & Plewa, T. 2007, Progress of Theoretical Physics Supplement, 169, 196
Mayer, P., Harmanec, P., Wolf, M., Božić, H., & Šlechta, M. 2010, A&A, 520, A89
McClintock, J. E., Rappaport, S., Joss, P. C., et al. 1976, ApJ, 206, L99
McErlean, N. D., Lennon, D. J., & Dufton, P. L. 1998, A&A, 329, 613
Meitner, L. 1922, Zeitschrift fur Physik, 9, 131
Mermilliod, J. C. 1995, VizieR Online Data Catalog, 2122, 0
Meynet, G. & Maeder, A. 2005, A&A, 429, 581
Mihalas, D. 1978, Stellar atmospheres /2nd edition/
Miller, N. A., Cassinelli, J. P., Waldron, W. L., MacFarlane, J. J., & Cohen, D. H. 2002, ApJ, 577, 951
Moffat, A. F. J. 1982, ApJ, 257, 110
Moffat, A. F. J. 1988, ApJ, 330, 766
Moffat, A. F. J. 1989, ApJ, 347, 373
Moffat, A. F. J. 1994, Ap&SS, 221, 467
Moffat, A. F. J. 1998, Ap&SS, 260, 225
Moffat, A. F. J., Breysacher, J., & Seggewiss, W. 1985, ApJ, 292, 511
Moffat, A. F. J., Corcoran, M. F., Stevens, I. R., et al. 2002, ApJ, 573, 191
Moffat, A. F. J., Drissen, L., Lamontagne, R., & Robert, C. 1988, ApJ, 334, 1038
Moffat, A. F. J., Marchenko, S. V., Bartzakos, P., et al. 1998, ApJ, 497, 896
Moffat, A. F. J., Niemela, V. S., & Marraco, H. G. 1990, ApJ, 348, 232
Moffat, A. F. J. & Seggewiss, W. 1977, A&A, 54, 607
Mokiem, M. R., de Koter, A., Vink, J. S., et al. 2007, A&A, 473, 603
Morel, M. & Magnenat, P. 1978, A&AS, 34, 477
Moshir, M. & et al. 1990, in IRAS Faint Source Catalogue, version 2.0 (1990), 0
Muijres, L., Vink, J. S., de Koter, A., et al. 2012, A&A, 546, A42
Muijres, L. E., de Koter, A., Vink, J. S., et al. 2011, A&A, 526, A32
Nazé, Y. 2009, A&A, 506, 1055
Nazé, Y., Broos, P. S., Oskinova, L., et al. 2011, ApJS, 194, 7
Nazé, Y., Corcoran, M. F., Koenigsberger, G., & Moffat, A. F. J. 2007, ApJ, 658, L25
Naze, Y., Petit, V., Rinbrand, M., et al. 2014, ArXiv e-prints
Negueruela, I., Maíz Apellániz, J., Simón-Díaz, S., et al. 2014, ArXiv e-prints
Negueruela, I., Smith, D. M., Reig, P., Chaty, S., & Torrejón, J. M. 2006, in ESA Special Publication, Vol. 604, The X-ray Universe 2005, ed. A. Wilson, 165
Negueruela, I., Torrejón, J. M., Reig, P., Ribó, M., & Smith, D. M. 2008, in American Institute of Physics Conference Series, Vol. 1010, A Population Explosion: The Nature & Evolution of X-ray Binaries in Diverse Environments, ed. R. M. Bandyopadhyay, S. Wachter, D. Gelino, & C. R. Gelino, 252–256
Nichols, J., Huenemoerder, D. P., Corcoran, M. F., et al. 2015, ApJ, 809, 133
Niemela, V. S. 1988, in Astronomical Society of the Pacific Conference Series, Vol. 1, Progress and Opportunities in Southern Hemisphere Optical Astronomy. The CTIO 25th Anniversary Symposium, ed. V. M. Blanco & M. M. Phillips, 381
Niemela, V. S., Gamen, R. C., Barbá, R. H., et al. 2008, MNRAS, 389, 1447
Niemela, V. S., Massey, P., Testor, G., & Giménez Benítez, S. 2002, MNRAS, 333, 347
Nugis, T., Annuk, K., & Hirv, A. 2007, Baltic Astronomy, 16, 227

Oey, M. S. & Clarke, C. J. 2005, ApJ, 620, L43
Oskinova, L. M. 2005, MNRAS, 361, 679
Oskinova, L. M., Feldmeier, A., & Hamann, W.-R. 2004, A&A, 422, 675
Oskinova, L. M., Feldmeier, A., & Kretschmar, P. 2012, MNRAS, 421, 2820
Oskinova, L. M., Hamann, W.-R., & Feldmeier, A. 2007, A&A, 476, 1331
Oskinova, L. M., Steinke, M., Hamann, W.-R., et al. 2013a, MNRAS, 436, 3357
Oskinova, L. M., Sun, W., Evans, C. J., et al. 2013b, ApJ, 765, 73
Oskinova, L. M., Todt, H., Ignace, R., et al. 2011, MNRAS, 416, 1456
Oudmaijer, R. D. & Parr, A. M. 2010, MNRAS, 405, 2439
Owocki, S. P., Castor, J. I., & Rybicki, G. B. 1988, ApJ, 335, 914
Owocki, S. P. & Cohen, D. H. 2006, ApJ, 648, 565
Owocki, S. P., Gayley, K. G., & Shaviv, N. J. 2004, ApJ, 616, 525
Owocki, S. P. & Puls, J. 1999, ApJ, 510, 355
Pablo, H., Richardson, N. D., Moffat, A. F. J., et al. 2015, ApJ, 809, 134
Packet, W. 1981, A&A, 102, 17
Paczyński, B. 1967, Acta Astron., 17, 355
Paczynski, B. 1973, in IAU Symposium, Vol. 49, Wolf-Rayet and High-Temperature Stars, ed. M. K. V. Bappu & J. Sahade, 143
Palate, M., Rauw, G., Koenigsberger, G., & Moreno, E. 2013, A&A, 552, A39
Pallavicini, R., Golub, L., Rosner, R., et al. 1981, ApJ, 248, 279
Parker, J. W., Garmany, C. D., Massey, P., & Walborn, N. R. 1992, AJ, 103, 1205
Pauldrach, A. W. A., Vanbeveren, D., & Hoffmann, T. L. 2012, A&A, 538, A75
Pellizza, L. J., Chaty, S., & Negueruela, I. 2006, A&A, 455, 653
Penny, L. R. 1996, ApJ, 463, 737
Perrier, C., Breysacher, J., & Rauw, G. 2009, A&A, 503, 963
Petit, P., Louge, T., Théado, S., et al. 2014, PASP, 126, 469
Pietrzyński, G., Graczyk, D., Gieren, W., et al. 2013, Nature, 495, 76
Pollock, A. M. T. 2007, A&A, 463, 1111
Pols, O. R., Cote, J., Waters, L. B. F. M., & Heise, J. 1991, A&A, 241, 419
Porquet, D., Mewe, R., Dubau, J., Raassen, A. J. J., & Kaastra, J. S. 2001, A&A, 376, 1113
Prilutskii, O. F. & Usov, V. V. 1976, Soviet Ast., 20, 2
Prinja, R. K. & Massa, D. L. 2010, A&A, 521, L55
Puls, J., Kudritzki, R.-P., Herrero, A., et al. 1996, A&A, 305, 171
Puls, J., Springmann, U., & Lennon, M. 2000, A&AS, 141, 23
Puls, J., Urbaneja, M. A., Venero, R., et al. 2005, A&A, 435, 669
Puls, J., Vink, J. S., & Najarro, F. 2008, A&A Rev., 16, 209
Quaintrell, H., Norton, A. J., Ash, T. D. C., et al. 2003, A&A, 401, 313
Raassen, A. J. J. & Pollock, A. M. T. 2013, A&A, 550, A55
Raghavan, D., McAlister, H. A., Torres, G., et al. 2009, ApJ, 690, 394
Rahoui, F. & Chaty, S. 2008, A&A, 492, 163
Ramírez-Agudelo, O. H., Sana, H., de Mink, S. E., et al. 2015, A&A, 580, A92
Ramírez-Agudelo, O. H., Simón-Díaz, S., Sana, H., et al. 2013, A&A, 560, A29
Rauw, G., De Becker, M., Nazé, Y., et al. 2004, A&A, 420, L9
Rauw, G. & Naze, Y. 2015, ArXiv e-prints
Rauw, G., Vreux, J.-M., & Bohannan, B. 1999, ApJ, 517, 416
Rauw, G., Vreux, J.-M., Gosset, E., et al. 1996, A&A, 306, 771
Rayner, J. T., Toomey, D. W., Onaka, P. M., et al. 2003, PASP, 115, 362
Reimer, A. & Reimer, O. 2009, ApJ, 694, 1139
Repolust, T., Puls, J., & Herrero, A. 2004, A&A, 415, 349
Richardson, N. D., Gies, D. R., & Williams, S. J. 2011, AJ, 142, 201
Robert, C., Moffat, A. F. J., Drissen, L., et al. 1992, ApJ, 397, 277
Romano, P., Bozzo, E., Mangano, V., et al. 2015, A&A, 576, L4
Romano, P., Sidoli, L., Cusumano, G., et al. 2009, ApJ, 696, 2068

Runacres, M. C. & Owocki, S. P. 2002, A&A, 381, 1015
Sadakane, K., Hirata, R., Jugaku, J., et al. 1985, ApJ, 288, 284
Sako, M., Liedahl, D. A., Kahn, S. M., & Paerels, F. 1999, ApJ, 525, 921
Salpeter, E. E. 1955, ApJ, 121, 161
Sana, H., de Koter, A., de Mink, S. E., et al. 2013, A&A, 550, A107
Sana, H., de Mink, S. E., de Koter, A., et al. 2012, Science, 337, 444
Sana, H., Le Bouquin, J.-B., Lacour, S., et al. 2014, ApJS, 215, 15
Sana, H., Rauw, G., & Gosset, E. 2001, A&A, 370, 121
Sander, A., Hamann, W.-R., & Todt, H. 2012, A&A, 540, A144
Sander, A., Shenar, T., Hainich, R., et al. 2015, A&A, 577, A13
Santolaya-Rey, A. E., Puls, J., & Herrero, A. 1997, A&A, 323, 488
Sato, N., Nagase, F., Kawai, N., et al. 1986, ApJ, 304, 241
Scargle, J. D. 1982, ApJ, 263, 835
Schmidt-Kaler, T. 1982, Landolt-Börnstein: Numerical Data and Functional Relationship in Science and Technology, Vol. VI/2b (Springer-Verlag. Berlin)
Schmutz, W., Hamann, W.-R., & Wessolowski, U. 1989, A&A, 210, 236
Schneider, F. R. N., Izzard, R. G., de Mink, S. E., et al. 2014a, ApJ, 780, 117
Schneider, F. R. N., Langer, N., de Koter, A., et al. 2014b, A&A, 570, A66
Schnurr, O., Casoli, J., Chené, A.-N., Moffat, A. F. J., & St-Louis, N. 2008a, MNRAS, 389, L38
Schnurr, O., Moffat, A. F. J., St-Louis, N., Morrell, N. I., & Guerrero, M. A. 2008b, MNRAS, 389, 806
Schnurr, O., Moffat, A. F. J., Villar-Sbaffi, A., St-Louis, N., & Morrell, N. I. 2009, MNRAS, 395, 823
Seaton, M. J. 1979, MNRAS, 187, 73P
Seward, F. D. & Chlebowski, T. 1982, ApJ, 256, 530
Sguera, V., Barlow, E. J., Bird, A. J., et al. 2005, A&A, 444, 221
Shakura, N., Postnov, K., Kochetkova, A., & Hjalmarsdotter, L. 2012, MNRAS, 420, 216
Shakura, N., Postnov, K., Sidoli, L., & Paizis, A. 2014, MNRAS, 442, 2325
Shara, M. M., Crawford, S. M., Vanbeveren, D., et al. 2015, ArXiv e-prints
Shaviv, N. J. 2000, ApJ, 532, L137
Shenar, T., Hainich, R., Todt, H., et al. 2016, A&A, 591, A22
Shenar, T., Hamann, W.-R., & Todt, H. 2014, A&A, 562, A118
Shenar, T., Oskinova, L., Hamann, W.-R., et al. 2015, ApJ, 809, 135
Sidoli, L. 2011, ArXiv e-prints
Sidoli, L., Mereghetti, S., Sguera, V., & Pizzolato, F. 2012, MNRAS, 420, 554
Sidoli, L., Paizis, A., & Mereghetti, S. 2006, A&A, 450, L9
Sidoli, L., Romano, P., Mangano, V., et al. 2009, ApJ, 690, 120
Sidoli, L., Romano, P., Mangano, V., et al. 2008, ApJ, 687, 1230
Sidoli, L., Romano, P., Mereghetti, S., et al. 2007, A&A, 476, 1307
Simmons, J. F. L. & Boyle, C. B. 1984, A&A, 134, 368
Simon, K. P. & Sturm, E. 1994, A&A, 281, 286
Simón-Díaz, S., Caballero, J. A., Lorenzo, J., et al. 2015, ApJ, 799, 169
Simón-Díaz, S. & Herrero, A. 2007, A&A, 468, 1063
Smartt, S. J., Dufton, P. L., & Lennon, D. J. 1997, A&A, 326, 763
Smith, L. F. 1968, MNRAS, 138, 109
Smith, L. F., Shara, M. M., & Moffat, A. F. J. 1996, MNRAS, 281, 163
Smith, N. 2014, ARA&A, 52, 487
Smith, R. C., Points, S., Chu, Y.-H., et al. 2005, in Bulletin of the American Astronomical Society, Vol. 37, American Astronomical Society Meeting Abstracts, 145.01
Song, H. F., Maeder, A., Meynet, G., et al. 2013, A&A, 556, A100
Song, H. F., Meynet, G., Maeder, A., Ekström, S., & Eggenberger, P. 2016, A&A, 585, A120
Soszynski, I., Udalski, A., Kubiak, M., et al. 2004, Acta Astron., 54, 347
Sota, A., Maíz Apellániz, J., Morrell, N. I., et al. 2014, ApJS, 211, 10
Sota, A., Maíz Apellániz, J., Walborn, N. R., et al. 2011, ApJS, 193, 24
St-Louis, N. & Moffat, A. F. J. 2008, in Clumping in Hot-Star Winds, ed. W.-R. Hamann, A. Feldmeier, &

L. M. Oskinova, 39
St.-Louis, N., Moffat, A. F. J., Drissen, L., Bastien, P., & Robert, C. 1988, ApJ, 330, 286
St-Louis, N., Moffat, A. F. J., Marchenko, S., & Pittard, J. M. 2005, ApJ, 628, 953
Stahl, O., Buzzoni, B., Kraus, G., et al. 1986, The Messenger, 46, 23
Stevens, I. R., Blondin, J. M., & Pollock, A. M. T. 1992, ApJ, 386, 265
Stevens, I. R. & Pollock, A. M. T. 1994, MNRAS, 269, 226
Struve, O. & Elvey, C. T. 1934, ApJ, 79, 409
Sturm, R., Haberl, F., Pietsch, W., et al. 2013, A&A, 558, A3
Sundqvist, J. O. & Owocki, S. P. 2013, MNRAS, 428, 1837
Sundqvist, J. O., Owocki, S. P., Cohen, D. H., Leutenegger, M. A., & Townsend, R. H. D. 2012, MNRAS, 420, 1553
Sundqvist, J. O., Puls, J., Feldmeier, A., & Owocki, S. P. 2011, A&A, 528, A64
Sunyaev, R. A., Grebenev, S. A., Lutovinov, A. A., et al. 2003, The Astronomer's Telegram, 190, 1
Swank, J. H., Smith, D. M., & Markwardt, C. B. 2007, The Astronomer's Telegram, 999
Szabados, L. 1997, in ESA Special Publication, Vol. 402, Hipparcos - Venice '97, ed. R. M. Bonnet, E. Høg, P. L. Bernacca, L. Emiliani, A. Blaauw, C. Turon, J. Kovalevsky, L. Lindegren, H. Hassan, M. Bouffard, B. Strim, D. Heger, M. A. C. Perryman, & L. Woltjer, 657–660
Taylor, W. D., Evans, C. J., Sana, H., et al. 2011, A&A, 530, L10
Todt, H., Kniazev, A. Y., Gvaramadze, V. V., et al. 2013, MNRAS, 430, 2302
Todt, H., Sander, A., Hainich, R., et al. 2015, A&A, 579, A75
Tokovinin, A., Mason, B. D., & Hartkopf, W. I. 2014, AJ, 147, 123
Torrejón, J. M., Schulz, N. S., Nowak, M. A., et al. 2015, ApJ, 810, 102
Torres, G., Andersen, J., & Giménez, A. 2010, A&A Rev., 18, 67
Torres, K. B. V., Lampens, P., Frémat, Y., et al. 2011, A&A, 525, A50
Torres-Dodgen, A. V. & Massey, P. 1988, AJ, 96, 1076
Tout, C. A., Aarseth, S. J., Pols, O. R., & Eggleton, P. P. 1997, MNRAS, 291, 732
Townsley, L. K., Broos, P. S., Garmire, G. P., et al. 2014, ApJS, 213, 1
Tramper, F., Gräfener, G., Hartoog, O. E., et al. 2013, A&A, 559, A72
Tramper, F., Sana, H., Fitzsimons, N. E., et al. 2016, MNRAS, 455, 1275
Trundle, C., Dufton, P. L., Hunter, I., et al. 2007, A&A, 471, 625
Ulaczyk, K., Szymański, M. K., Udalski, A., et al. 2012, Acta Astron., 62, 247
Unsöld, A. 1955, Physik der Sternatmosphären (Julius Springer)
Usov, V. V. 1992, ApJ, 389, 635
Usov, V. V. 1995, in IAU Symposium, Vol. 163, Wolf-Rayet Stars: Binaries; Colliding Winds; Evolution, ed. K. A. van der Hucht & P. M. Williams, 495
Šurlan, B., Hamann, W.-R., Aret, A., et al. 2013, A&A, 559, A130
Šurlan, B., Hamann, W.-R., Kubát, J., Oskinova, L. M., & Feldmeier, A. 2012, A&A, 541, A37
van Altena, W. F., Lee, J. T., & Hoffleit, D. 1995, VizieR Online Data Catalog, 1174, 0
van den Heuvel, E. P. J. & Heise, J. 1972, Nature Physical Science, 239, 67
van der Hucht, K. A. 2001, New A Rev., 45, 135
van Kerkwijk, M. H., van Paradijs, J., Zuiderwijk, E. J., et al. 1995, A&A, 303, 483
van Leeuwen, F. 2007, A&A, 474, 653
van Loon, J. T., Kaper, L., & Hammerschlag-Hensberge, G. 2001, A&A, 375, 498
Vanbeveren, D., De Loore, C., & Van Rensbergen, W. 1998, A&A Rev., 9, 63
Vanbeveren, D., Van Bever, J., & Belkus, H. 2007, ApJ, 662, L107
Vernet, J., Dekker, H., D'Odorico, S., et al. 2011, A&A, 536, A105
Vidal, N. V., Wickramasinghe, D. T., & Peterson, B. A. 1973, ApJ, 182, L77
Villamariz, M. R. & Herrero, A. 2000, A&A, 357, 597
Vink, J. S., ed. 2015, Astrophysics and Space Science Library, Vol. 412, Very Massive Stars in the Local Universe
Vink, J. S., de Koter, A., & Lamers, H. J. G. L. M. 1999, A&A, 350, 181
Vink, J. S., de Koter, A., & Lamers, H. J. G. L. M. 2000, A&A, 362, 295
Vink, J. S., Heger, A., Krumholz, M. R., et al. 2015, Highlights of Astronomy, 16, 51

Walborn, N. R. 1972, AJ, 77, 312
Walborn, N. R. 2008, in Revista Mexicana de Astronomia y Astrofisica Conference Series, Vol. 33, Revista Mexicana de Astronomia y Astrofisica Conference Series, 5–14
Waldron, W. L. & Cassinelli, J. P. 2001, ApJ, 548, L45
Waldron, W. L. & Cassinelli, J. P. 2007, ApJ, 668, 456
Waldron, W. L. & Cassinelli, J. P. 2010, ApJ, 711, L30
Walter, R., Lutovinov, A. A., Bozzo, E., & Tsygankov, S. S. 2015, A&A Rev., 23, 2
Walter, R. & Zurita Heras, J. 2007, A&A, 476, 335
Watanabe, S., Sako, M., Ishida, M., et al. 2006, ApJ, 651, 421
Weber, E. J. & Davis, Jr., L. 1967, ApJ, 148, 217
Weidner, C. & Vink, J. S. 2010, A&A, 524, A98
Werner, K., Deetjen, J. L., Dreizler, S., et al. 2003, in Astronomical Society of the Pacific Conference Series, Vol. 288, Stellar Atmosphere Modeling, ed. I. Hubeny, D. Mihalas, & K. Werner, 31
White, N. E. & Pravdo, S. H. 1979, ApJ, 233, L121
Williams, P. M., Dougherty, S. M., Davis, R. J., et al. 1997, MNRAS, 289, 10
Williams, P. M., van der Hucht, K. A., Pollock, A. M. T., et al. 1990, MNRAS, 243, 662
Wolinski, K. G. & Dolan, J. F. 1994, MNRAS, 267, 5
Woosley, S. E., Langer, N., & Weaver, T. A. 1993, ApJ, 411, 823
Zacharias, N., Finch, C. T., Girard, T. M., et al. 2012a, VizieR Online Data Catalog, 1322, 0
Zacharias, N., Finch, C. T., Girard, T. M., et al. 2012b, VizieR Online Data Catalog, 1322
Zacharias, N., Monet, D. G., Levine, S. E., et al. 2005, VizieR Online Data Catalog, 1297, 0
Zahn, J.-P. 1975, A&A, 41, 329
Zahn, J.-P. 1977, A&A, 57, 383
Zhekov, S. A. 2012, MNRAS, 422, 1332
Zhekov, S. A. & Skinner, S. L. 2015, MNRAS, 452, 872
Zsargó, J., Hillier, D. J., Bouret, J.-C., et al. 2008, ApJ, 685, L149
Zuiderwijk, E. J. 1995, A&A, 299, 79

Acknowledgements – Danksagung

The fact that I am on the verge of finishing a PhD is a direct result of the devoted and inspiring supervision of **Wolf-Rainer Hamann**, to whom I will forever be in debt. Whatever future holds in store for me, choosing you as a supervisor is a decision I will never reget.

Helge, you've been an incredible help and a reliable companion throughout these years. The number of times you rescued me from dreadful crushes is uncountable, but your scientific and strategic input was no less invaluable. Danke, für alles, was Du in diesen Jahren warst.

There's not a chance I would even get to this stage without **Ms. Andrea Brockhaus'** constant concern for making sure I'm not held back by bureaucracy – dafür, dass Du uns Mitarbeiter wie Familie behandelst, bin ich unendlich dankbar!

To my colleagues, **Lida Oskinova, Andreas Sander**, and **Rainer Hainich:** I've bugged you on a daily basis for the most trivial questions and always returned to my office with a solution. I've learnd a lot from you all, not to mention from the tea breaks and GoT marathons... ;)

I would like to thank **A. F. J. Moffat** for an incredible stay in Montreal, Canada, where Chapter 6 of this thesis was written, and where many other collaborative projects initiated. You've been as inspiring and knowledgable as you were (exhaustingly) witty and funny - I've had an amazing time learning from you and your colleagues.

I can't say you contributed much to the pace of my writing, **Marc W. Auell**, but you've contributed much to my emotional state in those final stages. :)...**פחות**

Emi & Claris: Am făcut-o! Mulţumesc din suflet pentru faptul că întotdeauna aţi vrut ce este mai bine pentru nepoţii voştri!

Mom 'n Dad: Now you can finally show off about your "brilliant" son! Of course, only possible with brilliant parents... ;) **תודה רבה על הכל**!

I wouldn't have made it without the support of my friends and family. You know who you are.

Appendix A.

A.1. Other sources

In this appendix we show the diagrams that are further discussed in Sect. 4.5, calculated from the available data in the literature, which is collected in Table A.1.

Parameters	J11215-5952 (SFXT)	GX 301-2 (SGXB)	X1908+075 (SGXB)	OAO 1657-415 (SGXB)
$P_{\rm orb}$ (d)	164.6^{a}	41.508^{d}	4.4007^{g}	10.44812^{i}
$P_{\rm spin}$ (s)	186.78^{b}	685^{e}	604.684^{g}	38.2^{j}
$M_\star/M_\odot$	30^{c}	43^{e}	15^{h}	14.3^{k}
$R_\star/R_\odot$	40^{c}	70^{e}	16^{h}	24.8^{k}
a (10^{12}cm)	27.2^{l}	11.0^{l}	2.4^{l}	4.2^{l}
a ($R_\star$)	9.8	2.3	2.1	2.5^{l}
B (10^{12}G)	1.45^{n}	3.8^{f}	1.45^{n}	1.45^{n}
$v_{\rm wind}$ (km/s)	1128^{c}	110^{e}	235^{h}	156^{k}
β	0.8^{n}	1.75^{e}	1.2^{h}	0.9^{k}

Notes. Parameters used in Appendix A.1.
References: (a) Romano et al. (2009) (b) Swank et al. (2007) (c) Lorenzo et al. (2014) (d) Sato et al. (1986) (e) Kaper et al. (2006) (For $P_{\rm spin}$, we used an intermediate value in the observed range 675s < $P_{\rm spin}$ < 700s in the 1974-2001 period). (f) Kreykenbohm et al. (2004) (g) Levine et al. (2004) (h) Martínez-Núñez et al. (2015) (i) Barnstedt et al. (2008) (j) White & Pravdo (1979) (k) Mason et al. (2012) (l) From $P_{\rm orb}$, total mass of the system and the 3rd Kepler's law. (n) Not based in any estimation. Assumed as the same value as in IGR J17544-2619.

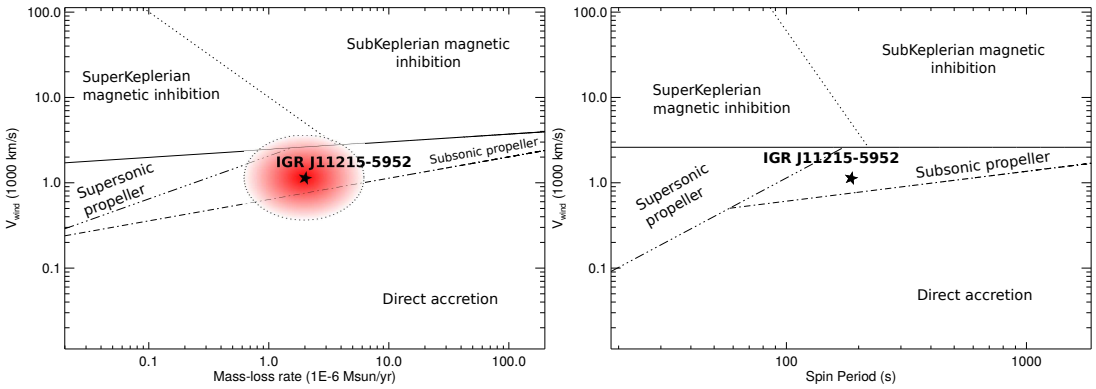

Figure A.1.: Left panel: position of IGR J11215-5952 (SFXT) in the $v_{\rm wind}$-$\dot{M}$ diagram. Right panel: position of IGR J11215-5952 in the $v_{\rm wind}$-$P_{\rm spin}$ diagram. Equations 25, 26, 27 and 28 by Bozzo et al. (2008) are represented by a solid, dotted, triple-dot-dashed and dot-dashed lines respectively.

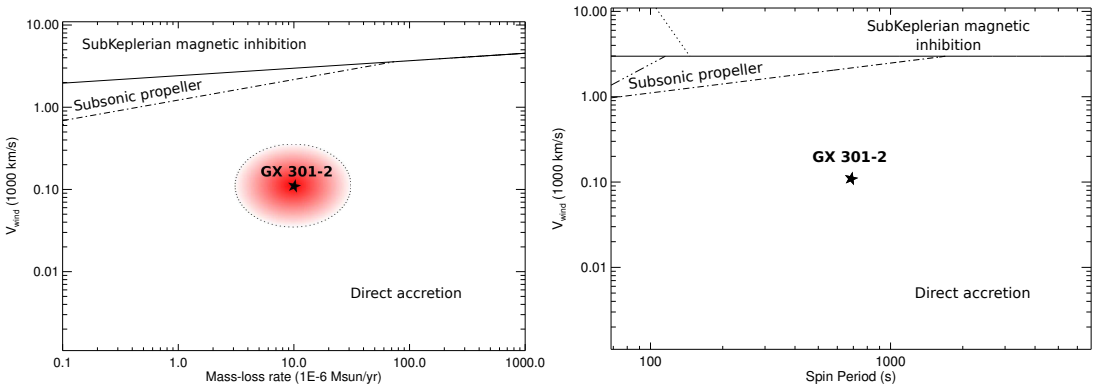

Figure A.2.: Left panel: position of GX 301-2 (SGXB) in the $v_{\rm wind}$-$\dot{M}$ diagram. Right panel: position of GX 301-2 in the $v_{\rm wind}$-$P_{\rm spin}$ diagram. Equations 25, 26, 27 and 28 by Bozzo et al. (2008) are represented by a solid, dotted, triple-dot-dashed and dot-dashed lines respectively.

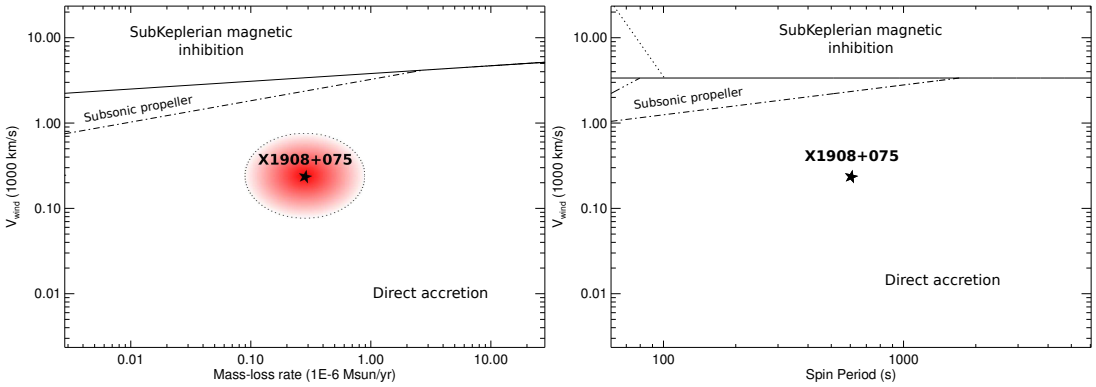

Figure A.3.: Left panel: position of X1908+075 (SGXB) in the $v_{\rm wind}$-$\dot{M}$ diagram. Right panel: position of X1908+075 in the $v_{\rm wind}$-$P_{\rm spin}$ diagram. Equations 25, 26, 27 and 28 by Bozzo et al. (2008) are represented by a solid, dotted, triple-dot-dashed and dot-dashed lines respectively.

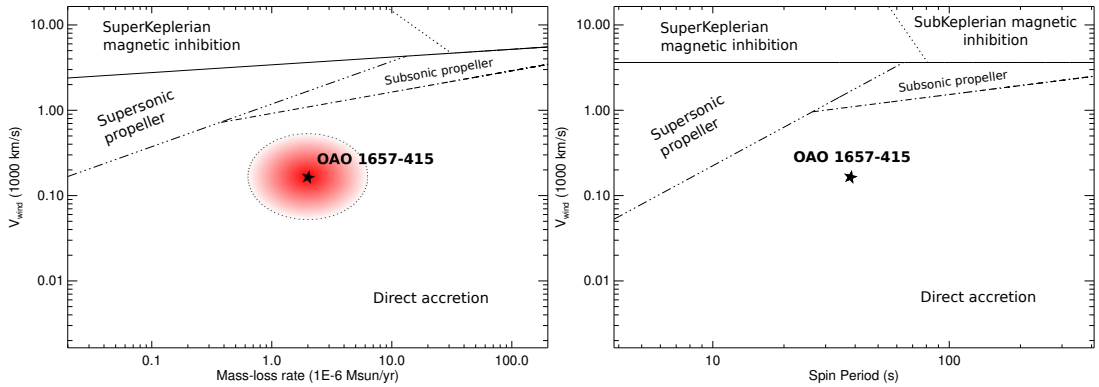

Figure A.4.: Left panel: position of OAO 1657-415 (SGXB) in the $v_{\rm wind}$-$\dot{M}$ diagram. Right panel: position of OAO 1657-415 in the $v_{\rm wind}$-$P_{\rm spin}$ diagram. Equations 25, 26, 27 and 28 by Bozzo et al. (2008) are represented by a solid, dotted, triple-dot-dashed and dot-dashed lines respectively.

A.2. Spectra

A.2.1. IGR J17544-2619

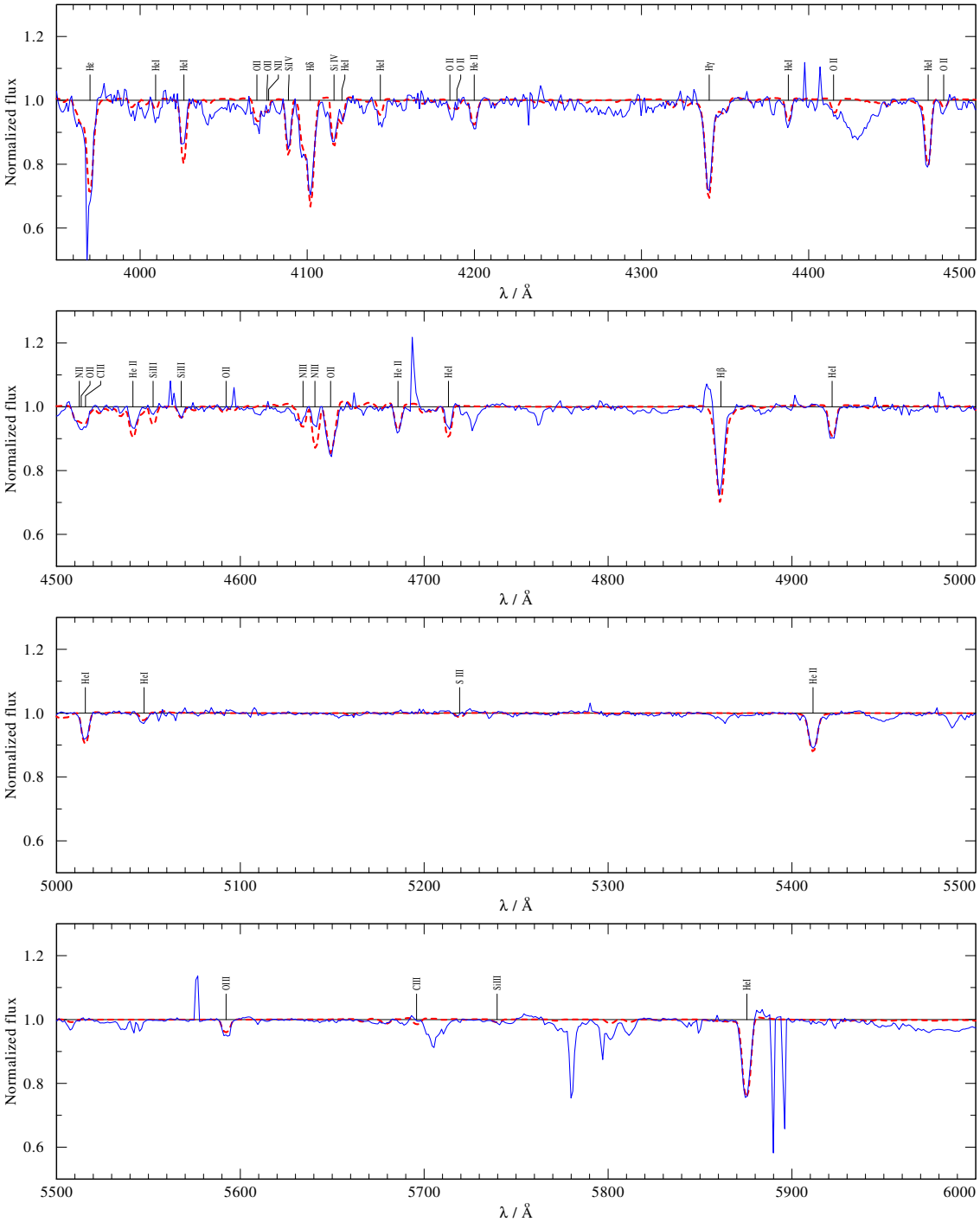

Figure A.5.: continued.

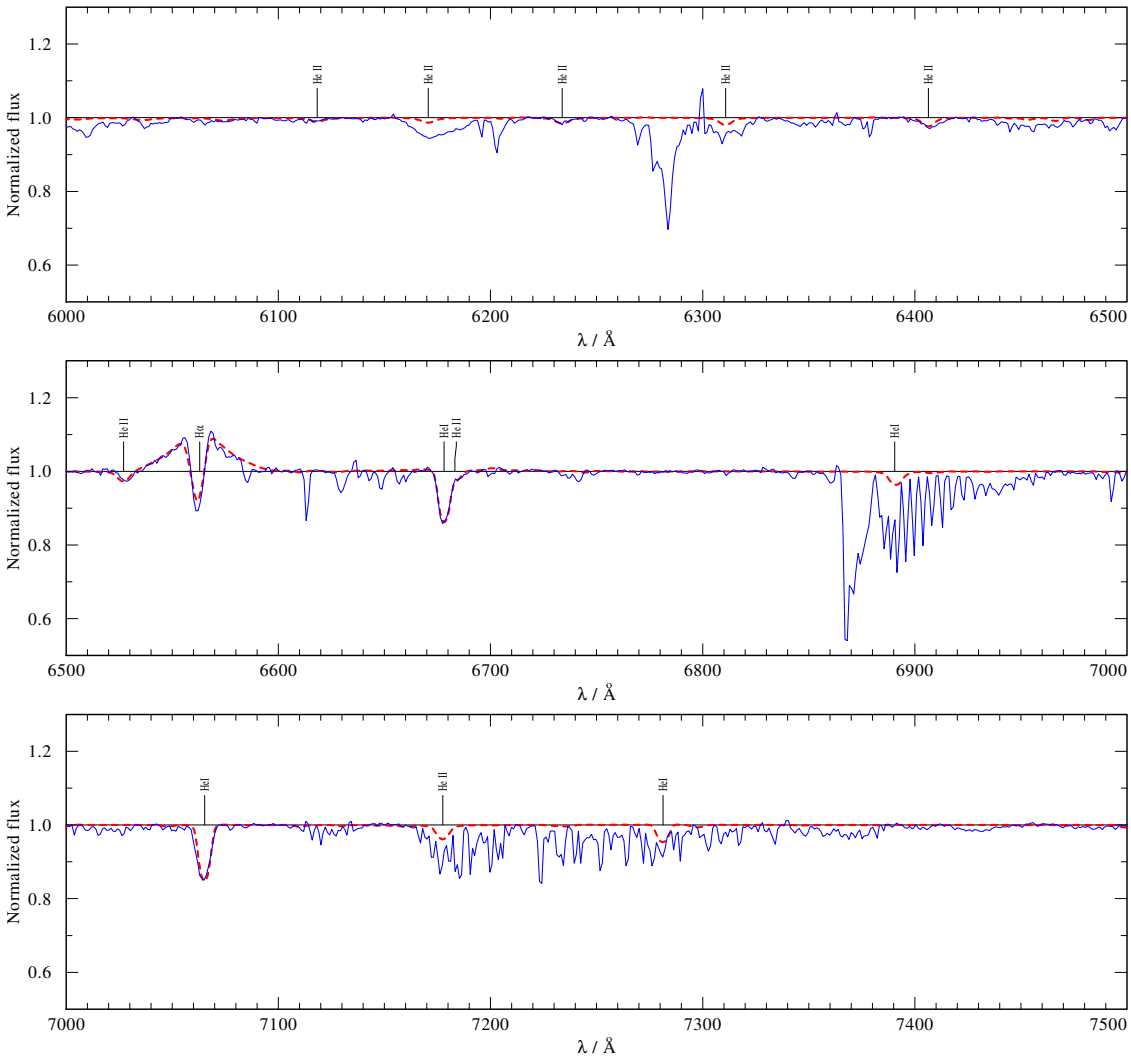

Figure A.6.: Optical spectrum of IGR J17544-2619 (blue), and the best fit model (red).

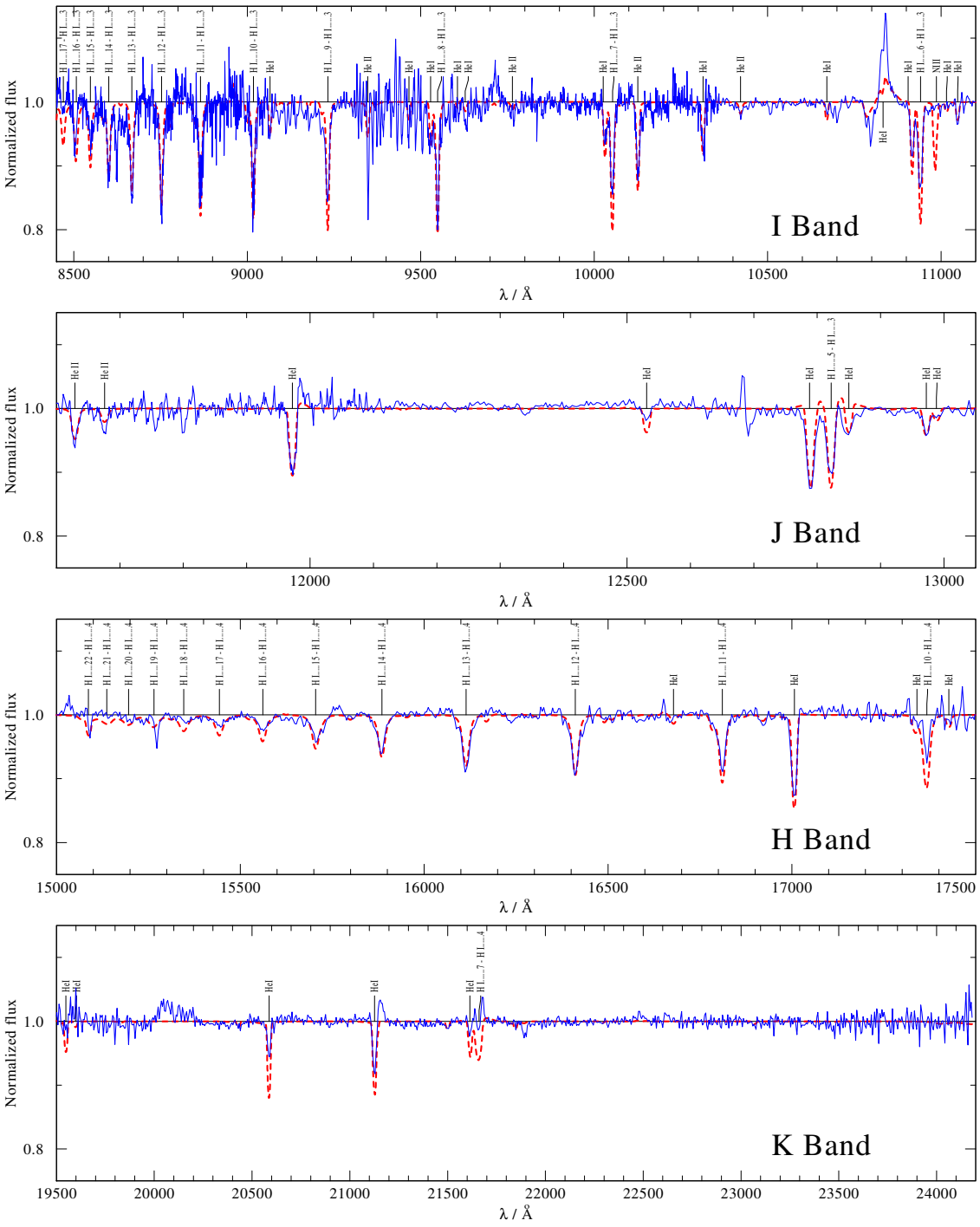

Figure A.7.: Infrared spectrum of IGR J17544-2619 (blue), and the best fit model (red).

A.2.2. Vela X-1

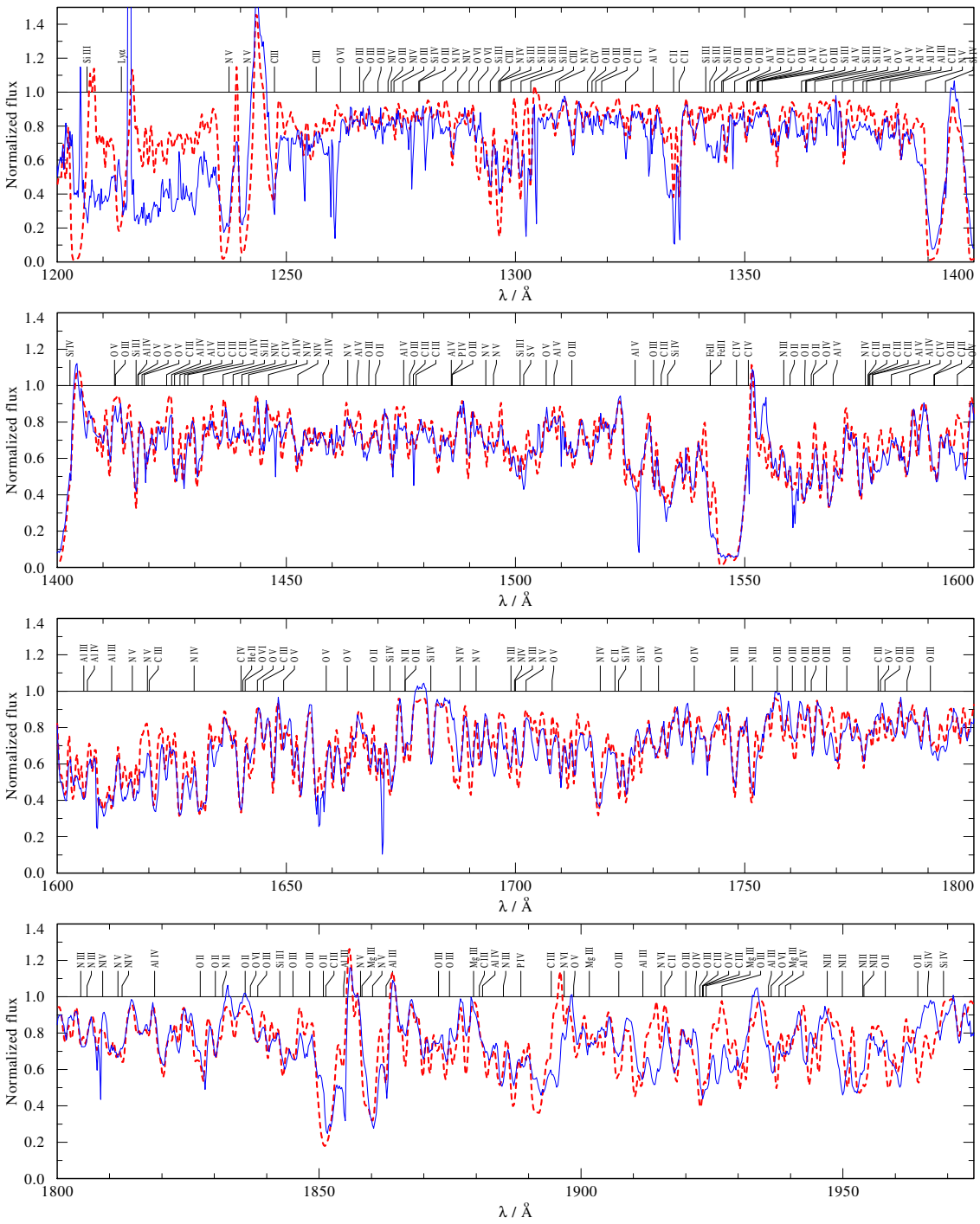

Figure A.8.: Ultraviolet spectrum of Vela X-1 (blue), and the best fit model (red).

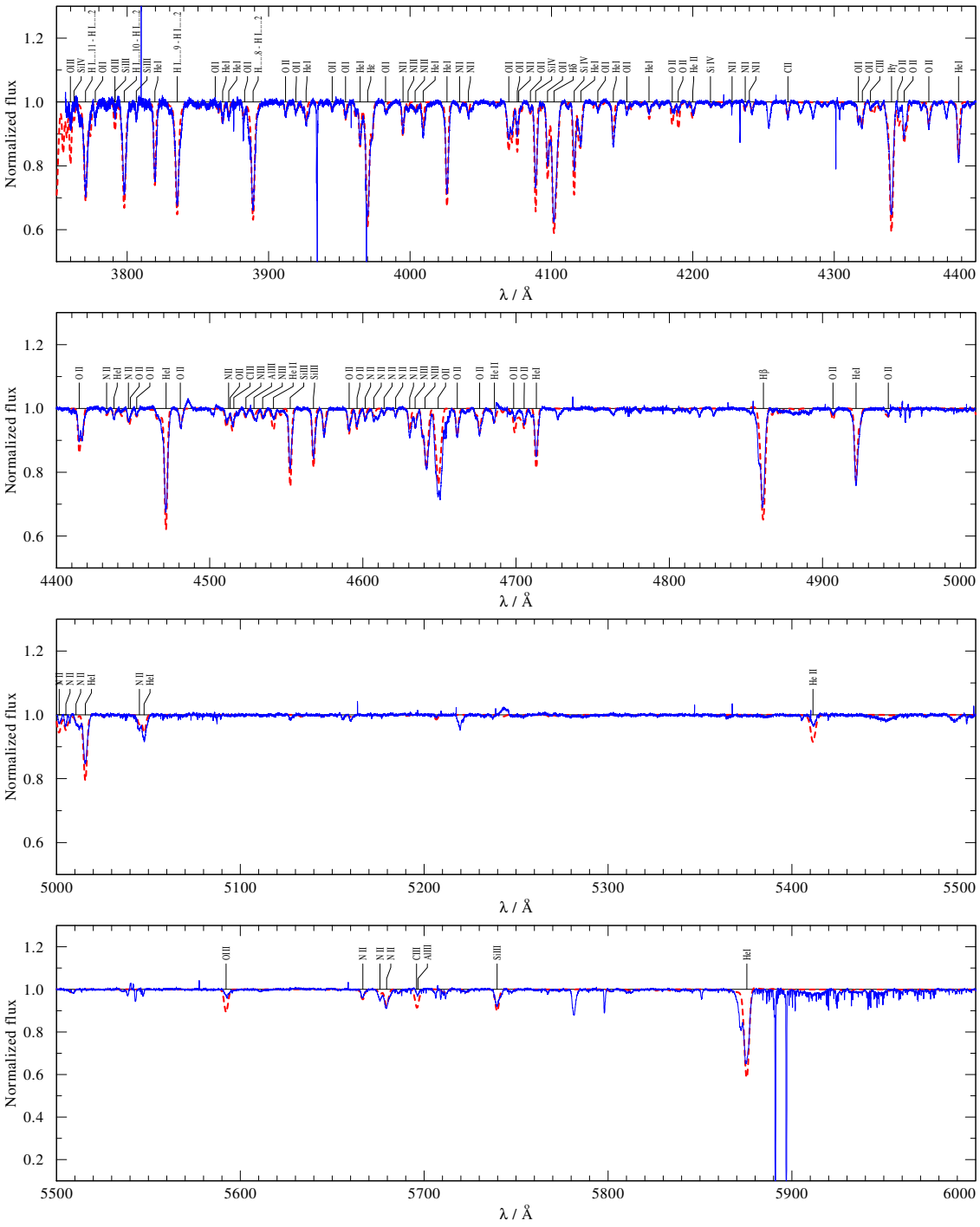

Figure A.9.: continued.

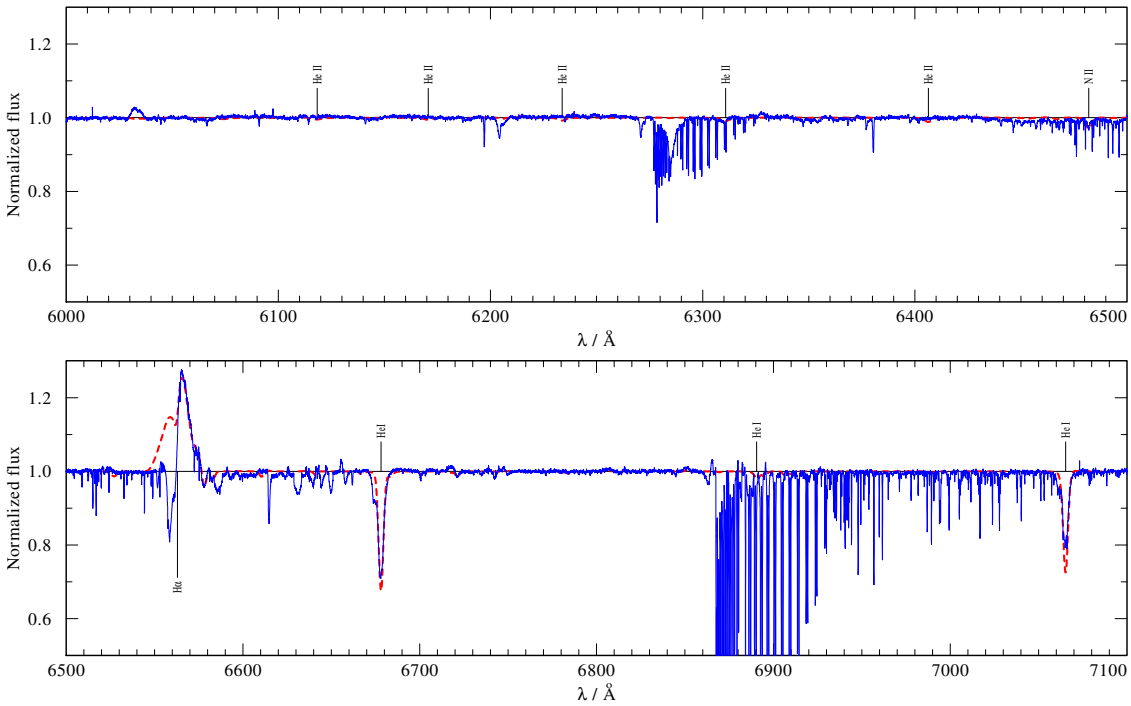

Figure A.10.: Optical spectrum of Vela X-1 (blue), and the best fit model (red).

Appendix B.

B.1. RV measurements for the primary and secondary

Table B.1.: RVs for primary (N IV) and secondary (Si IV) components

Spectrum	MJD	ϕ	N IV RV [km s^{-1}]	Si IV RV [km s^{-1}]
1	54794.18	0.27	230	302
2	54794.20	0.27	256	286
3	54794.24	0.27	220	298
4	54794.32	0.27	234	300
5	54798.29	0.29	234	288
6	54798.31	0.29	234	298
7	54804.07	0.33	266	288
8	54836.13	0.53	280	284
9	54836.16	0.53	280	278
10	54836.18	0.53	280	274
11	54836.20	0.53	280	274
12	54867.05	0.72	292	264
13	54867.07	0.72	296	260
14	55108.27	0.24	234	296
15	55108.29	0.24	234	298
16	56210.35	0.18	226	308
17	56210.37	0.18	220	306
18	56210.38	0.18	218	302
19	56217.33	0.23	234	300
20	56217.34	0.23	234	300
21	56217.35	0.23	234	294
22	56243.34	0.39	256	288
23	56243.35	0.39	252	300
24	56243.36	0.39	256	292
25	56256.26	0.47	270	278
26	56256.27	0.47	280	272
27	56256.28	0.47	276	268
28	56257.13	0.48	270	268
29	56257.14	0.48	270	278
30	56257.15	0.48	272	280
31	56277.31	0.61	282	268
32	56277.32	0.61	284	266
33	56277.33	0.61	276	262
34	56283.05	0.64	296	258
35	56283.06	0.64	268	298
36	56283.07	0.64	290	258
37	56294.20	0.71	302	258
38	56294.21	0.71	302	264
39	56294.23	0.71	294	252
40	56295.18	0.72	296	254
41	56295.19	0.72	294	258
42	56295.21	0.72	294	260
43	56304.24	0.77	294	250
44	56305.23	0.78	294	252
45	56305.24	0.78	294	244
46	56305.26	0.78	294	260

Spectrum	MJD	ϕ	N IV RV [km s^{-1}]	Si IV RV [km s^{-1}]
45	56305.24	0.78	294	244
46	56305.26	0.78	294	260
47	56306.22	0.79	294	238
48	56306.23	0.79	268	276
49	56306.24	0.79	294	246
50	56308.15	0.80	296	242
51	56308.17	0.80	296	242
52	56308.18	0.80	280	244
53	56316.21	0.85	296	234
54	56316.22	0.85	296	226
55	56316.23	0.85	310	236
56	56347.01	0.04	222	326
57	56347.03	0.04	232	326
58	56347.04	0.04	222	322
59	56349.02	0.06	206	328
60	56349.03	0.06	208	328
61	56349.05	0.06	204	328
62	56352.02	0.08	224	342
63	56352.04	0.08	268	284
64	56352.05	0.08	214	334
65	56356.00	0.10	268	284
66	56356.02	0.10	192	332
67	56356.03	0.10	202	322
68	56571.34	0.46	264	284
69	56571.35	0.46	272	288
70	56571.37	0.46	406	142
71	56571.38	0.46	270	286
72	56582.34	0.53	280	270
73	56582.35	0.53	280	274
74	56582.37	0.53	280	278
75	56586.25	0.55	280	280
76	56586.26	0.55	272	270
77	56586.27	0.55	280	278
78	56597.23	0.62	236	298
79	56597.24	0.62	276	262
80	56597.25	0.62	280	262
81	56620.26	0.76	294	250
82	56620.27	0.76	294	248
83	56620.28	0.76	294	262
84	56627.16	0.81	294	234
85	56627.18	0.81	294	246
86	56627.19	0.81	338	196
87	56645.04	0.92	256	298
88	56645.05	0.92	340	194
89	56645.07	0.92	338	196
90	56653.28	0.97	414	152
91	56653.29	0.97	408	146
92	56653.30	0.97	406	142
93	56693.11	0.22	234	304
94	56693.12	0.22	238	306
95	56693.13	0.22	240	304
96	56697.16	0.25	236	296
97	56697.17	0.25	236	288
98	56697.19	0.25	236	298
99	56703.13	0.29	252	300
100	56703.14	0.29	252	302
101	56703.16	0.29	246	292
102	56714.02	0.36	252	288
103	56714.03	0.36	252	288
104	56714.05	0.36	252	290
105	56719.02	0.39	256	286
106	56719.03	0.39	256	298
107	56719.04	0.39	268	298
108	56723.17	0.41	268	284
109	56723.18	0.41	268	276
110	56723.20	0.41	268	284

Appendix C.

C.1. Comments on individual targets

In the few paragraphs below, we give a short overview on each system, and discuss specific issues related to their analysis. We also include an overview of the X-ray properties of each system.

AB 3: This system is classified as WN3h + O9 and is found to have a period of $P = 10.0$ d (Moffat 1988, , FMG). An X-ray source (CXOU J004959.4-732211) was detected in the close vicinity of AB 3 by both *Chandra* and *XMM-Newton* at a separation of 2.9″. Within position uncertainties, the source could coincide with AB 3. If so, the X-ray luminosity of AB 3 is $L_X \approx 2 \times 10^{33}$ erg s^{-1}.

The spectrum is clearly dominated by the WR component; He I lines belonging to the secondary are only barely visible. The light ratio could be roughly constrained using the temperature-insensitive Balmer lines, and the implied luminosity obtained for the O companion suggests it is an O9 dwarf. The temperature of the WR star could be fairly well constrained due to the clear signatures of the C IV resonance doublet in the UV and the strong N V features in the optical, as well as the weak N IV features. R_t, v_∞ and D follow by fitting the strengths and shapes of the emission lines. We find a significant hydrogen content in the primary's atmosphere.

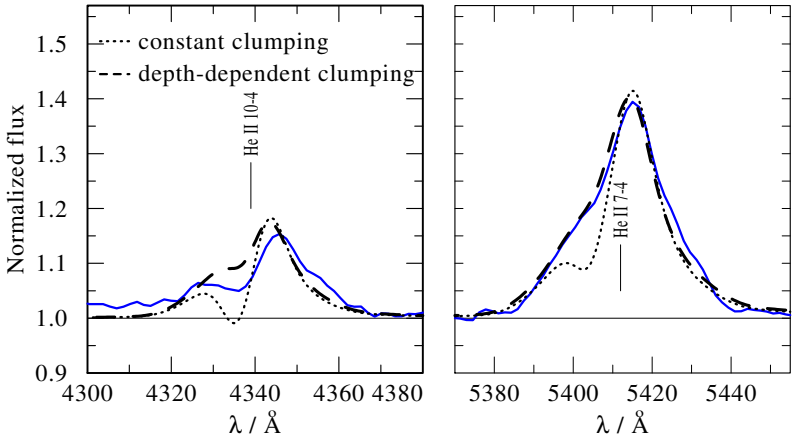

Figure C.1.: Two models corresponding to the WR model of AB 3 (cf. Table 6.2) with a constant clumping factor $D(r) = D = 10$ (black dotted line) and a depth-dependent clumping factor, where $D(R_*) = 1$ and $D(r) = 10$ at $v(r) \sim 0.5\, v_\infty$ (black dashed line) compared to observations (blue solid line). We note that the O model contributes very little to these lines and is therefore omitted from this figure for clarity.

The emission visible at $\lambda \sim 4640$ probably corresponds to the N III doublet $\lambda\lambda\, 4634, 4640$. No WR models are capable of reproducing this emission simultaneously with the N IV and N V features. It could only be reproduced by assuming higher temperatures and lower gravities for the O companion, and an extremely high N abundance, of the order of 30 times the SMC value. The potential nitrogen enrichment is given as an alternative X_N value in Table 6.2. Alternatively, this feature could arise from WWC (e.g. Rauw et al. 1999). The companion's terminal velocity is roughly estimated based on the shape of the badly resolved C IV resonance doublet, while the mass-loss rate is adopted from Vink et al. (2000).

AB 5: This strongly variable quadruple system, also known as HD 5980, contains four companions: an eclipsing binary system composing two WR stars (A:WNN6h + B:WN6-7) with a period of $P = 19.3$ d, and another, probably distant binary system (C: O7 I + ?), responsible for distinct and relatively static absorption features in the spectrum (Breysacher et al. 1982; Niemela 1988; Koenigsberger et al. 2010, 2014). Here, we treat star C as a single star, since the fourth component is not noticeable in the spectrum, and therefore should not influence our results. The primary star went through a powerful LBV-type eruption in the year 1994. Since the eruption, the primary gradually increased in temperature from ~ 25 to ~ 50 kK, while its mass-loss rate has been gradually decreasing from $\sim 10^{-3.7}$ to $\sim 10^{-4.4}\,M_\odot\,\mathrm{yr}^{-1}$, and the terminal velocity increasing from ~ 500 to $\sim 2400\,\mathrm{km\,s}^{-1}$ (Georgiev et al. 2011). The system is the most X-ray luminous WR star in the SMC, with an X-ray luminosity $L_X \approx 10^{34}\,\mathrm{erg\,s}^{-1}$. Orbital variations in its X-ray flux were reported and could be explained by WWCs between the components A and B (Nazé et al. 2007). AB 5 is a prominent candidate for producing a massive black hole binary system such as recently detected by LIGO via gravitational waves (Abbott et al. 2016; Marchant et al. 2016).

Georgiev et al. (2011) presented a thorough analysis of the stars A and C at different epochs since the 1994 eruption, taking advantage of the fact that, at least for optically thick lines, the eclipse at phase $\phi = 0$ (star A in front of star B) can be assumed to be full (Perrier et al. 2009). In our analysis, we use only the most recent spectra available. While the spectra taken during primary eclipse were taken at different epochs between the years 2002 and 2009 (see caption of Fig. C.4), the system was stable during this period (Georgiev et al. 2011), so fitting them simultaneously is justified. Using the same approach as Georgiev et al. (2011) to isolate the stars A and C during the eclipse of B ($\phi = 0$), we find similar parameters for both stars, although our solution implies a lower temperature for the primary (T_* =45 kK vs. 60 kK). Stars of subtype WN6h can have temperatures ranging between these values (e.g. Hamann et al. 2006).

We note that we neglect the effects of WWC here. Moffat (1998) claim that the phase-dependent width of the strongest optical emission lines is dominated by WWC during the eruptive era. Since the eruption, the primary's mass-loss has significantly decreased, so WWC are now not expected to be as dominant, but could still contribute to the spectrum. Indeed, we find the strong He II λ4686 line is broader at maximal width (quadrature) than can be reproduced by a superposition of two WR stars with the given velocity amplitudes. This does not hold for the weaker He II and nitrogen lines, partly because they form closer to the stellar surface, as Koenigsberger et al. (2014) noted. While He II λ4686 could be contaminated by WWC, our results do not depend on this line. However, WWC could potentially influence the strong He I λ5876 line, which was used to constrain T_* and $\dot{M}$. The discrepancy in T_* could therefore be partly due to WWC.

We can only perform a rough analysis of the out-of-eclipse spectra, since the most recent publicly available observations covering the range 1200 – 2000 Å were taken in 1999, closer to the eruption. We thus rely on previous analyses as much as possible. Perrier et al. (2009) performed a quantitative analysis of the system's light curve taken in 1979, before the 1994 eruption, and derived helpful constraints. They found that the relative contributions of stars A, B, and C in 1979 are approx. 0.4, 0.3, and 0.3 in the visual, respectively. Foellmi et al. (2008) present a comparison between this light curve and newer light curves taken in the years 2005 and 2006. While Foellmi et al. (2008) noted some interesting differences between the pre- and post-eruption light curves, the global behavior and strengths of flux minima during eclipse are virtually unchanged. This implies that the results published by Perrier et al. (2009) hold now as well. Furthermore, the fact that both primary and secondary minima are of very similar strengths implies that stars A and B have very similar temperatures. The clear appearance of N IV and N V lines which can be attributed to both components in the out-of-eclipse spectra confirms this. With the parameters of stars A and C fixed and the temperature of star B fixed to that of star A, the visual light ratios derived by Perrier et al. (2009) imply the luminosity of star B, and thus its radius. Finally, with these parameters fixed, we analyze the available out-of-eclipse spectra to derive the secondary's wind parameters. Applying a 3D integration technique (Shenar et al. 2015), an upper limit on the components' $v \sin i$ can be constrained using the N IV λ4058 line, which forms very close to the stellar surface and is thus sensitive to surface rotation.

AB 6: With a period of $P = 6.5$ d, this SB2 WR + O binary system, classified WN4 + O6.5 I by FMG, is the shortest period WR binary known in the SMC (Moffat 1982; Hutchings et al. 1984). Despite its short period, the system shows no significant photometric variability. AB 6 was detected in the *XMM-Newton* survey (Laycock et al. 2010; Sturm et al. 2013) with an X-ray luminosity of $L_X \approx 7 \times 10^{33}\,\mathrm{erg\,s}^{-1}$ (in the 0.2-4.5 keV band). The source was found to be variable, with the L_X reaching a peak of $\approx 10^{34}\,\mathrm{erg\,s}^{-1}$.

The luminosity of the WR component turns out to be very high, a fact which is not easy to explain given its orbital mass (see Sect. 6.6.1). Since this is a direct result of the derived light ratio, we briefly discuss its determination. The light ratio was derived on the basis of mainly three features: The P v λ 1128 and S iv λ1073 resonance lines, as well as the C iii λ1176 multiplet, all of which are observed in the FUSE domain (see Fig. 6.4).

Moreover, while we do not identify a "step" in the C iv resonance line (as in AB 5, see Fig. 6.5), it is clearly unsaturated at all phases, suggesting that it originates in only one of the binary components. We argue that this line originates in the O star. In Fig. C.2, we show two HST spectra at $\phi = 0.21$ (red line) and $\phi = 0.77$ (blue line), as well as one IUE spectrum at $\phi = 0.45$ (green line) in velocity space relative to the blue component of the C iv resonance doublet (λ1548). The spectra are shifted by $-200\,\mathrm{km\,s^{-1}}$ to account for the systemic velocity of the system (FMG). While the line shows significant variability whose origin should be subjected to further study, no obvious radial velocity variation with phase can be seen in the line. If the line originates in the WR component, there should be a difference of roughly $500\,\mathrm{km\,s^{-1}}$ between the velocities of the lines at phases $\phi = 0.21$ and $\phi = 0.73$, but no shift is observed. While emission lines need not strictly follow the orbital motion, some shift would be expected at such an RV amplitude. We conclude that this line originates in the O star, whose RV amplitude is ~ 4 times smaller, and that the WR star does not show this line at all, as is typical for early WN stars. This line helps us determine the light ratio as well, and puts constrains on the wind parameters of the O star. Lastly, the light ratio is consistent with He i and Balmer absorption lines in the optical spectrum.

As in AB 3, we find a clear signature of N iii λ4640, which is very unlikely to originate in the WR component given its spectral class and derived temperature; indeed, we could not produce N v at its observed strength simultaneously to any N iii features. To reproduce it, an N-enrichment of roughly ten times the typical SMC value is assumed in the model of the O component, noted as an alternative value in Table 6.2. This feature could also originate in WWC, however.

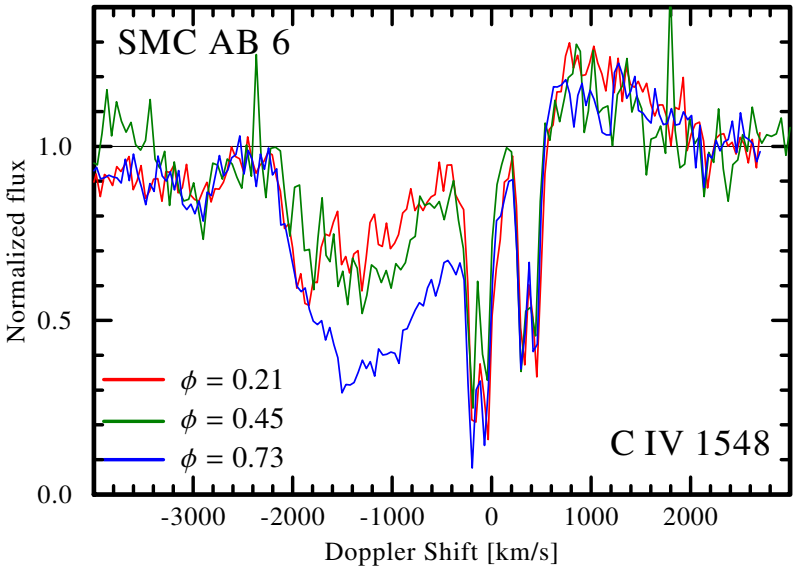

Figure C.2.: Two HST spectra taken in 1992 (red line: Z0Z30402T, $\phi = 0.21$, blue line: Z0Z30602T, $\phi = 0.73$) and an IUE spectrum taken in 1991 (green line, sp41784, $\phi = 0.45$) are plotted, showing the C iv resonance doublet of AB 6 in velocity space relative to the blue component at λ1548.

AB 7: Classified as WN4 + O6 I(f), this SB2 binary has a detected period of $P = 19.6$ d (FMG). The system was also observed with *XMM-Newton* and is found to have a smaller X-ray luminosity than that of AB 6 ($L_X \approx 4 \times 10^{33}\,\mathrm{erg\,s^{-1}}$), which is also found to be variable (Guerrero & Chu 2008). Interestingly, although the mass-loss rates of WR stars in the SMC are on average lower than in those of their Galactic

counterparts, the colliding wind SMC binaries (AB 5, 6, and 7) do not appear to be weaker X-ray sources than the Galactic ones. This suggests that the components' mass-loss rates and the resulting X-ray luminosities may be related in a non-trivial way, or may even be uncorrelated (e.g. Ignace et al. 2000).

The temperature of the WR component is hard to constrain; The N v resonance line at λ1240 is visible, but could in principle arise in both companions. There is a clear signature of N III, but Niemela et al. (2002) associate it with the O companion based on RV shifts, and there are no N IV lines observed. Very weak N v lines in the optical can be seen, and suggest that the WR companion is indeed hot and suffers from strong line dilution, similar to AB 6. To avoid strong N v lines in the optical (which are not observed), one could either reduce the N abundance to abnormally low values (roughly a factor 0.3 times the abundance given in Table 6.2), or increase the temperature to $\sim 10^5$ K, where the N v lines become very weak (because of dominance of the N VI ion). The latter solution provides a better fit to the available data.

Most peculiarly, the C IV resonance line only shows a narrow absorption, likely blended with interstellar absorption. For this reason, this line cannot help us to deduce the light ratio. As in the case of AB 6, we use the P v λ 1128 and S IV λ1073 resonance lines, as well as the C III λ1176 multiplet to constrain the light ratio, and derive the remaining parameters for both components based on the strengths of He I and He II lines in the optical. To reproduce the unusual C IV feature (or, more accurately, lack thereof), we assume a low mass-loss rate for the O-star companion, and include X-rays in its model such that the total X-ray luminosity observed in this system is reproduced. The X-rays strongly depopulate the C IV ground state via Auger ionization.

As in the case of AB 3 and 6, the N III emission excess at λ4640 can be reproduced if a nitrogen abundance of roughly a factor 10 times the typical SMC abundance is assumed in the secondary. In fact, Niemela et al. (2002) showed that the feature roughly follows the orbital velocity of the O companion. We thus find possible signatures for nitrogen enrichment in SMC AB 3, 6, and 7. If true, this can be a consequence of either contamination by the primaries' nitrogen-rich winds, or accretion during the primaries' RLOF. Alternatively, this feature could originate in colliding winds, which are likely present in all of these systems.

AB 8: This system contains the only non-WN star known among the SMC WR sample. It was reclassified several times, most recently as WO4 + O4 V by Bartzakos et al. (2001a). Moffat et al. (1985) inferred an orbital period of $P = 16.6$ d for the system. Interestingly, AB 8 is the only WR binary in our sample not detected in X-rays. The star was in the field of view of *Chandra* and *XMM-Newton* observations (Oskinova et al. 2013b), but only an upper limit of 5×10^{32} erg s^{-1} could be established for its X-ray luminosity. Given the very strong wind of the primary, it is difficult to explain such a low X-ray luminosity; Zhekov & Skinner (2015) recently reported that the X-ray luminosity of the Galactic WO binary WR 30a is $> 10^{34}$ erg s^{-1}. In fact, St-Louis et al. (2005) report clear signatures of colliding winds in AB 8. While there are possible resolutions to this problem (e.g. large opacity of the surrounding material), it remains difficult to explain why AB 8 does not exhibit a high X-ray luminosity.

The light ratio of the components could be fairly well deduced by taking advantage of the fact that the N v resonance line clearly belongs to the O companion (see Fig. 6.5). The light ratio is consistent with the C IV resonance line and with the other clear features belonging to the secondary, e.g. Balmer and He lines in the optical. The terminal velocity of the companion is found to be comparable to that of the primary. The ratio of carbon to helium in the WO component is constrained using the diagnostic line pair He II λ5412; C IV λ5471, whose ratio is primarily sensitive to X_C/X_{He} (Koesterke & Hamann 1995). The abundances derived are generally supported by the remaining carbon and oxygen features.

There is a very strong $\dot{M}$-T_* degeneracy for the WR companion which arises from the fact that, for optically thick winds, one could arbitrarily vary the temperature and the mass-loss rate simultaneously to obtain a "photosphere" ($\tau \sim 2/3$) which has approximately the same effective temperature and emitting surface (see Fig. 4 in Todt et al. 2015). The temperature is clearly higher than ~ 120 kK, because lower values cannot reproduce the optical O VI $\lambda\lambda$ 3812, 3835 emission. For $T_* \gtrsim 120$ kK, the degeneracy just mentioned makes it possible to reproduce the O IV λ3400 line regardless of the value of T_*, as long as $\dot{M}$ is large enough. Temperatures in the vicinity of 200 kK produce emission of the O VI $\lambda\lambda$ 1032, 1038 resonance doublet that is too strong. $T_* \approx 150$ kK is chosen as a compromise. Note that despite the very large uncertainty in T_*, we can constrain $T_{2/3}$ fairly well, since all well-fitting models reach a similar temperature at their "photospheres".

From the profiles of the O IV, O v and O VI lines in the optical, it is clear that the O IV line is formed far

out (flat topped profile), while the O v and O vi features form closer in. At any temperature within the range mentioned above, reproducing the O iv emission requires large $\dot{M}$ values which produce too strong emission for most features in the spectrum (especially the strong C iv lines in the UV and optical and the He ii λ4686 line), while strongly weakening the O vi emission in the optical below the observed value. Tramper et al. (2013), who were also unable to simultaneously fit both O iv and O vi lines at their observed strengths, suggested this discrepancy may be related to soft X-ray K-shell ionization. However, we are unable to verify this claim. Zsargó et al. (2008) show that O vi could be sensitive to a hot, inter-clump medium, not accounted for in our models currently. Overall, the multitude of lines belonging to carbon and oxygen make the problem of modeling WO stars more difficult, and the fit quality is indeed inferior to that of other systems (cf. Appendix C.3). Our fit represents a compromise to the most important features which could be recognized in the spectrum of AB 8.

St-Louis et al. (2005) studied variability in the system and obtained helpful constraints on the stellar parameters of both companions. The mass-loss rates derived for both components are in agreement (within errors), as are the radii of both stars. One very strong discrepancy lies in the bolometric luminosity ratio of both companions: St-Louis et al. (2005) infer $L_\mathrm{O}/L_\mathrm{WR} = 3.5$ by modeling the variability of the O vi resonance line, while we find $L_\mathrm{O}/L_\mathrm{WR} \approx 0.5$ from our spectral modeling. Assuming the luminosity and radii ratio inferred by St-Louis et al. (2005), however, the Stefan-Boltzmann relation implies $T_\mathrm{WR} \sim 1.35 T_\mathrm{O}$. For a typical temperature of an O4 V star (45 kK; Martins et al. 2005), one would find a temperature of only $T_\mathrm{WR} \approx 60$ kK for the WO component, which is less than half the derived temperature, and much lower than temperatures derived for other WO stars (e.g. Tramper et al. 2013). We therefore believe that our results are more consistent.

Another interesting spectral feature which we could not reproduce is the strong absorption seen in the FUSE spectra around $\lambda \approx 1160$ Å. This absorption feature is persistent in all observations and follows the orbital motion of the WO component. It likely belongs to either to C iv or C iii, but its strength is much larger than what can be reproduced by the models, especially given the deduced light ratio. It is possible that this feature is a manifestation of the components' interaction.

C.2. Following the binary evolution of each system

In this section, we discuss the evolutionary path of each system in more detail, as inferred from the corresponding binary evolution tracks. We note that the best-fitting tracks should be at best seen as an approximation to the system's evolution, as we work with a coarse grid of evolutionary models. Calculating individual tracks for the analyzed systems is beyond the scope of this paper.

AB 3: The solution to this system is found to reproduce all observable quantities, and is not sensitive to small changes in the weighting (i.e. changes in σ_n). The system starts off with $M_1 = 60\,M_\odot$ and $M_2 = 20\,M_\odot$, an initial period of ≈ 40 d, and a separation of $200\,R_\odot$. The primary is thus already born very massive and luminous ($\log L_1 \sim 5.7$) while being on the main sequence, whereas the secondary's parameters correspond to an O 7 dwarf. After about 3.8 Myr, the primary becomes a supergiant and reaches a radius of roughly $100\,R_\odot$, at which point it fills its Roche lobe and a case B (shell H-burning) mass-transfer phase initiates, during which the primary rapidly loses mass in a non-conservative fashion because of the secondary's inability to accrete matter (see Sect. 2.2.2 in Eldridge et al. 2008). During the RLOF phase, which lasts $\sim 4 \cdot 10^4$ yr, the mass of the primary sharply drops from 55 to $25\,M_\odot$, while the secondary maintains a roughly identical mass of $\sim 20\,M_\odot$. During the mass-transfer phase, the period drastically decreases from its initial value to ~ 10 d, while the separation decreases to $\sim 55\,R_\odot$. It lasts roughly 10^5 yr until the system evolves to its current state, roughly 3.9 Myr after its birth.

AB 5: The best-fitting solution reproduces all parameters within a $2\,\sigma$ level, although the components' masses are overpredicted by $\approx 1.5\sigma$. According to the best-fitting track, the system starts off with very large masses of $M_1 = 150$ and $M_2 = 75\,M_\odot$, an initial period of ≈ 16 d and a separation of about $160\,R_\odot$. Strong stellar winds remove more mass from the system during its evolution. After roughly 2.3 Myr, the primary reaches a radius of $\approx 80\,R_\odot$ and, with the primary still core hydrogen burning, a partially conservative case A RLOF phase initiates for a short duration of $\approx 2.5 \cdot 10^4$ yr, during which roughly $25\,M_\odot$ are transferred from the primary onto the secondary. The period and separation do not change significantly during this

time. We observe the system "shortly" hereafter at an estimated age of 2.6 My, with the primary's mass now $\approx 85\,M_\odot$ and the secondary's $\approx 95\,M_\odot$.

By assigning more weight to the masses during the fitting procedure (e.g. by making σ_M artificially smaller), a different solution is found with $M_\mathrm{i} = 120\,M_\odot, q_\mathrm{i} = 0.3$, and $P_\mathrm{i} = 10\,\mathrm{d}$, which reproduces the masses better (difference $< 1\sigma$), but underpredicts the period by more than 2σ and the secondary's luminosity by 1.5σ. Generally, the solution space for this system is very non-linear and sensitive to small variations of σ_n, with the initial mass of the primary ranging between $100\,M_\odot$ and $150\,M_\odot$. Given that this system is currently in a highly variable, rapidly changing evolutionary state, it is perhaps not surprising that we find it difficult to constrain a unique solution in this case.

Koenigsberger et al. (2014) claimed that RLOF is unlikely to have occurred in this system due to the very similar masses and hydrogen content of both companions. These authors developed an evolutionary model that avoids a RLOF phase by assuming QCHE, and obtain results similar to those given in this study for the homogeneous case (Table 6.4). In this scenario, both components move along a diagonal towards the upper-left corner of the HRD after leaving the main sequence, remaining compact throughout their evolution. In this study, the QCHE scenario does not fit well to the system (cf. Tables 6.3 and 6.4). The reason is that Koenigsberger et al. (2014) adopt a temperature which is higher than derived here (45 kK vs. 60 kK). A higher temperature is more consistent with QCHE (see right panel of Fig. 6.7). As we discuss in Appendix C.1, WWC in the system lead to uncertainty in the true temperature of the primary and secondary.

We find several binary solutions which successfully produce similar post-RLOF masses at roughly the observed T_* and $\log L$ inferred for the primary and secondary. However, as discussed in Sect. 6.6.3, although the BPASS code does not deliver the scondary's hydrogen abundance, it would require some fine-tuning to obtain scenarios which include mass-transfer and which would predict a significant hydrogen depletion for both components in the system simultaneously. All things considered, QCHE without mass-transfer seems to offer a more natural explanation to the current state of the system.

However, it is noteworthy that the primary has in fact been observed at much lower temperatures of about 20 kK during the 1994 eruption (Georgiev et al. 2011), while the QCHE scenario suggested by Koenigsberger et al. (2014) implies that the primary's temperature continuously increased from its initial value of ≈ 50 kK. Koenigsberger et al. (2014) suggest that the 1994 erruption may involve an instability arising from an increase of the full Eddington Gamma Γ beyond unity. Indeed, such instabilities are not dealt with in the current generations of codes. And yet, since we know that the star *did* travel towards the right side of the HRD, it is dubious to assume that no mass-transfer occurred throughout the system's evolution. In fact, the solution offered by Koenigsberger et al. (2014) suggests that a similar instability should have occurred in star B even earlier for the same reason. Moreover, one would have to explain the apparent discrepancy between the necessary near-critical ($\sim 400 - 500\,\mathrm{km\,s^{-1}}$) rotation rates needed to induce QCHE and the velocities implied by orbital synchronization ($50 - 100\,\mathrm{km\,s^{-1}}$). To obtain a definite answer to this question, accurate modeling of this system, which would account for rotation, tidal forces, and mass-transfer from both components consistently, is necessary. This is beyond the scope of the current paper.

AB 6: As could be anticipated, no ordinary binary evolutionary track can reproduce the peculiar combination of large luminosity ($\log L \sim 6.3$) and hydrogen content ($X_\mathrm{H} \sim 0.4$) simultaneously with the small orbital mass ($9\,M_\odot$) of the primary component. For this system, we therefore ignored the primary's orbital mass in the fitting procedure.

The system was originally composed of two massive stars with $M_1 = 100$ and $M_2 = 50\,M_\odot$ at a short initial period of $P \approx 6\,\mathrm{d}$ and an initial separation of $\approx 80{,}R_\odot$. As the primary starts to fill its Roche lobe, roughly 2.5 Myr after its formation, a case A RLOF phase initiates, lasting for a long period of $\sim 4 \cdot 10^5$ yr. During this time, $\approx 20\,M_\odot$ are removed from the primary to the secondary, and the primary's hydrogen content drops from $X_\mathrm{H} = 0.7$ to $X_\mathrm{H} = 0.35$. Strong stellar winds are responsible for a further decrease of the hydrogen content and the stellar masses. The state closest to the observables of this system is reached at an age of ~ 3.0 Myr, although the hydrogen content of the primary is underestimated by the track. This is possibly due to overestimated stellar winds in the BPASS code. Alternatively, RLOF from the secondary onto the primary (not accounted for in the code) could also lead to a hydrogen enrichment.

AB 7: The solution to this system reproduces its observables well and is not sensitive to small changes in σ_n. The system originally comprised of two very massive stars, with the primary having twice the mass of

the secondary: $M_1 = 80$ and $M_2 = 40\,M_\odot$. The initial separation is large, $\approx 250\,R_\odot$, and the initial period is ≈ 40 d. After roughly 3.3 Myr, the primary went through a case B RLOF for $\approx 3 \cdot 10^4$ yr, removing about $30\,M_\odot$ from the primary, which is lost from the system because of the secondary's inability to accrete. During RLOF, the orbital period is halved, while the separation reduces to $\sim 150\,R_*$. After $\approx 10^5$ yr, at an age of 3.4 Myr, the system reaches its currently observed state, with $X_\mathrm{H} = 0.15$ remaining in the outer envelope of the primary, and the secondary becoming an evolved, luminous star.

AB 8: The best-fitting solution reproduces most observables to a satisfactory level. However, the initial mass of the primary is sensitive to small changes in the weighting, and ranges between 100 and $150\,M_\odot$. According to the best-fitting track, the system was originally composed of two hot and massive stars of masses $M_1 = 150$ and $M_2 = 45\,M_\odot$, with a very short initial period of 10 d. As the primary leaves the main sequence and reaches a radius of $\sim 50\,R_\odot$ after about 2.2 Myr, it goes through a case B RLOF phase lasting for $\approx 10^5$ yr, losing $\sim 25\,M_\odot$ in a conservative fashion and transferring it onto the secondary, until the masses become $M_1 \approx 100$ and $M_2 \approx 70\,M_\odot$. The period and separation are reduced by $\sim 30\%$ at the end of the RLOF phase. During the next 0.8 Myr, the primary suffers extreme mass-loss, until it reaches a mass of about $25\,M_\odot$, while the secondary's mass remained roughly constant. This is the current state of the system, at an estimated age of roughly 3 Myr.

C.3. Spectral fits

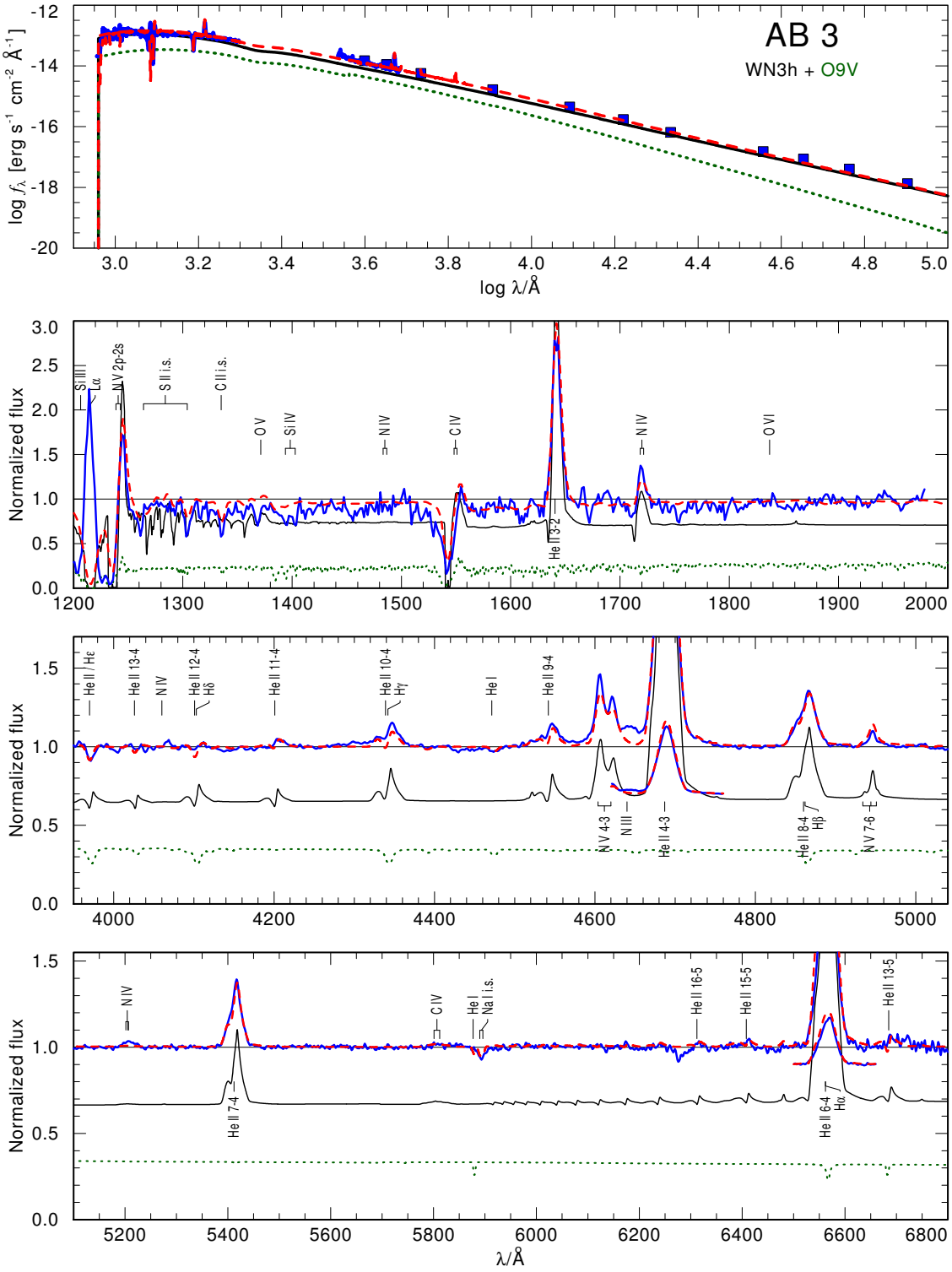

Figure C.3.: A comparison between the best fitting composite model spectrum (red line) and the observations (blue squares and lines) for the SED (upper panel) and normalized spectra (lower panels) of SMC AB 3. The composite model is the sum of the WR model (black line) and companion model (green line). The observed UV spectrum was taken with IUE in 1988 (ID:sp33457, $\phi = 0.3$), and the optical spectrum are co-added spectra from FMG (see Sect. 6.3).

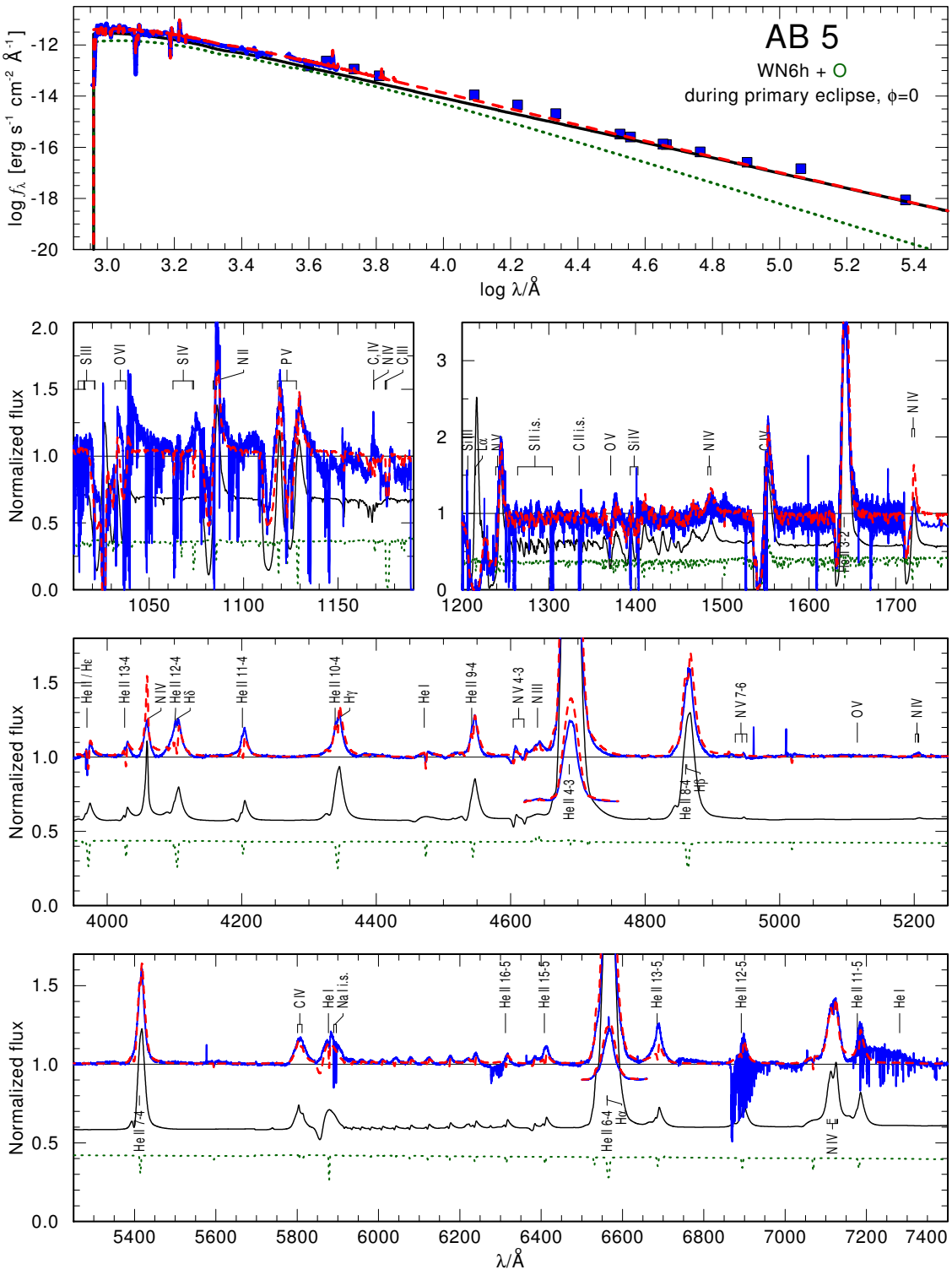

Figure C.4.: Same as Fig. C.3, but for SMC AB 5 during an eclipse of the primary by the secondary ($\phi = 0$). The UV spectra shown were taken with FUSE in 2002 (ID:p223010100000, $\phi \approx 0$) and HST in 2009 (ID:ob2na1020, $\phi \approx 0$). The optical spectrum consists of the co-added FEROS spectra at $\phi \approx 0$, described in Sect. 6.3. Note that most photometry measurements (blue squares) were taken outside eclipse, which is why the total model fails to reproduce their values. Fig. C.5 shows a fit to the system outside eclipse.

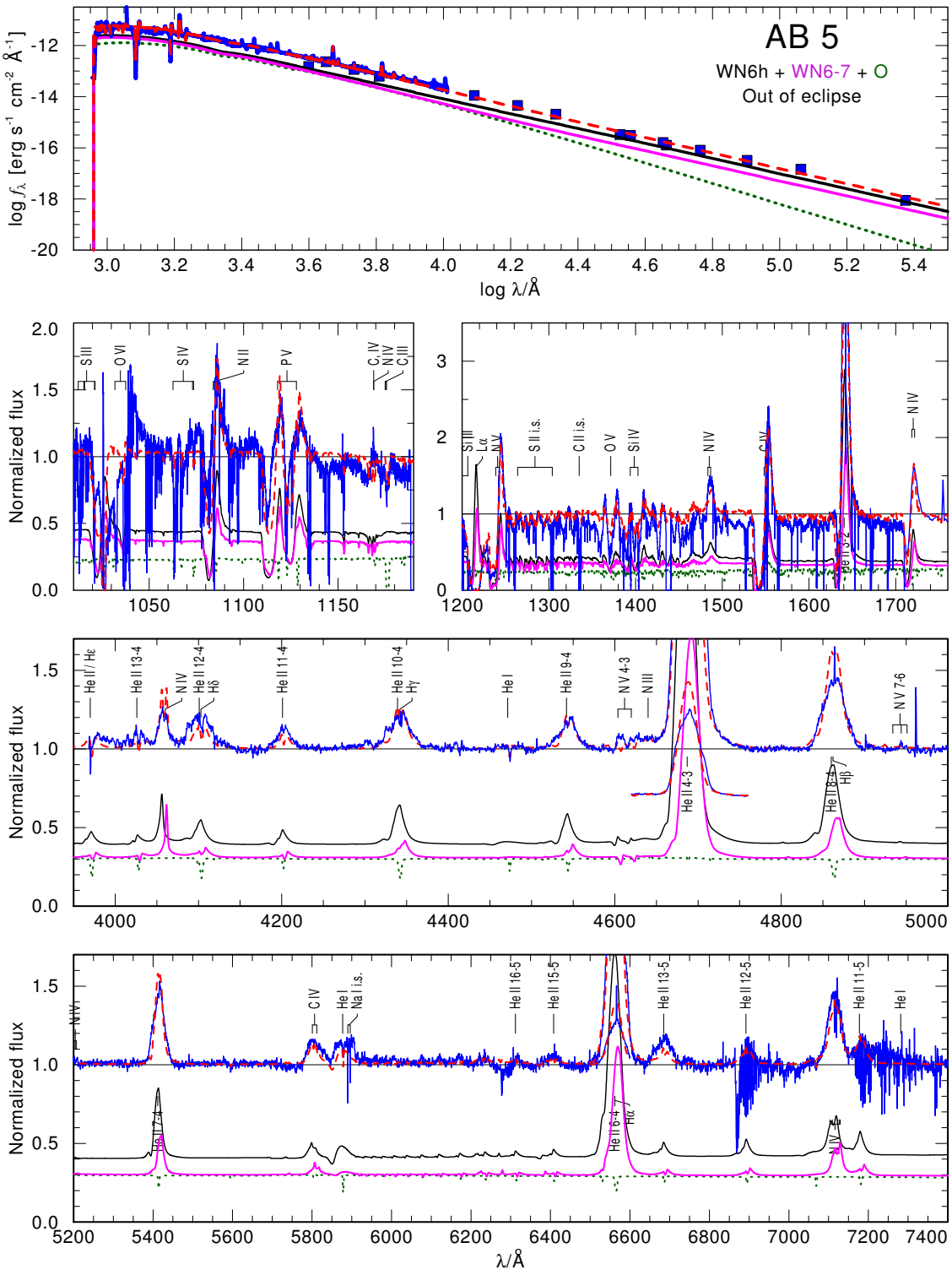

Figure C.5.: Same as Fig. C.4, but showing a fit to out-of-eclipse spectra of SMC AB 5. The UV spectra were taken with FUSE in 2002 (ID:p223010700000, $\phi = 0.74$) and HST in 1999 (ID:O55Q01070, $\phi = 0.83$). The optical spectrum was taken with FEROS in 2005 (ID:f0921331, $\phi = 0.81$).

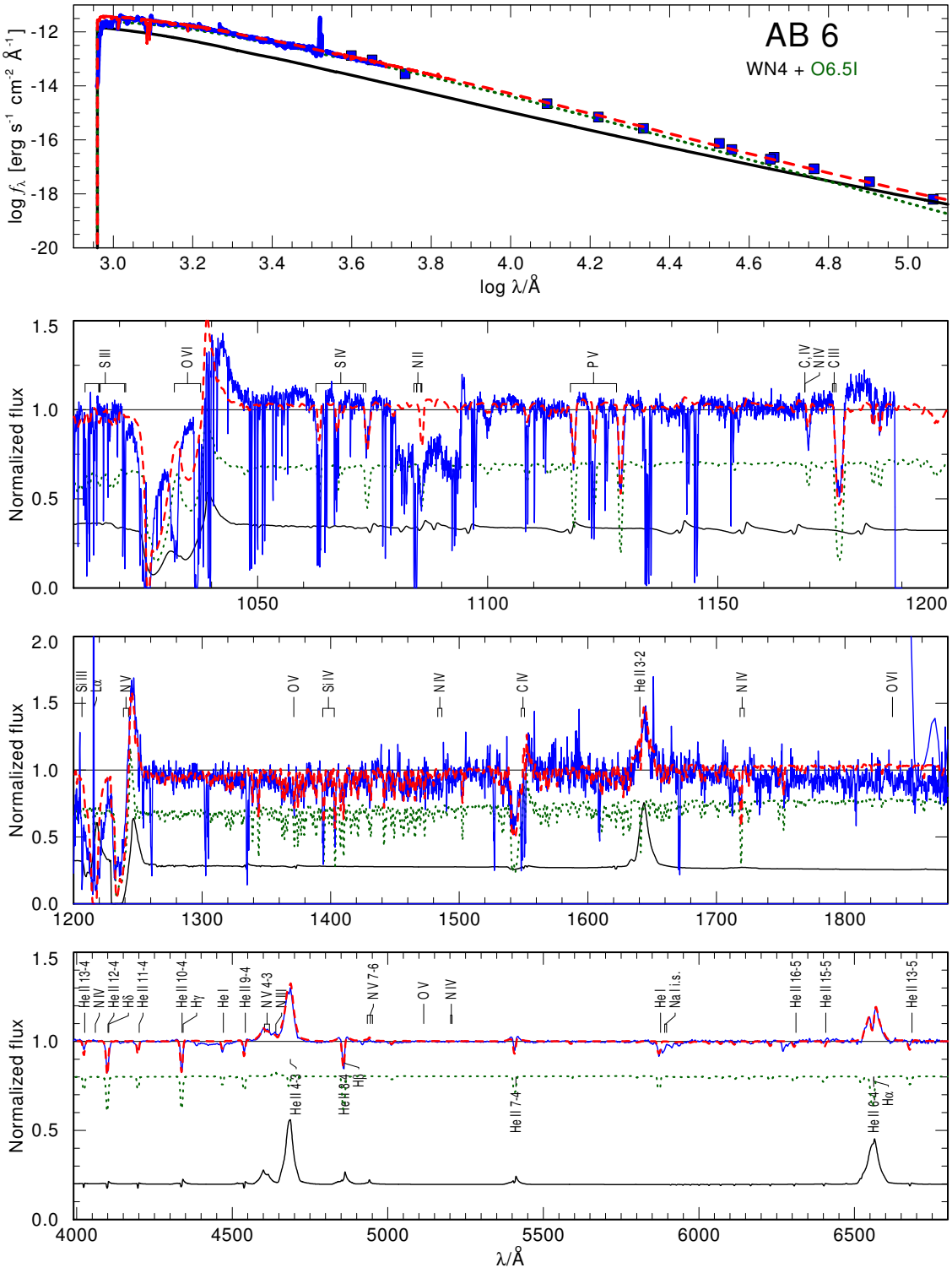

Figure C.6.: Same as Fig. C.3, but for SMC AB 6. The UV spectra were taken with FUSE in 2000 (ID:p103040100000, ϕ = 0.42) and IUE in 1997 (ID:sp41784, ϕ = 0.48). The optical spectrum consists of co-added spectra (see Sect. 6.3).

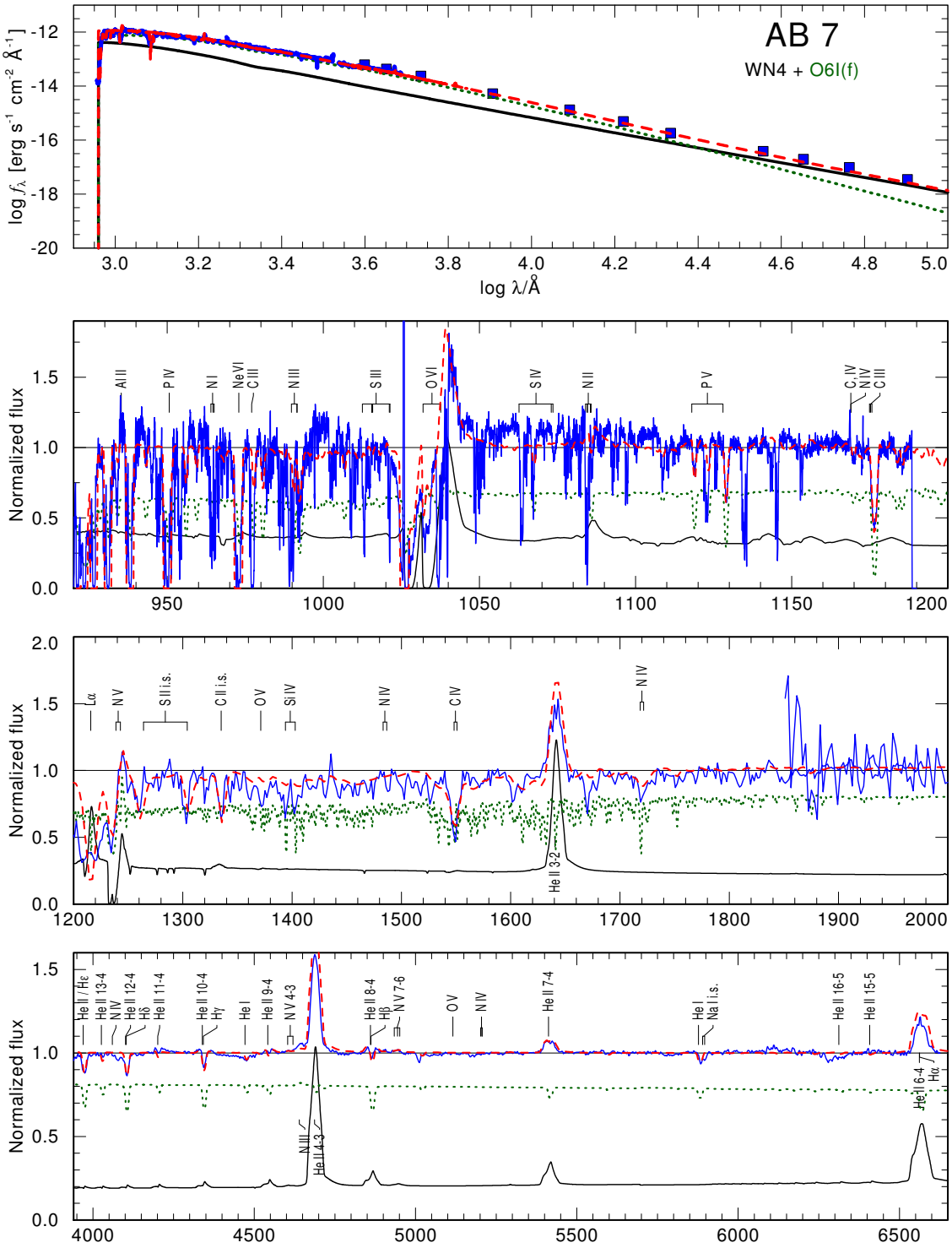

Figure C.7.: Same as Fig. C.3, but for SMC AB 7. The UV spectra were taken with FUSE in 2001 (IDLp2430101000, $\phi = 0.93$) and IUE in 1988 (ID:SWP33300, $\phi = 0.69$). The optical spectrum consists of co-added spectra (see Sect. 6.3).

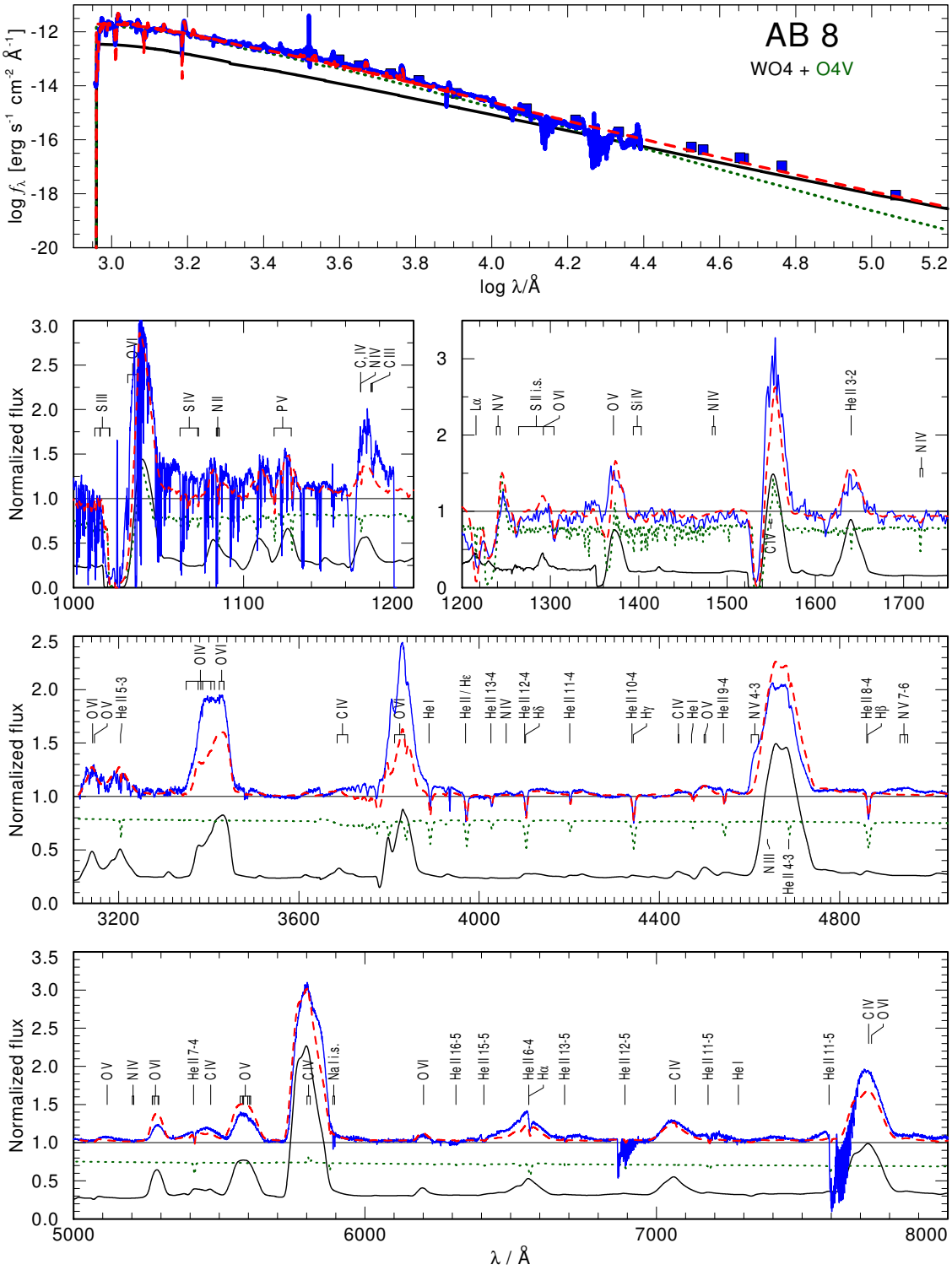

Figure C.8.: Same as Fig. C.3, but for SMC AB 8. The UV spectra were taken with FUSE in 2000 and IUE in 1980 (ID:sp07623, $\phi = 0.79$). The FUSE spectrum consists of co-added spectra around phase $\phi = 0.5$. The optical spectrum was taken with XSHOOTER in 2013 (see Sect. 6.3).